

**The University of
Nottingham**

UNITED KINGDOM • CHINA • MALAYSIA

**Enhanced Flame Retardant Polymer
Nanocomposites**

Sherif Elbasuney

Thesis submitted to the University of Nottingham for
The degree of Doctor of Philosophy
January 2013

Declaration

I, Sherif Elbasuney, hereby certify that this Thesis has been composed by myself and that it is a record of my own work over the period from January 2010 to December 2012.

Except where specific reference is made to other sources or collaborators, the work presented in this Thesis is the original work of the author. It has not been submitted, in whole or in part, for any other Degree.

Signed

Sherif Elbasuney

Abstract

Fire is a continuous threat to life and property. The total annual UK fire loss is estimated to be 0.25% of its gross domestic product (GDP) (Goddard, 1995). According to fire statistics, more than 12 million fires break out every year in the United States, Europe, Russia, and China killing about 166,000 people and injuring several hundreds of thousands (Morgan and Wilkie, 2007). Polymers which take up 80% of the organic chemical industry, are known for their high flammability with the production of heat, corrosive toxic gases, and smoke (Bent, 2010). Improving the fire retardancy of polymeric materials is a major concern and also a major challenge. Nanotechnology could have a significant impact on polymeric materials through the achievement of polymer nanocomposites (PNs) with enhanced functional properties (Giannelis, 1996, Schartel and Batholmai, 2006). If this can be achieved, there will be an enormous increase in the use of improved flame retardant (FR) PNs in mass transportation, aerospace, and military applications where fire safety will be of utmost importance (Horrocks and Price, 2008).

In this research project nanoparticles that could have a synergistic effect with traditional FR systems, or that could have a FR action (nano-fire extinguishers), were formulated and surface modified during continuous hydrothermal synthesis (CHS). The bespoke nanoparticles were developed in a structure that could be easily integrated and effectively dispersed into a polymeric matrix. A solvent blending approach for integrating and dispersing colloidal organic modified nanoparticles into polymeric matrices was developed. The impact of nanoparticles of different morphologies including nanospheres, nanoplates, and nanorods on epoxy mechanical, thermal, and flammability properties was evaluated. A laboratory based technique using a Bunsen, video footage, and image analysis was developed to quantify the nanocomposite's direct flame resistance in a repeatable fashion. A new self extinguishing epoxy nanocomposite was developed which showed an enhanced performance in extreme conditions and with good mechanical properties.

Acknowledgement

Firstly I would like to thank my supervisor Prof. Edward Lester for giving me the chance to work on this research project, for his help, time, wide discussions, and for his endless support.

I would like to thank my co-supervisor Prof. Irevine Derek for his collaboration, guidance, time, and helpful advices.

Also I would like to offer thanks to my colleagues Selina Tang and Gimeno Fabra Miquel for their support in doing some lab work.

I would like to thank all lab technical staff who supported me through my research work especially David Clift, Thomas Buss, and Vikki Archibald.

I also want to express my gratitude to my father, my mother, and my entire family members.

Especial gratitude and thanks to my wife for her support and advices through my research study.

I would like to express my gratitude to my sponsor the Egyptian Armed Forces for the financial support to my research study.

Contents

List of Figures	vi
List of abbreviations	xix
List of symbols.....	xxiv
CHAPTER 1.....	- 1 -
1. INTRODUCTION	- 1 -
1.1 Motivation.....	- 2 -
1.2 Aims.....	- 3 -
1.3 Objectives.....	- 3 -
1.4 Thesis structure.....	- 5 -
CHAPTER 2.....	- 7 -
2. LITERATURE REVIEW.....	- 7 -
2.1 Introduction to flame retardancy.....	- 7 -
2.1.1 Physical properties of flame retardants.....	- 9 -
2.1.2 Chemical properties of flame retardants.....	- 9 -
2.2 Fire testing methods.....	- 10 -
2.2.1 Limiting oxygen index (LOI).....	- 11 -
2.2.2 UL 94 V.....	- 12 -
2.2.3 Cone calorimeter.....	- 14 -
2.2.4 Fire resistance.....	- 15 -
2.3 Flame retardant additives and mechanisms.....	- 16 -
2.3.1 Metal hydroxides.....	- 16 -
2.3.1.1 Aluminium tri-hydroxide (ATH).....	- 17 -
2.3.1.2 Magnesium di-hydroxide (MDH).....	- 19 -
2.3.2 Halogenated flame retardants.....	- 20 -
2.3.3 Antimony-halogen synergism.....	- 21 -
2.3.4 Phosphorous-based flame retardants.....	- 22 -
2.3.4.1 Inorganic phosphates.....	- 23 -
2.3.4.2 Metal phosphinates.....	- 24 -
2.3.5 Nitrogen based flame retardants.....	- 24 -
2.3.6 Reactive flame retardants.....	- 25 -
2.3.7 Intumescent flame retardant system.....	- 25 -
2.3.8 Nanoparticles.....	- 28 -
2.3.8.1 Nanoclays.....	- 29 -
2.3.8.2 Carbon nanotubes (CNTs).....	- 30 -
2.3.8.3 Nanoscale particulate additives.....	- 32 -
a) Silsesquioxane (POSS).....	- 32 -

b) Metal oxides.....	- 33 -
2.4 Flame retardant synergism	- 34 -
2.5 Intumescent coating.....	- 36 -
2.6 Nanoparticle synthesis	- 39 -
2.6.1 Continuous hydrothermal synthesis (CHS)	- 41 -
2.7 Nanoparticle stabilization	- 46 -
2.7.1 Electrostatic stabilization	- 47 -
2.7.2 Steric stabilization	- 49 -
2.8 Integration of nanoparticles into polymers.....	- 50 -
2.8.1 Grafting to approach.....	- 51 -
2.8.2 Grafting from approach	- 51 -
2.9 Previous work.....	- 52 -
2.10 New aspects of flame retardancy	- 55 -
2.11 Summary of literature review	- 57 -
CHAPTER 3.....	- 58 -
3. EXPERIMENTAL PROCEDURE	- 58 -
3.1 Methodology.....	- 58 -
3.2 Formulation and functionalization of nanoparticles by using continuous hydrothermal synthesis.....	- 61 -
3.2.1 Standard operating procedure for the CHS rig	- 63 -
3.3 Characterization of nanoparticles.....	- 65 -
3.3.1 X-ray diffraction (XRD)	- 65 -
3.3.2 Scanning electron microscope (SEM).....	- 67 -
3.3.3 Energy dispersive X-ray spectrometry (EDX).....	- 69 -
3.3.4 Transmission electron microscope (TEM)	- 70 -
3.3.5 Dynamic light scattering (DLS)	- 72 -
3.3.6 Zeta potential measurement	- 73 -
3.3.7 Fourier transform infra-red (FTIR)	- 75 -
3.3.8 Ultra violet-Visible (UV-Vis) spectroscopy	- 77 -
3.3.9 Thermogravimetric analysis (TGA).....	- 78 -
3.4 Characterization of epoxy nanocomposites	- 79 -
3.4.1 The mechanical properties of epoxy nanocomposites	- 80 -
3.4.2 The thermal stability of epoxy nanocomposites	- 81 -
3.5 Summary of experimental procedure.....	- 81 -
CHAPTER 4.....	- 82 -
4. INTEGRATION AND DISPERSION OF DRY TITANIA NANOPARTICLES INTO EPOXY RESIN - 82	
4.1 Integration of dry titania nanoparticles into epoxy resin.....	- 83 -

4.2 Dispersion characteristics of titania nanoparticles into epoxy resin	86 -
4.3 The impact of solid loading level and mechanical mixing on nano-oxide dispersion ..	88 -
4.4 The impact of solid loading level and mechanical mixing on the aggregate morphology..	90 -
4.5 The impact of heating during mixing on nano-oxide dispersion	93 -
4.6 Summary of integration and dispersion of dry titania nanoparticles into epoxy resin-	96 -
CHAPTER 5.....	98 -
5. TITANIA SURFACE MODIFICATION WITH ORGANIC LIGANDS.....	98 -
5.1 Synthesis of titania nanoparticles	99 -
5.2 Titania post-synthesis modification with dodecyl succinic anhydride	103 -
5.2.1 Characterization of DDSA-titania	106 -
5.2.1.1 EDX of DDSA-titania	106 -
5.2.1.2 FTIR of DDSA-titania	106 -
5.2.1.3 XRD of DDSA-titania	107 -
5.2.1.4 TEM of DDSA-titania	108 -
5.2.1.5 UV-Vis of DDSA-titania	109 -
5.2.2 The DDSA surfactant loading level	110 -
5.3 Optimization of titania post-synthesis modification approach	111 -
5.3.1 The impact of capping temperature on surfactant decomposition	111 -
5.3.2 The impact of DDSA feed rate on surface coating efficiency	112 -
5.3.3 The impact of capping solvent on surfactant loading level	116 -
5.4 Synthesis of DDSA-titania via surface modification in the reactor.....	118 -
5.4.1 Surface modification in the reactor for organic metal salt precursor.....	119 -
5.4.2 Surface modification in the reactor for aqueous metal salt precursor	122 -
5.5 Titania surface modification with tributyl phosphate	124 -
5.6 Summary of titania surface modification with organic ligands	129 -
CHAPTER 6.....	130 -
6. STERIC AND ELECTROSTATIC STABILIZATION OF COLLOIDAL TITANIA NANOPARTICLES - 130	-
6.1 Steric stabilization via surface modification with polymeric surfactants	130 -
6.1.1 Titania surface modification with poly acrylic acid	132 -
6.1.1.1 Characterization of PAA-titania.....	134 -
6.1.1.2 Stability mechanism of PAA-titania colloid	137 -
6.1.2 Titania surface modification with poly(ethylene-co-acrylic acid) copolymers...	139 -
6.1.2.1 Titania surface modification with poly(ethylene-co-AA 5 wt %).....	140 -
6.1.2.2 Titania surface modification with poly(ethylene-co-AA 15 wt %).....	143 -
6.2 Electrostatic stabilization of titania colloid	145 -
6.2.1 Post-synthesis electrostatic stabilization of titania colloid	148 -
6.2.1.1 Stability of electrostatically stabilized titania colloid	151 -

6.2.2 In situ electrostatic stabilization of titania colloid	154 -
6.2.3 Post-collection electrostatic stabilization of titania colloid	156 -
6.3 Summary of steric and electrostatic stabilization of colloidal titania nanoparticles	159 -
CHAPTER 7.....	160 -
7. FORMULATION AND FUNCTIONALIZATION OF NANOPARTICLES WITH FLAME RETARDANT PROPERTIES.....	160 -
7.1 Formulation and functionalization of hydroxyapatite ($Ca_5(OH)(PO_4)_3$) (HA)	160 -
7.1.1 Synthesis of hydroxyapatite (HA).....	162 -
7.1.2 Hydroxyapatite surface modification with DDSA.....	163 -
7.1.3 HA surface modification with poly(ethylene-co-acrylic acid 15 wt %).....	167 -
7.1.4 HA surface modification with dodecanedioic acid.....	170 -
7.2 Formulation and functionalization of aluminium-oxide-hydroxide ALOOH (AOH)....	173 -
7.2.1 Synthesis of AOH.....	175 -
7.2.2 Surface modification of AOH.....	177 -
7.2.3 The endothermic action of AOH	180 -
7.3 Summary for formulation and functionalization of nanoparticles with flame retardant properties.....	182 -
CHAPTER 8.....	184 -
8. INTEGRATION AND DISPERSION OF NANOPARTICLES INTO POLYMERIC MATRIX	184 -
8.1 The impact of dry nano-oxide size and shape on dry nanoparticle dispersion.....	185 -
8.2 The impact of surface modification on dry nano-oxide dispersion	188 -
8.3 The impact of the capping solvent on dry DDSA-titania dispersion	190 -
8.4 Direct integration and dispersion of colloidal DDSA-titania into epoxy resin	191 -
8.5 Integration and dispersion of hydroxyapatite into epoxy resin.....	196 -
8.5.1 Dispersion of dry HA and DDSA-HA nanoparticles in epoxy resin	196 -
8.5.2 The direct integration and dispersion of colloidal DDSA-HA into epoxy resin ...	198 -
8.6 Integration and dispersion of poly(acrylamide-co-AA)-AOH into epoxy resin.....	199 -
8.7 Summary of integration and dispersion of nanoparticles into polymeric matrix.....	201 -
CHAPTER 9.....	202 -
9. IMPACT OF NANOPARTICLES ON POLYMERIC MATRIX	202 -
9.1 Mechanical properties of epoxy nanocomposites.....	203 -
9.1.1 Mechanical properties of titania-epoxy nanocomposites	203 -
9.1.2 Mechanical properties of HA-epoxy nanocomposites	205 -
9.1.3 Mechanical properties of AOH-epoxy nanocomposites	207 -
9.2 Thermal stability of titania-epoxy nanocomposite	209 -
9.2.1 The impact of DDSA surfactant on epoxy nanocomposite thermal stability	211 -

9.3 Changes in titania-epoxy nanocomposite structure as a result of heating.....	- 212 -
9.3.1 Quantifying titania-epoxy nanocomposite structural integrity under heating ..	- 213 -
9.4 The direct flame resistance of epoxy resin	- 216 -
9.4.1 The Bunsen flame test	- 216 -
9.4.2 The direct flame resistance of virgin epoxy	- 217 -
9.4.3 Quantifying virgin epoxy direct flame resistance using image analysis	- 218 -
9.5 The direct flame resistance of titania-epoxy nanocomposites.....	- 220 -
9.6 The direct flame resistance of epoxy nanocomposite based on nano-fire extinguishers ...	- 221 -
9.7 Summary of the impact of nanoparticles on polymeric matrix	- 223 -
CHAPTER 10.....	- 224 -
10. MULTI-COMPONENT FLAME RETARDANT SYSTEMS	- 224 -
10.1 Development of multi-component epoxy nanocomposite	- 225 -
10.1.1 Synergism between titania nanoparticles and AP750	- 228 -
10.1.2 Synergism between bespoke nanoparticles and AP750	- 230 -
10.2 Synchronization between AP750 FR action and epoxy initial degradation	- 232 -
10.3 Direct flame resistance of multi-component epoxy nanocomposite	- 234 -
10.3.1 The direct flame resistance of multi-component epoxy nanocomposite based on nano-oxides.....	- 234 -
10.3.2 The direct flame resistance of multi-component epoxy nanocomposite based on nano-fire extinguishers	- 237 -
10.3.3 Summary of multi-component epoxy nanocomposite direct flame resistance ..	- 238 -
10.4 Flammability properties of multi-component epoxy nanocomposites.....	- 240 -
10.4.1 The impact of AP750 on epoxy flammability performance	- 241 -
10.4.2 The flammability performance of multi-component epoxy nanocomposites based on nano-oxides.....	- 242 -
10.4.3 Flammability performance of multi-component epoxy nanocomposite based on nano-fire extinguishers	- 247 -
10.5 Intumescent coating.....	- 250 -
10.6 Conclusion of multi-component flame retardant systems	- 252 -
CHAPTER 11.....	254
11. Conclusions and future work	254
11.1 Conclusions.....	254
11.2 Future work	259
References	263

List of Figures

Figure		Pg.
2.1	Experimental set up for LOI measurement	12
2.2	Experimental set up for the UL94 flammability test	13
2.3	Experimental set up of cone calorimeter measurement	15
2.4	Coated steel plates, (a) before and (b) after, the burning test	16
2.5	European flame retardant consumption in 2007	17
2.6	LOI values of an EVA-compound with different filling level	18
2.7	The gas phase chemical action mechanism of halogenated compounds	20
2.8	Chemical structure of commonly employed halogenated FRs	20
2.9	The chemical structure of commonly used phosphorous-based FRs	22
2.10	The chemical structure of APP	23
2.11	The chemical structure of aluminium diethyl phosphinates	24
2.12	Thermal decomposition of melamine and related products	25
2.13	The interaction of the intumescent components to form a char	26
2.14	The different layers formed during the combustion process	27

2.15	The formed char in a cone calorimeter test (a), the assigned chemical structure of the char from infra red analysis (b)	27
2.16	Nano-additives used for fabrication of the PNs	29
2.17	Unmodified layered silicate (a), layered silicate with interlayer-exchanged alkyl amine ions (b)	30
2.18	The structure of multi wall carbon nanotube (MWNT) (a), single wall carbon nanotube (SWNT) (b)	31
2.19	The effect of SWNTs dispersion on PMMA flammability	31
2.20	Schematic representation of CNT good dispersion on polymer flammability	32
2.21	The chemical structure of silsesquioxane (POSS)	33
2.22	Cone calorimeter test of PMMA-metal oxides nanocomposites	34
2.23	Cone calorimeter test of nano metal oxide with phosphinate in PMMA	36
2.24	Standard fire time/temperature curves	38
2.25	Schematic for nanoparticle synthesis and assembly approaches	40
2.26	Difference in nanoparticle processing by hydrothermal and conventional techniques	40
2.27	Phase change of fluid with pressure and temperature	41
2.28	Water pressure-temperature phase diagram	42
2.29	Water properties versus temperature at 24 MPa	43
2.30	The schematic counter current reactor design and fluid mixing simulation	45

2.31	The flow diagram of CHS technique at University of Nottingham	46
2.32	Electrical double layer near the surface of colloidal particles	48
2.33	Steric stabilization by polymer over colloidal particle surface	49
2.34	Principal routes to inorganic organic core-shell nanoparticles	52
2.35	The residue integrity of epoxy/oMMT (a), epoxy/MWCNT (b)	53
2.36	The structure of a laboratory fire-protection testing furnace	54
3.1	Schematic of continuous hydrothermal synthesis technique	61
3.2	Extraction (a), stabilization (b), and flocculation (c) of colloidal nanoparticles via surface modification using CHS technique. The material in the images is TiO ₂ at 10 nm produced at a reactor temperature of 415 °C	64
3.3	Diffraction of X-rays by a crystal	65
3.4	Schematic diagram of XRD	66
3.5	Schematic of SEM with both electron and X-ray detection	68
3.6	Schematic of TEM	71
3.7	Schematic of light scattering measurement	72
3.8	Schematic of electrophoretic mobility measurement	75
3.9	Schematic of single-beam FTIR spectrometer	76
3.10	Schematic of double-beam UV-Vis spectrometer	78
3.11	Basic components of TGA instruments	79

3.12	The universal mechanical testing machine	80
4.1	The chemical structure of epoxy resin and triethylene tetramine	84
4.2	Mechanical mixing with heating (a), vacuum cast (b)	85
4.3	The impact of vacuum cast onto epoxy nanocomposite structural integrity	85
4.4	Image analysis for the dispersion of 1 wt % TiO ₂ into epoxy	87
4.5	The impact of mechanical mixing and solid loading level on titania P25 dispersion	89
4.6	The impact of solid loading level and mechanical mixing on the P25 aggregate size in epoxy resin	91
4.7	The impact of solid loading level and mechanical mixing on the P25 aggregate perimeter in epoxy resin	92
4.8	The dispersion of 15 wt % titania P25 into epoxy resin after: (a) mechanical mixing only, (b) mechanical mixing with heating	94
4.9	The impact of heating during mechanical mixing on titania P25 dispersion into epoxy resin	94
5.1	Diagram of the continuous hydrothermal synthesis (CHS) apparatus used to generate the nanoparticles	99
5.2	The molecular structure of TIBALD	100
5.3	XRD diffractogram of TiO ₂ nanoparticles produced by CHS	100
5.4	EDX spectrum of titania nanoparticles produced by CHS	101
5.5	TEM image of titania nanoparticles produced by CHS	101

5.6	SEM image of freeze dried TiO ₂ nanoparticles produced by CHS	102
5.7	Adsorption mechanisms of carboxylate ligands on titania nanoparticles	103
5.8	The chemical structure of DDSA	104
5.9	Extraction of DDSA-titania to the organic phase	105
5.10	Schematic of DDSA ring opening and anchoring titania surface	106
5.11	FTIR spectrum of DDSA-titania to that of uncoated titania	107
5.12	XRD diffractograms of DDSA-titania and uncoated titania	108
5.13	TEM image of DDSA-titania	108
5.14	UV-Vis spectrums of DDSA-titania to that of uncoated titania	109
5.15	TGA profiles of DDSA-titania and uncoated titania	110
5.16	DDSA decomposition at capping temperature higher than 270 °C (a), colloidal DDSA-titania at capping temperature 200 °C (b)	112
5.17	The colloidal organic layers for DDSA in toluene (5 ml/min) at: (a) 0.005 M, (b) 0.05 M	113
5.18	The UV-Vis absorption of aqueous layers from colloid dispersion made using different DDSA concentrations	114
5.19	The decrease of DDSA-titania centrifuged layer with the increase of DDSA feed at the capping point	115
5.20	SEM images of DDSA-titania samples produced by using (a) toluene, (b) ethanol, as a capping solvent	117

5.21	TGA profile of DDSA-titania produced by using ethanol as a capping solvent compared to uncoated titania	118
5.22	Schematic for nanoparticle surface modification directly within the CHS reactor	119
5.23	Extraction of DDSA-titania to the organic layer when coating was conducted directly in the reactor using the TIPO	120
5.24	TEM image of DDSA-titania synthesized using TIPO modification in the reactor	120
5.25	FTIR spectrum of DDSA-titania produced by TIPO modification directly within the reactor	121
5.26	TGA profile of DDSA-titania produced by TIPO modification in the reactor compared to uncoated titania	122
5.27	TEM image of DDSA-titania produced via TIBALD modification directly within the reactor using water:IPA mixed solvent system	123
5.28	Mono-, bi-, and tridentate anchorage of phosphonate ligands	124
5.29	The molecular structure of TBP	125
5.30	Extraction of TBP-titania using post-modification process	125
5.31	SEM image of TBP-titania	126
5.32	FTIR spectrum of TBP-titania to that of uncoated titania	127
5.33	TGA profile of TBP-titania to that of uncoated titania	128
6.1	Schematic diagram of adsorbed polymer molecule at the solid-liquid interface	132
6.2	Chemical structure of poly acrylic acid	133

6.3	Steric stabilized PAA-titania colloid in water	133
6.4	Schematic of steric stabilization through: (a) the volume restriction, (b) the osmotic effect	134
6.5	TEM image of PAA-titania	135
6.6	The thickness of the adsorbed PAA layer	135
6.7	Size of colloidal PAA-titania particles by DLS	136
6.8	FTIR spectrum of PAA-titania	137
6.9	Chemical structure of poly(ethylene-co-acrylic acid) copolymer	140
6.10	Extraction of poly(ethylene-co-AA 5 wt %)-titania to the organic phase	140
6.11	TEM image of poly(ethylene-co-AA 5 wt %)-titania	141
6.12	FTIR spectrum of poly(ethylene-co-AA 5 wt %)-titania	142
6.13	Extraction of: (a) poly(ethylene-co-AA 15 wt %)-titania, (b) poly(ethylene-co-AA 5 wt %)-titania to the organic phase	143
6.14	TEM image of poly(ethylene-co-AA 15 wt %)-titania	144
6.15	FTIR spectrum of poly(ethylene-co-AA 15 wt %)-titania	144
6.16	Schematic of London attractive forces	145
6.17	Electrical double layer and corresponding potentials near the surface of negatively charged colloidal particle	147
6.18	Potential energy curves for the interaction of two charged particles	148

6.19	Titania colloid, stabilized via post-synthesis electrostatic stabilization using ammonium phosphate ions	149
6.20	TEM image of electrostatically stabilized titania colloid	150
6.21	The size of electrostatically stabilized titania colloid by DLS	150
6.22	Zeta potential of electrostatically stabilized titania colloid	151
6.23	The dependence of zeta potential on colloid pH	152
6.24	Image of (a) electrostatically stabilized titania colloid, (b) the flocculated titania colloid	153
6.25	Critical coagulation concentrations against counter ion charge	154
6.26	DLS of stabilized titania colloid via electrostatic stabilization in the reactor	155
6.27	The proposed reactor design for in situ electrostatic stabilization	156
6.28	The Zeta potential of electrostatically stabilized titania colloid by phosphoric acid	157
6.29	Schematic for titania electrostatic stabilization with phosphoric acid	158
7.1	TEM image of HA	162
7.2	The XRD diffractogram of HA	163
7.3	DDSA-HA extraction to the organic layer	164
7.4	TEM image of DDSA-HA	164
7.5	FTIR spectrum of DDSA-HA	165

7.6	The TGA profile of DDSA-HA	166
7.7	TEM image of poly(ethylene-co-AA 15 wt %)-HA	168
7.8	FTIR spectrum of HA and poly(ethylene-co-AA 15 wt %)-HA	169
7.9	TGA profile of poly(ethylene-co-AA 15 wt %)-HA	170
7.10	The chemical structure of dodecanedioic acid	171
7.11	The proposed chemical structure of DDA-HA	171
7.12	FTIR spectrum of DDA-HA	172
7.13	TGA profile of DDA-HA	173
7.14	Endothermic decomposition of metal hydroxides versus temperature	174
7.15	AOH colloid for metal salt precursor (aluminium nitrate nonahydrate) at: (a) 0.2 M, (b) 0.05 M	176
7.16	The chemical structure of poly(acrylamide-co-acrylic acid)	177
7.17	The AOH colloidal gel (a), the flocculated poly(acrylamide-co-AA)-AOH nanoparticles (b)	178
7.18	TEM of poly(acrylamide-co-AA)-AOH	179
7.19	XRD diffractogram of poly(acrylamide-co-AA)-AOH	179
7.20	TGA profile of poly(acrylamide-co-AA)-AOH	180
7.21	DSC thermogram of AOH	181
7.22	Phase transition of AOH with XRD	182
8.1	The dispersion of 5 wt %: (a) titania P25, (b) titania	186

produced by CHS, in epoxy resin

8.2	The size of titania produced by CHS: (a) in its colloidal state by TEM, (b) dry powder by SEM	186
8.3	The dispersion of 10 wt %: (a) titania P25, (b) DDSA-titania in epoxy resin	189
8.4	The quantified dispersion of dry DDSA-titania to titania P25	189
8.5	Dispersion of 10 wt %: (a) uncoated titania P25, (b) DDSA-titania (produced by using ethanol as a capping solvent) in epoxy resin	191
8.6	The centrifuged colloidal DDSA-titania (a), the collected DDSA-titania viscous colloid material (b)	193
8.7	Dispersion of 10 wt %: titania P25 (a), colloidal DDSA-titania (b), in epoxy resin	194
8.8	The quantified dispersion of colloidal DDSA-titania to dry DDSA-titania and titania P25	195
8.9	The quantified dispersion of dry HA to DDSA-HA in epoxy resin	197
8.10	Dispersion of 5 wt %: uncoated HA (a), DDSA-HA (b), in epoxy resin	197
8.11	The dispersion of 10 wt %: (a) HA, (b) colloidal DDSA-HA, in epoxy resin	199
8.12	The dispersion of poly(acrylamide-co-AA)-AOH in epoxy resin at: (a) 5 wt %, (b) 10 wt %	200
9.1	Compressive stress-strain response of titania-epoxy nanocomposites	204
9.2	The compressive stress-strain response of HA-epoxy nanocomposites	206

9.3	The mechanical properties of AOH-epoxy nanocomposites	208
9.4	TGA profile for titania-epoxy nanocomposites	209
9.5	The dW/dt profiles for: (a) virgin epoxy, (b) virgin epoxy and the 1% TiO ₂ , (c) all the composite samples	210
9.6	The impact of DDSA on epoxy nanocomposite thermal stability	212
9.7	The morphological evolution of virgin epoxy and epoxy nanocomposite with 10 wt % titania	213
9.8	Structural integrity of titania-epoxy nanocomposites to virgin epoxy under heating	214
9.9	The dimensional stability of titania-epoxy nanocomposites to virgin epoxy	215
9.10	The flammability behaviour of virgin epoxy in direct flame	217
9.11	(a) Virgin epoxy resistance to direct flame, (b) flame removed	218
9.12	Image processing of virgin epoxy, (a) footage frame , (b) binary image	219
9.13	The quantified flame size with time for virgin epoxy	219
9.14	The quantified flame size of titania-epoxy nanocomposite	220
9.15	The quantified flame size of epoxy nanocomposites based on nano-fire extinguishers	222
10.1	The structural integrity of: (a) virgin epoxy, (b) AP750/epoxy, and (c) titania/AP750/ epoxy	227
10.2	The XRD diffractogram of the formed char layer	228

10.3	Effect of TiO ₂ on the degradation of APP	229
10.4	The structural integrity under heating effect of multi-component epoxy nanocomposites based on nanofire extinguishers and nano-oxides	231
10.5	The harmonization between, AP750 FR action (a), and virgin epoxy initiation (b)	233
10.6	The structural integrity under heating effect of, multi-component epoxy nanocomposite (a), and virgin epoxy (b)	234
10.7	The impact of silica on AP750/epoxy direct flame resistance	235
10.8	Direct flame resistance of self extinguishing multi-component epoxy nanocomposite based on nano-oxides	236
10.9	The quantified flame size of titania/AP750/epoxy and alumina/AP750/epoxy compared with virgin epoxy	236
10.10	The quantified flame size of multi-component epoxy nanocomposite based on nano-fire extinguishers	237
10.11	The dimensional stability of, virgin epoxy (a), AP750-epoxy (b), and multi-component epoxy nanocomposite (c), after Bunsen flame test	238
10.12	The cone calorimeter test set up	241
10.13	Evolution of HRR for AP750/epoxy to virgin epoxy	242
10.14	Evolution of HRR for silica/AP750/epoxy, AP750/epoxy, and virgin epoxy	243
10.15	Evolution of HRR for multi-component epoxy nanocomposites based on titania and alumina nanoparticles	244
10.16	The intumescent action of multi-component epoxy nanocomposite based on: (a) titania, (b) alumina, nanoparticles	245

10.17	Evolution of HRR for multi-component epoxy nanocomposites: HA/AP750/epoxy and AOH/AP750/epoxy	247
10.18	The intumescent action of multi-component epoxy based on: HA (a), and AOH (b) nanoparticles	248
10.19	The temperature/time curve for steel and coated steel	251
11.1	TEM Images of: titanate nanotubes (a), titanate nanofibers (b)	260
11.2	Surface functionalization of titanate nanotubes using chemical reactions	260
11.3	Preparation of BTC-MWCNTs/epoxy composites	261

List of abbreviations

AHRR	Average heat released rate
AOH	Aluminium-oxide-hydroxide
AP	Ammonium phosphate dibasic
APP	Ammonium polyphosphate
AP750	APP with an aromatic ester of tris(2-hydroxy methyl)-isocyanurate
ATH	Aluminum tri-hydroxide
BDP	Bisphenol A Bis(Diphenyl phosphate)
CCC	Critical coagulation concentrations
CHS	Continuous hydrothermal synthesis
CNTs	Carbon nanotubes
DDSA	Dodecanyl succinic anhydride
DLS	Dynamic light scattering
DDA	Dodecanedioic acid
EDX	Energy dispersive X-ray spectrometry

EVA	Poly(ethylene-co-vinyl acetate)
FPI	Flammability performance index
FRs	Flame Retardants
FTIR	Fourier transform infrared
FPI	Fire performance index
GDP	Gross domestic product
HA	Hydroxyapatite
HBCD	Hexabromocyclododecane
HC	Hydrocarbon curve
HCM	Hydrocarbon modified curve
HRR	Heat released rate
I_0	The intensity of the incident UV-vis. beam
I	The intensity of the transmitted UV-vis. beam
ICDD	International Centre for Diffraction Data
IFR	Intumescent flame retardant
IPA	Isopropyl alcohol

JCPDS	Joint Committee on Powder Diffraction Standards
K_w	Water dissociation constant
LDH	Layered double hydroxide
LOI	Limiting oxygen index
MDH	Magnesium di-hydroxide
ME	Melamine
MLR	Mass loss rate
MWCNT	Multiwall carbon nanotube
NIST	National Institute of Standard and Technology
oMMT	Organic modified mentmonronolite
PNs	Polymer nanocomposites
PAA	Poly acrylic acid
PBDE	Polybromodiphenylether
PE	Penta erithritol
PHRR	Peak/Maximum heat released rate
POSS	Silsesquioxane

PZC	Point of zero charge
PMMA	Poly(methyl-methacrylate)
RDP	Resorcinol bis-(diphenyl phosphate)
RFPI	Relative fire performance index
ScF	Supercritical fluid
ScW	Supercritical water
ScWHS	Supercritical water hydrothermal synthesis
SEM	Scanning electron microscopy
SWCNT	Single-wall carbon nanotube
TBBPA	Tetrabromobisphenol A
TBP	Tributyl phosphate
TBPA	Tetrabromophthalic anhydride
TPP	Triphenyl phosphate
TTPHRR	Time to peak heat released rate
TEM	Transmission electron microscopy
TGA	Thermogravemetric analysis

TIBALD	Titanium IV bis (ammonium lactato) di-hydroxide
THR	Total heat released
TIPO	Titanium (IV) isopropoxide
TOC	Time of combustion
TTI	Time to ignition
TPP	Triphenyl phosphate
TSNCs	Thermoset nanocomposites
UV-Vis	Ultra violet visible spectroscopy
XRD	X-ray diffraction

List of symbols

$^{\circ}\text{C}$	Degree Celsius
bar	Unit of pressure, 1 bar = 100 000 pascals
M	Molarity
min	Minute
ml	Millilitre
nm	Nanometer
P_c	Critical pressure
T_c	Critical temperature
Φ_{ξ}	Zeta potential
Φ_H	Helmholtz potential
Φ_0	Surface potential
U_E	The electrophoretic mobility of charged particle
ε	The dielectric constant of charged particle
ΔE_{tot}	The total energy of valence electron,

ΔE_{rot}	The rotation energy of valence electron
ΔE_{vib}	The vibration energy of the valence electron
ΔE_{elect}	The electric energy of valence electron
D	Diffusion coefficient
R	Universal gas constant
T	The absolute temperature
rh	Hydrodynamic radius
N_o	Avogadro's number
η	Viscosity
V_A	Attraction potential
V_R	Repulsion potential
V_{tot}	Total interaction energy
K	Boltzmann constant
W	Stability by a factor
T_{10}	Temperature at which 10 wt % loss takes place
T_{50}	The temperature at which 50 wt % loss takes place

CHAPTER 1

1. INTRODUCTION

The work in this thesis follows and brings together research in nanoparticle production (Adschiri et al., 1992, Adschiri et al., 2000, Cabañas et al., 2000), (Lester et al., 2006) by continuous hydrothermal synthesis (CHS); nanoparticle stabilization (Baraton, 2003, Neouze and Schubert, 2008) (Farrokhpay, 2009); and flame retardant hybrid nanocomposites (Horrocks and Price, 2008, Laoutid et al., 2009) (Wilkie and Morgan, 2010).

This thesis focuses on:

- The formulation and the functionalization of bespoke nanoparticles that could improve the flammability properties of polymeric materials.
- The integration and the dispersion of the developed nanoparticles into a polymeric matrix (epoxy resin).
- How the effective level of dispersion can be quantified by using image analysis techniques.
- The impact of the developed nanoparticles on epoxy mechanical, thermal, and flame resistance properties.
- The new trends in flame retardant (FR) PNs by investigating the synergism between well-dispersed nanoparticles and traditional FR agents.

- The development of a multi-component epoxy nanocomposite that is able to self extinguish in real fire conditions with balanced mechanical properties.
- The development of laboratory testing techniques to retrieve some flammability parameters in a repeatable fashion.
- The achievement of an effective intumescent coating as a means of passive fire protection.

1.1 Motivation

Fire is a unique destructive force; it consumes whatever it touches and leaves nothing behind but ash. Global fire losses are estimated to be \$500 million a year (Morgan and Wilkie, 2007). Plastics are a part of almost every component used by man but are known for their high flammability (Bent, 2010); once they are ignited a sequence of exothermic oxidation reactions take place with the evolution of heat, corrosive toxic gasses, and smoke. Flammable dripping can take place; this flammable behaviour can spread out the flame and complicate the fire hazards (Madorsky, 1964, Wilkie and Morgan, 2010). For instance, the fire risk scenario in modern cars is not just from the fuel tank rupturing and leading to fire but also from the fact that there is 90-100 kg of plastic (solid fuel) inside the automotive compartment where passengers are located (Digges et al., 2008). There is a great demand for FR products in domestic houses, transportation, aerospace, and military applications.

Improving the fire retardancy of polymeric materials is a priority and also a major challenge. According to the National Institute of Standard and Technology (NIST), FR materials can increase the allowable escape time by

a factor of 15, minimizing the heat release by 75%, and evolving less smoke and toxic gases (Nelson and Wilkie, 2001). The human and economic cost of fire can be significantly reduced by the appropriate use of FR materials and fire protection systems.

1.2 Aims

- The development of nanomaterials that can be integrated into polymers in order to improve their FR properties.
- The development of techniques for integrating chemical additives or surfactants onto the nanoparticles to improve their dispersion in the polymeric matrix and subsequent FR properties.
- The evaluation of the PNs mechanical and thermal properties and the quantification of their FR properties.
- The development of an intumescent coating that is capable of outperforming current materials such as in terms of heat transfer properties.

1.3 Objectives

- To develop continuous hydrothermal/solvothermal synthesis methods to produce nanomaterials such as, TiO_2 , Al_2O_3 , SiO_2 , $\text{AlO}(\text{OH})$, $\text{Al}(\text{OH})_3$, and $\text{Ca}_5(\text{OH})(\text{PO}_4)_3$ in dispersion. These materials must be produced in a form that can be easily integrated into a monomer or polymer for subsequent nanocomposite production.
- To understand how changing the size, morphology and quantity of nanoparticles in the polymer composite impacts on mechanical, chemical, and physical properties. Particles will be produced at size

ranges from 5nm to 100nm and with different morphologies from flat sheets to rolls, scrolls and solid spheres. These different characteristics may have an impact on flame retardancy.

- To investigate how organic ligands such as dicarboxylates, phosphinates, and diketones, and carboxylic polymeric surfactants such as poly acrylic acid (PAA) and poly(ethylene-co-acrylic acid) can be bound effectively to the surface of nanoparticles to improve their dispersion properties into the organic polymeric matrix. The temperatures that are suitable for capping will also be investigated from 25 °C to 420 °C. These ligands and polymeric surfactants will be mixed at various stages in manufacture: with the metal precursors, immediately after particle production, and post collection.
- Epoxy resin will be used as a case study material where the effects of TiO₂ will be investigated thoroughly. Different types of TiO₂ will be manufactured and compared with commercially available (but dry) TiO₂ powder called Degussa P25. The tests will use different amounts of TiO₂, dispersed as effectively as possible, and the flame retardant, mechanical, and thermal degradation properties will be evaluated.
- The final objective of the project will be to develop a novel nanocomposite resin that can char readily in the presence of heat whilst retaining excellent physical/mechanical resistance to provide a thermally resistant barrier that is greater than the current industry standard of hydrocarbon fire resistance test.

1.4 Thesis structure

- Chapter 1 provides the motivation and the structure of the thesis.
- Chapter 2 reviews the literature regarding flame retardancy mechanisms, additives, testing, formulation and functionalization of nanomaterials during continuous hydrothermal synthesis (CHS), and the development of polymer nanocomposites.
- Chapter 3 represents the research methodology, experimental procedure for commonly used techniques, instruments, and software throughout the work.
- Chapter 4 investigates the relationship between nanocomposite characteristics with processing factors such as solid loading level, mechanical mixing, and heating during mixing.
- Chapter 5 investigates how titania nanoparticles can be surface modified with carboxylic ligands by using CHS, the tuning of hydrothermal parameters to achieve an effective surface modification and the adjustment of surface modification for the purpose of flame retardancy.
- Chapter 6 investigates steric stabilization of colloidal titania nanoparticles via surface modification with organic polymeric surfactants, and electrostatic stabilization of titania colloid via creating a repulsive potential between the colloidal particles.
- Chapter 7 investigates the formulation and the functionalization of bespoke nanoparticles that could have a flame retardant action mainly $\text{Ca}_5(\text{OH})(\text{PO}_4)_3$ (phosphorous-based

retardant action), and AlO(OH) (heat sink material).

- Chapter 8 investigates the integration and dispersion of different nanoparticles of varying morphologies into epoxy resin, and the formulation of polymer nanocomposites via a solvent blending approach with colloidal organic modified nanoparticles.
- Chapter 9 investigates the impact of different nanoparticle morphologies (nanospheres, nanoplates, nanorods) on the mechanical, thermal, and flame resistance properties of epoxy resin and the quantification of nanocomposite direct flame resistance by using image analysis.
- Chapter 10 represents the development of self extinguishing multi-component epoxy nanocomposite with high flammability performance, based on the synergism between bespoke nanoparticles and intumescent FR system.
- Chapter 11 brings together the findings of the thesis and suggests possible avenues for future work.

CHAPTER 2

2. LITERATURE REVIEW

2.1 Introduction to flame retardancy

Fire is a continuous threat to human life and a drain on the economy. For instance, in the United States homes suffer an unwanted fire every 10 seconds and every 2 hours somebody is killed in a home fire (Grand and Wilkie, 2000). Polymers, which account for about 80 % of the organic chemical industry, are known for their high flammability. Once a polymeric material is ignited, a series of thermo-oxidative degradation reactions with flammable dripping take place (Bishop and Smith, 1970). This means that the chemical bonds have been broken, causing the polymer to depolymerize and break up into potential fuel molecules (Cullis and Hirschler, 1981). Clearly, improving the flame retardancy of polymeric materials is a potential method for reducing deaths and damage to property.

Flame retardancy does not mean that the polymeric material will not burn, but rather it will be harder to burn, and in some cases self extinguishing could occur after being ignited (Laoutid et al., 2009). FR systems are introduced to inhibit or to decrease the polymeric material combustion. Halogenated FRs are being phased out due to environmental and toxicological concerns; so much effort is being directed to the development of halogen free FR systems (Buser, 1987, Addink and Olie, 1995). The worldwide market for halogen free FRs increased from US\$ 1.62 billion in 2005 to 2.72 billion in 2010, with a global annual growth rate of 11% due

to the massive increase in polymer applications (Wilkie and Morgan, 2010). The combination between conventional FRs and nanoparticles seems to offer potential for commercial applications as high flame retardancy performance can be achieved at low filler loading levels (Pinnavia and Beal, 2000).

Polymers can be made more fire resistant in different ways. One method is to prevent the access of oxygen to the flame. Another method is to introduce flame inhibitors such as Br[•], Cl[•], or P[•] free radicals (Noto et al., 1996). These free radicals can behave as scavengers for the combustion reactive species such as H[•] and OH[•] (Rosser et al., 1958). This could be accomplished by including FR additives during polymer formulation; these FR additives release the flame inhibitors when the polymer is heated near its ignition temperature. An alternative approach is to introduce reactive additives which are able to integrate into the polymeric matrix through chemical reactions; they are called reactive FRs (Wang and Lin, 1999, Chang and Chang, 1999).

The combustion can be halted and further degradation can be prevented by introducing heat sink materials which decompose endothermically - such as aluminium tri-hydroxide (ATH), and magnesium di-hydroxide (MDH) (Rothon, 2003b). The formation of a barrier against heat and mass loss, such as a char (or an intumescent barrier), is another successful approach (Bourbigot and Duquesne, 2007). Such barriers can be accomplished by introducing intumescent additives such as ammonium polyphosphate (APP), or nano-additives, or a combination of both together (Zhang et al., 2006).

The purpose of the FR system is to reduce the heat supplied to the polymer below the critical level for flame stability. The properties of the FR systems can be further classified into two main categories. The first category is physical properties, which can cool down the reaction medium, form a protective layer, or affect fuel dilution. The second category is chemical properties which can include chemical reactions that can inhibit or slow down the combustion process (Laoutid et al., 2009).

2.1.1 Physical properties of flame retardants

The endothermic decomposition of some metal hydroxides such as ATH and MDH involves cooling down of the reaction medium below the polymer ignition temperature. Such a marked endothermic reaction is known to act as a heat sink (Rothon, 2003b). When the FR agent decomposes with the formation of inert gases such as N_2 , CO_2 , and H_2O these gases dilute the burnable gas mixture, limits the reagent concentration, and the possibility of combustion propagation. Some nano-additives such as metal oxides, layered silicates (mainly organic modified montmorillonite (oMMT)), carbon nanotubes (CNTs), and silsesquioxane (POSS) can provoke the formation of a protective solid barrier between the gas phase where combustion occurs and the solid phase where the thermal degradation takes place. This solid layer acts as a barrier against mass and heat transfer (Laoutid et al., 2009).

2.1.2 Chemical properties of flame retardants

The chemical properties include chemical modification of the exothermic reactions in fire. This modification can occur either in the gas phase, or in

the condensed phase, or in both. The main chemical action mechanisms include:

A) The free radical mechanism is a gas phase reaction. It includes incorporation of FR additives that release specific free radicals such as Cl^\bullet , Br^\bullet , or P^\bullet in the gas phase (Rosser et al., 1958, Wilkie and Morgan, 2010). These radicals can act as scavengers for combustion reactive species such as OH^\bullet and H^\bullet . This modification in the reaction path may lead to a marked decrease in the reaction exothermicity, leading to a decrease in the reaction temperature and the evolved reactive species (Rosser et al., 1958).

B) The condensed phase mechanism includes two types of chemical reaction mechanisms triggered by the FRs. In the first mechanism, the FR accelerates the rupture of the polymer chains, thus the polymer drips and moves away from the reaction zone (Laoutid et al., 2009). In the second mechanism, the FR can provoke polymeric material dehydration, creating a carbonized char layer at the polymer surface. This char layer acts as a physical insulating barrier between the gas phase and the condensed phase (Cunliffe, 2005). In fact, the synchronization between the FR action temperature and the polymer degradation temperature is of utmost importance. Otherwise, the polymer can continue burning and the FR ingredient will not work (Laoutid et al., 2009).

2.2 Fire testing methods

The flammability of polymers can be characterized by their ease of ignition (ignitability), heat released rate, and flame spread rate. These properties

should be determined by using appropriate flammability tests. The following are the most commonly used standard flammability tests.

2.2.1 Limiting oxygen index (LOI)

Limiting oxygen index (LOI) is employed mainly to indicate the material flammability. The LOI value is defined as the minimal oxygen concentration $[O_2]$ in the oxygen nitrogen mixture $[O_2/N_2]$ that either maintains the flame combustion of the material for 3 minutes or consumes a length of 5 cm of the sample, with the sample placed in the vertical position (Wilkie and Morgan, 2010). The sample is inflamed from the top. Equation 2.1 expresses the LOI value.

$$LOI = 100 \frac{[O_2]}{[O_2] + [N_2]} \quad (2.1)$$

According to ISO 4589, the standard sample dimensions are $80 \times 10 \times 4$ mm³ and the sample should be placed vertically at the centre of the glass chimney. The gas mixture flowing upward is homogenized by passing through a glass bed. Materials with LOI value below 21 are said to be combustible. By contrast materials with LOI value above 21 are said to be self extinguishing, because their combustion cannot be sustained without an external energy source (Laoutid et al., 2009). The higher the LOI index the better the polymer flame retardancy. Figure 2.1 shows the experimental LOI set up.

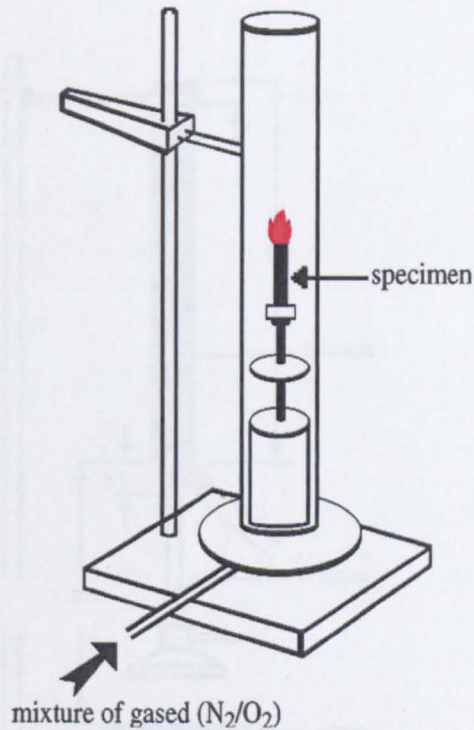


Fig. 2.1: Experimental set up for LOI measurement, adapted from (Wilkie and Morgan, 2010)

2.2.2 UL 94 V

There is a set of standard UL94 tests for the flammability of plastic parts in appliances and devices (Laoutid et al., 2009). The most commonly employed test is UL94 V for measuring the flame spread and ignitability (ease of ignition) of a vertical sample exposed to a small flame. A blue flame with a power of 50 W, and 20 mm height is applied to the bottom of the sample for 10 seconds, and then removed. The afterflame time t_1 (the time required for the flame to extinguish) is noted. The flame is then applied again for another 10 seconds. Then, the afterflame time t_2 is noted, and the afterglow time t_3 is noted (the time required for the fire glow to disappear). According to the standards, five samples must be tested (Morgan and Bundy, 2007). Figure 2.2 shows the experimental set up for the UL94 flammability test.

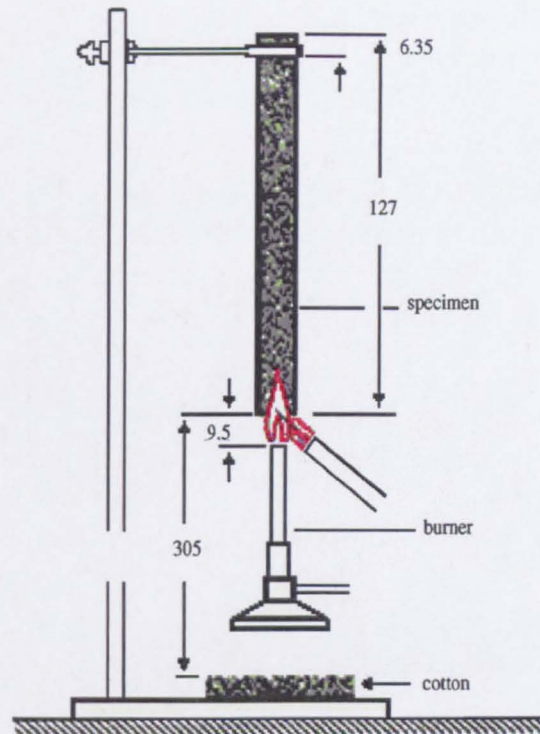


Fig. 2.2: Experimental set up for the UL94 flammability test, adapted from (Laoutid et al., 2009)

The polymer sample is then classified as V_0 , V_1 , or V_2 according to the values of t_1 , t_2 , and t_3 (see Table 2.1).

Table 2.1: The polymer classification according to UL94 flammability test, adapted from (Laoutid et al., 2009)

Fire Classification	
UL94 V_0	<ul style="list-style-type: none"> t_1 and t_2 less than 10 s for each specimen $t_1 + t_2$ less than 50 s for the five specimens $t_2 + t_3$ less than 30 s for each specimen No after flame or afterglow up to the holding clamp No burning drops

UL94 V ₁	<p>t₁ and t₂ less than 30 s for each specimen</p> <p>t₁ + t₂ less than 250 s for the five specimens</p> <p>t₂ + t₃ less than 60 s for each specimen</p> <p>No after flame or afterglow up to the holding clamp</p> <p>No burning drops</p>
UL94 V ₂	<p>t₁ and t₂ less than 30 s for each specimen</p> <p>t₁ + t₂ less than 250 s for the five specimens</p> <p>t₂ + t₃ less than 60 s for each specimen</p> <p>No afterflame or afterglow up to the holding clamp</p> <p>Burning drops allowed</p>

2.2.3 Cone calorimeter

Cone calorimeter is one of the most efficient polymer fire behaviour tests. In this test, a sample of dimensions 100×100×4 mm is placed on a load cell and subjected to a given heat flux generally from 10 to 100 kW/m². The sample is uniformly irradiated from above. The measurements of oxygen concentration in the combustion gases are employed to quantify the heat released per unit time and surface area. The basic principle is Huggett's observation that the released heat from most organic materials is proportional to the quantity of oxygen consumed during burning (Babrauskas, 1984, Laoutid et al., 2009). The peak/maximum heat released rate (PHRR), which is the key point in polymer flame retardancy, can be measured. The average heat released rate (AHRR) and the total heat released (THR) can be measured as well. Furthermore, the cone calorimeter test enables the measurements of time to ignition (TTI), mass loss rate (MLR), and time of combustion (TOC). During combustion, the quantities of CO, CO₂, and the released smoke can be quantified. Figure 2.3 shows the experimental set up for the cone calorimeter testing.

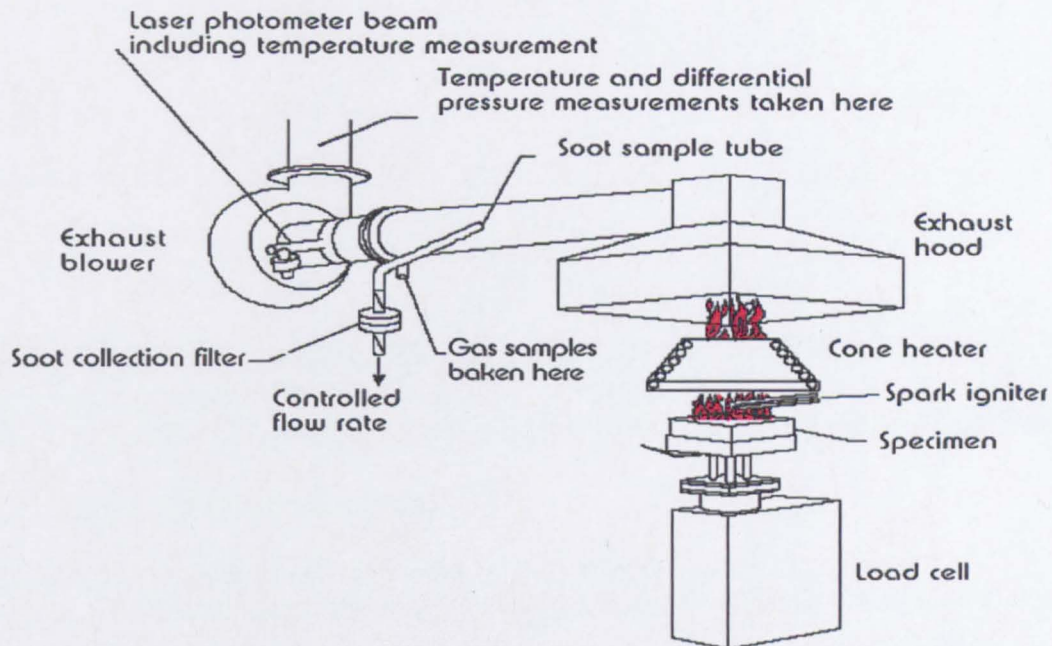


Fig. 2.3: Experimental set up of cone calorimeter measurement, adapted from (Grand and Wilkie, 2000)

2.2.4 Fire resistance

Industrial furnace tests have been carried out according to the standard hydrocarbon fire test UL 1709 (Underwriter-Laboratories, 1994). In this test, steel plates coated with intumescent coating are burned. Generally, the intumescent coating consists of the polymer resin, the intumescent solid additives, and the cross linking agent. The thickness of the coating is 3.5 mm, this is then cured for 1 week at room temperature. Five thermocouples are attached to the back of each plate, so that the average temperature can be obtained. Four plates are evaluated at the same time. The burning conditions simulate the ramp of a hydrocarbon fire temperature through heating rate 200 °C/min up to 1200 °C. The fire protection parameter is the time required for the temperature to reach 400 °C. It is called the time of failure. The longer it is, the higher the

protection is achieved. This test produces time/temperature curves and characterizes the heat protective effect of the different coatings in a hydrocarbon fire (Jimenez et al., 2006c). Figure 2.4 shows the coated steel plates in furnace testing.

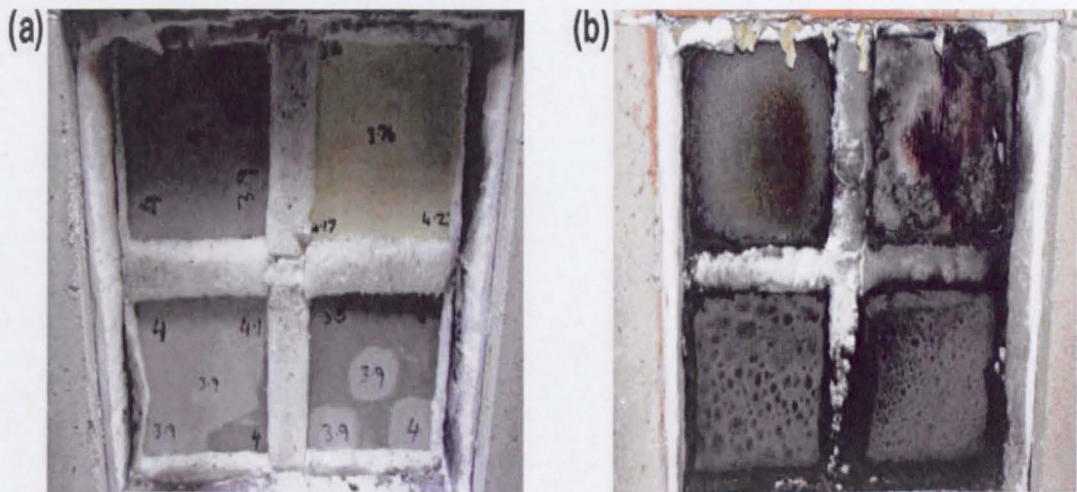


Fig. 2.4: Coated steel plates, (a) before and (b) after, the burning test, adapted from (Jimenez et al., 2006c)

2.3 Flame retardant additives and mechanisms

2.3.1 Metal hydroxides

Inorganic hydroxides represent more than 50% of FRs sold globally. This is due to their low cost, low toxicity, and minimum corrosivity (Wilkie and Morgan, 2010). During their FR action, they reduce the smoke emission during polymer combustion (Lawson et al., 1975, Moseman and Ingham, 1978). Figure 2.5 shows European FR consumption in 2007.

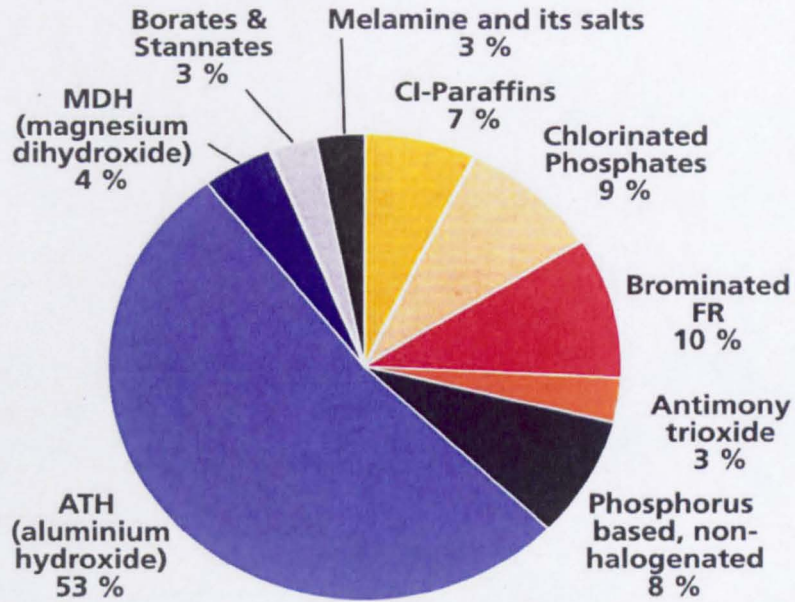
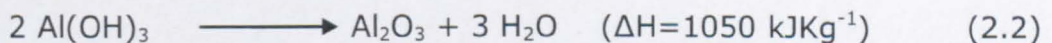


Fig. 2.5: European flame retardant consumption in 2007, adapted from (Pinfa, 2010)

2.3.1.1 Aluminium tri-hydroxide (ATH)

Aluminium tri-hydroxide (ATH) is the largest FR in use by weight. ATH represents about 53% of European FR consumption in 2007 (Wilkie and Morgan, 2010). Over 100,000 ton/year are used in the United States as a FR (Grand and Wilkie, 2000). The major applications are in cable jackets, carpet padding, and unsaturated polyester resins (Grand and Wilkie, 2000). ATH starts to decompose in the range 180-220 °C with the formation of water and alumina (Camino et al., 2001). Equation 2.2 shows the endothermic decomposition reaction of ATH.



The effect of ATH can be summarized by the following main points (Pinfa, 2010):

- It acts as a heat sink material and cools down the burning surface via the endothermic reaction.
- A protective layer of Al_2O_3 is formed which acts as an insulating protective barrier.
- Dilution of the combustion gases through the released water vapour.

In accordance with ISO 4589, LOI is still the most commonly used test to describe the flammability of the insulating polymers for cables. LOI values of at least 30% oxygen are necessary to fulfil the basic flame retardancy in wide applications (Pinfa, 2010). A high solid loading level is required to achieve the limiting oxygen index. Figure 2.6 gives the relationship between LOI and different hydrated mineral loading levels in poly(ethylene-co-vinyl acetate) (EVA).

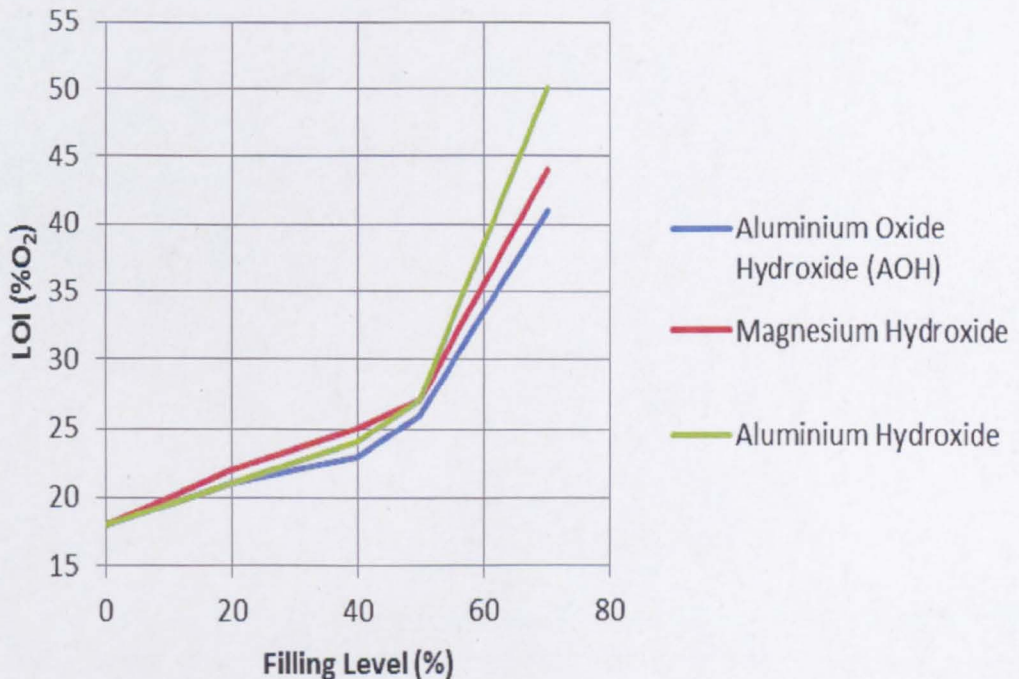


Fig. 2.6: LOI values of an EVA-compound with different filling level, adapted from (Pinfa, 2010)

This high loading level causes deterioration in the polymer's mechanical properties. Recently, much attention has been paid to enhancing the activity of ATH by incorporating small amounts of metal oxides which have a synergistic effect, most likely by stimulating the dehydrogenation during burning over extended temperature range (Grand and Wilkie, 2000).

2.3.1.2 Magnesium di-hydroxide (MDH)

Magnesium di-hydroxide (MDH) acts in similar way to ATH. It provokes an endothermic dissociation reaction accompanied with heat absorption and water release with the formation of MgO as a protective oxide layer (Pinfa, 2010). Equation 2.3 shows the endothermic decomposition reaction of MDH.



The main advantage of MDH over ATH is that the endothermic dissociation of MDH takes place in the high temperature range 300-340 °C, so it is compatible with high temperature processing, including extrusion and injection moulding (Laoutid et al., 2009). More recently, there have been many trials to produce MDH nanoparticles for FR applications. These trials include: sol-gel technique (Utamapanya et al., 1991), hydrothermal reaction, and precipitation of magnesium salts by using an alkaline solution (Laoutid et al., 2009). The replacement of 50 wt% micrometric (2–5 µm) MDH in EVA with nanometric MDH showed improved fire performance; the LOI value increased from 24% to 38.3%. The improved fire performance was attributed to the formation of more compact and cohesive char during the combustion process (Laoutid et al., 2009).

2.3.2 Halogenated flame retardants

Halogenated FR effectiveness depends mainly on the halogen type. Fluorinated compounds are the most thermally stable halides. This is mainly because of the strong carbon-fluorine bonding. The degradation of fluorinated compounds takes place at higher temperatures than most polymer combustion temperature. Conversely iodinated compounds are less stable and degradation takes place at most polymer processing temperatures (Krevelen, 1997). Bromine and chlorine can readily be released during polymer combustion as free radicals and take part in the combustion process in the gas phase by behaving as scavengers for the combustible active species. Figure 2.7 shows the gas phase FR mechanism of halogenated compounds.

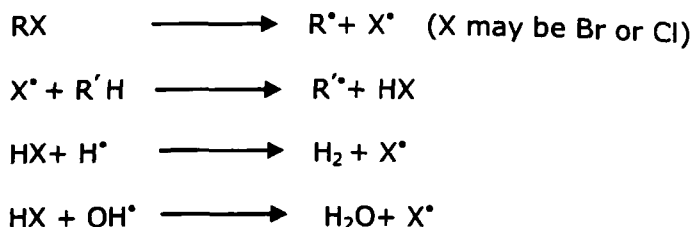


Fig. 2.7: The gas phase chemical action mechanism of halogenated compounds, adapted from (Noto et al., 1996).

The most commonly employed halogenated FR products are represented in Figure 2.8.

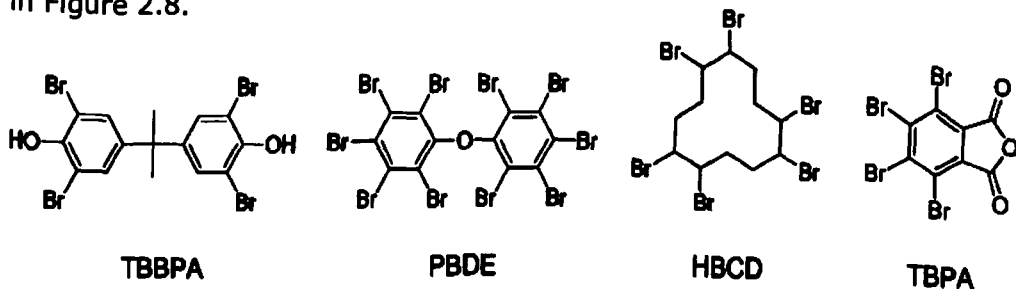


Fig. 2.8: Chemical structure of commonly employed halogenated FRs, adapted from (Laoutid et al., 2009)

Tetrabromobisphenol A (TBBPA) is the most commonly used halogenated FR. It is employed as a reactive FR especially in epoxy resin. Polybromodiphenylether (PBDE) is a large group of halogenated compounds, which can pick up to 10 bromine atoms. The most commonly developed as FRs are penta-, octa-, and deca- bromodiphenylethers. They are mainly used in nylons, polyesters, polyolefins, and styrenic polymers. Penta- and octa- bromodiphenyl ether have been identified as dioxine precursors, so they were phased out. Decabromodiphenyl ether is still in use in some countries outside Europe. Hexabromocyclododecane (HBCD) is currently employed in textiles and compact polystyrene. Tetrabromophthalic anhydride (TBPA) is employed in unsaturated polyesters (Laoutid et al., 2009).

2.3.3 Antimony-halogen synergism

A synergistic effect occurs when the effect of two components together is much greater than the sum of the effects of each individual component (Wilkie and Morgan, 2010). The combination between antimony oxide and halogenated compounds is reported to provide a highly synergistic effect. The commonly employed form of antimony is antimony tri-oxide but when translucency is required colloidal antimony pentoxide is used (Hastie, 1973). Almost halogenated compounds especially brominated compounds are employed with antimony oxide. The synergistic effect is attributed to the formation of antimony tri-halides, which volatilize in the vapour phase as a flame suppressant by scavenging the active radicals such as OH^{\bullet} and H^{\bullet} (Martin and Price, 1968). The optimum combination ratio between bromine or chlorine to antimony is 3:1 which may be proposed on the basis of the formation of SbX_3 (Sallet et al., 1989).

2.3.4 Phosphorous-based flame retardants

Phosphorous-based compounds constitute a large group of FRs. It includes red phosphorous, phosphine oxides, phosphates, phosphonates, and phosphinates (Green, 1996). Figure 2.9 gives the chemical structure of the commonly used phosphorous-based FR compounds. Phosphorous-based FRs are known to be effective in both phases, the condensed phase and the gas phase (Weil, 1986, Babushok and Tsang, 2000). This class of FRs is effective with heterogeneous polymers especially ones that contain oxygen and nitrogen atoms; this can be mainly ascribed to the dehydration and dehydrogenation reactions during these polymers' degradation which result in char formation (Bishop and Smith, 1970).

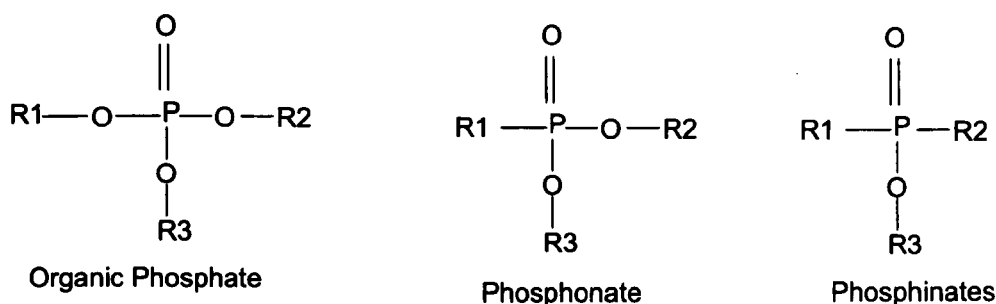


Fig. 2.9: The chemical structure of commonly used phosphorous-based FRs, adapted from (Laoutid et al., 2009)

Phosphoric acid resulted from phosphorous-based FRs decomposition can catalyse the polymer dehydration leading to double bond formation, polymer charring, and subsequently the formation of a cross-linked carbonized structure. The carbonized layer acts as a barrier against heat and mass transfer (Wilkie and Morgan, 2010). Its effect can be summarized as follow:

- Minimizing the volatilization and inhibiting the formation of new active species (H^* , OH^*).

- Minimizing the diffusion of oxygen therefore reducing the combustion.
- Protects the under-layer polymeric materials from combustible reactive species and heat source.

Furthermore, phosphorous-based FRs were identified to have a gas phase effect due to the formation of active species such as PO_2^\bullet , PO^\bullet , and HPO^\bullet . These species vaporize in the gas phase and act as scavengers for combustible reactive species such as H^\bullet , OH^\bullet (Grand and Wilkie, 2000). These compounds are the most effective free radical scavengers. They are 10 times more effective than chlorine, and 5 times more effective than bromine (Babushok and Tsang, 2000, Laoutid et al., 2009).

2.3.4.1 Inorganic phosphates

Ammonium polyphosphate (APP) is an inorganic salt of ammonia and polyphosphoric acid. APP with longer crystalline chains (number of repeating units (n) >1000) is characterized by lower water solubility. It is non volatile and has a high thermal stability. Crystalline APP begins decomposition above 300 °C, leading to the formation of a highly cross linked structure, with the evolution of phosphoric acid which promotes charring. APP is very efficient with heterogeneous polymers (Horrocks, 1986, Laoutid et al., 2009). Figure 2.10 gives the chemical structure of APP.

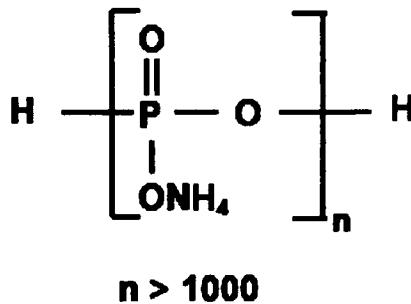


Fig. 2.10: The chemical structure of APP, adapted from (Pinfa, 2010)

2.3.4.2 Metal phosphinates

Metal phosphinates are a new class of non halogenated FRs. Unlike most other phosphorous compounds, metal phosphinates are neither hygroscopic nor toxic and have extremely low water solubility. The key aspects are the high phosphorous content >23 wt % and its good thermal stability (>300°C). To achieve UL94 V₀ rating, solid loading level of 20 wt % is recommended (Pinfa, 2010). Figure 2.11 shows the chemical structure of aluminium diethyl phosphinates.

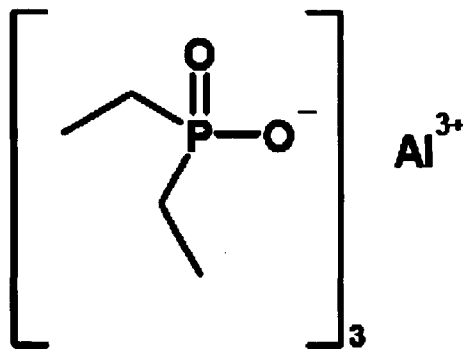


Fig. 2.11: The chemical structure of aluminium diethyl phosphinates, adapted from (Pinfa, 2010)

2.3.5 Nitrogen based flame retardants

Melamine (ME) is a thermally stable crystalline product with a nitrogen content of 67 wt %. ME can sublime with the absorption of a great amount of heat when heated up to 350 °C. The sublimation reaction competes with the decomposition reaction. The decomposition reaction is accompanied with ammonia evolution. The evolved ammonia dilutes the combustion gas species. The decomposition reaction provokes the formation of thermally stable cross linked phase known as melan, melem, and melon (Figure 2.12).

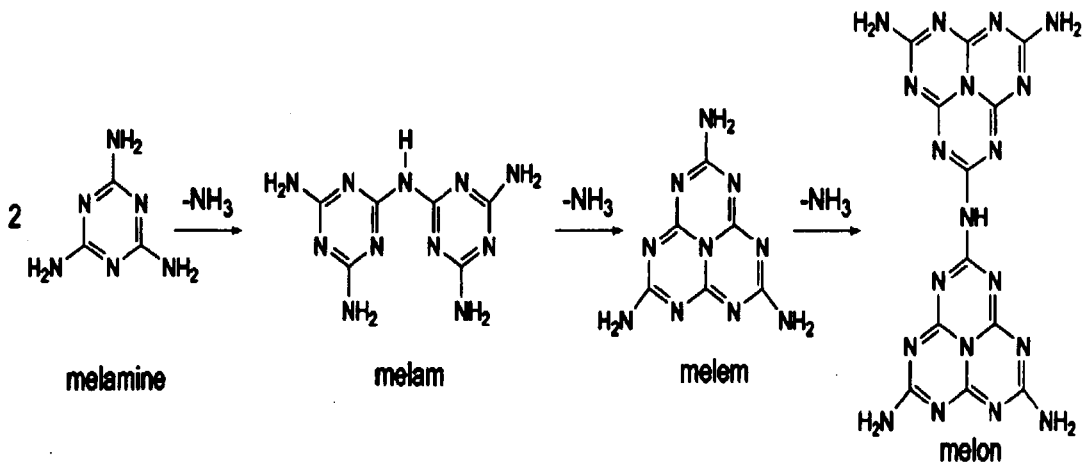


Fig. 2.12: Thermal decomposition of melamine and related products, adapted from (Laoutid et al., 2009)

2.3.6 Reactive flame retardants

Reactive FRs show many advantages (Wang and Lee, 2000, Horrocks and Price, 2008): They have high compatibility with the polymer, minimize the bad impact by heterogeneous additives on the polymer mechanical properties, and minimize the FRs migration to the polymer surface. Halogenated monomers and copolymer can be integrated in the polymer structure. Many studies were directed to achieve curing of epoxy resin with tetrabromobisphenol A (TBBPA), and phosphorous containing compounds (Lin, 2004). However these materials require further synthesis steps which might be problematic at industrial scale (Tchatchoua et al., 1997).

2.3.7 Intumescent flame retardant system

Intumescence is an interesting phenomenon, in which fire is resisted by the formation of an expendable insulating char foam (Bourbigot et al., 2004). This char foam layer separates the oxygen and heat from the polymer surface and extinguishes the fire spread. These FRs were initially

developed for protective coatings. The main components of the intumescent system are (Camino et al., 1984):

- Dehydrating agent (an acid source) such as APP
- Carbonific agent (a carbon rich material) such as penta erithritol (PE)
- Spumific agent (a blowing agent) such as ME

The interaction of these components together to form the char foam is shown in Figure 2.13.

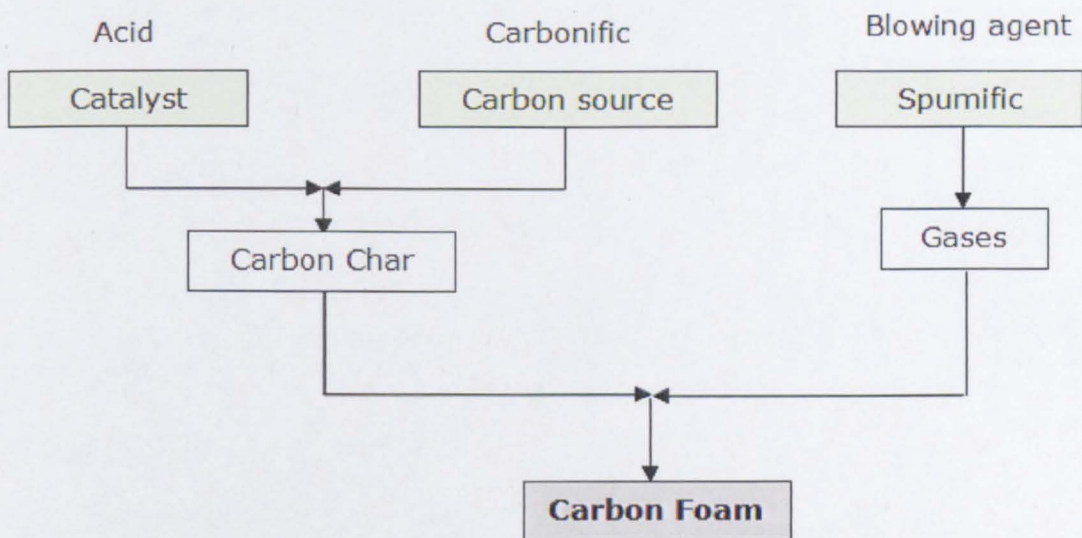


Fig. 2.13: The interaction of the intumescent components to form a char, adapted from (Bras and Gamingo, 1998)

The intumescent system benefits from the synergistic effect between the phosphorous FRs and the nitrogen FRs. Figure 2.14 shows the different layers formed during the combustion process. The intumescent system is known to be effective in polymers containing oxygen and nitrogen. APP is the most commonly used acid source and ME is the most commonly used spumific agent (Camino et al., 1985b). For polymers that resist charring such as poly olefins, a highly charring agent is to be incorporated.

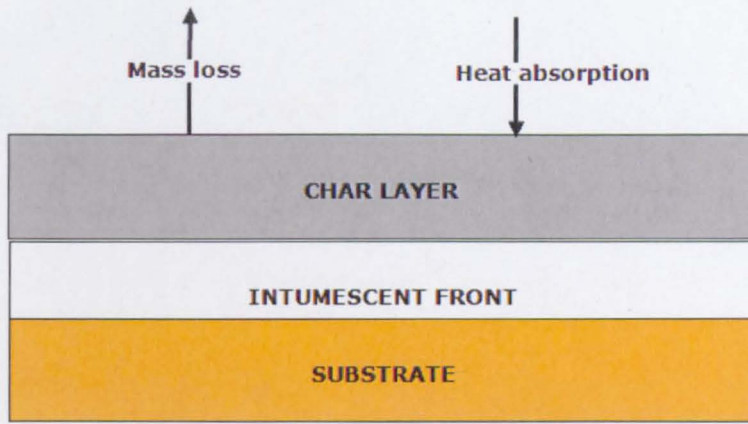


Fig. 2.14: The different intumescent layers formed during the combustion process, adapted from (Bras and Gamingo, 1998)

The most employed charring agent is PE. Unfortunately, PE is hygroscopic and tends to migrate to the surface during the injection and moulding process (Camino et al., 1985b, Kandola et al., 2002). Figure 2.15 shows the formed char by an intumescent system in cone calorimeter testing and the char chemical structure. The tested sample showed 36 wt % loss with self extinguishing. About 10 cm of foamed char was formed and the unburned substance still white.

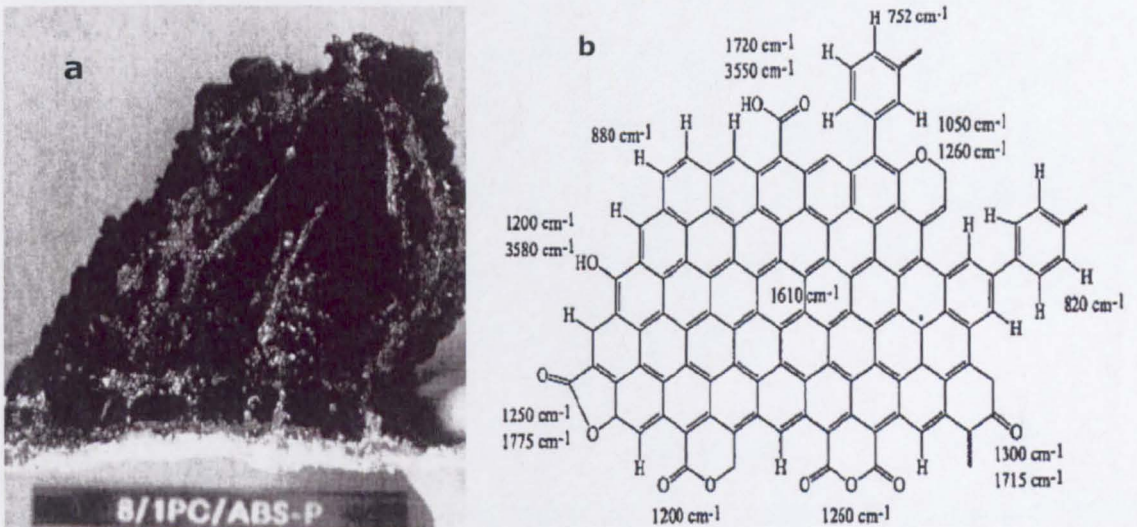


Fig. 2.15: The formed char in a cone calorimeter test (a), the assigned chemical structure of the formed char from infra red analysis (b), adapted from (Bras and Gamingo, 1998, Grand and Wilkie, 2000)

2.3.8 Nanoparticles

The incorporation of low concentrations of nanometer-sized fillers has become an important strategy to improve and diversify polymeric materials (Becker and Simon, 2005). The incorporation of nanometric particles into polymeric matrix results in unique properties when compared with conventional filled polymers. For example, nylon6-layered silicate nanocomposite showed excellent mechanical properties and improved flammability with nanofiller loading of 5 wt % (Grand and Wilkie, 2000). This highlights the main advantage of nanoadditive use i.e. the reduction in weight loading of the additive itself, whilst still achieving the target performance criteria.

PNs can be achieved by incorporating inorganic nanoadditives which have at least one dimension measuring less than 100 nanometer (nm) into the polymeric matrix. The nanoadditives can be classified into four categories according to their dimensionality. The 0-d nanoparticles could be nano-oxide such as titania, silica, alumina, or POSS (Brass et al., 2005). The 1-d nanofiber could be carbon nanofiber, or CNTs which might be single-wall carbon nanotube (SWCNT) or multiwall carbon nanotube (MWCNT) (Dalmas et al., 2006). The 2-d nano-layers include layered silicate e.g. montmorillonite (MMT), and layered double hydroxide (LDH) (Costache et al., 2007b). The 3-d nano networks are rarely used (Figure 2.16).

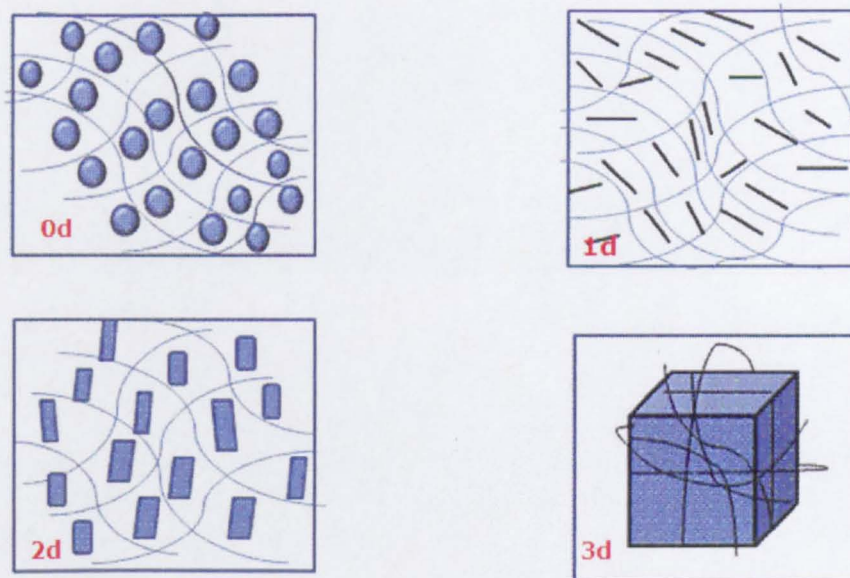


Fig. 2.16: Nano-additives used for fabrication of polymer nanocomposites, adapted from (Giannelis, 1996, Wilkie and Morgan, 2010)

2.3.8.1 Nanoclays

Polymer-clay nanocomposites have unique properties in comparison with conventional filled polymers. The incorporation of relatively low quantities (around 5 wt %) of nanoclay into the polymeric matrix improves its mechanical and FR properties (Horrocks and Price, 2008). It creates a protective layer during combustion which prevents heat and mass loss (Lepoittevin et al., 2002a, Lepoittevin et al., 2002b). In order to increase the compatibility between the nanoclay and the polymeric matrix, natural nanoclay (NaMMT) is often modified with alkyl ammonium, or alkyl phosphonium, or alkyl idizonium cations leading to the formation of organic modified nanoclay (oMMT) (Giannelis et al., 1999). Figure 2.17 shows a model of the structure of unmodified and organic modified layered silicates.

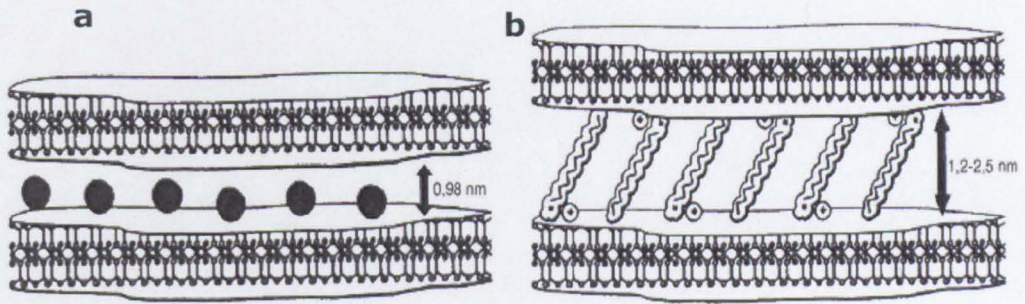


Fig. 2.17: Unmodified layered silicate (a), organic modified layered silicate (b), adapted from (Becker and Simon, 2005)

Layered silicate composite structures fall into three different classes: (a) microcomposites with no interaction between the clay galleries and the polymer, (b) intercalated nanocomposites where the silicate is well-dispersed into the polymeric matrix with polymer chains inserted into the galleries between the parallel silicate platelets, and (c) exfoliated nanocomposites with fully separated silicate platelets individually dispersed or delaminated within the polymeric matrix (Alexender and Dubbies, 2000).

2.3.8.2 Carbon nanotubes (CNTs)

The high aspect ratio of CNTs (length to diameter) enables them to be an interesting alternative to nanoclays and traditional FRs (Cipiriano et al., 2007). At low loading level (0.3 wt %), CNTs have been reported to improve the flammability of a large range of polymers such as EVA (Morlat-Therias et al., 2007), polystyrene (PS) (Kota et al., 2007), and poly(methyl-methacrylate)(PMMA) (Kashiwagi et al., 2005). Figure 2.18 shows the chemical structure of CNTs.

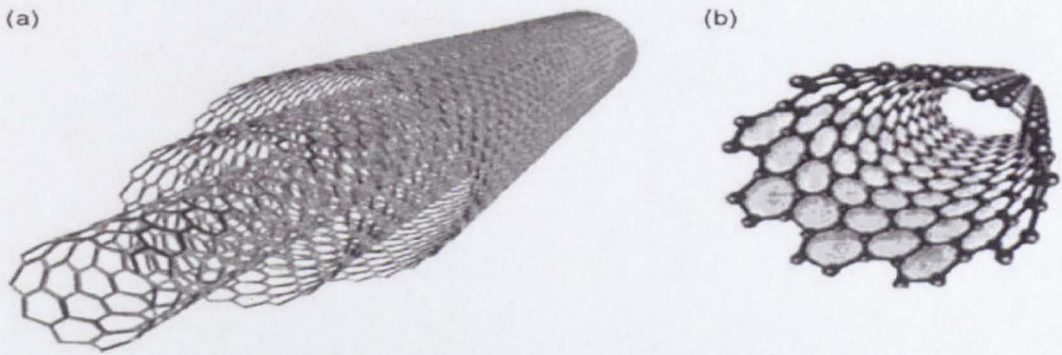


Fig. 2.18: The structure of multi-wall carbon nanotube (a), single-wall carbon nanotube (b), adapted from (Laoutid et al., 2009)

The improved flammability performance can be ascribed to a physical process in the condensed phase. The finely distributed CNTs network can act as a shield and re-emit much of the incident radiation back to the gas phase, in this way the polymer degradation rate is reduced (Kashiwagi et al., 2004). The polymer conductivity increases as the CNTs content increases, thus the heat released rate increases with the increase in CNT content (Cipiriano et al., 2007). Figure 2.19 shows the effect of SWCNT dispersion and concentration on PMMA flammability by cone calorimeter test.

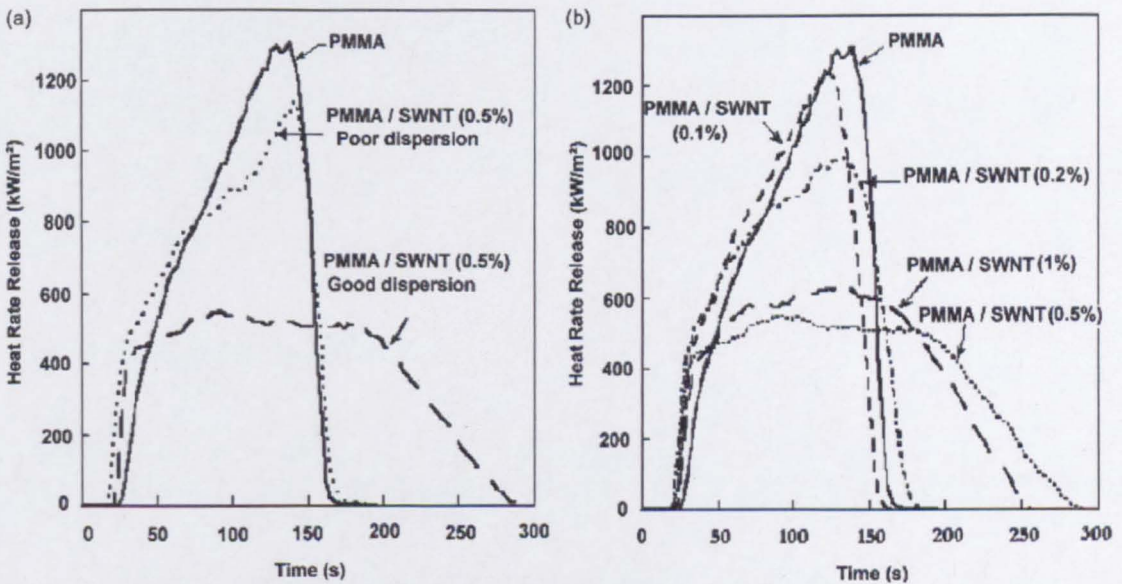


Fig. 2.19: The effect of SWCNTs dispersion (a) and concentration (b) on PMMA flammability, adapted from (Cipiriano et al., 2007)

In fact good dispersion of CNTs is a vital requirement to achieve proper flame retardancy. Figure 2.20 is a schematic presentation of the effect of CNT dispersion on polymer flammability.

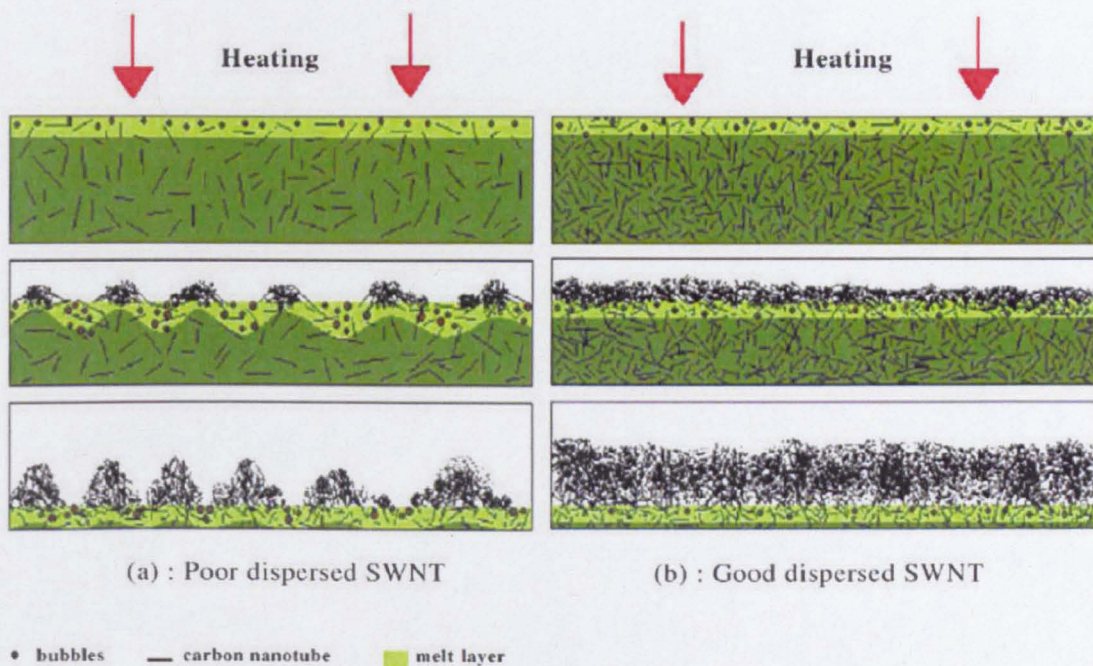


Fig. 2.20: Schematic of the impact of CNT dispersion on polymer flammability, adapted from (Cipiriano et al., 2007)

2.3.8.3 Nanoscale particulate additives

Nanoscale particulate additives include nano-metal oxides and POSS. These nanoparticles are characterized by their isometric dimensions. They proved to be very interesting additives with regard to FR systems (Laoutid et al., 2009).

a) Silsesquioxane (POSS)

Silsesquioxane (POSS) is an inorganic silica-like nanocage with the chemical structure $((\text{RSiO}_{1.5})_8)$. R may be methyl, phenyl, isobutyl, or isooctyl (Horrocks and Price, 2008). This wide range of functionalization

enables the selective use of POSS according to the polymeric matrix (Fina et al., 2005). Figure 2.21 shows the chemical structure of POSS.

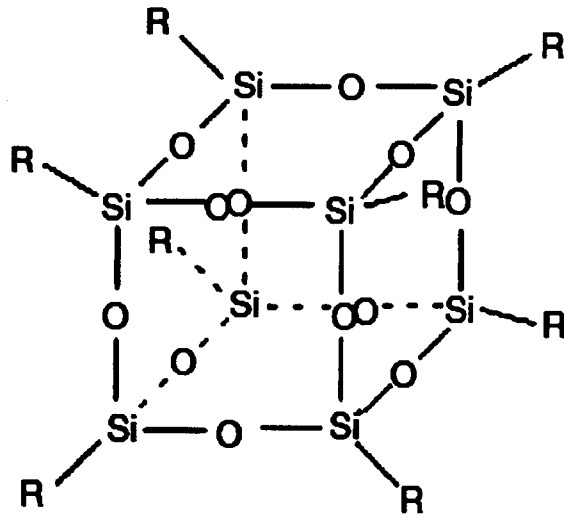


Fig. 2.21: The chemical structure of silsesquioxane (POSS), adapted from (Qiang et al., 2009)

It was reported that POSS plays an effective role in minimising the heat released rate upon polymer combustion throughout the shielding effect in the condensed phase (Qiang et al., 2009).

b) Metal oxides

The incorporation of a small amount (5 wt %) of nano-metal oxides was reported to improve the PMMA thermal stability and flammability properties (Laachachi et al., 2005a). The improved flame retardancy of nano-oxide/polymer nanocomposites can be attributed to the restriction of the polymer chains mobility resulting from the strong interaction between the polymer chains and the nanoparticle surface (Laoutid et al., 2009). It was reported that the flame retardancy of nano-oxides depends on their particle size and surface area (Fu and Qu, 2004, Laachachi et al., 2007).

The PHRR was reduced by 45% when 15 wt % nanometric TiO_2 was used with PMMA, whereas it was reduced by 39% when the same amount of TiO_2 was used in micrometric scale; in both cases the time to ignition increased by 20 seconds (Laachachi et al., 2005a). Figure 2.22 shows the impact of TiO_2 and Fe_2O_3 size on PMMA flammability by cone calorimeter testing.

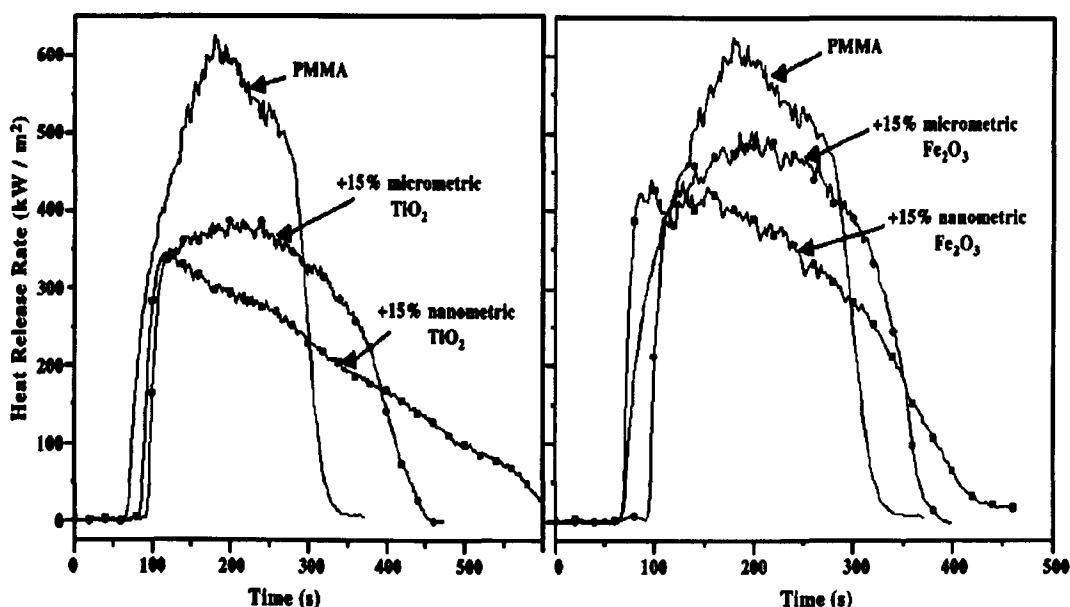


Fig. 2.22: Cone calorimeter test of PMMA-metal oxides nanocomposites, adapted from (Laachachi et al., 2005a)

2.4 Flame retardant synergism

Synergism is achieved when the performance level of a mixture of additives together is greater than that predicted from their linear combination (Samyn et al., 2007, Fontaine et al., 2008). The halogenated-antimony system is being phased out due to environmental and toxicological concerns (Drinker, 1937). The intumescent system based on phosphorous-nitrogen synergism is not a general phenomenon for all polymers; many polymers such as styrenic resins and poly olefins resist charring (Horrocks and Price, 2000). Their thermal degradation is chain scission reactions accompanied with flammable dripping and volatile gases

(Ballice and Reimert, 2002). The commonly employed carbonific agent, penta erithritol (PE), is hygroscopic and migrates to the polymer surface (Halpern et al., 1984).

A high loading level of hydrated minerals (up to 60 wt %) is required to fulfil the flammability standard tests; this high loading level dramatically destroy the polymer mechanical properties (Rothon, 2003b). Recently, most of the research has been directed toward the development of nanocomposite FR materials (Costache et al., 2007a). The new trend in nanocomposite FR materials is the combination between traditional FRs and nanoparticles to achieve high synergistic effect; that fulfils the fire performance standards at low solid loading levels (Laachachi et al., 2005a).

Nanoparticles can be defined as particles with at least one dimension less than 100 nm. The incorporation of nanoparticles such as nano-oxides, layered silicates (oMMT), CNTs, and POSS can improve polymer rheology, mechanical, thermal, and flame resistance properties under fire conditions (Nachtigall et al., 2006). But these PNs still burn, with lower rates, over an extended period of time, with approximately the same total released heat (Marosi et al., 2003). In order to achieve a high flammability performance at low solid loading levels, these nano-fillers should be used in combination with other FRs (Almeras et al., 2003).

In 2005, Laachachi investigated the synergistic effect between phosphinate FR and nano-oxides. The partial substitution of phosphinate by nano-alumina reported a synergistic effect with a marked decrease in peak/maximum heat released rate (PHRR) in cone calorimeter test. However, no significant improvement was achieved through the partial substitution of phosphinate by nano-TiO₂ (Figure 2.23).

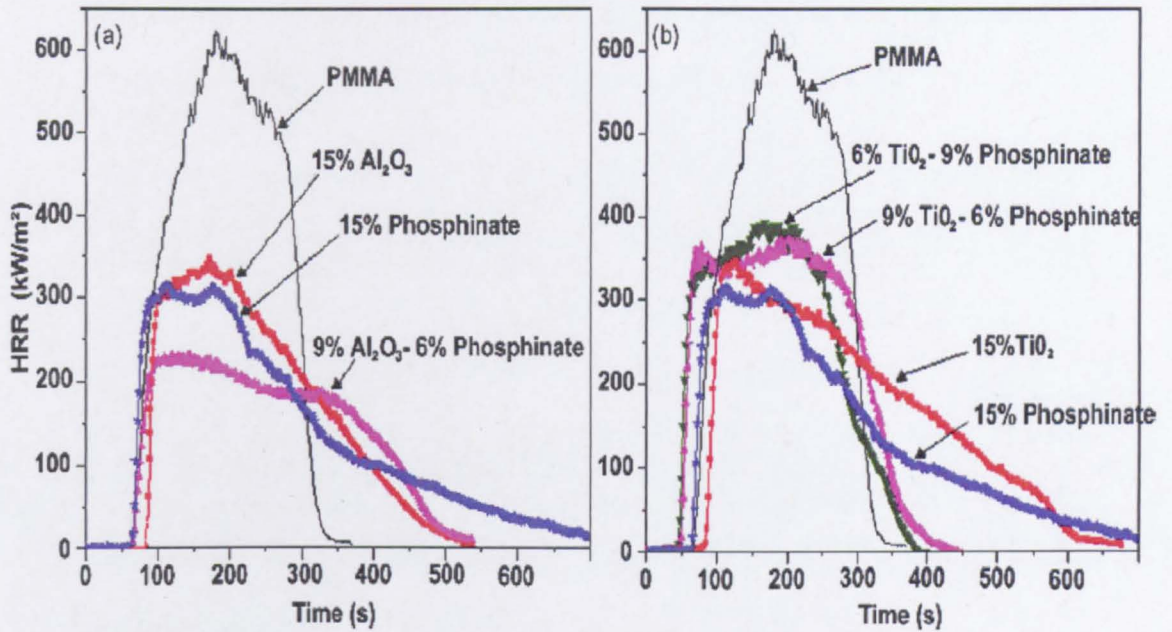


Fig. 2.23: Cone calorimeter test of nano-metal oxide with phosphinate in PMMA, adapted from (Laachachi et al., 2005a)

The synergistic effect seems to depend on the type of the FR system and the nanofiller (Laachachi, 2005). Whereas alumina-phosphinate showed a reinforced continuous protective char layer, titania-phosphinate showed no catalytic effect. This can be ascribed to a certain interaction between the nanofiller and the FR agent in the condensed phase (Gallo et al., 2010).

2.5 Intumescent coating

Intumescent coatings have had a large increase in use as a mean of passive fire protection over the past few years (Xiao, 2010). During heating, the coating swells and its volume increases by 50 fold and in some cases by 200 fold, thus forming a protective barrier against heat transfer from the heat source to the substrate (Wladyka-Przybylak and Kozlowski, 1999). Thermoset nanocomposites (TSNCs) are capable of substantially improving coating performance, in terms of the coating's mechanical, barrier, and flame resistance properties (Xiao et al., 2010).

The ultimate goal is to maintain the integrity and the functionality of the substrate as long as possible in real fire conditions.

Protection of metallic structures against fire has become an important issue in construction, petrochemical industries as well as in the marine and military fields (Jimenez et al., 2006b). Steel structures lose a significant part of their load-carrying ability when their temperature exceeds 500 °C (Kruppa et al., 1998). Intumescent coatings are designed to perform under severe conditions to maintain the integrity of steel structures for 1-3 hrs when the temperature of the surrounding is in excess of 1100 °C (Wilkie and Morgan, 2010).

The intumescent coating performance can be evaluated by standard fire testing. The standard fire test depends on the fire source that the material should resist (Marosi et al., 2003). There are three main categories of standard fire testing curves that simulate the temperature ramp for the three main fire sources (Wang et al., 2007b, Wilkie and Morgan, 2010):

- The cellulosic fire curve (ASTM E119) simulates the rate of temperature increase when the main source of fire is cellulosic in nature, such as wood, furniture, and common building materials. The fire curve is characterized by a slow temperature rise to about 920 °C after 60 min (British-Standard-Institute, 1972).
- The hydrocarbon curve (HC) simulates the temperature increase rate when the fire source is hydrocarbon in nature such as oil or natural gas. The temperature increased rapidly to 900 °C within 4 minutes (Underwriter-Laboratories, 1994).

- The hydrocarbon modified curve (HCM) simulates the jet fire scenarios where the fire source is high pressure hydrocarbon gases, ignited to produce intense erosive jet flames. In this test, the temperature is increased very rapidly up to 1300 °C in a few minutes (HSE-Offshore-Technology, 1996). Figure 2.24 shows the standard time/temperature curves.

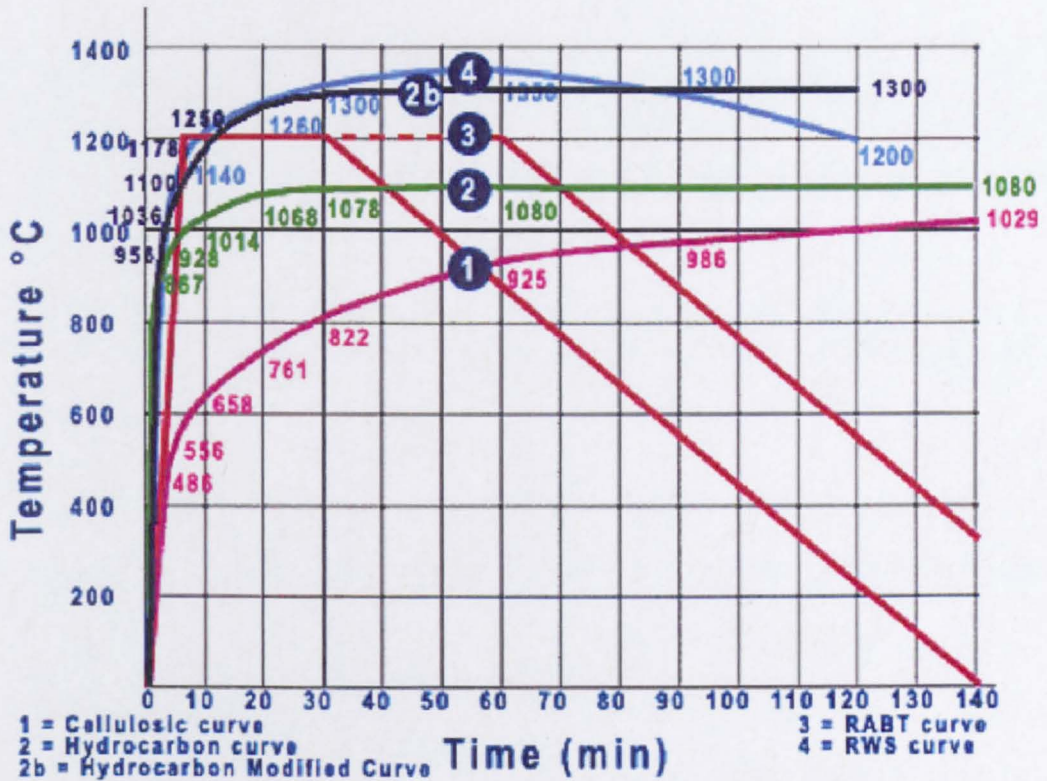


Fig. 2.24: Standard fire time/temperature curves, adapted from (Jimenez et al., 2006b)

Intumescent coating performance is evaluated by monitoring the temperature of the substrate as a function of time under the effect of the fire source. These tests require large industrial scale equipment that is very expensive and time consuming.

The development of small scale laboratory testing should be investigated (Jimenez et al., 2006a). Much research has been directed to establish a lab scale furnace test. In this test, the coated steel plate was placed on a hole

with the coating facing the inner side of the furnace. A digital thermocouple was fixed on the back side of the tested steel plate. The furnace temperature ramp was adjusted to simulate the ramp of hydrocarbon fire source (Li et al., 2007).

2.6 Nanoparticle synthesis

Nanoparticle properties are intermediate between micron sized or bulk materials, and atom scale particles and hence represent opportunities in many applications. In general, there are two strategies to synthesize nanoparticles, the "top-down" and "bottom-up" approaches (Figure 2.25). In top-down approach, a bulk material is broken to smaller pieces by using mechanical, chemical, or other forms of energy such as milling, lithography, and etching (Baraton, 2003).

The bottom-up approach enables the nanomaterial synthesis from atomic or molecular species via vapour condensation/deposition or chemical reactions (Prescott and Schwartz, 2008a). The advantage of the bottom-up approach is that a large variety of structures may be fabricated in a controlled manner. However, the difficulties with all these techniques are in the control of the particles, preventing particle agglomeration, and ensuring the reaction completion (Li, 2008).

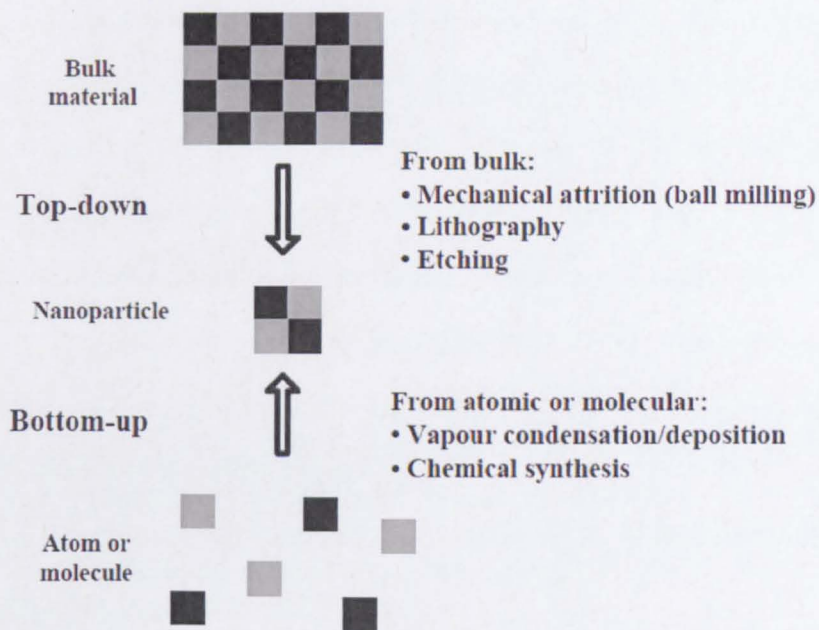


Fig. 2.25: Schematic for nanoparticle synthesis and assembly approaches

Recently, hydrothermal synthesis is becoming one of the most valuable nanomaterial fabrication tools and it has an edge over all other processing techniques (Cabañas et al., 2000, Yoshimura and Byrappa, 2007). Figure 2.26 shows the major product differences between hydrothermal synthesis and all other techniques such as ball milling, sintering, and firing.

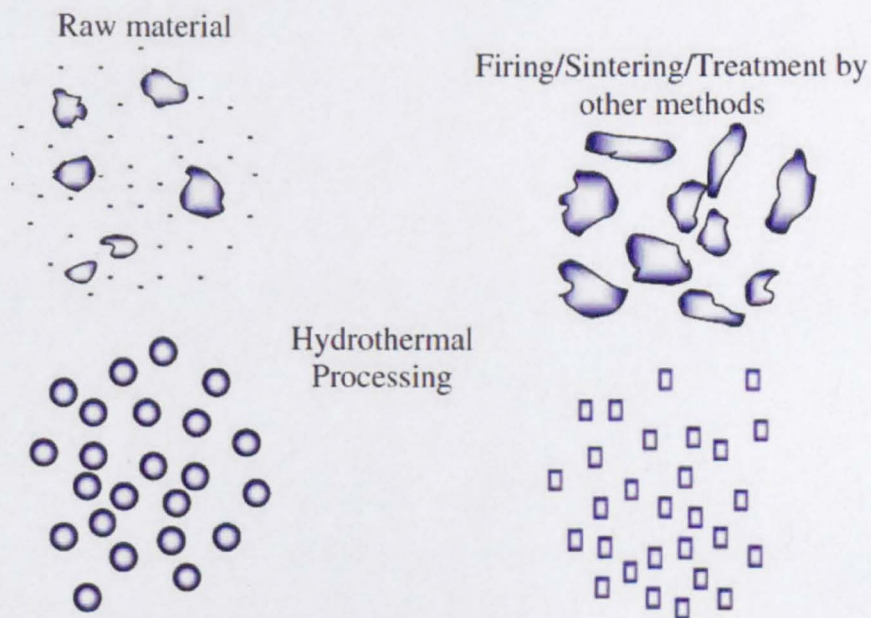


Fig. 2.26: Difference in nanoparticle processing by hydrothermal and conventional techniques, adapted from (Yoshimura and Byrappa, 2007)

Hydrothermal synthesis could be an ideal technique for very fine powder processing with high purity, narrow particle size distribution, and less structure defects with controlled stoichiometry (Li, 2008). Hydrothermal synthesis is characterized by excellent reproducibility and micro structure controlling (Yoshimura and Byrappa, 2008). Through hydrothermal synthesis, the nanoparticle surface properties can be significantly altered from hydrophilic to hydrophobic and vice versa by the proper selection of the capping agent (Yoshimura and Byrappa, 2007).

2.6.1 Continuous hydrothermal synthesis (CHS)

Hydrothermal processing can be defined as any homogenous or heterogeneous chemical reactions that take place at temperature and pressure above normal conditions (25 °C and 1 bar) (Yoshimura and Byrappa, 2007). The employed fluids for hydrothermal synthesis are at supercritical or near supercritical conditions (Byrappa and Yoshimura, 2001). A supercritical fluid (ScF) is defined as any substance at temperature and pressure above its critical values. In a two phase system, near the critical point the gas becomes denser and the liquid becomes less dense. Above the critical point, the phase boundary disappears and a homogenous supercritical phase exists (Savage et al., 1995) (Figure 2.27).

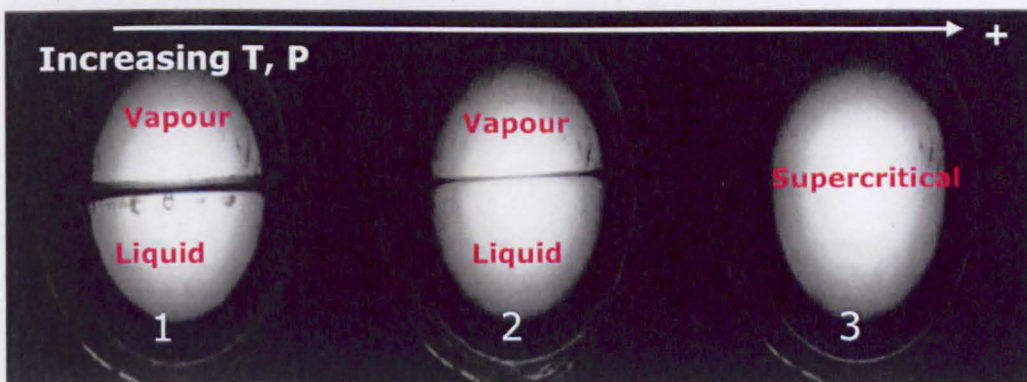


Fig. 2.27: Phase change of fluid with pressure and temperature, adapted from (Hobbs, 2006)

The supercritical phase is a hybridization of liquid and gas properties. ScF has unique properties as it can diffuse through solids like a gas and dissolve materials like a liquid (Morley et al., 2002). Even though, supercritical water (ScW) requires extreme conditions (T_c 374.2 °C, P_c 220.5 bar); it is relatively non-polar but highly acidic (Darr and Poliakoff, 1999). Figure 2.28 shows the water pressure-temperature phase diagram.

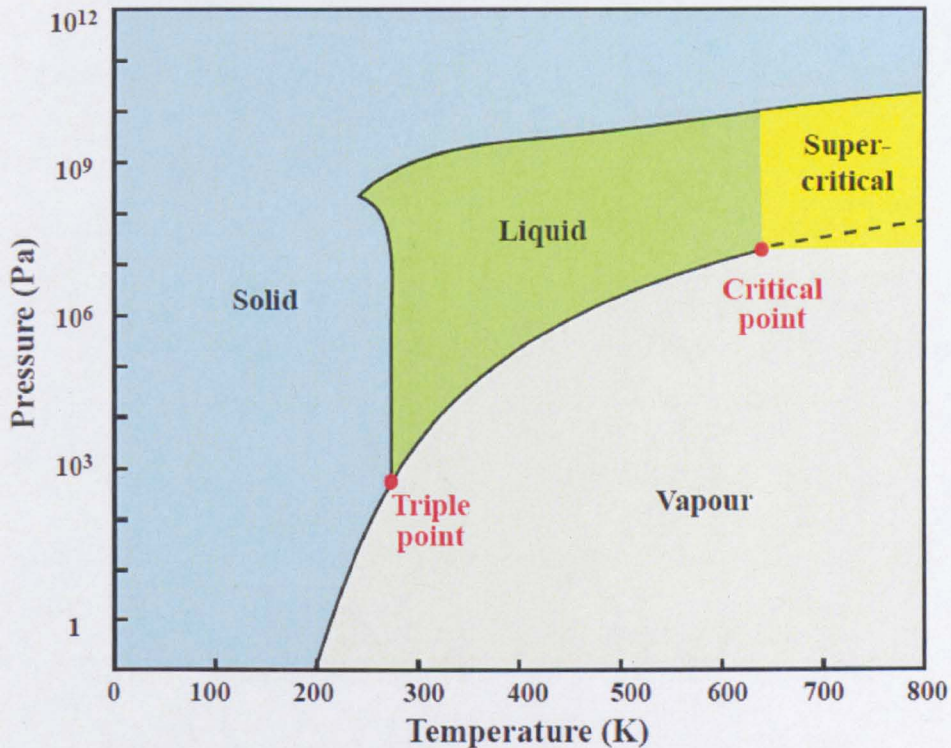
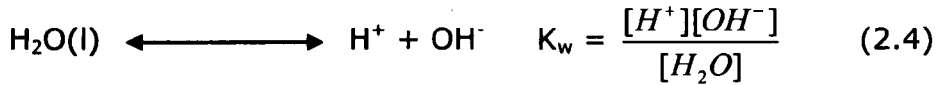


Fig. 2.28: Water pressure-temperature phase diagram

ScW is an ideal supercritical fluid medium; the most important property of ScW is the ability to dissolve gases and organic compounds 100 times more readily than liquid water (Li, 2008). The hydrogen bond strength decreases in ScW; which results in low dielectric constant causing ScW to exhibit non-polar behaviour (Kritzer et al., 1999). The dielectric value of ScW is similar to that of organic solvents such as ethanol, acetonitrile, and acetone under ordinary conditions; in the meantime it is high enough to dissolve and process electrolytes. Furthermore, ScW imposes unique properties related to the number of hydrogen ions (H^+) and hydroxide ions

(OH⁻). Water dissociation constant (K_w) is represented by Equation 2.4 (Perry and Green, 1984).



At standard conditions K_w has the value of 1×10^{-14} mol/l (Perry and Green, 1984, Adschiri et al., 2000). As water approaches its critical point, its dissociation constant increases to about 3 orders of magnitude higher than its dissociation constant at normal conditions; therefore it becomes a suitable solvent for ionic compounds and free radical processing (Savage et al., 1995). However, K_w decreases dramatically over the critical point, e.g. K_w at 600 °C and 250 bar is nine times lower than at ambient conditions (Savage, 1999). Figure 2.29 shows the changes in dielectric constant, density, and ionic product of water with temperature at 24 MPa.

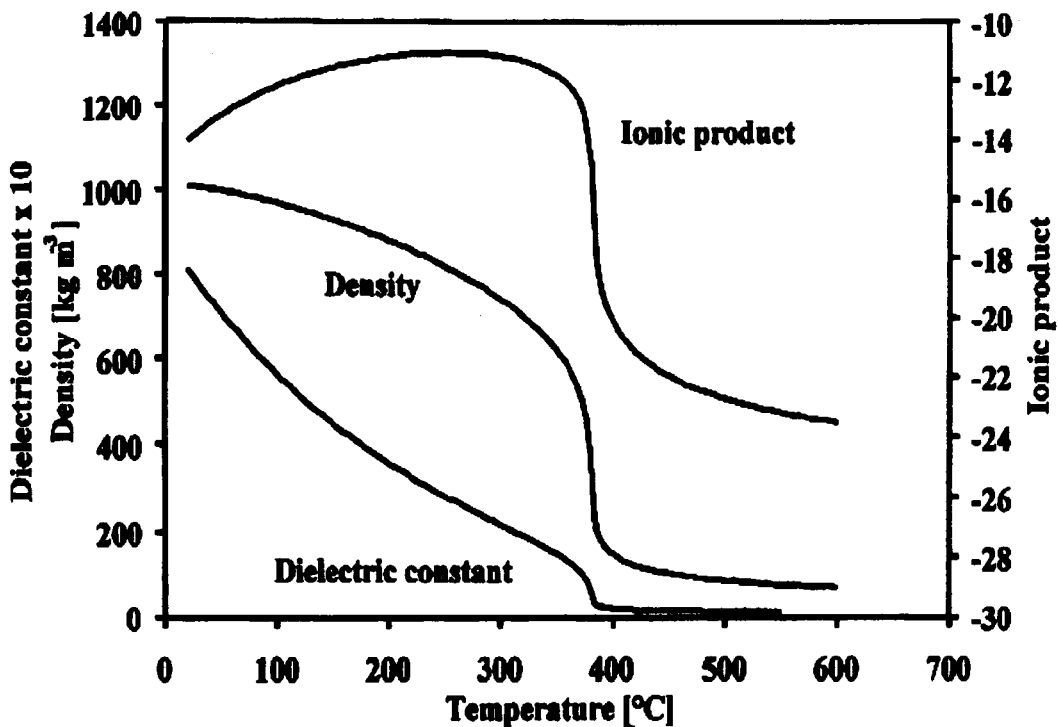
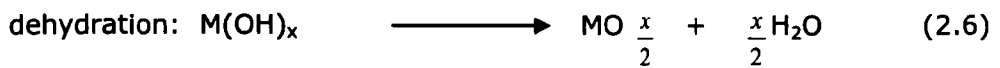


Fig. 2.29: Water properties versus temperature at 24 MPa, adapted from (Kritzer et al., 1999)

The enhanced OH^- level at the critical point can be exploited for nanoparticle synthesis. This can be achieved through hydrolysis of metal salt (Equation 2.5) immediately followed by a dehydration step (Equation 2.6) (Adschiri et al., 1992). Synthesis of metal-oxide nanoparticles can be carried out through these two reactions (Adschiri et al., 2000).



In the past century, hydrothermal synthesis of nanomaterials was performed in batch mode. The batch technique has several drawbacks such as: time consuming, low yield, and poor reproducibility. These factors limit its application on the industrial scale (Matson et al., 1994, Cabañas et al., 2000). Many attempts have been performed to establish continuous hydrothermal synthesis techniques.

In 2006, Lester and Blood established a new continuous nozzle reactor design, which involved counter current mixing of an aqueous metal salt stream with a ScW stream. The design exploited the density difference between the two feed streams; therefore instantaneous and strong mixing was achieved. The metal salt was kept cold until it became in contact with the ScW. There was no upstream mixing inside either reactor inlets. The resultant turbulent micro mixing eddies was streamlined toward the reactor outlet with no stagnation zones. Figure 2.30 shows the counter-current reactor design and the fluid mixing simulation.

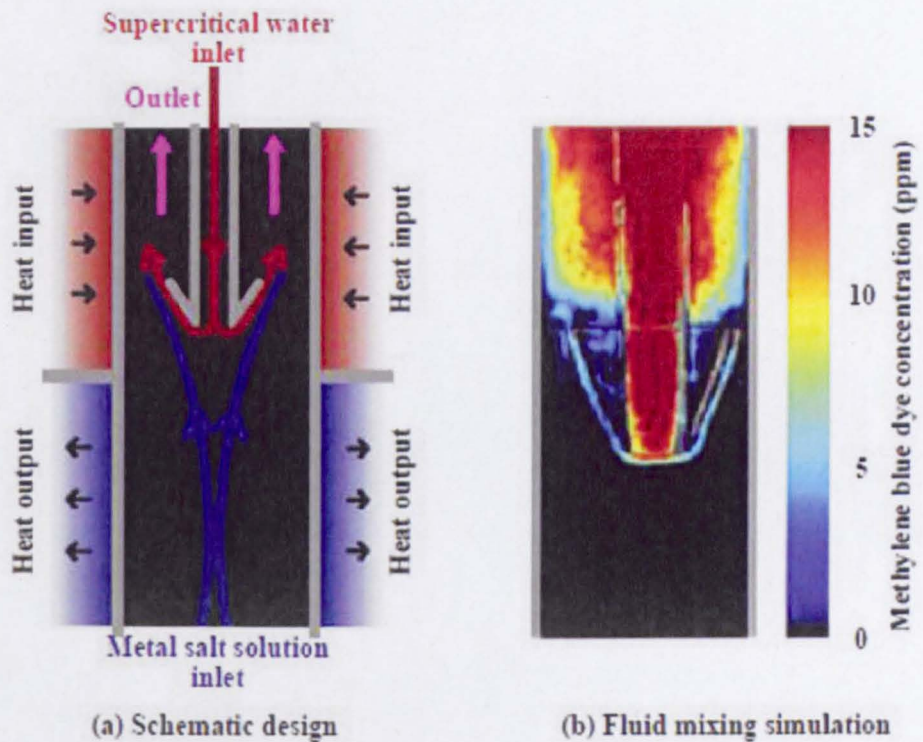


Fig. 2.30: Schematic for counter-current reactor design and fluid mixing, adapted from (Lester et al., 2006)

This approach could be an ideal scenario for nanoparticle synthesis near the critical and supercritical conditions. Therefore CHS offers a relatively simple route which is inherently scalable and chemically much more benign than many other nano production technologies (Lester et al., 2006). Nanoparticles of narrow size distribution are expected to form when instantaneous nucleation occurs and subsequent growth takes place at the same rate for all particles. Figure 2.31 shows a simple flow diagram of the continuous hydrothermal synthesis (CHS) technique at The University of Nottingham. This rig with the new reactor design can be exploited for nanomaterial fabrication and surface modification near and above critical conditions.

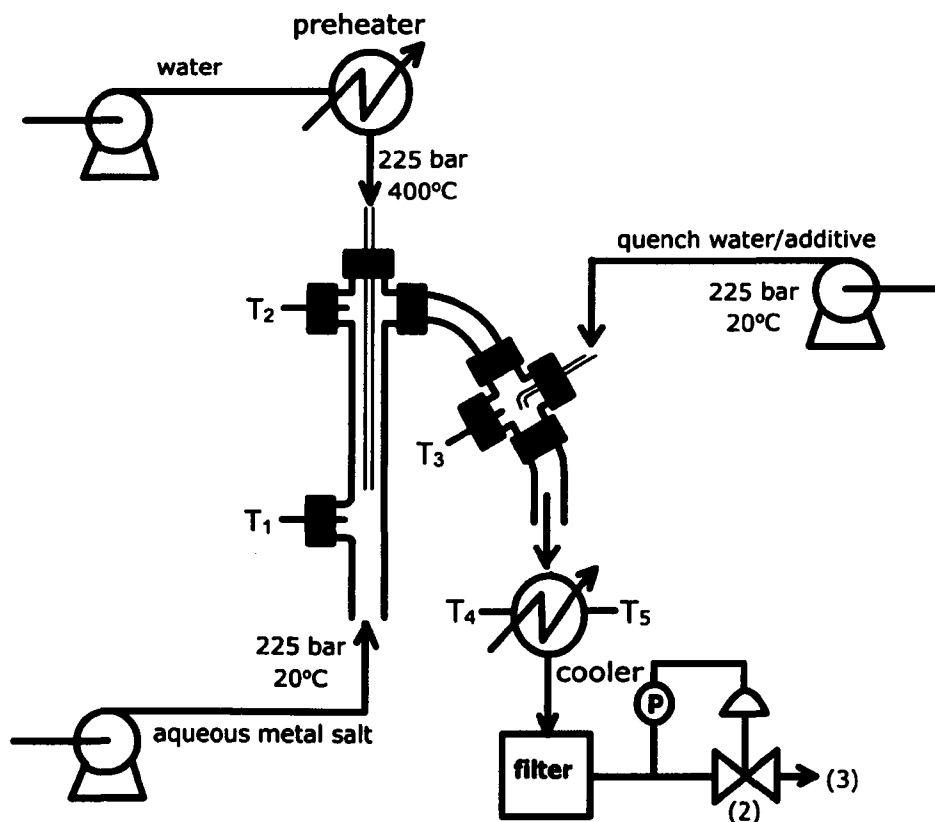


Fig. 2.31: The flow diagram of CHS technique at University of Nottingham

2.7 Nanoparticle stabilization

As nanoparticles produced by hydrothermal synthesis are in the form of colloids. During processing and storage, they are likely to collide with each other, and this can cause excessive aggregation of the nanoparticles, due to their Brownian motion (Grate and Abraham, 1991, Khanna, 1997). A stable nano-colloidal suspension is essential to prevent aggregation, and to produce mono-dispersed particles for different applications. In colloidal solution, there is an attractive dispersion force between particles (van der Waals attractive force), which tends to aggregate the particles (Napper, 1983). For particles having a plate like shape separated by a distance h ,

the attraction potential (V_A) is given by Equation 2.7 (Mahanty and Ninham, 1976, Baraton, 2003).

$$V_A = \frac{A}{12\pi h^2} \quad (2.7)$$

Where: A is Hamaker constant (it is the material property, its value in the order 10^{-19} - 10^{-20} J), h is the distance from the particle surface (m). The attraction force decays in proportion to $1/h^2$ for plate particles and it decays in proportion to $1/h^6$ for atoms (Brinker and Scherer, 1990). There are two possible approaches to achieve colloidal stabilization and prevent coagulation.

2.7.1 Electrostatic stabilization

The colloidal oxides have OH^- groups on their surface (hydrous surface), thus the protonation and deprotonation of the M-OH bonds result in the creation of a charged surface (Parks, 1965). The protonation and deprotonation reactions of hydrous nano-oxides are represented by Equations 2.8 and 2.9 (Brinker and Scherer, 1990).



The colloid pH indicates whether H^+ or OH^- will be the charge determining ion. It also indicates whether the surface is positively, negatively charged or it is neutral (Brinker and Scherer, 1990). The pH at which the particle surfaces have no charge is called "point of zero charge" (PZC) (Parks, 1965). If $\text{pH} < \text{PZC}$ then H^+ will be the charge determining ion and the particles will be positively charged. If $\text{pH} > \text{PZC}$, then OH^- will be the charge

determining ion and the particles will be negatively charged (Parfitt, 1981). The surface of the colloidal charged particles attracts counter ions of opposite charge from the solution.

An electrical double layer is created by the charge determining ions and counter ions (Hunter, 1981). Figure 2.32 is a schematic diagram of the electrical double layers near the surface of colloidal charged particles. Where: ϕ_{ξ} is the zeta potential, ϕ_H is Helmholtz potential, and ϕ_0 is the surface potential. The created electrical double layer is associated with each particle and is responsible for generating an electrostatic repulsive force between the two neighbouring particles (Parfitt, 1981).

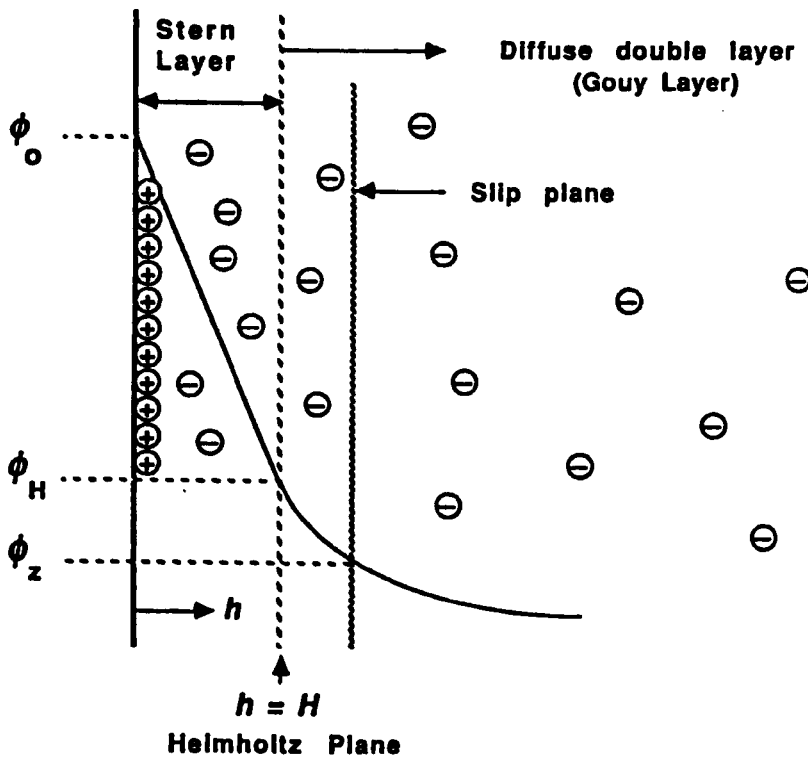


Fig. 2.32: Electrical double layer near the surface of colloidal particles, adapted from (Brinker and Scherer, 1990)

2.7.2 Steric stabilization

Although the electrostatic double layer takes part in the stabilization of aqueous systems, it is also possible to stabilize the colloidal particles and prevent coagulation by introducing a thick adsorbed polymer layer which constitutes a steric barrier (Sato and Ruch, 1980). The coating layer must be thick enough (typically > 3 nm) to be able to keep the points of closest approach outside the van der Waals forces range (Figure 2.33) (Tadors, 1982, Boisvert et al., 2001).

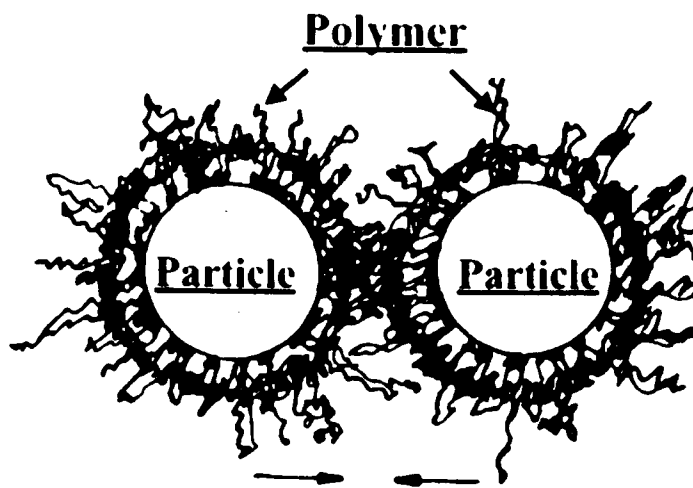


Fig. 2.33: Steric stabilization created by polymer over colloidal particle surface, adapted from (Baraton, 2003).

The adsorbed polymer layer can prevent coagulation in two possible ways: entropically; when the two particles approach each other, the adsorbed polymer layers overlap resulting in a decrease in the degree of motion of the polymer chains thus taking part against particle coagulation (Tadors, 1982). In terms of enthalpy; as the particles move closer together, the solvent molecules which surround the particles are squeezed out, thus an osmotic pressure is created. The generated osmotic pressure tends to suck the liquid into the space between the particles, thus increasing the energy

required for the particles to coagulate (Sato and Ruch, 1980, Tadors, 1982).

There are two main routes for nanoparticle surface modification. The post-synthesis modification approach: Where the functionalized nanoparticles are synthesized in two steps, which are distinctly separated from each other. The first step is the formation of the nanoparticles (core). The second step is the functionalization, where the functional organic molecules are introduced later in a different stage. In situ functionalization: In this technique the nanoparticles are formed in the presence of functional organic molecules. The clusters assembly occurs where organic groups are exclusively bonded to the atom surface (Baraton, 2003). The growth of the cluster core is controlled by the organic groups.

The sequences of reactions that may lead to surface modification are rarely known and not always obvious. Multi functional ligands containing carboxylic groups have been used effectively for coupling with metal oxide colloids (Farrokhpay, 2009). These surfactants can be designed to strongly bind to the nanoparticle surface, in the mean time bind to selective target compounds such as polymer chain, thus proper nanoparticle dispersion can be achieved (Baraton, 2003, Neouze and Schubert, 2008).

2.8 Integration of nanoparticles into polymers

Inorganic-organic nanocomposites are a special class of inorganic-organic hybrid materials. These materials might have improved mechanical, thermal, and flame resistance properties due to the synergism between both component properties (Giannelis, 1996). The simplest approach is to entrap an inorganic component into an organic host. There are two

principle routes to integrate the nanoparticles into the polymeric matrix: (i) the coupling of the nanoparticles with polymers that have reactive groups to attach the particles to the polymer surface (grafting to). (ii) Polymerization on or from the surface of organic modified particles (grafting from) (Baraton, 2003).

2.8.1 Grafting to approach

Many kinds of interaction that may range from the van der Waals force to covalent bonding can be developed between the nanoparticle surface and the polymer (Neouze and Schubert, 2008, Farrokhpay, 2009). This type of interaction depends mainly on the specific surface area of the particles, the molecular weight of the polymer, and the portion of reactive substituent at the polymer chains (Fleer et al., 1993, Farrokhpay, 2004). Polymers with pendent reactive groups such as sulfonates or carboxylates were grafted to the surface of nano-ferrite, silica, or titania (Farrokhpay et al., 2004, Neouze and Schubert, 2008). This technique has many drawbacks, such as insufficient surface coverage due to steric hindrance or macromolecule's competition between adsorption and chemical bonding (Baraton, 2003).

2.8.2 Grafting from approach

Grafting from approach is one of the main routes to encapsulate the nanoparticles into organic polymer. Polymerization from the surface of modified particles is crucial especially in the case of nanoparticles with large specific surface area (Baraton, 2003, Vaia et al., 2003). This can be achieved by carrying out polymerization in the presence of performed nanoparticles (Baraton, 2003). Figure 2.34 gives the main routes to encapsulate the nanoparticles into polymeric matrix.

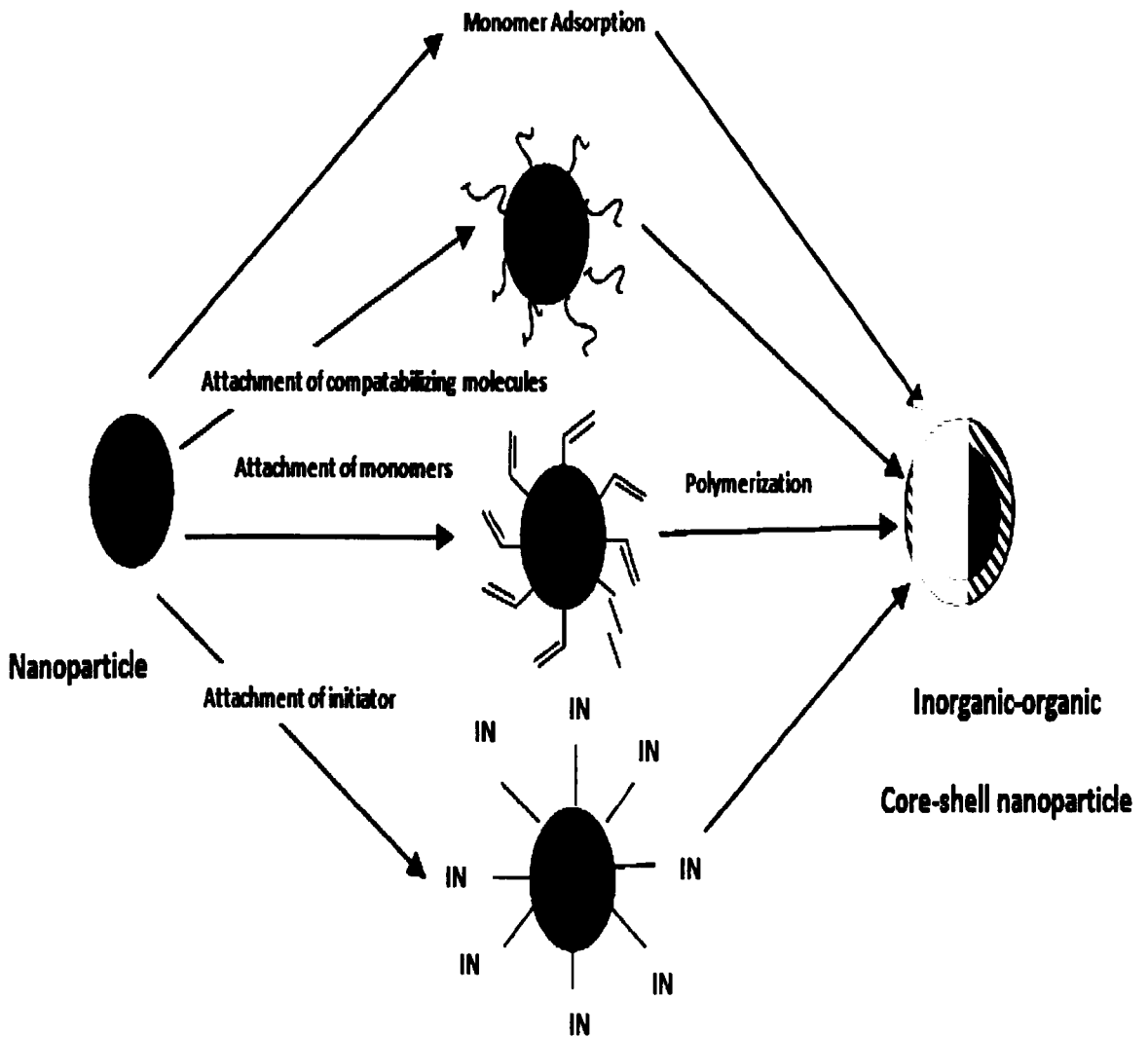


Fig. 2.34: Principal routes to inorganic-organic core-shell nanoparticles, adapted from (Baraton, 2003)

2.9 Previous work

In 2010, Rahatekar investigated the effect of MWCNTs and oMMT onto the flammability of epoxy nanocomposites. He investigated the mass loss as the sample was exposed to an external heat flux of 50 kW/m^2 under an inert atmosphere. All epoxy/MWCNTs nanocomposite residues showed good integrity with no visible cracks, which were clearly seen in the residues of epoxy/oMMT nanocomposite (Figure 2.35).



Fig. 2.35: The residue integrity of: (a) epoxy/OMMT, (b) Epoxy/MWCNT, adapted from (Rahatekar et al., 2010)

Mass loss rate alone cannot provide a sufficient evaluation of the material flame retardancy. Epoxy is a charring polymer (Wilkie and Morgan, 2010), therefore improved flammability performance could be achieved by investigating the synergistic effect between CNTs and intumescent FR system.

In 2007, Guoxin investigated the synergistic effect of expandable graphite (EG), molybdenum disilicide (MoSi_2), and EG/ MoSi_2 on the fire protection performance of an intumescent coating based on ammonium poly phosphate (APP)-penta erithritol (PE)-melamine (ME). The employed resins were acrylic resin and amino resin in the ratio of 3:1. The ratio of employed resins (binder) to intumescent flame retardant (IFR) was 2:3. The ratio between IFR ingredients APP:PE:ME was 2:1:1. The partial substitution by EG, MoSi_2 and EG/ MoSi_2 on the fire protection parameter of steel substrate was evaluated. About 11 formulations were investigated. Table 2.2 shows the chemical composition of formulations 9-11.

Table 2.2: The composition of different intumescent coating formulations, adapted from (Li et al., 2007)

Sample No.	Acrylic resin (Wt %)	Amino resin (Wt %)	APP (Wt %)	PE (Wt %)	ME (Wt %)	EG (Wt %)	MOSi ₂ (Wt %)
9	27.6	9.2	27.6	13.8	13.8	5.0	3.0
10	26.7	8.9	26.7	13.35	13.35	5.0	6.0
11	25.8	8.6	25.8	12.9	12.9	5.0	9.0

The fireproofing parameter of the intumescent coating was evaluated by a self made high temperature furnace established according to the Chinese standard GB 15442.2-1995 (Chinese-standard, 1995). An intumescent coating of 2 mm thickness was applied on a steel plate of dimensions of 75 mm × 75 mm × 6 mm. The coated steel plate was placed on a hole with dimensions of 70 mm × 70 mm, with the coating facing the inner side of the furnace. A digital thermocouple was fixed on the back side of the tested steel plate (Figure 2.36).

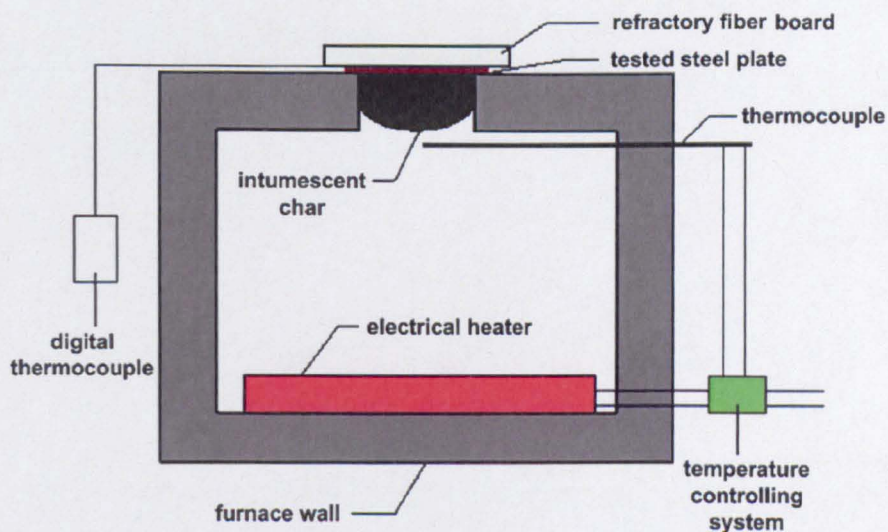


Fig. 2.36: The structure of a lab fire-protection testing furnace, adapted from (Li et al., 2007)

The furnace temperature was raised and kept at 800 °C in about 20 minutes. The temperature of the tested plate and the temperature of the furnace were recorded every 10 minutes. Formulations 9-11 showed improved fire-protection parameter compared with other formulations. The prolonged fire-protection time (120 minutes) for formulations 9-11, provided an evident of the synergistic effect between EG/MoSi and the IFR system (APP-PE-ME).

The employed binder was not ideal as it starts decomposition at low temperatures (125 °C), and this may cause an early degradation of the intumescent coating under the effect of fire. More thermally stable binders such as epoxy resin could be more efficient. The employed high solid loading level might cause processing difficulties for practical applications. This high solid loading might also dramatically affect the coating's mechanical properties.

2.10 New aspects of flame retardancy

Most of the research work has been dedicated to the development of layered silicates, mainly oMMT, and CNTs nanocomposites (Quiang et al., 2009). However, oMMT systems will likely be limited to polymer formulations that melt below 200 °C, the reason being that the thermal stability of the commercially available surfactants above 200 °C is poor, and up to 30 wt % of surfactant is required to achieve proper dispersion (Dharaiya and Jana, 2005, Bellucci et al., 2007). Other nanocomposite fillers such as silsesquoxane (POSS) and CNTs are still too expensive for commodity use, or even speciality use (Horrocks and Price, 2008).

Nano-oxides could be essential constituents in multi-component FR systems. They are able to improve the polymer viscosity in the molten state during polymer degradation (Wilkie and Morgan, 2010). They have the potential to react with conventional FR agents and induce a synergistic effect via the formation of a compact insulating barrier against further heat and mass loss (Scharf and Nalepa, 1992, Fu and Qu, 2004).

Nanoparticles can have a FR action through the release of effective flame inhibitors such as PO_2^* , PO^* , and HPO^* (Levchik and Weil, 2006), by absorbing heat with the release of H_2O and CO_2 (Rothon, 2003c), or by preventing the access of oxygen to the burning material (Camino and Delobel, 2000). The proper combination between selected nanoparticles and conventional FR systems, to achieve highly synergistic effect, is vital to fulfil the flammability standards at low solid loading level (Zammarano et al., 2005, Laoutid et al., 2009). To date, little research has been dedicated to nano-oxide and nano-fire extinguisher nanocomposites.

This thesis is apart of the ongoing research for the development of enhanced flame retardant PNs. In this research work, nanoparticles that can enhance the polymeric material flammability performance will be developed and organic modified by using hydrothermal synthesis technology. The nanoparticles will be developed in a form that can be easily integrated and effectively dispersed into the polymeric matrix. The impact of the developed nanoparticles onto epoxy mechanical, thermal, and flammability performance will be evaluated.

Furthermore, the proper assortment between the bespoke nanoparticles with an intumescent agent will be investigated in an attempt to achieve a new self extinguishing multi-component epoxy nanocomposite for

extended applications in extreme firing conditions, with balanced mechanical and thermal properties.

2.11 Summary of literature review

This Chapter has highlighted the human and economic cost of fire and the impact of flame retardancy on fire safety; reviewed the flame retardancy mechanisms, additives, and testing; represented the formulation and surface modification of bespoke nanoparticles via hydrothermal synthesis; signified the possible approaches for integrating nanoparticles into polymeric matrix; reviewed the previous work in the development of flame retardant PNs; showed up the new aspects in flame retardancy and the possible research avenues.

CHAPTER 3

3. EXPERIMENTAL PROCEDURE

This Chapter represents the experimental methodology, nanoparticle synthesis and characterisation methods, and the evaluation of PNs performance (i.e. mechanical properties and thermal stability).

3.1 Methodology

The experimental work in this thesis can be divided into main different research stages that are integrated and linked together as follows:

1) The dispersion of dry titania nanoparticles (with a 25 nm particle size) known commercially as P25 was tested as a 'base reference' to investigate how nanoparticles, particularly nano-oxides, could be effectively dispersed into polymeric matrix, and to investigate the impact of different processing parameters mainly solid loading level, mechanical mixing, and heating on nanoparticle dispersion. The nanoparticle dispersion was investigated with SEM and quantified by using Lab view (National Instruments) for image analysis.

2) Nanoparticles that could have a synergistic effect with traditional FR systems mainly TiO_2 , and that could have a FR action mainly $\text{Ca}_5(\text{OH})(\text{PO}_4)_3$ and AlOOH were formulated and surface modified by using CHS technique devised by the University of Nottingham. Different organic ligands and polymeric surfactants were employed for nanoparticle surface modification in an attempt to prevent aggregation and to enhance the compatibility between the inorganic nanoparticles and the organic

polymeric matrix. The employed surfactants were injected at various manufacture stages: with the metal precursors, or immediately after nanoparticle formulation, post reaction but prior to collection.

3) Characterization of the developed nanoparticles is an essential part to assess their chemical structure and surface modification, and to establish the relationship with the hydrothermal synthesis conditions. The synthesized nanoparticles were characterized by using a set of analytical techniques including: X-ray diffraction (XRD), scanning electron microscope (SEM), transmission electron microscope (TEM), dynamic light scattering (DLS), fourier transform infra-red (FTIR), ultra violet-visible (UV-Vis), and thermogravimetric analysis (TGA).

4) The successful achievement of nanocomposites requires the dispersion of the nanoparticles to the molecular level with minimum aggregation. Different approaches for integrating and effectively dispersing the developed nanoparticles into epoxy resin were investigated in an attempt to achieve nano-scale dispersion. A solvent blending approach for integrating colloidal organic modified nanoparticles into polymeric matrix was developed. This approach enabled the elimination of freeze drying and the re-dispersion of aggregated dry nanoparticles into polymeric matrix. The nanoparticle dispersion was investigated with SEM and quantified using Labview (National Instruments).

5) The impact of the developed nanoparticles onto epoxy mechanical properties was evaluated by mechanical compressive test. The thermal stability of the developed nanocomposites was evaluated by TGA. The direct flame resistance was evaluated based on Bunsen testing, video footage, and image analysis to quantify the flammability behaviour from

initial ignition, flame size and shape, flammable dripping , until self extinguish. This technique enabled the quantification of nanocomposite direct flame resistance in a repeatable fashion. To the knowledge of the author, this is the first time image analysis has been used to quantify direct flame resistance.

6) Multi-component epoxy nanocomposites based on the synergism between bespoke nanoparticles (nano-oxides and nano-fire extinguishers) and intumescent FR system were developed. Each nanocomposite was tested for its ability to resist a direct flame source and to self extinguish directly after the flame source was removed. The direct flame resistance was evaluated by bunsen testing with video footage and image analysis.

7) The flammability performance of the developed multi-component epoxy nanocomposites was evaluated by standard cone calorimeter testing. In this test, a sample of 100×100×4 mm was placed on a load cell and subjected to a constant heat flux of 35 Kw/m². The sample was uniformly irradiated from above. The measurement of oxygen concentration in the combustion gases was employed to quantify the heat released per unit time and surface area. The developed nanocomposites reported enhanced flammability performance with a marked decrease in the peak/maximum heat released rate compared with virgin epoxy.

8) A nanocomposite intumescent coating as a means of passive fire protection was developed. The fireproofing parameter of the developed intumescent coating was evaluated by measuring the temperature of the steel substrate with time while the coating faced a heat source at 900 °C. The employed intumescent coating developed an expanded protective char layer that protected the substrate from the heat source.

3.2 Formulation and functionalization of nanoparticles by using continuous hydrothermal synthesis

The controlled hydrothermal reaction environment makes CHS an attractive technology as mono-dispersed nanoparticles with controlled morphology can be developed. Bespoke nanoparticles that could enhance the polymeric material flammability performance were formulated and surface modified by using CHS technique devised by the University of Nottingham. Figure 3.1 is a schematic for CHS technique, and it adds to Figure 2.31 by showing where nucleation and formulation occurs.

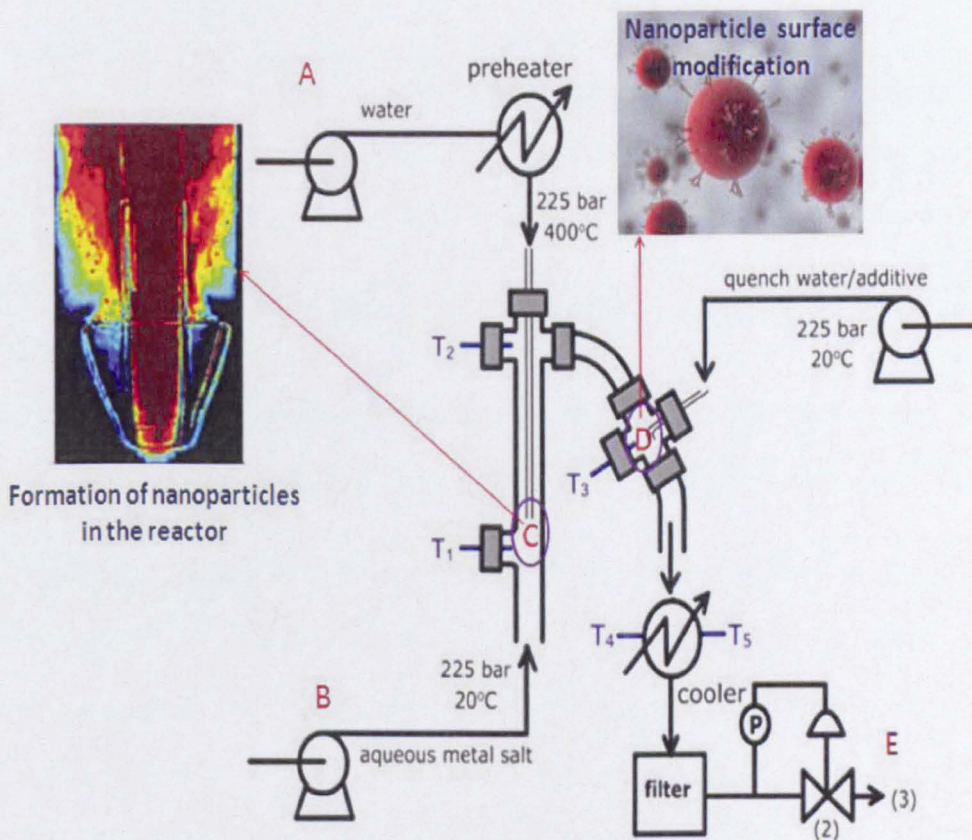


Fig. 3.1: Schematic of continuous hydrothermal synthesis technique, adapted from (Lester et al., 2006).

From Figure 3.1 the superheated fluid (ScW) passed down an inner nozzle pipe (A) against an up flow of cold metal salt (B). Nanoparticles formed at

the interface of the two fluids (C) and the buoyancy of the heated flow caused the nanoparticle slurry to be carried upwards (downstream). The nanoparticle flow stream was cooled down prior to collection at point (E).

The nanoparticle surface modification was performed at different manufacture stages. It was performed either in the reactor (C) by injecting the surfactant with the metal salt or in a separate stage by injecting the surfactant at the capping point (D), post reaction but prior to collection. Toluene was injected at the capping point as a solvent for the used surfactant in case of surface modification at the capping point, or for extracting the nanoparticles that were surface modified in the reactor.

The system was pressurized by using Gilson HPLC pumps and Swagelock check valves. The system pressure was maintained at fixed value by using Tescom back pressure regulator (BPR). The system pressure value was displayed by using Swagelock pressure gauge and also by using pressure trip box manufactured by the University of Nottingham. For safety reasons, Swagelock pressure release valves were fixed to the system; these valves will open automatically if the pressure inside the system exceeds 300 bars.

The water stream was heated up to the reaction temperature by using an electrical heater controlled by a heater controller unit. The value of the reaction temperature adopted in this Thesis is the temperature of the ScW measured at the heater outlet. The temperature values through the whole system stages were recorded by using digital thermocouples; and were displayed on a computer screen by using picolog software. For safety reasons the trip box will shut down the whole system automatically if the system temperature reaches 500 °C or if the system pressure reaches 4000 PSI.

3.2.1 Standard operating procedure for the CHS rig

Start up

1. Switch on the power to all the system units.
2. Reset the temperature and the pressure trips.
3. Flush the system with de-ionized water by using water, metal salt, and capping pumps.
4. Set the PBR for the required pressure.
5. Check the system for leaks.
6. Turn on the cooling water through the heat exchanger.

Heating

1. Set the pre-heater controller unit to the required heating temperature.
2. Wait until the required temperature will be established.

Nanoparticle synthesis

1. Pump the aqueous metal salt solution to the system.
2. Pump the surfactant to the capping point.
3. Allow an equilibrium period of 15 minutes before starting a sample collection.

Shut down

1. Replace the all the pumping feeds to de-ionized water.

2. Switch off the heater controller.
3. Reduce the system pressure regularly by using the BPR.
4. Once the entire system temperature goes below 80 °C switch off all pumping units.
5. Switch off the cooling water.

The tuneable hydrothermal reaction conditions make CHS an ideal scenario for nanoparticle formulation and on line surface modification. Nanoparticles with controlled size, morphology, crystallinity, and surface properties can be achieved by using CHS technique. The developed nanoparticle surface properties can be altered from hydrophilic to hydrophobic and vice versa via surface modification. Throughout the research work, the organic modified nanoparticles were harvested from the water layer to the organic layer (Toluene), or stabilized in water. Furthermore, surface modification enabled the flocculation of colloidal gel nanoparticles from water. Figure 3.2 shows the changes in nanoparticle surface properties via surface modification.

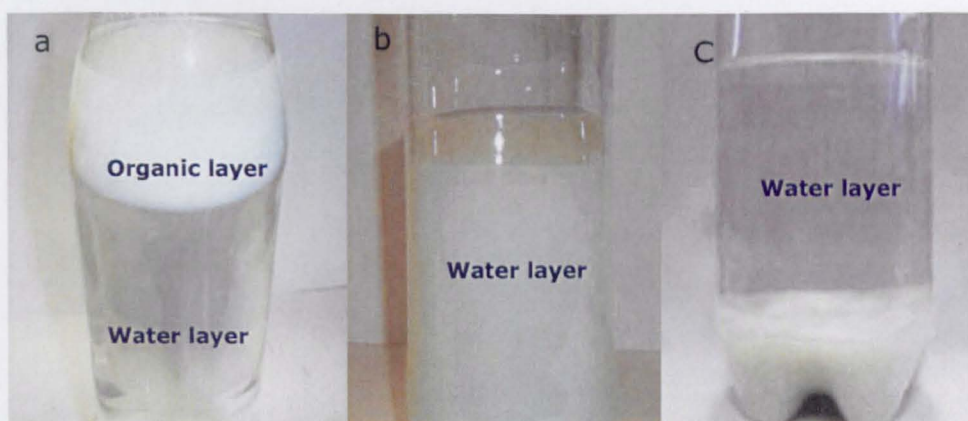


Fig. 3.2: Extraction (a), stabilization (b), and flocculation (c) of colloidal nanoparticles via surface modification using CHS technique. The material in the images is TiO_2 at 10 nm produced at a reactor temperature of 415 °C.

Nanoparticle surface modification with organic ligands and polymeric surfactants of different polarities can minimize nanoparticle aggregation and enhance the nanoparticle dispersion into polymeric matrices of different polarities.

3.3 Characterization of nanoparticles

3.3.1 X-ray diffraction (XRD)

The nanoparticle crystalline phase can be characterized by X-ray diffraction (XRD). Each crystalline phase has its own characteristic interlayer spacing between the lattice planes (Connolly, 2007). When an X-ray beam strikes the sample surface at an angle θ , a portion of the incident radiation is scattered by the atoms at the surface. The unscattered portion continues to the second layer of atoms where again a fraction is scattered, and the remaining pass to the third layer and so on (Figure 3.3).

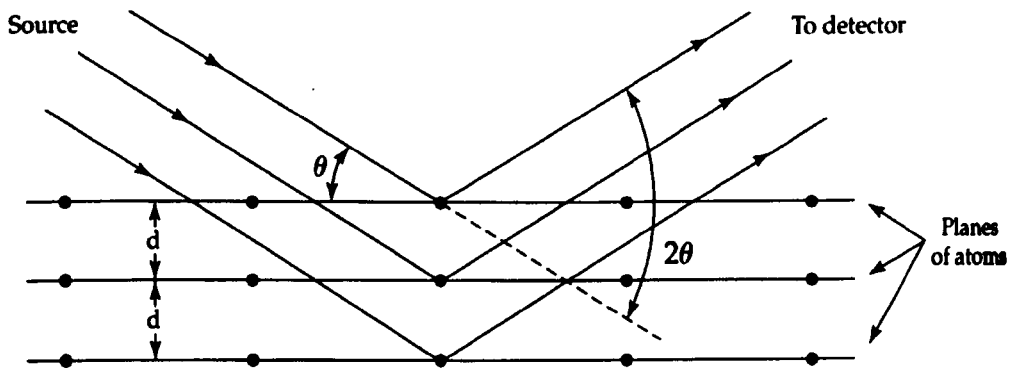


Fig. 3.3: Diffraction of X-rays by a crystal, adapted from (Skog and Holler, 1999)

Each crystalline phase has its own diffraction pattern (diffractogram). W. Bragg concluded the conditions for constructive interference of scattered X-rays at an angle θ (Equation 3.1).

$$n\lambda = 2d \sin\theta \quad (3.1)$$

Where: n is an integer, λ is the wave length of the x-ray, d is the interlayer spacing between the planes in the lattice, and θ is the angle between the incident X-rays and the scattering crystal. X-rays will be reflected (constructive interference will occur) from the crystal only if the angle of incidence satisfies Equation 3.1 (Ewald, 1962). Figure 3.4 shows a schematic diagram of XRD diffractometer system.

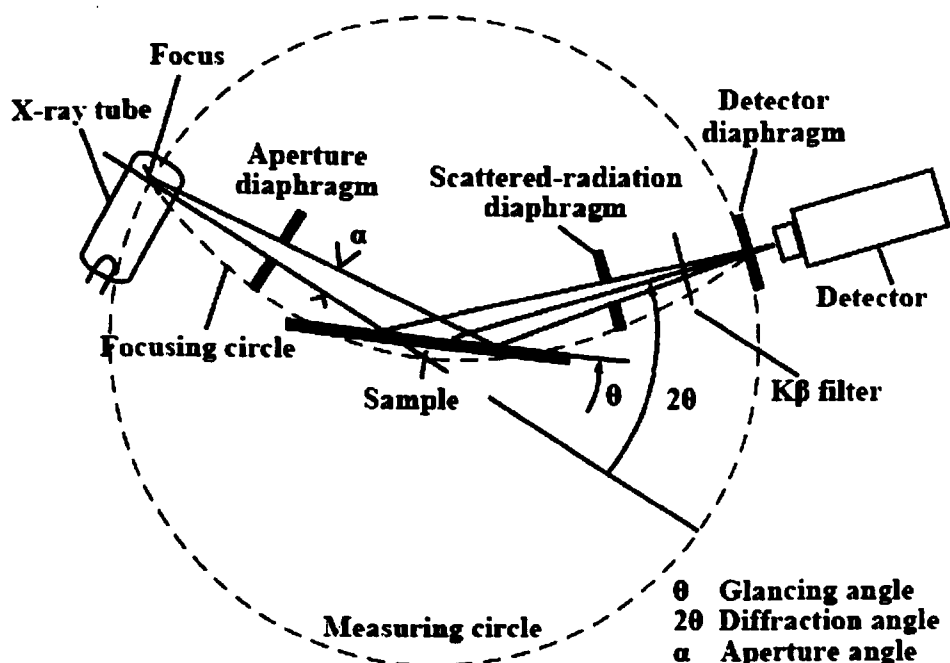


Fig. 3.4: Schematic diagram of XRD, adapted from (Connolly, 2007)

The employed XRD instrument was Hiltonbrooks X-ray diffractometer. A powder sample was spread and slightly pressed inside the sample compartment and scanned over the angle range 2θ from 5 to 65 degrees with a scan speed of 2 degrees per minute. The sample identification was achieved by comparing the obtained XRD diffractogram with standard data from joint committee on powder diffraction standards (JCPDS).

3.3.2 Scanning electron microscope (SEM)

The scanning electron microscope (SEM) can form a virtual image of the tested sample. This virtual image can be magnified and employed to assess the nanoparticle size, shape, morphology, and their dispersion into the polymeric matrix. In this technique an electron gun generates a beam of electrons. The generated electrons are focused and accelerated down a column with energies from few hundreds to tens of thousands of electron volts (Skog and Holler, 1999). As the electron beam scans the sample surface the emitted signals can be monitored by a simple imaging device called cathode ray tube (CRT). CRT can collect and monitor the emitted electrons from the sample from one end and accelerate them to phosphorous on the other end of the tube. Phosphorous converts them to a visible light signal (Reimer, 1998, Joel, 2006). By synchronizing the CRT scan with SEM scan, the system maps the sample surface point by point and a visualising image is generated on the viewing surface of the CRT (Skog and Holler, 1999).

There are many types of emitted signals when the sample surface is subjected to primary electrons. The main two types that are commonly employed for surface scan are secondary electrons (SE) and back scattered electrons (BSE) (Reimer, 1998). SE are sample electrons that have been ejected by the incident electron beam. They provide the best imaging resolution; contrast in SE comes from sample topography. More secondary electrons are able to escape from the top of a peak than for a point at the bottom of a valley (Newbury et al., 1986).

BSE are primary (incident) beam of electrons that have scattered back from the sample surface by elastic collision with the nuclei of sample atoms.

Contrast in the backscattered images comes primarily from point to point difference in the sample atomic number (Reimer, 1998). The higher the atomic number the more backscattered electrons, the more bright the areas in the image. High quality back scattered image can provide important information about chemical composition (Griffith and Danilatos, 1993). Figure 3.5 shows a schematic of SEM.

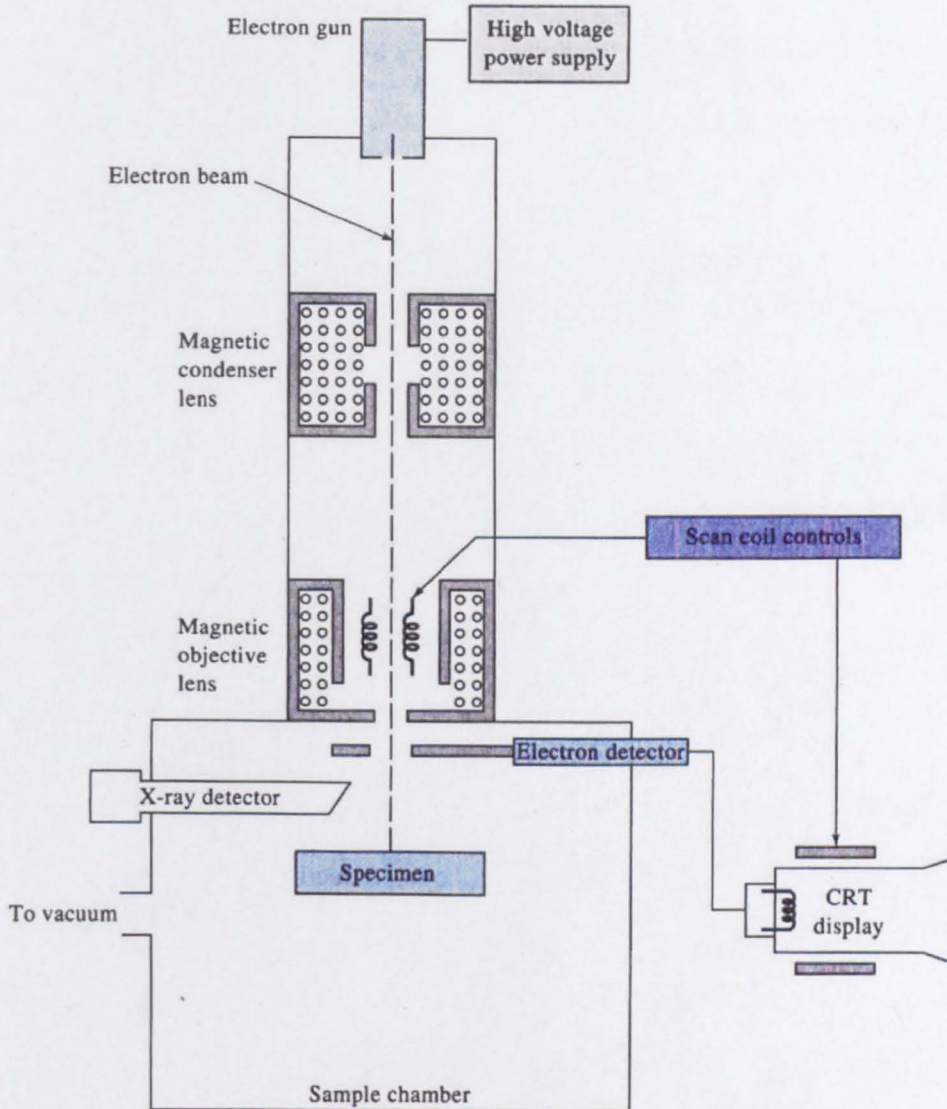


Fig. 3.5: Schematic of an SEM with both electron and X-ray detection, adapted from (Skog and Holler, 1999)

The employed SEM was Quanta 600 by FEI Corporation, and it had three types of detectors SE, BSE, and energy dispersive X-ray spectrometer (EDX). The dried powder was spread over the sample holder and gold plated to prevent sample vaporization in the electron gun chamber. The coated nanoparticles were subjected to high vacuum (2.3×10^{-5} torr) and then to high energy electron beam (25 KeV). The detection mode was adjusted to SE detector to create an imaginary image of the nanoparticles.

3.3.3 Energy dispersive X-ray spectrometry (EDX)

Energy dispersive X-ray spectrometry (EDX) is an essential tool for nanoparticle elemental composition analysis. In this technique a highly energetic electron beam is generated and directed toward the sample surface. The interaction of this energetic electron beam with the sample atoms results in scattering of the inner shell electrons and vacancies are formed. Each excited atom releases characteristic X-rays when the higher outer shell electrons of the same atom fill these vacancies.

The emitted X-rays are characteristics of the emitting atom (Barr, 1994). An energy dispersive X-ray spectrometer collects the characteristic X-rays, counts (quantizes), and sorts the emitted X-rays on the basis of energy (energy dispersive spectrometry). The vertical axis of the resulted spectrum represents the counts of X-rays; whereas the horizontal axis represents the X-ray energies. Each peak on the spectrum corresponds to a specific element present in the sample. The energy level of each peak indicates which element is present in the sample, whereas the number of counts of each peak is proportional to the element concentration (Lachance and Claisse, 1995, Skog and Holler, 1999).

The employed EDX spectrometer was a detector fixed to the SEM (Quanta 600). The tested sample was prepared in the same way for SEM imaging. EDX detector was employed to investigate the nanoparticle elemental composition and to verify the attachment of the organic surfactant to the nanoparticle surface.

3.3.4 Transmission electron microscope (TEM)

Transmission electron microscope (TEM) operates in the same basic principle as light microscope, where a beam of high voltage electrons is employed as a light source. Owing to the low de Broglie wavelength of high voltage electrons, it is possible to get a resolution thousands of times better than the light microscope. Modern gadgets have powers of resolution that range from 0.1 nm and the magnification up to 2,000,000 times (JEOL, 2006). TEM is composed of an evacuated cylinder of about 2 meters height. A heated tungsten filament at the top of the cylinder (the cathode) will emit electrons when it is heated. The emitted electrons are accelerated to the anode by applying a high accelerating voltage from 100 keV to 1 MeV ranges (Egerton, 1996, JEOL, 2006). Some of the accelerated electrons passed through tiny holes in the anode to form an energetic electron beam which passes down the column. Electro-magnets are placed at intervals down the column to focus the accelerated electron beam (Pulokas et al., 1999, Dykstra and Reuss, 2003).

The double condenser lenses focus the electron beam onto the sample specimen which is clamped into a removable specimen stage. As the electron beam passes through the sample specimen, some of the electrons are scattered, whilst the remaining are focused by the objective lenses either onto a fluorescent screen or photographic film to get a shadow

image of the nanoparticles. The unfocused electrons are blocked out by the objective aperture resulting in an enhancement of the image contrast (Kirkland, 1998, Reimer and Khol, 2008). Figure 3.6 is a schematic diagram of the TEM.

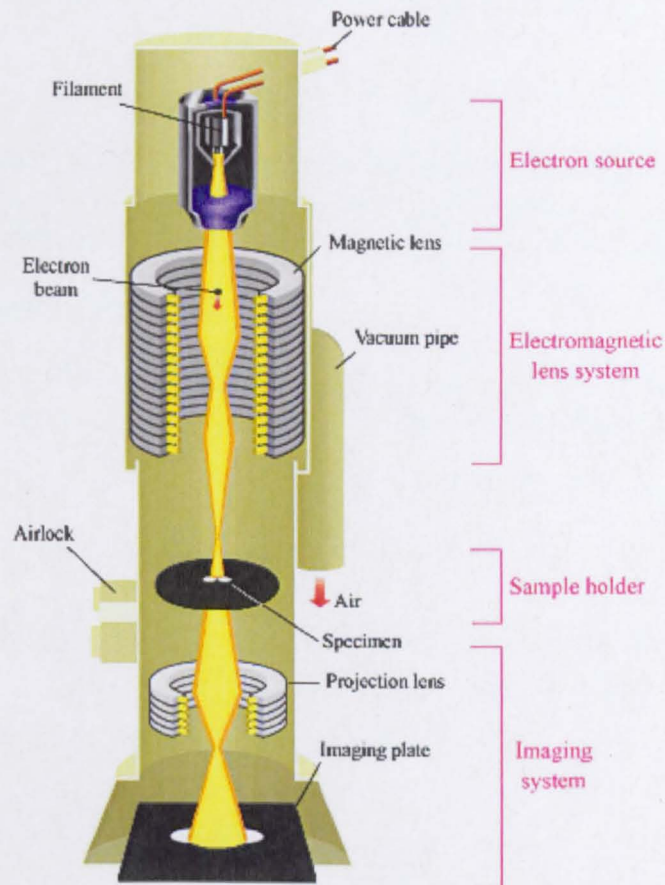


Fig. 3.6: Schematic of TEM, adapted from (Shapman, 1986)

The employed TEM was JEM-2100F by Joel Corporation. This high resolution TEM can reveal the details up to 0.5 nm. A few drops (2 ml) of colloidal nanoparticles or organic modified nanoparticles were dispersed in 20 ml deionized or toluene respectively, afterwards the nanoparticles were spread over a copper grid. The sample specimen was dried under vacuum to vaporize the solvent. The copper grid was fixed into a removable sample

specimen stage. The nanoparticles were visualized through a beam of high energetic electrons (200 keV); the electron beam transverse through the sample specimen creating a shadow image of the nanoparticles on a fluorescent screen.

3.3.5 Dynamic light scattering (DLS)

It is possible with a light scattering measurement to retrieve the molar mass (M), size (r_g), second virial coefficient (A_2), and translational diffusion coefficient (DT) of a solute in solution (Schärfl, 2007). When a polarized laser beam light interacts with solute molecules, the oscillating light electric field creates an oscillating dipole in the particle, which can then reradiate the light, much like an antenna for a radio station. The amount of scattered light is directly proportional to the solute molar mass and to its concentration (Sartor, 2003). Figure 3.7 is a schematic drawing of light scattering measurement.

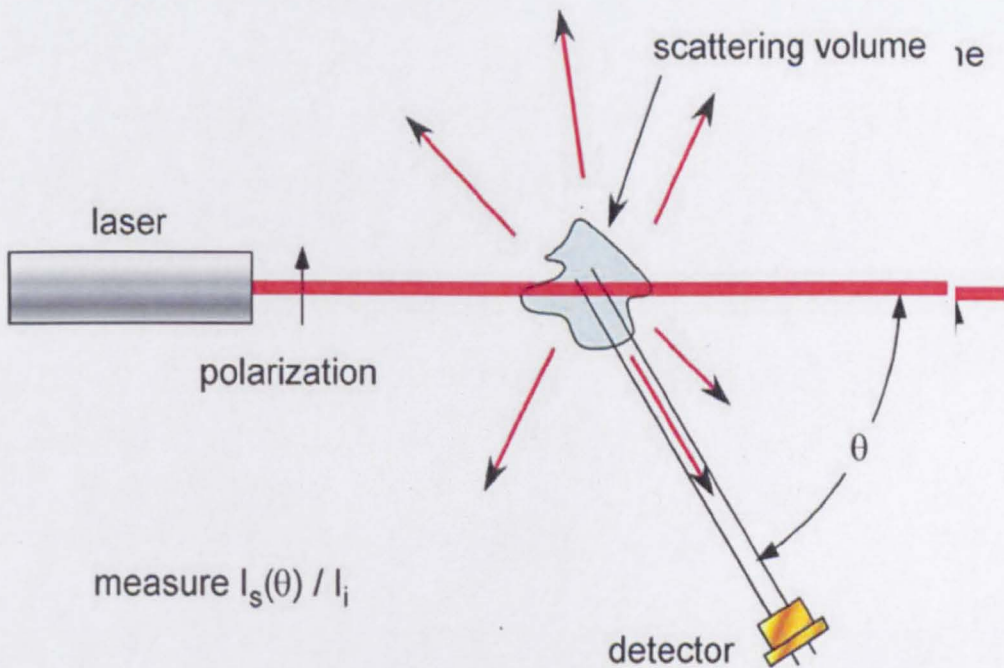


Fig. 3.7: Schematic of light scattering measurement, adapted from (Wyatt, 2005).

The angular variation (scattered light intensity at the measuring angle θ) of the scattered light is directly related to the size of the scattering molecules. Equation 3.2 is the correlation between the angular scattered light with solute molar mass, concentration, and size.

$$I(\theta)_{\text{scattered}} \propto M C \left(\frac{dn}{dc} \right)^2 P(\theta) \quad (3.2)$$

Where: $I(\theta)$ is the intensity of the scattered light at an angle (θ), M is the molar mass of the solute, C is the solute concentration, $P(\theta)$ is the mathematical relationship describing the angular variation of the scattered intensity as a function of particle size, and $\left(\frac{dn}{dc} \right)$ is the refractive index increment (Wyatt, 2005).

It is also possible to measure the fast (nanosecond) fluctuations of the scattered intensity in a technique known as dynamic light scattering (DLS). This type of measurement determines the translational diffusion coefficient for the solute, which is converted to an effective solute hydrodynamic radius (r_h) based on the assumption that the solute is a sphere (Wyatt, 2010). The size of colloidal nanoparticles was determined by using Malvern Zetasizer nano series (ZEN 3600) by Malvern Ltd. The sample cuvette was filled up to 1/3 of its height with colloidal nanoparticles and fixed in the sample compartment for colloidal nanoparticle size measurement.

3.3.6 Zeta potential measurement

Nano-oxides produced by CHS are in the colloidal state. Therefore, they have a great tendency to aggregate (reduce their number with time) due to their Brownian motion (Parfitt, 1981). Colloidal oxides can acquire

positive or negative charge depending on the colloidal pH (Equations 2.8 and 2.9 in Section 2.5.1). Ions of opposite charge will be attracted to the surface of the charged particles creating an ionic double layer associated with each particle. This ionic double layer will induce a repulsive potential between the neighbouring particles (Brinker and Scherer, 1990). The electrical double layer includes a boundary called a slipping plane. Ions within this boundary move with the dispersed particle whereas ions outside the slipping plane do not travel with the particle (Voyutsky, 1978, Hunter, 1981).

The potential at this boundary (slipping plane) is known as the zeta potential (Verwey and Overbeek, 1948). The magnitude of the zeta potential gives an indication of the colloidal system stability. Particles with a zeta potential more positive than +30 mV or more negative than -30 mV are normally considered stable (Morris et al., 1999); as there will be enough force for the particles to repel each other and there will be no tendency to flocculate (Hunter, 1981).

The employed instrument for zeta potential measurement was Malvern's Zetasizer nano-series. Zeta potential was determined by measuring the electrophoretic mobility of the charged particles in a liquid medium when an electrical field was applied (Figure 3.8).

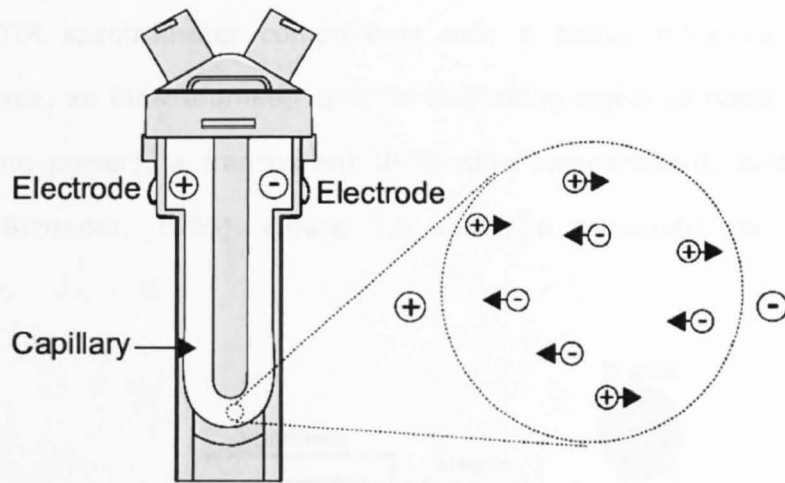


Fig. 3.8: Schematic of electrophoretic mobility measurement, adapted from (Malvern-Instruments., 2004)

At equilibrium, the charged particles moved with a constant velocity toward electrodes of opposite charge. The electrophoretic mobility was employed to determine the zeta potential (Z) by using Henry equation (Equation 3.3).

$$U_E = \frac{2 \varepsilon Z f(ka)}{3h} \quad (3.3)$$

Where: U_E is electrophoretic mobility, Z is zeta potential, ε is dielectric constant, $f(ka)$ is Henry function determination either 1 or 1.5, and h is the strength of the electric field.

3.3.7 Fourier transform infra-red (FTIR)

FTIR technique is a powerful tool to verify the nanoparticle chemical structure. It can be employed for qualitative and quantitative analysis (Zyka, 1993). In this technique the tested sample is mounted in a transparent IR compartment and subjected to IR beam (Coleman, 1993). IR absorption can be ascribed to transitions of molecular vibrational or rotational energy to another state (Rubinson and Rubinson, 2000).

The main FTIR spectrometer components are: A stable infra-red (IR) radiation source, an interferometer unit for improving signal to noise ratio (high resolving power), a transparent IR sample compartment, and IR transducer (Schrader, 1995). Figure 3.9 shows a schematic for FTIR spectrometer.

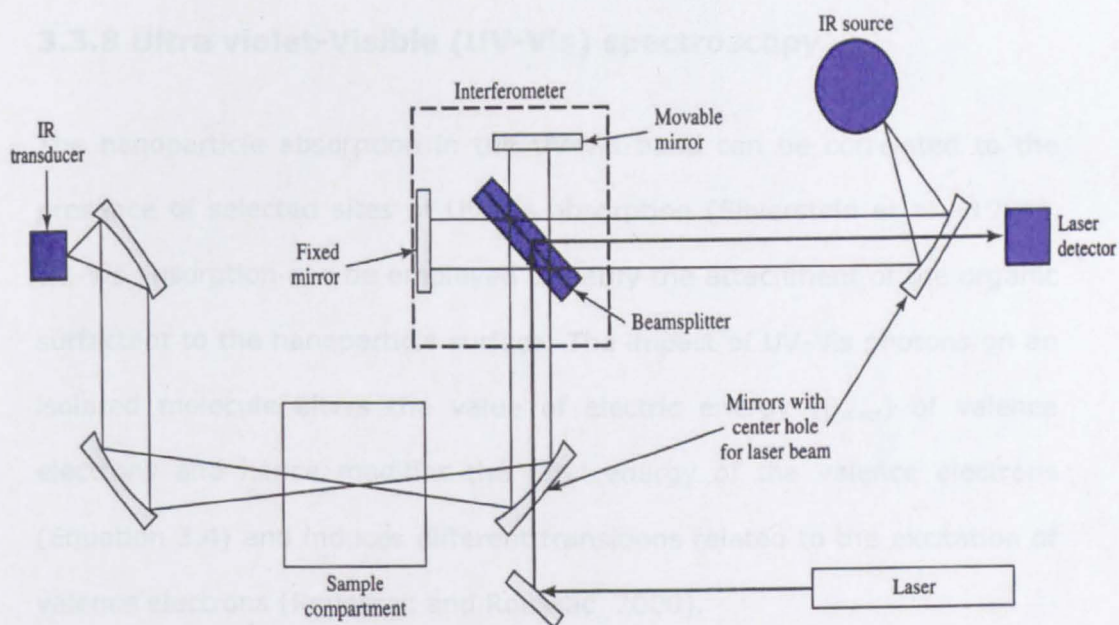


Fig. 3.9: Schematic of single-beam FTIR spectrometer, adapted from (Rouessac and Roussac, 2000)

The employed FTIR spectrometer was Nicolet 380 FTIR spectrometer by Thermoelectron Corporation. It was employed to investigate the nanoparticle chemical structure and the attachment of the organic surfactant to the nanoparticle surface. 2 mg of nanoparticle dry powder was grinded with 200 mg KBr (KBr is transparent to IR radiation) and pressed into a solid pellet. The solid pellet was mounted into the sample holder compartment. The IR beam transverse across the tested sample. The IR spectrum was generated by monitoring the intensity of the transmitted IR beam as function of the wavenumber (cm^{-1}). The generated IR spectrum was employed as a fingerprint of the nanoparticle chemical

structure; no two compounds could have identical IR spectra (Davide, 1994, Lambert et al., 1998). The obtained IR spectrum was employed mainly to verify the attachment of the organic surfactant to the nanoparticle surface, by comparing the IR spectrum of organic modified nanoparticles to uncoated counterparts.

3.3.8 Ultra violet-Visible (UV-Vis) spectroscopy

The nanoparticle absorption in the UV-Vis band can be correlated to the presence of selected sites of UV-Vis absorption (Silverstein et al., 1991). UV-Vis absorption can be employed to verify the attachment of the organic surfactant to the nanoparticle surface. The impact of UV-Vis photons on an isolated molecule alters the value of electric energy (E_{elect}) of valence electrons and hence modifies the total energy of the valence electrons (Equation 3.4) and induces different transitions related to the excitation of valence electrons (Rouessac and Roussac, 2000).

$$\Delta E_{\text{tot}} = \Delta E_{\text{rot}} + \Delta E_{\text{vib}} + \Delta E_{\text{elect}} \quad (3.4)$$

Where: ΔE_{tot} is the total energy of valence electron, ΔE_{rot} is the rotation energy of valence electron, ΔE_{vib} is the vibration energy of the valence electron, and ΔE_{elect} is the electric energy of valence electron. The molecular electronic state raises from ground state to higher energy excited state results in absorption of quantized photons (Thomas and Ando, 1996). The amount of absorbed radiation is defined by absorption (A), which is given by Equation 3.5 (Sommer, 1989).

$$A = \text{Log} \left(\frac{I_0}{I} \right) \quad (3.5)$$

Where: I_0 is the intensity of the incident beam, and I is the intensity of the transmitted beam. The main UV-Vis spectrometer components are radiation source, wave length selector, sample container, radiation transducer, and signal processing (read out devices) (Figure 3.10).

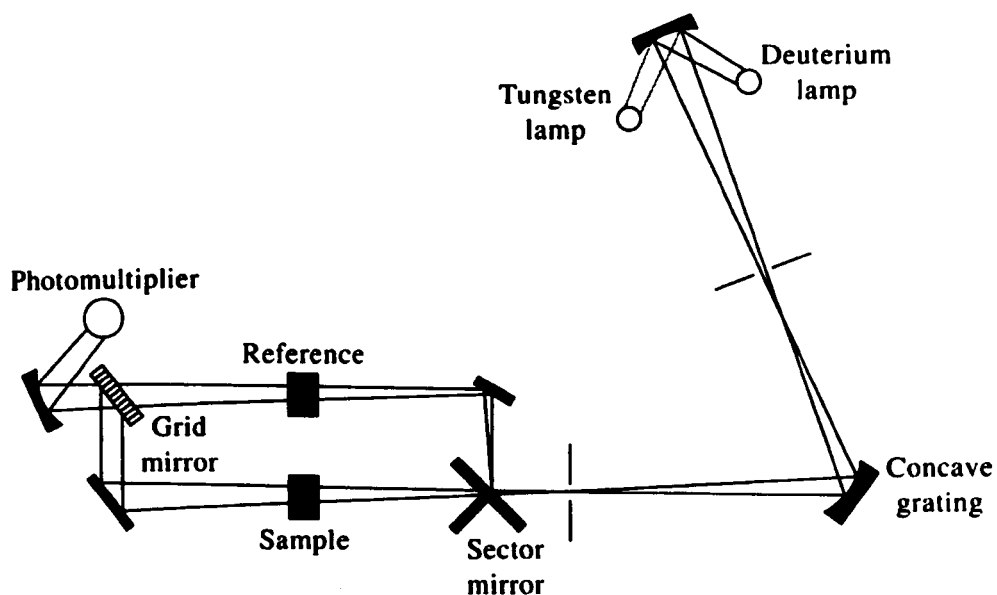


Fig. 3.10: Schematic of double-beam UV-Vis spectrometer, adapted from (Skog and Holler, 1999)

The employed UV-Vis spectrophotometer was Shimadzu 1240 by Shimadzu Corporation. The UV-Vis absorbance of colloidal nanoparticles was performed by using a UV-Vis transparent quartz cuvette. The UV-Vis spectrum of colloidal nanoparticles was generated by quantifying the absorption as a function of wave length over the UV-Vis band.

3.3.9 Thermogravimetric analysis (TGA)

Thermogravimetric analysis (TGA) technique is an essential tool to investigate the thermal stability of nanoparticles and nanocomposites, and to evaluate the surfactant loading level of organic modified nanoparticles. In this technique the mass of the tested sample was recorded as a function

of temperature or time as it is heated at a controlled heating rate in a controlled atmosphere. Modern commercial TGA instrument consists mainly of: (1) sensitive analytical balance, (2) furnace, (3) purge gas system to control the atmosphere, (4) microprocessor for instrument control, and (5) data acquisition (Figure 3.11).

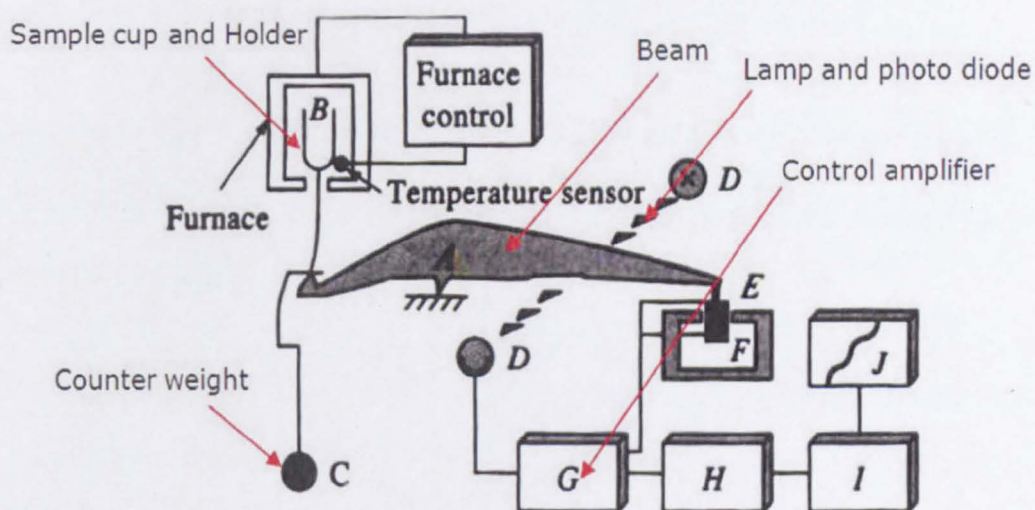


Fig. 3.11: Basic components of TGA instruments, adapted from (Skog and Holler, 1999)

The employed instrument was Pyris1 TGA by Perkin Elmer Corporation. The tested sample was heated from 30 °C to 100 °C. The temperature was held at 100 °C for 30 minutes to evaporate humidity. The sample was then heated from 100 °C to 800 °C. The heating rate was 10 °C/min. The air flow rate was 10 ml/min. The surfactant loading level of surface modified nanoparticles was determined by comparing the TGA profile of coated nanoparticles to uncoated counterparts.

3.4 Characterization of epoxy nanocomposites

It has been suggested that the incorporation of nanometric particles into polymeric matrix could result in improved mechanical, thermal, and

flammability properties when compared with conventional filled polymers (Vaia et al., 1999). The impact of different nanoparticles of different morphologies, ranging from nanospheres, nanoplates, to nanorods, onto epoxy resin mechanical and thermal properties was evaluated by mechanical compressive testing and TGA respectively.

3.4.1 The mechanical properties of epoxy nanocomposites

The impact of different nanoparticles onto epoxy mechanical properties was evaluated by mechanical compressive testing. Epoxy nanocomposite samples were prepared in the shape of cylinder (30 mm diameters and 12 mm height). The height of each tested sample was measured accurately. The prepared specimens were tested by using universal mechanical testing machine model 5985 by Instron Corporation (Figure 3.12). The compressive head speed was 1 mm/minute. The compressive stress of the tested specimen was measured as function of its strain.



Fig. 3.12: The universal mechanical testing machine

The compressive-stress strain response of the developed epoxy nanocomposites was evaluated and compared to virgin epoxy, in an

attempt to evaluate the impact of different nanoparticles of different morphologies onto epoxy resin mechanical properties.

3.4.2 The thermal stability of epoxy nanocomposites

It was reported that nanoparticles can improve the hosting polymer rheology under heating, and can improve the polymer viscosity in the molten state (Fu and Qu, 2004). The impact of different nanoparticles onto epoxy thermal stability was evaluated by using Pyris1 TGA instrument. The tested sample was heated from 30 °C to 800 °C at 10 °C/min heating rate. The air flow rate was 10 ml/min. The wt % of the tested sample was recorded as a function of the oven temperature.

3.5 Summary of experimental procedure

This Chapter represented the research work methodology, the experimental procedure for nanoparticle formulation and surface modification by using CHS techniques, the scientific fundamentals for different analytical techniques and instruments that were employed for nanoparticle and epoxy nanocomposite characterization. However, the successful achievement of PNs requires the dispersion of the nanoparticles to the molecular level with minimum aggregation. The following chapter will investigate the different factors that could affect the dispersion of dry nano-oxides (TiO_2) into epoxy resin.

CHAPTER 4

4. INTEGRATION AND DISPERSION OF DRY TITANIA NANOPARTICLES INTO EPOXY RESIN

The advantage of polymer nanocomposites (PNs) over conventional composites is the strong interaction between the nanoadditives and the polymeric matrix. This is why PNs exhibit unique properties that are not shared by their microscale counterparts (Giannelis et al., 1999). The real achievement of PNs requires the dispersion of the nanoadditives at the molecular level with minimum aggregation (LeBaron et al., 1999). Most polymers are hydrophobic thus they are neither compatible nor miscible with inorganic nanoadditives; this might lead to the inability to achieve PNs with nanoscale dispersion (Wilkie and Morgan, 2010). The first encountered problem is how to integrate and effectively disperse the inorganic nanoparticles into the organic polymeric matrix. Different approaches can be employed to integrate nanoparticles into polymers; these approaches can be classified into three main categories:

- In situ polymerization involves polymerization within dispersed nanoparticles in a solvent-free system or solvent-based system. Stirring/mixing is an important factor; as it provides the required shearing force to separate the nanoparticles and to break down the aggregates (Xu et al., 2003, Voorn et al., 2006).
- Solvent blending involves dispersing the nanoadditives and dissolving the polymeric matrix in a solvent/solvent mixture. It is still being used

at the lab scale. It may have an industrial applications for operations where the organic solvent can be recovered (Vaia et al., 2003).

- Melt blending is the most widely employed approach for PNs preparation. In this approach the polymer and the nanoparticles are injected as one feed to the compounding equipment such as an extruder and then compound at the temperature required for the polymeric matrix melting (Alexandre and Dubois, 2000).

This Chapter represents the studies done to investigate how nano-oxides (TiO_2) could be effectively dispersed into epoxy resin, and how the effective dispersion could be quantified by image analysis. To the best of the auther knowledge, this is the first time image analysis has been employed to quantify the dispersion characteristics of nanoparticles into polymers.

4.1 Integration of dry titania nanoparticles into epoxy resin

There are well known problems with the dispersion of dry nanoparticles into polymers; as the nanoparticles tend to aggregate and agglomerate and act like micron sized particles rather than nanoparticles. The nanoscale dispersion of dry nanoparticles into polymeric matrix is the key factor for the successful achievement of PNs. Dry titania of 25 nm particle size (commercially known as P25) produced by Degussa was employed as a standard reference to investigate how nano-oxides could be integrated and effectively dispersed into the polymeric matrix.

Epoxy resin, one of the most commonly used polymers in engineering applications, was employed as the dispersing medium. The employed

4. Integration and dispersion of dry titania nanoparticles into epox resin

epoxy resin was bisphenol-A (epichlorohydrin) with number average molecular weight ≤ 700 gm/mol, commercially known as Epofix resin, produced by Struers. The cross linking agent was triethylene tetramine also produced by Struers. Figure 4.1 shows the chemical structure of epoxy resin and the cross linking agent.

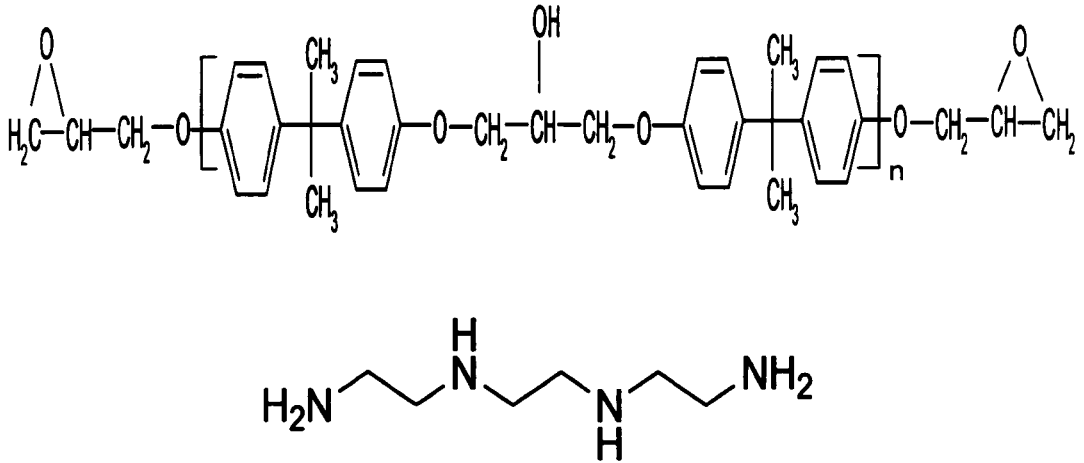


Fig. 4.1: The chemical structure of epoxy resin and triethylene tetramine

Epoxy nanocomposite formulations were prepared by in situ polymerization (solvent-free system). The solid nanoparticles were added to epoxy resin. Mechanical mixing at 1200 rpm was employed for 1 hour to provide the required shearing force to separate the nanoparticles and break down the aggregates. The cross linking agent was added at the end of the mixing time. The prepared formulations were cast under vacuum (0.1 bar) into a mould. Vacuum casting minimized the entrapped air bubbles and enabled the achievement of a compact structure with minimum air voids. Figure 4.2 shows the mechanical mixing set up and the vacuum casting unit.

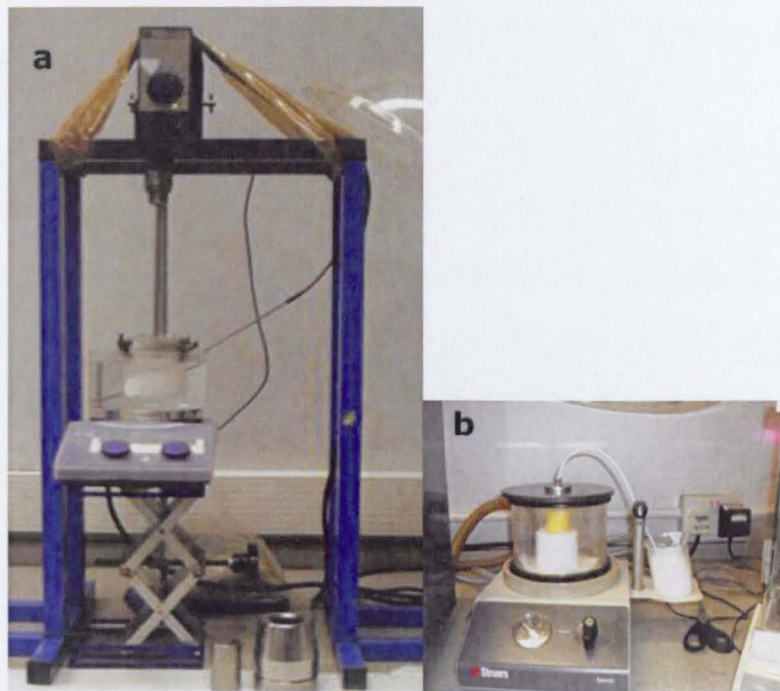


Fig. 4.2: Mechanical mixing with heating (a), vacuum cast (b)

Epoxy nanocomposite formulations prepared by vacuum cast showed enhanced structural integrity (minimum air voids) compared with the formulations prepared by normal cast (Figure 4.3).

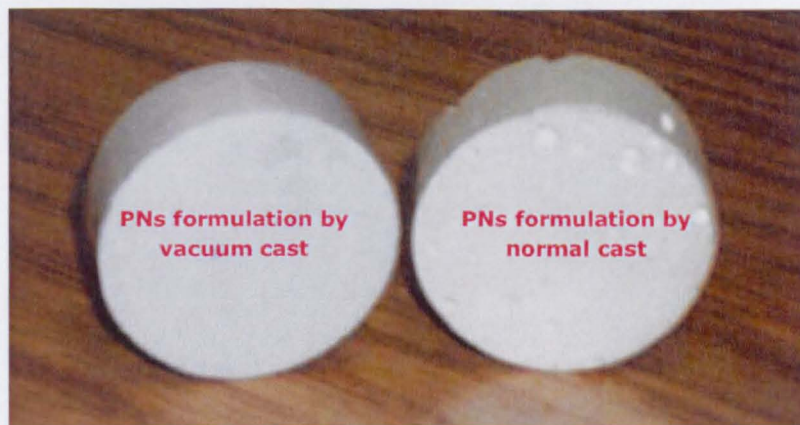


Fig. 4.3: The impact of vacuum cast onto epoxy nanocomposite structural integrity

4.2 Dispersion characteristics of titania nanoparticles into epoxy resin

The potential for commercial exploitation of PNs depends on the ease with which the nanoparticles can be introduced into polymers and the polymer processing system (Horrocks and Price, 2008). The aim of this Section of work is to investigate how dry nanoparticles particularly nano-oxides (TiO_2), can be effectively dispersed into epoxy resin and how the effective level of dispersion can be quantified by using image analysis technique. Commercially available TiO_2 known as P25 (by Degussa) with an average particle size of 25 nm was used as a dry nanopowder. The impact of solid loading level, mechanical mixing, and heating on titania P25 dispersion was evaluated by quantifying the dispersion of P25 at different solid loading levels, mixing times, and at different mixing temperatures.

Titania/epoxy nanocomposite specimens in the shape of cylinders of 30 mm diameter and of 12 mm height were prepared by mechanical mixing and vacuum casting. The nanocomposite cylinders were polished for smooth surface with no scratches. The nanoparticle dispersion was investigated with SEM. Mapping titania dispersion by using EDX detector caused damage to the polymer specimen; as the sample surface had to be subjected to highly energetic electron beam for 30 minutes. The nanoparticle dispersion of was mapped with BSE detector. The contrast in backscattered images comes primarily from point to point difference in the sample atomic number (Reimer, 1998). The magnification value of the BSE detector was 1300 X.

The nanoparticle dispersion was quantified by using image analysis Labview (National Instruments) version 2009. A script was established

4. Integration and dispersion of dry titania nanoparticles into epox resin

where each SEM image was loaded onto the software and then converted to a grey scale image by thresholding the red, green, and blue (RGB) colours. The grey image was then threshold into a binary image. The threshold was adjusted to threshold out all detectable particles. Figure 4.4 shows the transformation process of epoxy nanocomposite (1 wt % titania) SEM image to grey scale image, and then to binary image where all the aggregated particles were captured.

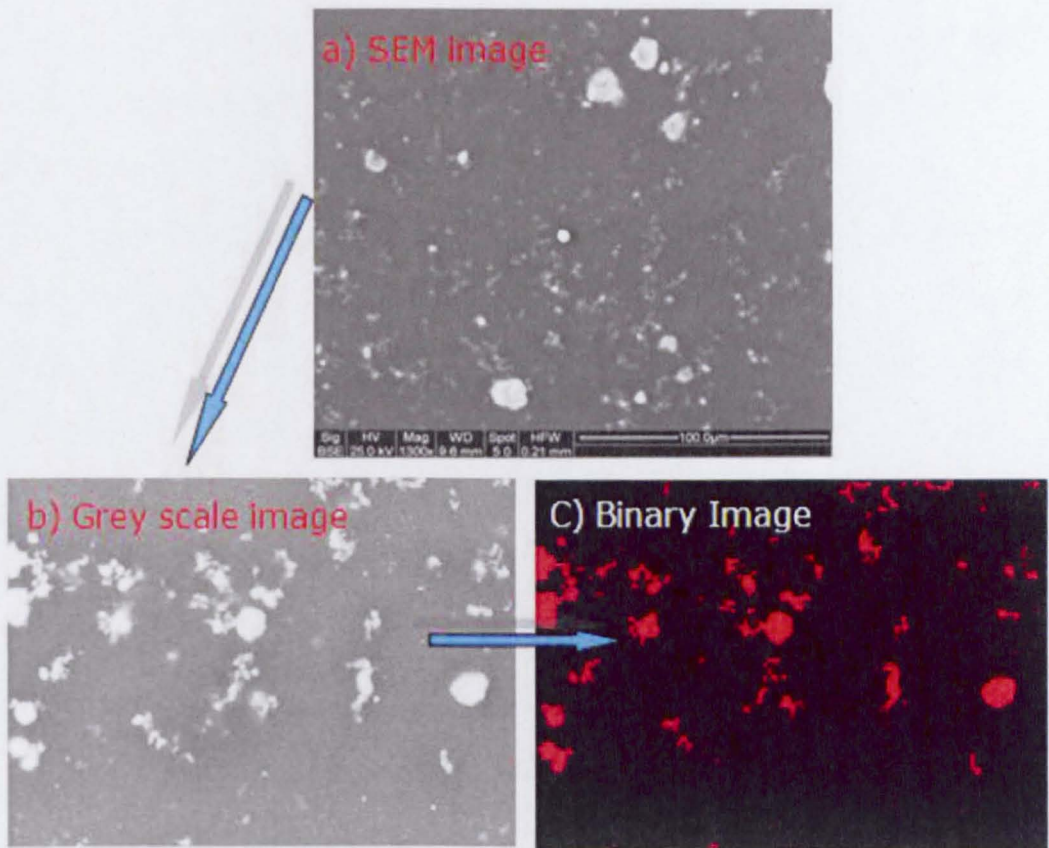


Fig. 4.4: Image analysis process for the dispersion of 1 wt % TiO₂ into epoxy resin

The binary image was processed using image analysis to calculate each aggregate size; the total aggregate area to the image area was calculated. Equation 4.1 expresses the polymer area %, which is the area % of the nanocomposite where there is no aggregation.

$$\text{Polymer area \%} = \frac{(\text{image area}) - (\text{aggregate area})}{(\text{image area})} \times 100 \quad (4.1)$$

The critical limitation of this technique is the detection limit of the process which is dictated, in part, by the resolution of the SEM images. Each image was of about 193×209 microns in width with a total pixel number of about 902 000. This means that each pixel in the binary image is equivalent to a square of 212 nm side of the SEM image. Therefore, the smallest particles that could be detected are limited to 212 nm diameter. This meant that aggregates smaller than 212 nm could not be detected and therefore it would be possible to image a block with epoxy and TiO₂ particles and only see epoxy. In reality the resolution is certainly higher than 212 nm, since a pixel containing, say, 50% TiO₂, would have a higher reflectance than a pixel with 100% epoxy, resulting in an increased average reflectance. The sensitivity of the thresholding therefore allows pixels with smaller clusters of TiO₂ (than 212nm) to be 'detected'. In practice, most aggregates were generally significantly larger than a single pixel and therefore easy to detect. The dispersion characteristics of dry nano-oxides (TiO₂) into epoxy resin were investigated, in an attempt to achieve nanoscale dispersion.

4.3 The impact of solid loading level and mechanical mixing on nano-oxide dispersion

Physical mixing is an important factor for nanoparticle dispersion; as it provides the required shearing force to separate the particles and breakdown the aggregates (Vaia et al., 2003). The impact of solid loading level and mechanical mixing on dry titania P25 dispersion into epoxy resin were investigated; epoxy nanocomposites of different titania P25 loading

4. Integration and dispersion of dry titania nanoparticles into epox resin

levels of 1, 5, 10, 15, and 30 wt % were prepared by mechanical mixing and vacuum cast. Different mixing times of 2, 10, 30, and 60 minutes were employed for each loading level. The nanoparticle dispersion was investigated with SEM and quantified by using image analysis. Figure 4.5 shows how the different loading levels of P25 disperse with mixing time. There was no direct trend for the 1, 5, 10, 15, and 30 wt % loadings i.e. the highest weight loading exhibited a better dispersion than the 5 wt % loading.

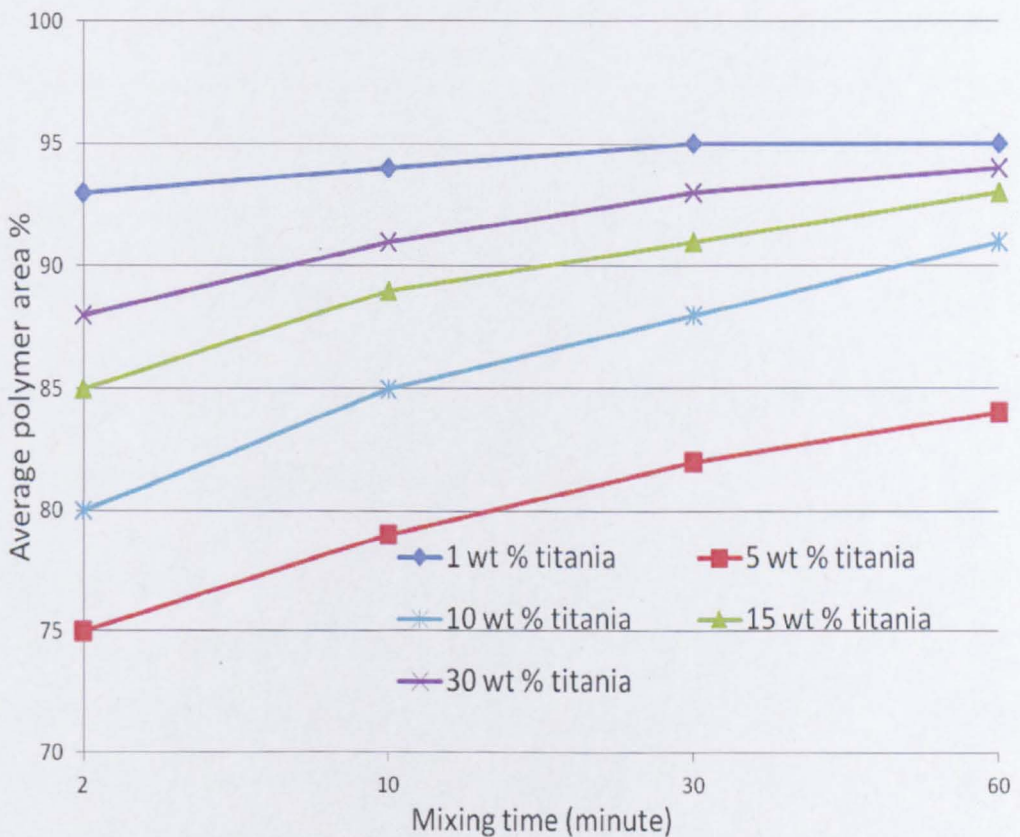


Fig. 4.5: The impact of mechanical mixing and solid loading level on titania P25 dispersion

There was clearly an improvement in P25 dispersion with mechanical mixing and solid loading level. This can be related to the attrition between the aggregates during mechanical mixing (Baraton, 2003, Voorn et al.,

2006). Mechanical mixing did not show a noticeable effect on 1 wt % titania loading level. This can be ascribed to the reduced viscosity and subsequently the minimized attrition between the aggregates at low solid loading levels.

5 wt % loading showed the poorest dispersion (with the lowest polymer area detected) which is counter-intuitive i.e. 15 wt % and 30 wt % showed a better dispersion than 5 wt % and the 10 wt % loading. This is probably due to the enhanced attrition (between aggregated particles) that is possible with higher weight loadings which breaks down the aggregates more effectively with the increase in solid loading and polymer viscosity. However, solid loading levels higher than 10 wt % also started to exhibit increased viscosity, processing difficulties, and issues with entrapped air bubbles.

4.4 The impact of solid loading level and mechanical mixing on the aggregate morphology

The Labview (National Instruments) software enabled the quantification of different characteristic dimensions of the thresholded aggregates. For each aggregated particle, it was possible to quantify the perimeter (length of a boundary of a region), maximum feret diameter (Line segment connecting the two perimeter points that are the furthest apart), average horizontal segment length, average vertical segment length, and the aggregate size. All these characteristic measurements were produced as pixel values and then converted to microns using scaling from the image.

The impact of solid loading level and mechanical mixing on the aggregate morphology was evaluated by quantifying the average aggregate perimeter,

4. Integration and dispersion of dry titania nanoparticles into epox resin

maximum feret diameter, and size for different titania P25 solid loading levels and mixing times (investigated formulations in Section 4.3). Figure 4.6 shows how solid loading level and mechanical mixing affect the average aggregate size. The average aggregate size was represented in (μm^2) as each pixel of the binary image represented a square of 212 nm side of the SEM image.

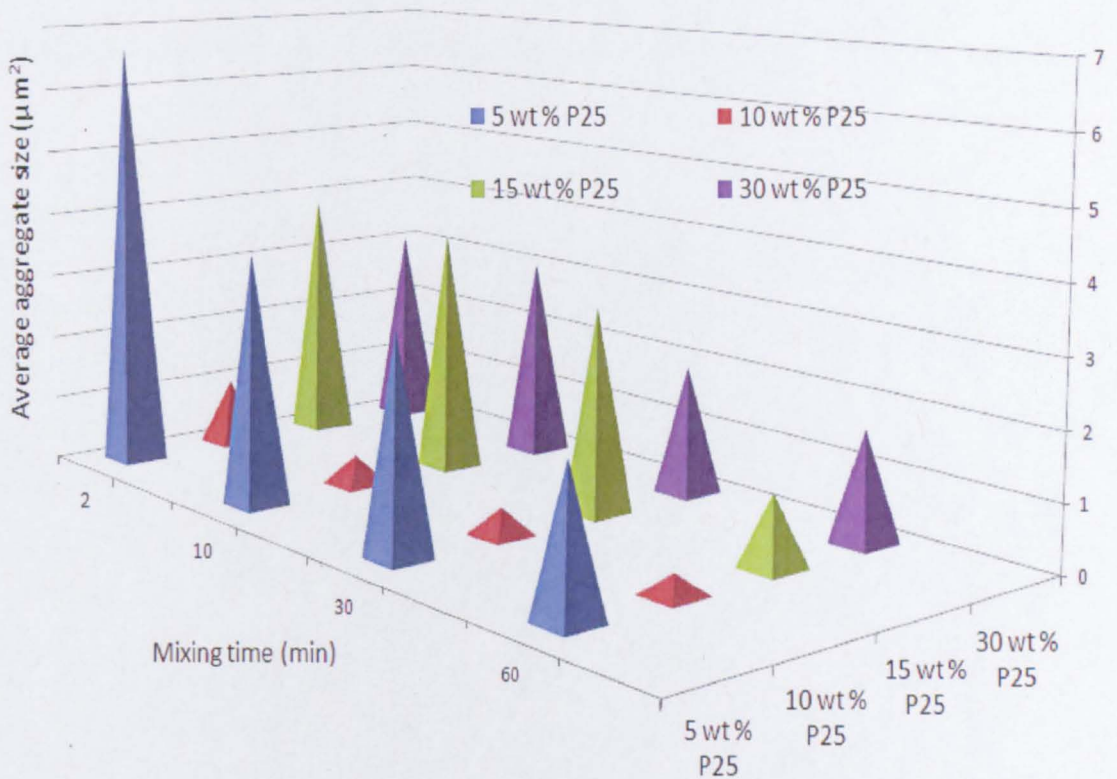


Fig. 4.6: The impact of solid loading level and mechanical mixing on the P25 aggregate size in epoxy resin

The obtained data demonstrated that there was a decrease in the aggregate size with mixing time for all investigated solid loading levels. At low solid loading level (5 wt % or less), the low viscosity could minimize the attrition force value below the limit required to breakdown the aggregates. 10 wt % solid loading level exhibited the smallest average aggregate size; this could be ascribed to the enhanced formulation

4. Integration and dispersion of dry titania nanoparticles into epox resin

viscosity which might enable uniform attrition force during mechanical mixing with no stagnation zone. At high solid loading level (15 wt % or more), the high viscosity could greatly minimize the attrition force and could induce stagnation zones. The obtained results gives an indication that 10 wt % solid loading level could be the recommended loading level regarding processing, casting, and nanoparticle dispersion. Furthermore, the impact of solid loading level and mechanical mixing on the average aggregate perimeter was evaluated (Figure 4.7).

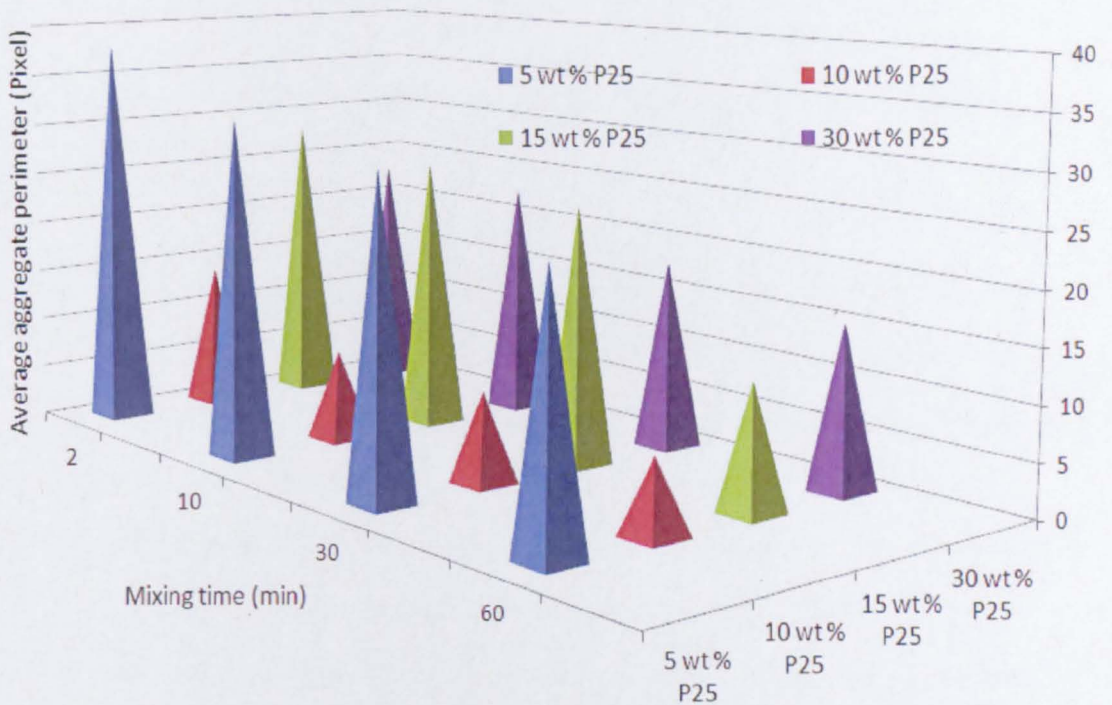


Fig. 4.7: The impact of solid loading level and mechanical mixing on the P25 aggregate perimeter in epoxy resin

All investigated formulations showed a decrease in the average aggregate perimeter with mixing time. Again, 10 wt % solid loading level exhibited the least average aggregate perimeter. This finding confirmed the previous results regarding the impact of solid loading level and mixing time on the average aggregate size (Figure 4.6). It was concluded that 10 wt % solid

loading level with mechanical mixing for 1 hour is the recommended procedure to develop epoxy nanocomposite with enhanced nanoparticle dispersion and subsequently flame retardancy. Wilkie has reported that the acceptable limit of solid loading to improve flame retardancy is restricted to 10 wt % or less, owing to the strong increase in polymer viscosity, impairing processability, and also due to the breakdown of the ultimate mechanical properties (Wilkie and Morgan, 2010). To the best of the author's knowledge, this is the first time image analysis has been used to evaluate nanoparticle dispersion and quantify aggregate morphology.

4.5 The impact of heating during mixing on nano-oxide dispersion

Heating could be helpful in reducing the viscosity of the epoxy during mixing and therefore improve processing, particularly at high solid loadings (15 wt % onwards). However heating could also affect the behaviour of the nanoparticle aggregates. The impact of heating during mechanical mixing on titania P25 dispersion was investigated by quantifying the dispersion of titania P25 formulations prepared by mechanical mixing with heating to those prepared by mechanical (only) at the same solid loading levels and mixing time.

Epoxy nanocomposites of different titania P25 loading levels of 1, 5, 10, 15, 20, 25, and 30 wt % were prepared by mechanical mixing with heating at 80 °C for 1 hour followed by vacuum cast. The same formulations were prepared by mechanical mixing only. The impact of heating on nanoparticle dispersion was investigated with SEM and quantified by image analysis. Figure 4.8 shows the effect of heating on titania P25 dispersion at 15 wt % solid loading level.

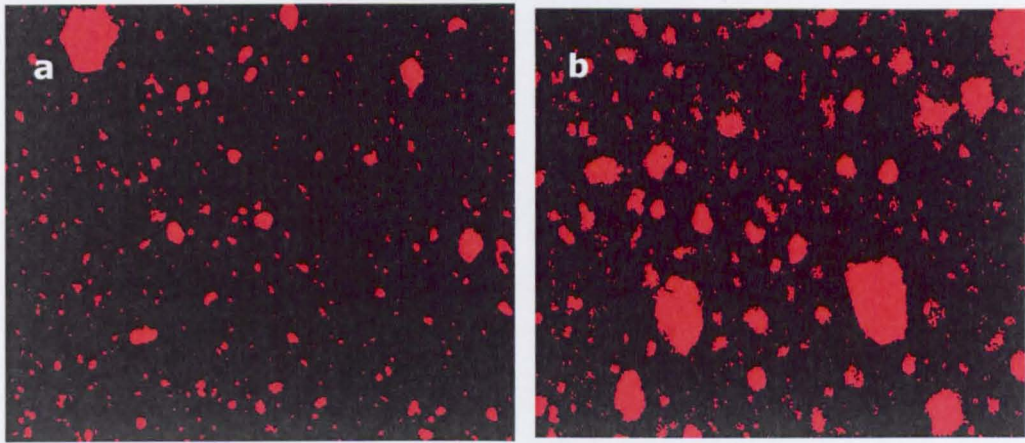


Fig. 4.8: The dispersion of 15 wt % titania P25 into epoxy resin after: (a) mechanical mixing only, (b) mechanical mixing with heating

The effective dispersion of titania nanoparticles decreased dramatically under the effect of heating. Figure 4.9 shows the quantified nanoparticle dispersion (polymer area) for different titania loading levels, produced by mechanical mixing with heating compared with those produced by mechanical mixing only.



Fig. 4.9: The impact of heating during mechanical mixing on titania P25 dispersion in epoxy resin

4. Integration and dispersion of dry titania nanoparticles into epox resin

Even though heating improved the polymer processing by decreasing the polymer viscosity at high solid loadings (higher than 15 wt %); it appeared to increase the rate of aggregation particularly at loading levels below 15 wt % as a result of the reduced viscosity and subsequently the reduced attrition between the aggregates. Table 4.1 shows how heating can affect the aggregate perimeter and size.

Table 4.1: The impact of mechanical mixing and heating on the average aggregate perimeter and size of titania P25 in epoxy resin

Solid loading level (wt %)	Mechanical mixing with heating		Mechanical mixing only	
	Average aggregate Perimeter (Pixel)	Average aggregate size (μm)	Average aggregate Perimeter (Pixel)	Average aggregate size (μm)
5	20.8	2.5	25	2.1
10	21.6	2.6	7	0.3
15	12.1	1.2	12	1
20	12.6	1.5	17	1.7
25	11.5	1.3	15	1.4
30	7.8	0.8	15	1.7

The green shaded cells show the least aggregate perimeter and size for mechanical mixing and mechanical mixing with heating. It can be concluded that heating improved the viscosity and processing at high solid loading levels particularly at 30 wt %, but adversely affected dispersion at

low solid loadings. Furthermore increased the aggregation rate due to the increase in the inter particle 'Brownian motion'.

Experimentally it was found that solid loading level up to 10 wt % can be processed and cast under vacuum without heating, therefore any aggregation caused by heating could be avoided. Mechanical mixing for 1 hour followed by vacuum cast could be the recommended procedure for integrating and dispersing dry titania nanoparticles into epoxy resin at solid loading levels up to 10 wt %. Mechanical mixing with heating at 80 °C for 1 hour, followed by vacuum cast could be the recommended procedure for dry nanoparticle loading levels 15-30 wt % to overcome the increased viscosity and entrapped air bubbles.

A solvent blending approach to integrate colloidal organic modified nanoparticles dispersed in organic solvent directly into epoxy resin was developed. This approach enabled the elimination of nanoparticle freeze drying and the re-dispersion of aggregated dry nanoparticles into polymeric matrix. Furthermore, enhanced nanoparticle dispersion was achieved via this approach; as nanoparticles were kept in dispersion during all processing stages. Further details about nanocomposite formulations via solvent blending approach will be discussed in details in Chapter 8.

4.6 Summary of integration and dispersion of dry titania nanoparticles into epoxy resin

This Chapter represented an experimental work to investigate the integration and the dispersion characteristics of dry nano-oxides (commercial TiO₂ nanoparticles) into epoxy resin. The processing parameters that could affect dry nano-oxide dispersion into polymeric

4. Integration and dispersion of dry titania nanoparticles into epox resin

matrix were investigated. The investigated parameters were solid loading level, mechanical mixing, and heating.

There was an improvement in titania P25 dispersion with solid loading level, and with mechanical mixing due to the induced attrition action between the nanoparticles under the effect of mechanical mixing. Even though, heating decreased the nanocomposite viscosity and improved processing particularly at high solid loading level; it provoked aggressive aggregation. The maximum or optimal solid loading level appears to be 10 wt %, as it exhibited enhanced nanoparticle dispersion and also enabled processing and casting with no heating. The recommended procedure for dry nanoparticle dispersion into epoxy resin is mechanical mixing for 1 hour followed by vacuum cast.

Enhanced nanoparticle dispersion might be achieved via surface modification; as the organic surfactants has been reported to increase the compatibility between the inorganic nanoparticles and the organic dispersing medium. In the following chapter, CHS techniques will be exploited for the formulation and surface modification of TiO₂ nanoparticles in an attempt to enhance their dispersion into epoxy resin and its consequent flammability performance.

CHAPTER 5

5. TITANIA SURFACE MODIFICATION WITH ORGANIC LIGANDS

Nano-metal oxides have been reported to improve polymer flammability properties, where the enhanced performance of oxide-nanocomposites have been attributed to the restriction of the polymer chain mobility and improved viscosity under the conditions associated with burning polymer (Fu and Qu, 2004). Furthermore, this behaviour has been linked to the strong interaction between the nanoparticles and the polymer chains (Laachachi et al., 2005a). Consequently, it have also been reported that the flame retardancy benefit achieved from including nano-oxides within a material depends on their particle size and surface area (Laachachi et al., 2006).

In this Chapter, nano-oxides with some flame retardant potential were synthesized and surface modified with organic ligands by using CHS in an attempt to improve their dispersion into polymeric matrix. Furthermore, the hydrothermal synthesis conditions used in the nanoparticle manufacture were tuned together to achieve an effective surface modification. Finally, the nature of the surface modification agent used was adjusted to further improve/optimize the flame retardancy performance by including flame retardant active elements, mainly phosphorous (P), into the surface active compound.

5.1 Synthesis of titania nanoparticles

Titania nanoparticles have been found to be an important constituent in certain multi-component FR systems; firstly because their inclusion into composite materials can improve the polymer viscosity when in the molten state and secondly they have the potential to react with different FR agents (Fu and Qu, 2004). In this study, the titania nanoparticles utilised were synthesized by using CHS technique devised at the University of Nottingham a diagram of which is included as Figure 5.1.

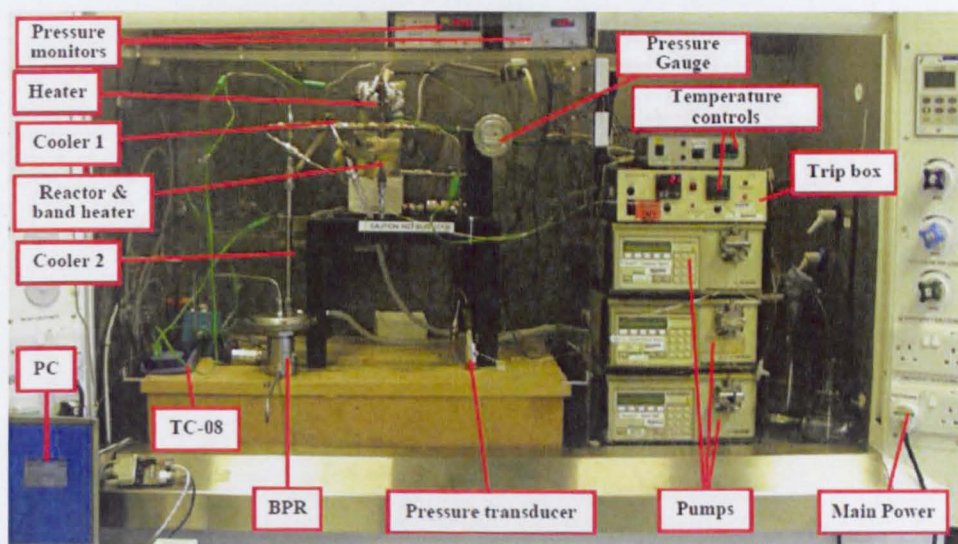


Fig. 5.1: Diagram of the continuous hydrothermal synthesis (CHS) apparatus used to generate the nanoparticles in this study

The basic principles and the operating procedure for CHS technique were described in Section 3.2. The used metal salt to generate the nanoparticles was titanium (IV) bis (ammonium lactato) dihydroxide (TIBALD), (Aldrich). The molecular structure of TIBALD is included as Figure 5.2.

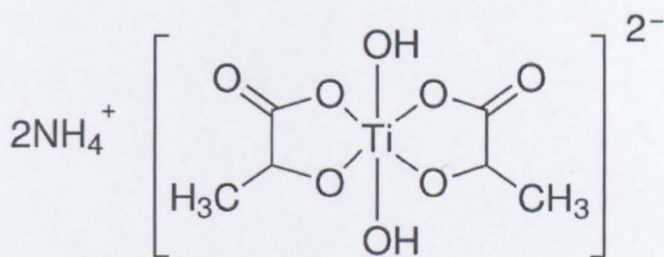


Fig. 5.2: The molecular structure of TIBALD

The metal salt feed was 0.05 M TIBALD in water (10 ml/min). ScW was utilised at 240 bars and 400 °C (20 ml/min). The colloidal titania nanoparticles were then centrifuged, and freeze dried. The crystalline phase of dry titania nanoparticles was investigated by XRD (Figure 5.3).

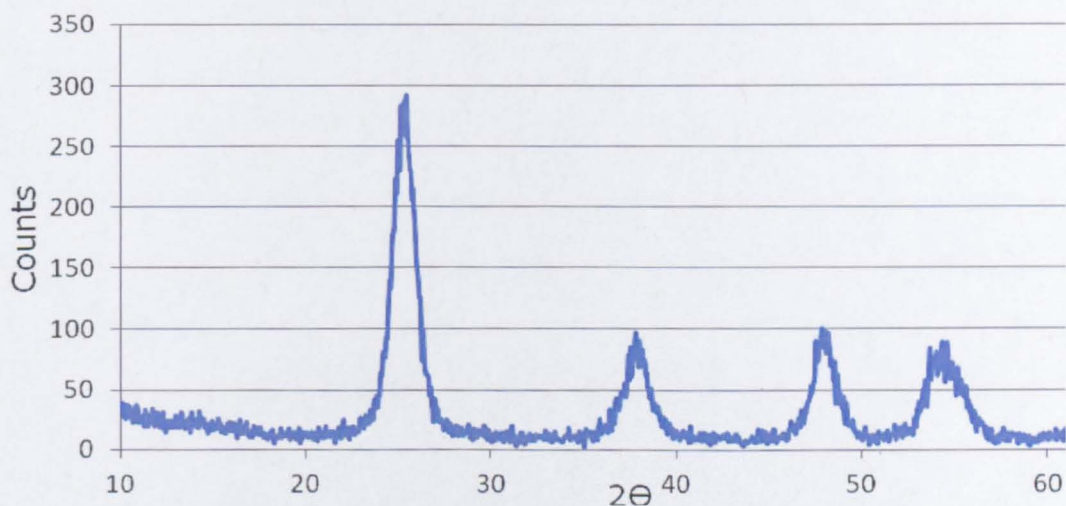


Fig. 5.3: XRD diffractogram of TiO_2 nanoparticles produced by CHS (XRD was described in section 3.3.1)

The prepared titania exhibited an anatase crystalline phase with an interspacial distance of 52 Å. Additionally, the chemical structure of titania nanoparticles was investigated by EDX (as described in Section 3.3.3) to verify the elemental composition, and typical data obtain from this technique is included as Figure 5.4. Titania elemental composition was found to be $\text{Ti}_{31.58} \text{O}_{68.42}$, which can also be expressed as a value normalised onto the quantity of titanium present as, $\text{TiO}_{2.17}$. In this case,

the excess oxygen atoms (0.17) can be ascribed to the tender of titania produced by CHS to exhibit hydroxyl functional group on the surface.

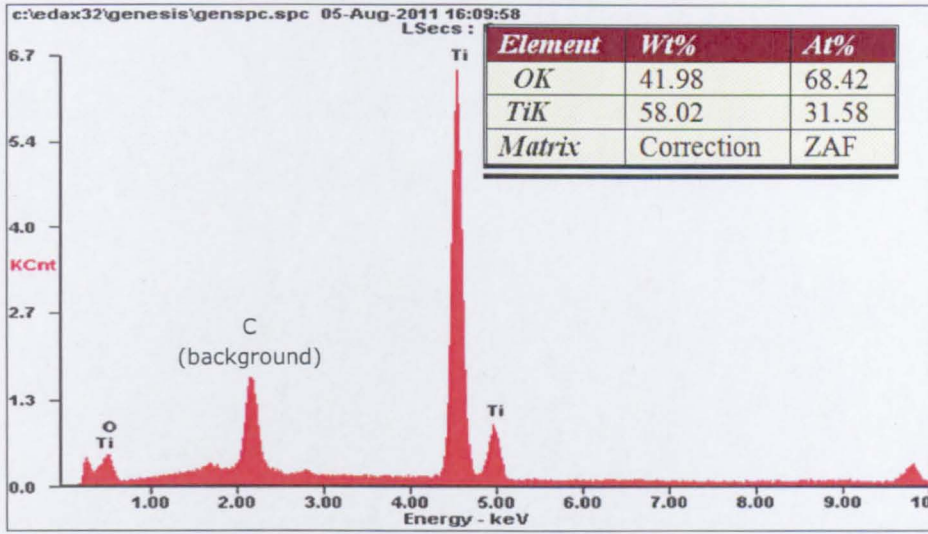


Fig. 5.4: EDX spectrum of titania nanoparticles produced by CHS

The size of titania nanoparticles was evaluated by using TEM (as described in Section 3.3.4), and typical data obtain from this technique is included as Figure 5.5.

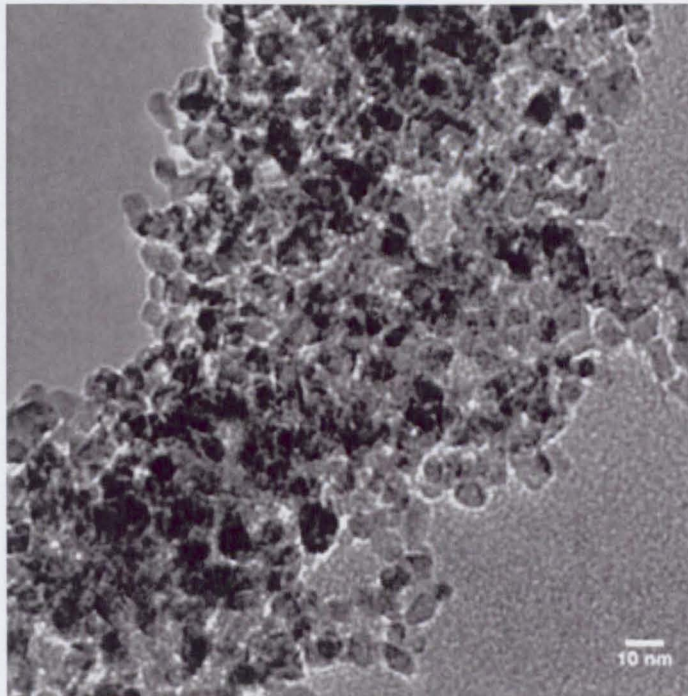


Fig. 5.5: TEM image of titania nanoparticles produced by CHS

The TEM image demonstrated that spherical titania nanoparticles with an average particle size of 5.4 nm had been achieved. The particle size was quantified by measuring the particle diameter to the image scaling. The subsequent freeze dried powder was submitted to SEM analysis (as described in Section 3.3.2) and showed that spherical titania nanoparticles of 44.1 nm average aggregate size was measured from SEM image (Figure 5.6).

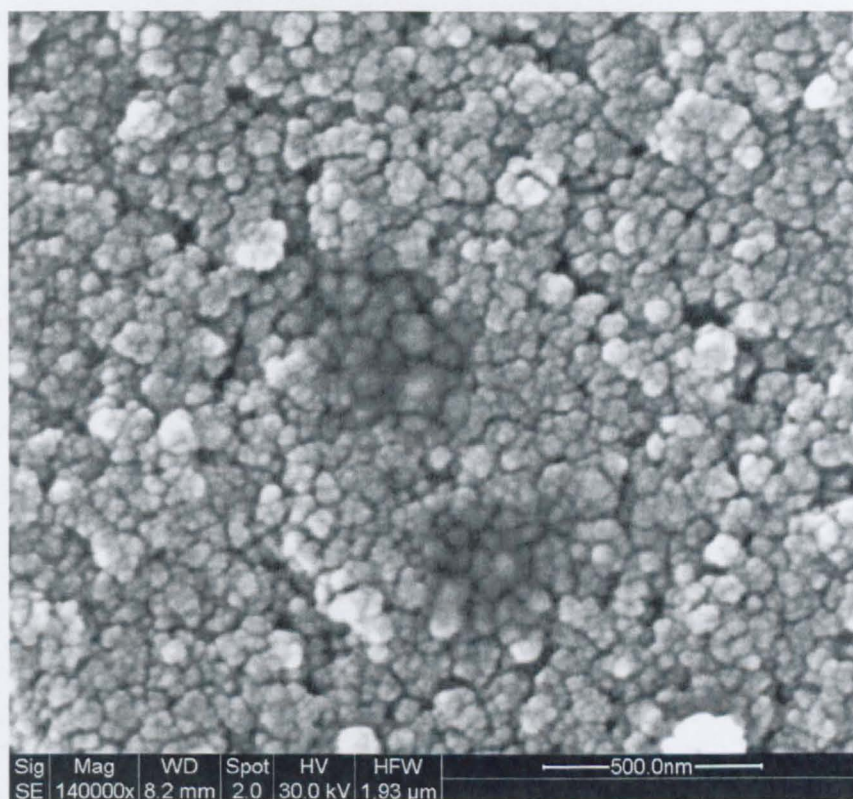


Fig. 5.6: SEM image of freeze dried TiO_2 nanoparticles produced by CHS. The aggregation of the titania nanoparticles during freeze drying was attributed to the particles coming into direct contact with each other during solvent sublimation that is a part of the preparative process to obtain dry nanopowder for SEM analysis.

5.2 Titania post-synthesis modification with dodeceny succinic anhydride

Nano-oxide particles produced by CHS are in the form of colloids (Yoshimura and Byrappa, 2007). Collision during the manufacture process may cause excessive aggregation of the nanoparticles (Grate and Abraham, 1991, Khanna, 1997). Therefore, a route to produce a stable nano-oxide colloidal suspension is essential if mono-dispersed nanoparticles are to be successfully synthesised, isolated, and used in subsequent composite manufacture. Certain organic ligands have been reported to stabilize colloidal nanoparticles and prevent coagulation by introducing a adsorbed layer which constitutes a significant enough steric barrier (Napper, 1977) to prevent the particle surfaces from coming into direct contact. The most commonly used interfacial agents/dispersants to achieve this are capable of hydrogen bonding with the metal oxide surface (Yu and Somasundaran, 1996, Mathur and Moudgil, 1997). Consequently, carboxylate ligands are often used for modifying metal oxide nanoparticles (Neouze and Schubert, 2008) via this mechanism. Figure 5.7 shows the adsorption mechanisms of carboxylate dispersants to nano-oxide surface.

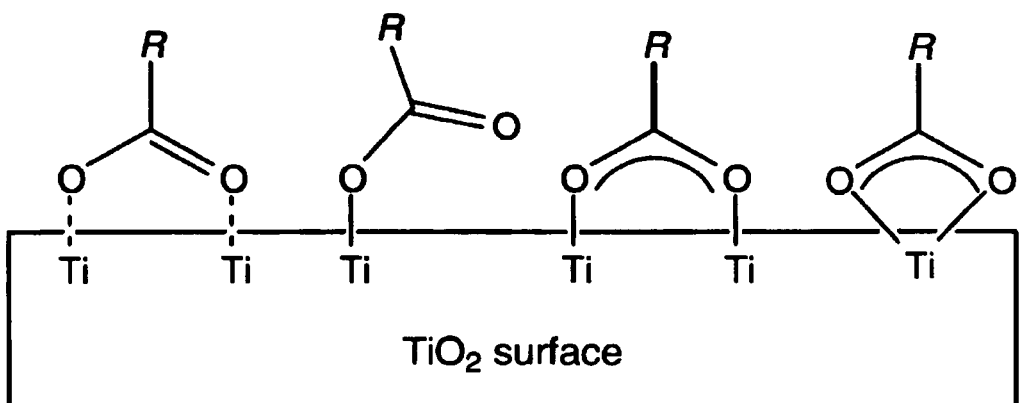


Fig. 5.7: Adsorption mechanisms of carboxylate ligands on titania nanoparticles, adapted from (Neouze and Schubert, 2008)

In this Section of the study, the titania nanoparticle formulation and online surface modification was performed via a post-synthesis surface modification approach (as described in Figure 3.1 position D). In this approach, nanoparticle synthesis was performed in the reactor and surface modification was carried out in a second separated step at the capping point in the apparatus. The carboxylic dispersant employed was dodeceny succinic anhydride (DDSA, Aldrich, 90%), the molecular structure of which is included as Figure 5.8.

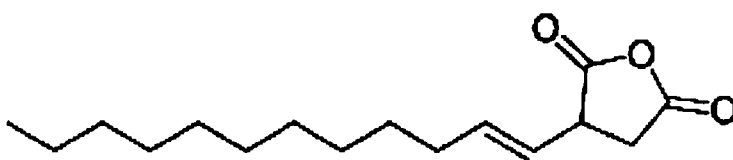


Fig. 5.8: The chemical structure of DDSA

In practice, the concentration of metal precursor and capping agent used were 0.05 M TIBALD in water (10 ml/min) and 0.005 M DDSA in toluene (5 ml/min) respectively, whilst the ScW conditions applied were 240 bars and 400 °C (20 ml/min). The temperature at the capping point was 185 °C and the molar feed ratio of DDSA:TiO₂ at the capping point was 1:20. The obtained titania colloid was left to settle overnight in a separating funnel. The colloid was observed to separate into two layers, the aqueous layer (water) at the bottom, and the organic layer (toluene) at the top. In this separation process, the DDSA-titania was extracted from the aqueous layer to the organic layer (see Figure 5.9).

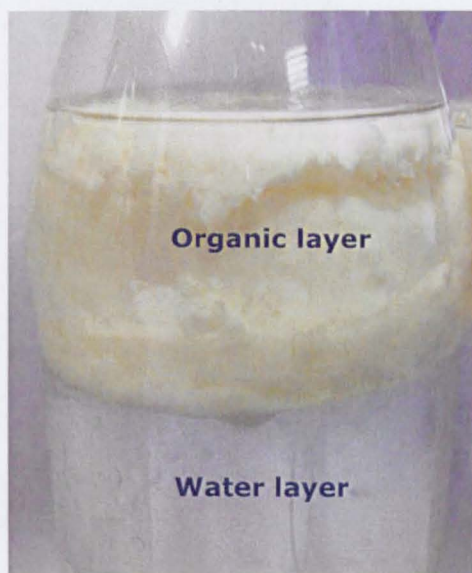


Fig. 5.9: Extraction of DDSA-titania to the organic phase

The dispersant at this concentration had proved sufficient efficiency that it had completely extracted the titania from the aqueous phase to the organic phase via the formation of a hydrogen bonded link to the surface of the nanoparticle. Such hydrogen bonding interactions have been reported to be the main mechanism for achieving carboxylic acid functionalised adsorption onto the surface of nanoparticles in previous reports (Elbhiri et al., 2000, Vaidyanathan et al., 2007).

The DDSA essentially represents a protected di-carboxylic acid, in which the functional group is "activated" by undergoing a thermally triggered ring opening process at the capping point. As a result, the H^+ functionality of the newly created diacid interact with the hydroxyl functionality on the surface of the titania to produce an electrostatic attraction to titania surface through the two pendant carboxylic groups. Figure 5.10 shows the proposed mechanism for titania surface modification with DDSA.

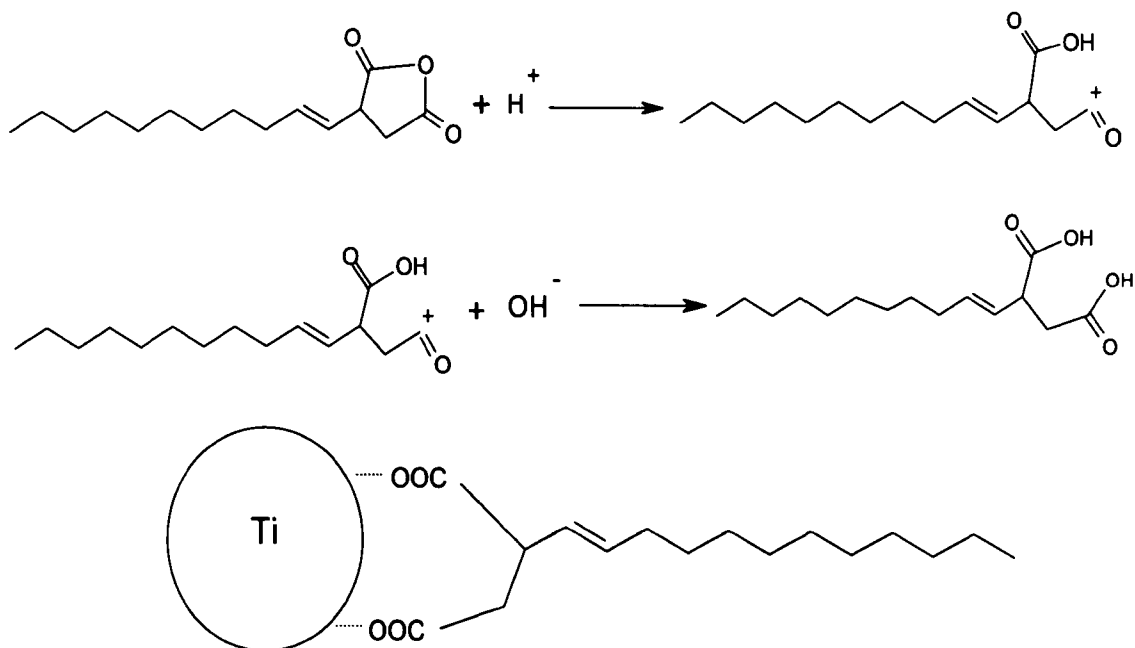


Fig. 5.10: Schematic of DDSA ring opening and anchoring titania surface

5.2.1 Characterization of DDSA-titania

5.2.1.1 EDX of DDSA-titania

The elemental composition of DDSA-titania was investigated with EDX using the method described in the experimental Section. The summary formula of DDSA-titania obtained by this technique was $Ti_{30.32} O_{61.49} C_{8.19}$. Thus the DDSA-titania summary formula can be normalized on the Ti concentration to be as $Ti O_{2.028} C_{0.27}$. The ratio between Ti and O is noted to be almost 1:2 and the excess of oxygen and carbon compared to that noted for the original nanoparticles have been ascribed to the attached dispersant.

5.2.1.2 FTIR of DDSA-titania

The chemical structure of DDSA-titania was investigated using FTIR (as described in Section 3.3.7) to verify the attachment of DDSA to titania

surface. Figure 5.11 shows the comparison of the FTIR spectrum for DDSA-titania and that of the uncoated titania and highlights the key functional groups that give rise to the absorption level in the spectrum which were compared to those that have been reported in the literature (Skog and Holler, 1999).

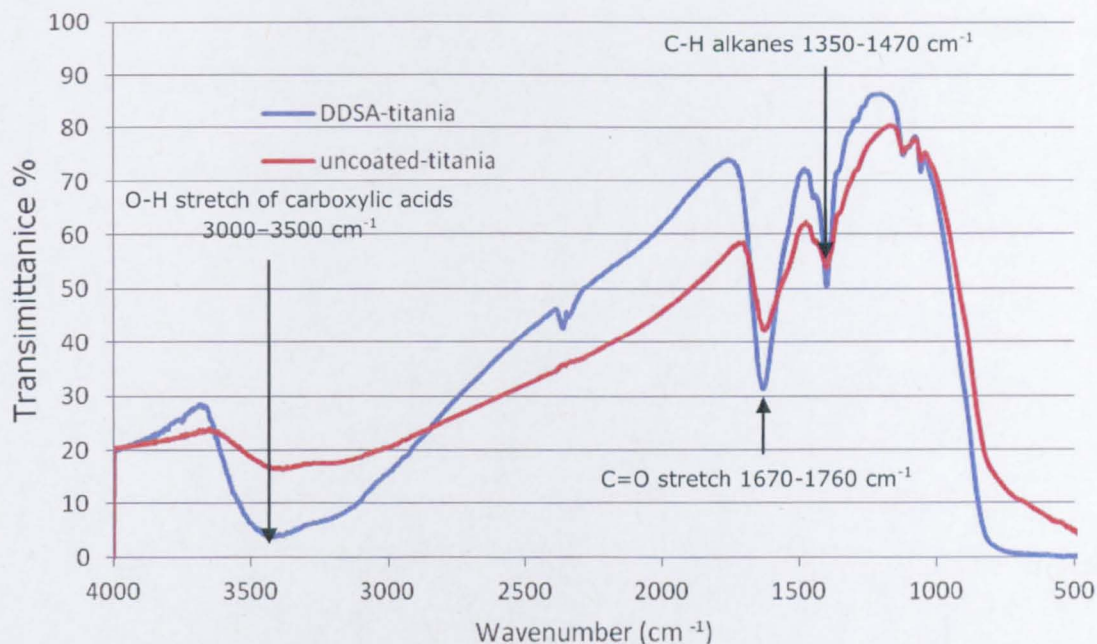


Fig. 5.11: FTIR spectrum of DDSA-titania to that of uncoated titania

DDSA-titania showed enhanced levels of IR absorption compared with uncoated titania which can be correlated to the carboxylic group stretch (O-H and C=O stretch) of the attached DDSA, the hydrogen bonding to the nanoparticle surface, and the C-H stretch of the attached dispersant.

5.2.1.3 XRD of DDSA-titania

The crystalline phase of DDSA-titania was investigated using XRD analysis and again it was compared to the data from uncoated titania produced by CHS. Both the DDSA-titania and uncoated titania nanoparticles showed the same crystalline phase (anatase crystalline structure) (Figure 5.12).

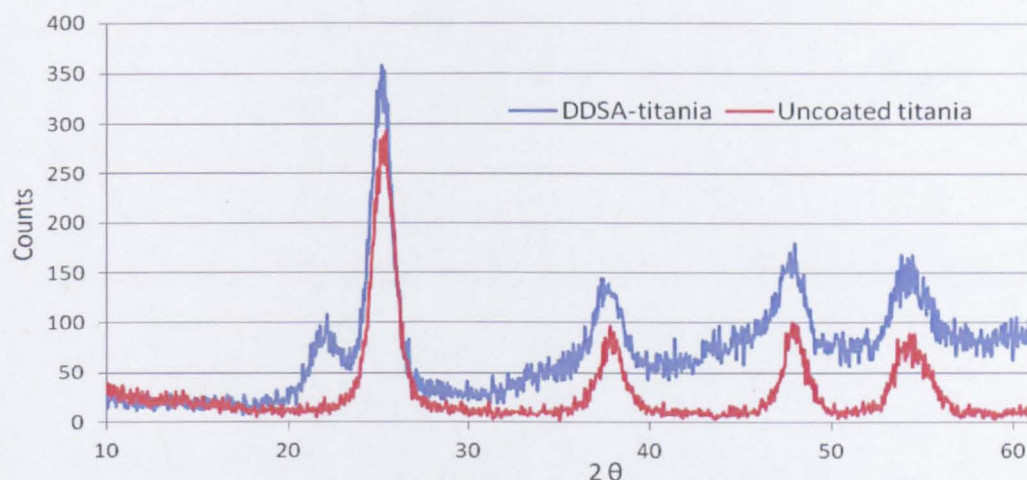


Fig. 5.12: XRD diffractograms of DDSA-titania and uncoated titania

DDSA clearly did not affect titania crystalline phase; as the nanoparticles were modified in a separated stage at the capping point, post reaction but prior to collection.

5.2.1.4 TEM of DDSA-titania

The size of DDSA-titania nanoparticles dispersed in toluene was investigated using TEM and DDSA-titania nanoparticles with an average particle size of 5.7 nm were reported. A typical TEM image of DDSA-titania is included as Figure 5.13.

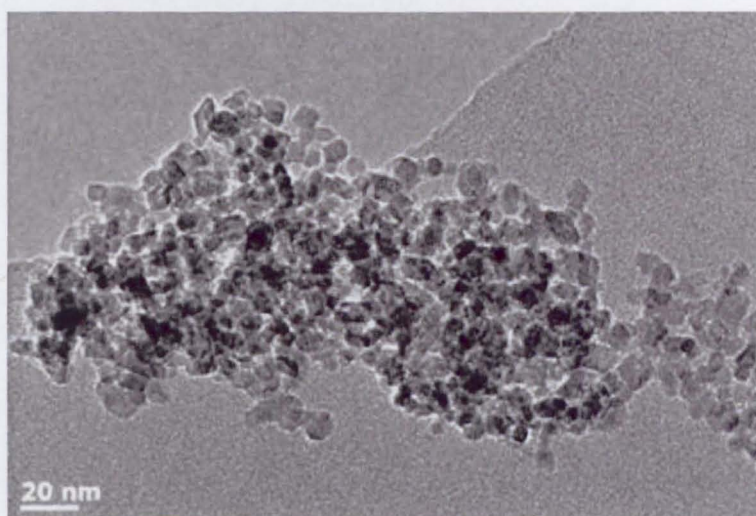


Fig. 5.13: TEM image of DDSA-titania

It was also observed that the size of DDSA-titania and uncoated titania nanoparticles was found to be almost identical of 5.7 nm average particle size with a difference of only ± 0.3 nm. Thus it was concluded that DDSA had been successfully bonded to titania surface at the capping point and this steric dispersant layer had aided in the process of extracting the nanoparticles to the organic layer without further aggregation.

5.2.1.5 UV-Vis of DDSA-titania

The UV-Vis absorption of the DDSA-titania colloid in water was evaluated and again compared with a similar uncoated titania system; UV-Vis was described in Section 3.3.8. Figure 5.14 demonstrated that the DDSA-titania sample showed enhanced absorption in the UV region compared with the uncoated counterparts.

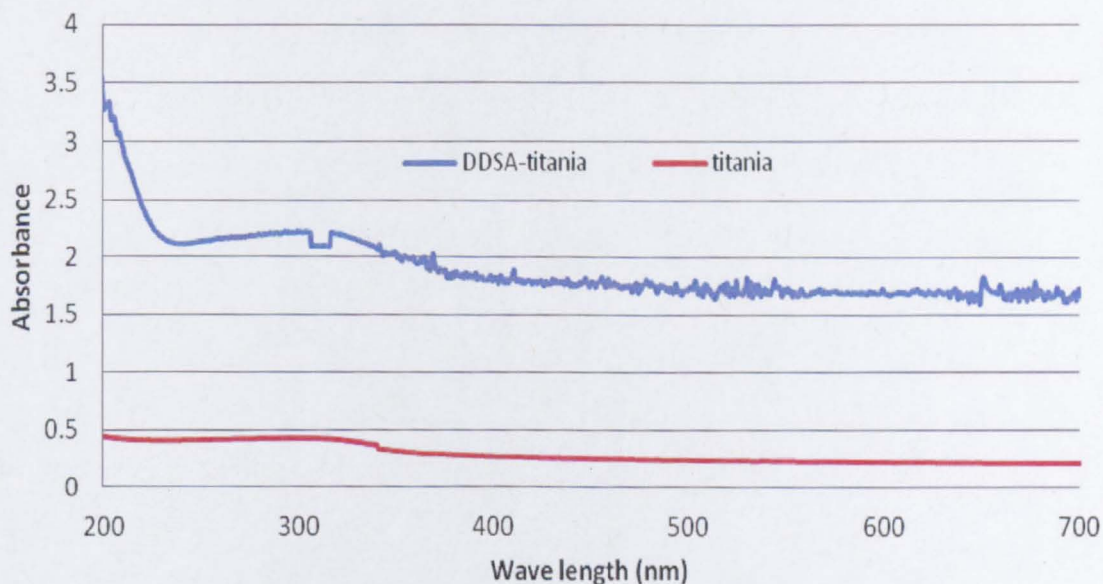


Fig. 5.14: UV-Vis spectrums of DDSA-titania to that of uncoated titania

The UV-Vis absorption of DDSA-titania colloid was attributed to the organic dispersant double bonds that are present in the main chains. Carbon-carbon double bonds are known to be sites of UV radiation absorption; as

the weakly bonded π electrons can be easily excited to higher energy levels by UV photons (Sommer, 1989, Rubinson and Rubinson, 2000).

5.2.2 The DDSA surfactant loading level

The DDSA loading level of DDSA-titania dry powder was evaluated by TGA analysis as described in Section 3.3.9. The surfactant loading level was calculated by using equation 5.1.

$$\text{Surfactant loading level \%} = (W_1 - W_2) - (W_1' - W_2') \quad (5.1)$$

Where: W_1 and W_2 is the wt % of the coated nanoparticles at 100 °C and 800 °C respectively. W_1' and W_2' is the wt % of the uncoated nanoparticles at 100 °C and 800 °C respectively. The reason for using the 100 °C weight because at this temperature the sample can be regarded as being dry and so any included water will not affect the results. The DDSA loading level was determined to be 3.5 wt % from this TGA analysis and using Equation 5.1, a representative TGA profile has been included as Figure 5.15.

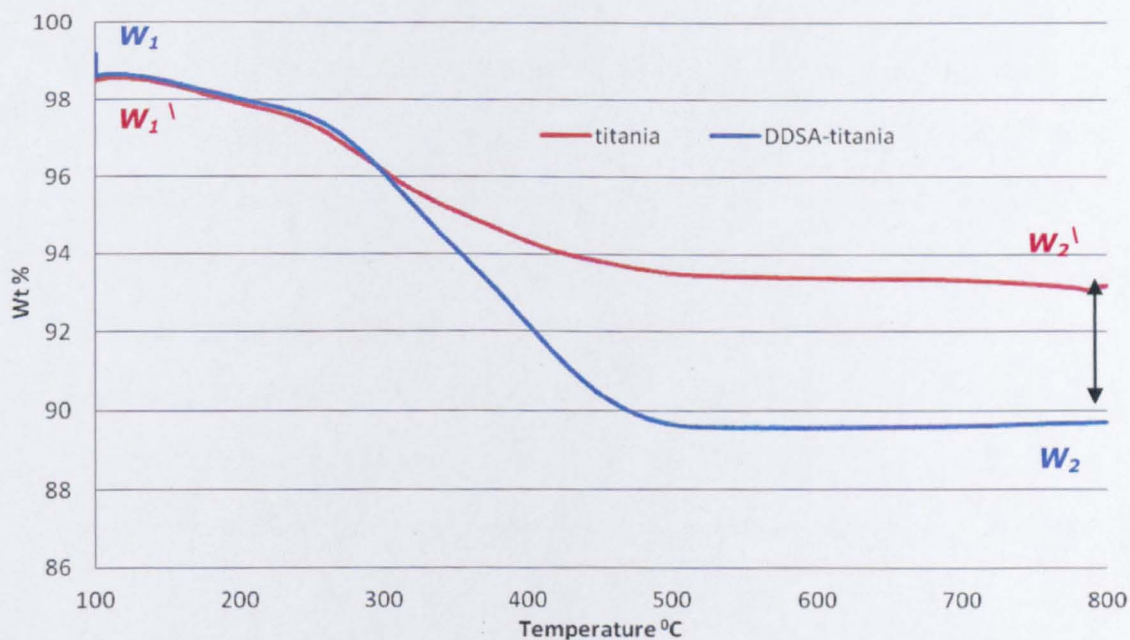


Fig. 5.15: TGA profiles of DDSA-titania and uncoated titania

5.3 Optimization of titania post-synthesis modification approach

The CHS operating parameters were investigated in an attempt to determine if the experimental work conducted so far had achieved a uniform titania surface modification and to optimise the dispersant (DDSA) loading levels to maximise the nanoparticle dispersion into/throughout the polymeric matrix. For these experiments, the following conditions for the nanoparticle synthesis were kept constant, i.e. the ScW conditions used were 240 bars and 400 °C (20 ml/min), using a metal salt precursor which was 0.05 M TIBALD in water (10 ml/min). However, the capping point parameters such as temperature, capping agent feed rate, and capping solvent were manipulated in an attempt to optimize the post-synthesis surface modification approach.

5.3.1 The impact of capping temperature on surfactant decomposition

The capping point temperature was found to be a critical factor in achieving successful DDSA ring opening and binding to titania surface whilst preventing any DDSA decomposition. The impact of the capping point temperature on nanoparticle surface modification was investigated by monitoring the capping temperature over the range 180-300 °C. It was observed that a red colour started to emerge into the collected sample as the capping temperature reached 270 °C (see Figure 5.16). This red colour was attributed to DDSA decomposition.

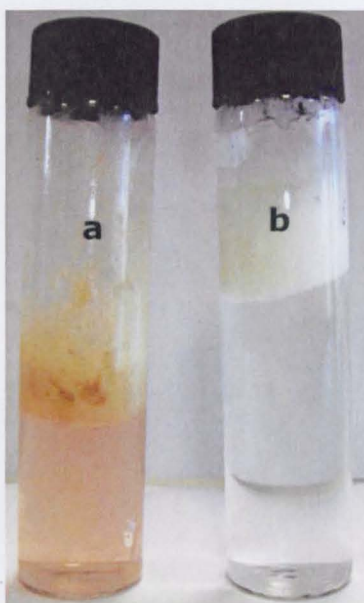


Fig 5.16: DDSA decomposition at capping temperature higher than 270 °C (a), and colloidal DDSA-titania at capping temperature 200 °C (b)

Thus, the recommended capping point temperature range was defined to be 180–240 °C to ensure that DDSA ring opening had occurred and binding to titania nanoparticles achieved with no DDSA decomposition.

5.3.2 The impact of DDSA feed rate on surface coating efficiency

The molar feed ratio of DDSA to titania nanoparticles at the capping point will affect the number of surfactant molecules available for titania surface modification. Therefore it is clear that this factor may also affect the coating efficiency and the achieved surfactant loading level. Consequently, different DDSA concentrations in toluene (0.001, 0.002, 0.005, 0.01, 0.02, and 0.05 M) were introduced at the capping point at a flow rate of 5 ml/min, and the samples collected from these treatment regimes were given numbers 1-6 respectively.

The prepared DDSA-titania colloids were then left to be separated into two layers. It was found that, when the DDSA concentration was higher than 0.01 M, the the organic layer started to exhibit a yellow colour and uncoated titania nanoparticles started to settle into the aqueous layer. Figure 5.17 shows the colloidal organic layers for DDSA concentrations of 0.005 and 0.05 M in toluene as a capping agent.

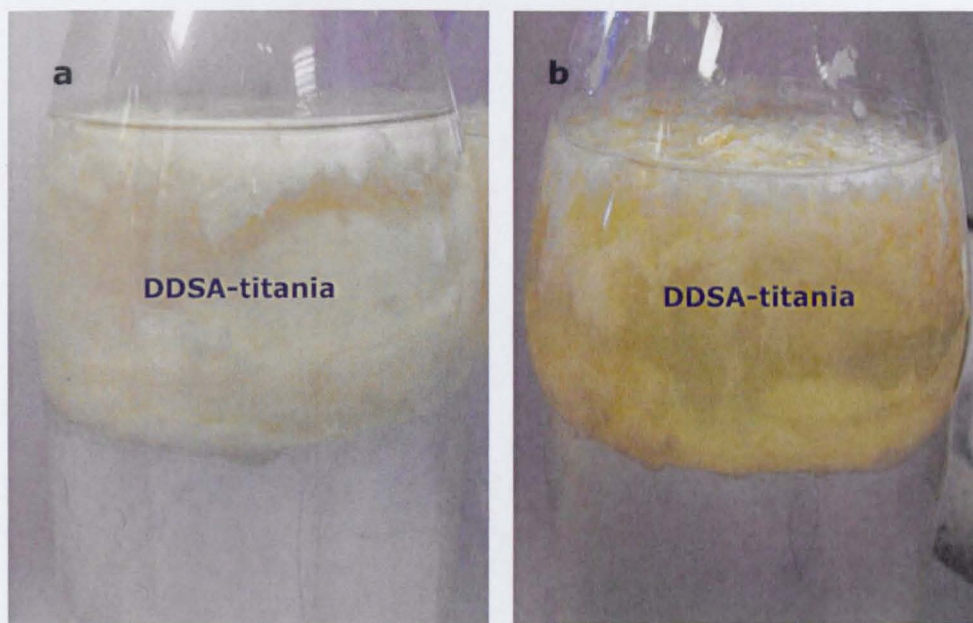


Fig. 5.17: The colloidal organic layers for DDSA in toluene (5 ml/min) at: (a) 0.005 M, and (b) 0.05 M

The development of the yellow colour of the organic layer in Figure 5.17 (b) was ascribed to the presence of excess non-reacted DDSA and the tendency of the hydrophobic segments in this free dispersant to minimize contact with the dispersing medium by forming oily microdomains (micelles) within the solvent. The aqueous layer for each employed DDSA concentration was tested by UV-Vis. There was an increase in the aqueous layer UV-Vis absorption with the increase in DDSA feed at the capping point (see Figure 5.18).

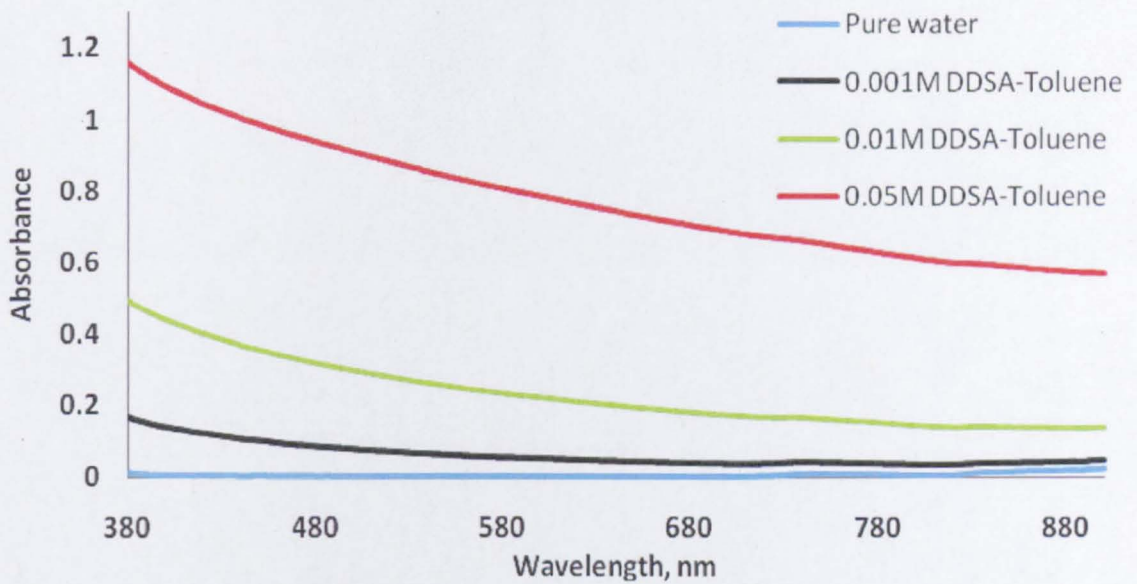


Fig. 5.18: The UV-Vis absorption of aqueous layers from colloid dispersion made using different DDSA concentrations

At low DDSA feed ratio (samples 1-4), it was proposed that the DDSA coating was sufficient in its integrity to overcome the attractive force between the nanoparticles. Therefore, the nanoparticles were sufficiently well surface modified that they were extracted to the organic phase. However, as the DDSA feed increased (samples 5-6) the fact that there was free DDSA present could increase the possibility of particle-particle bridging by the dispersant. Consequently, this interdispersant interaction increased the tendency for the system to exhibit flocculation and to reduce the coating efficiency. Therefore uncoated nanoparticles started to settle down in the aqueous layers which in turn increased the UV-Vis absorption of these aqueous layers.

Subsequently, the organic layers of samples 1-6 were separated using a separating funnel and 50 ml of each organic layer was then centrifuged to remove the excess toluene and water. Toluene was separated at the top, water at the bottom, and DDSA-titania at the interface between the two

layers. It was observed that the thickness of DDSA-titania layer decreased with the increase of DDSA feed at the capping point (Figure 5.19).

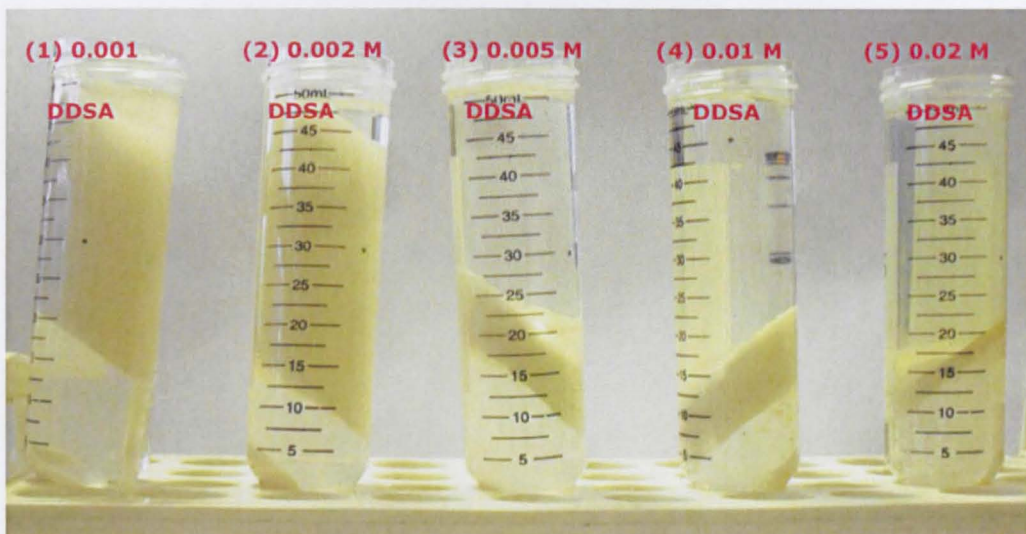


Fig. 5.19: The decrease of DDSA-titania centrifuged layer with the increase of DDSA feed at the capping point

The decrease in DDSA-titania layer thickness with the increase of DDSA feed is again an indication of increased DDSA-titania particle that cluster together. Finally, the separated water and toluene layers were removed from the centrifuged samples; afterwards the samples were freeze dried.

Samples number 1 and 2 showed aggregated particles with a yellow colour. This can be ascribed to the excess non-bonded DDSA that remained within the nanoparticles as the nanoparticles were not able to separate from the excess toluene and non-bonded DDSA (see Figure 5.19). The DDSA loading level for samples 1-2 was evaluated by TGA; it was not possible to attain representative results due to the non-bonded dispersant. Samples 5-6 exhibited a big clump of aggregated particles as a result of the minimized coating efficiency (particle-particle bridging) and again the evaluation of DDSA loading level by TGA did not demonstrate representative results.

Samples 3 and 4 showed white dry particles with minimum aggregation as the samples were able to separate from the excess toluene and the non-bonded DDSA. DDSA loading level of samples 3 and 4 was evaluated by TGA. Samples 3 and 4 showed identical DDSA loading level of 3.5 wt % within ± 0.2 wt % difference.

It was not possible to achieve different surfactant loading levels by manipulating the surfactant feed rate, but rather an effective surface modification approach had been developed. Using this approach the titania nanoparticles were uniformly surface modified, extracted to the organic layer, and separated from excess (non-reacted) DDSA and toluene. It was concluded that the optimum molar feed ratio of DDSA:titania at the capping point was 1:20 which was achieved by injecting 0.005 M DDSA in toluene at 5 ml/min.

5.3.3 The impact of capping solvent on surfactant loading level

The impact of capping solvent on titania surface modification was evaluated by using ethanol. As ethanol is miscible with water, the DDSA coated titania particles could be separated from the water layer and freeze dried with minimum use of organic solvents. This is desirable because organic solvents can badly affect the freeze dryer pumping units and reduce the sustainability of the nanoparticle manufacturing/coating process. 0.005 M DDSA in ethanol was employed as a capping agent at the same hydrothermal conditions for titania particle synthesis. In these experimental work, the DDSA-titania was collected from the water layer, centrifuged, and freeze dried. The particle size of the dried powder was investigated by SEM. DDSA-titania nanoparticles with an average individual

particle size of 52 nm were observed. However, the nanoparticles were found to be aggregated into larger particles, typically of 1 μm in size. Figure 5.20 shows the impact of capping solvent on DDSA-titania morphology by comparing samples made using toluene and an ethanol.

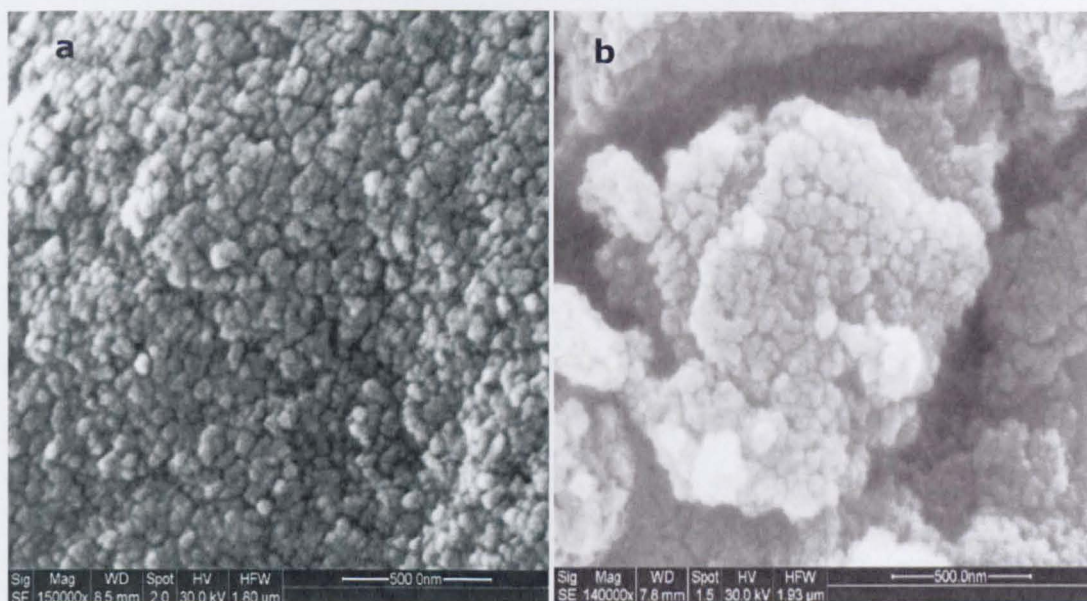


Fig. 5.20: SEM images of DDSA-titania samples produced by using (a) toluene and (b) ethanol as a capping solvent

The aggregation of DDSA-titania produced by using ethanol as a capping solvent was attributed to the lyophobic nature of DDSA-titania colloid in water. In such a system there is no affinity between the colloidal nanoparticles and the dispersing medium (i.e. water). The hydrophobic surfactant segments are therefore repelled by the water present and so they will self-associate to minimise their exposure to the water. This agglomeration can dramatically affect the quality of any nanoparticle dispersion into a polymeric matrix. The surfactant loading level of the ethanol produced DDSA-titania was determined by TGA and a DDSA loading level of 2 wt % observed from the TGA profile (Figure 5.21) and Equation 5.1.

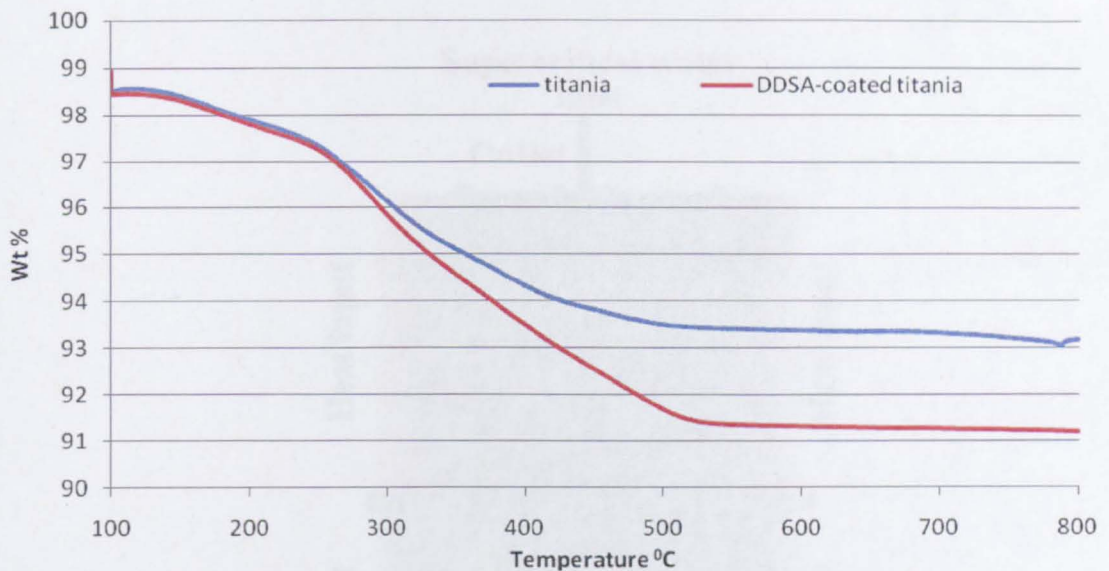


Fig. 5.21: TGA profile of DDSA-titania produced by using ethanol as a capping solvent compared to uncoated titania

This lower DDSA loading level pointed to the decrease in coating efficiency and the conclusion that ethanol appears not be a good solvent for the hydrophobic DDSA as toluene. Comparison of the TGA profiles of uncoated and DDSA coated titania showed that the DDSA started to decompose at 280 °C as the DDSA-titania started to exhibit a greater weight loss with temperature when compared to the uncoated titania. This result confirmed the finding about the impact of capping point temperature on DDSA decomposition described in Section 5.3.1.

5.4 Synthesis of DDSA-titania via surface modification in the reactor

The ability to achieve efficient nanoparticle surface modification via surface modification in the reactor was also investigated. In this approach, nanoparticle surface modification was performed exclusively during their formation in the reactor. The chosen surfactant was introduced into the reactor (Figure 5.22) along with the metal salt precursor.

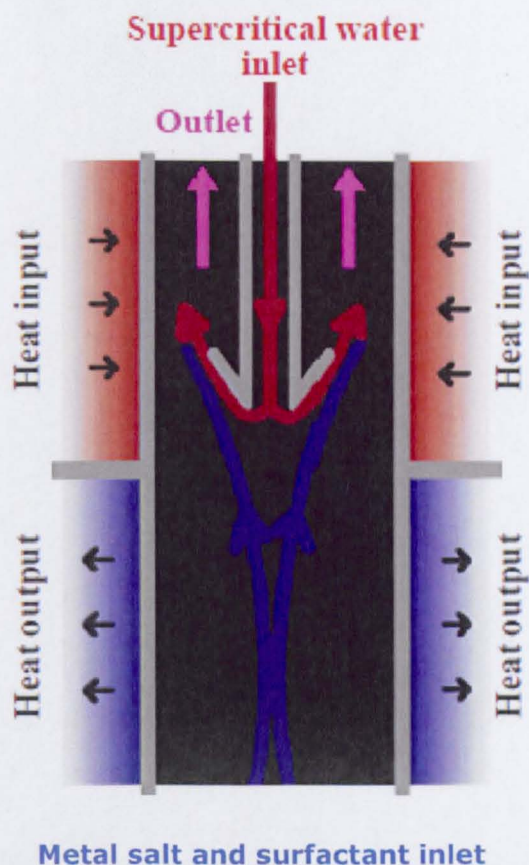


Fig. 5.22: Schematic for nanoparticle surface modification directly within the CHS reactor

5.4.1 Surface modification in the reactor for organic metal salt precursor

The chosen precursor for this investigation was a solution of 0.05 M titanium (IV) isopropoxide (TIPO) (Aldrich, 97%) with 0.0025 M DDSA in isopropyl alcohol (IPA) (10 ml/min) and the ScW conditions adopted were 400 °C and 240 bars (20 ml/min). Toluene was introduced at the capping point (5 ml/min) to extract the coated-titania to the organic phase and as a result the DDSA-titania was found to be uniformly extracted to the organic layer (see Figure 5.23).



Fig. 5.23: Extraction of DDSA-titania to the organic layer when coating was conducted directly in the reactor using the TIPO precursor

The size of DDSA-titania was investigated via TEM and titania nanoparticles of 6 nm average particle size, with a uniform DDSA coating layer of 1 nm thickness, were reported from TEM image (Figure 5.24).

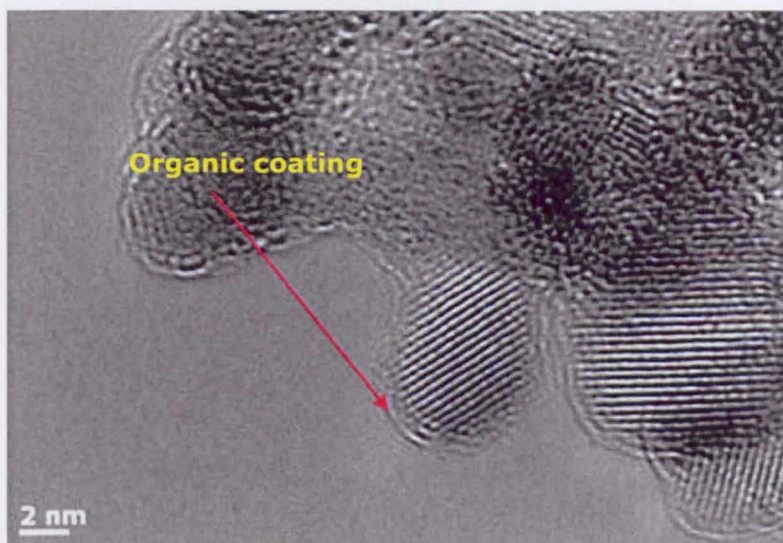


Fig. 5.24: TEM image of DDSA-titania synthesized using TIPO modification in the reactor

The toluene layer from the separation process was separated, centrifuged, and freeze dried. The chemical structure of the dried powder was subjected to FTIR analysis to verify the attachment of DDSA to titania

surface. Figure 5.25 shows the FTIR spectrum of DDSA-titania to uncoated titania and ascribes the peaks observed to key functional groups (Skog and Holler, 1999).

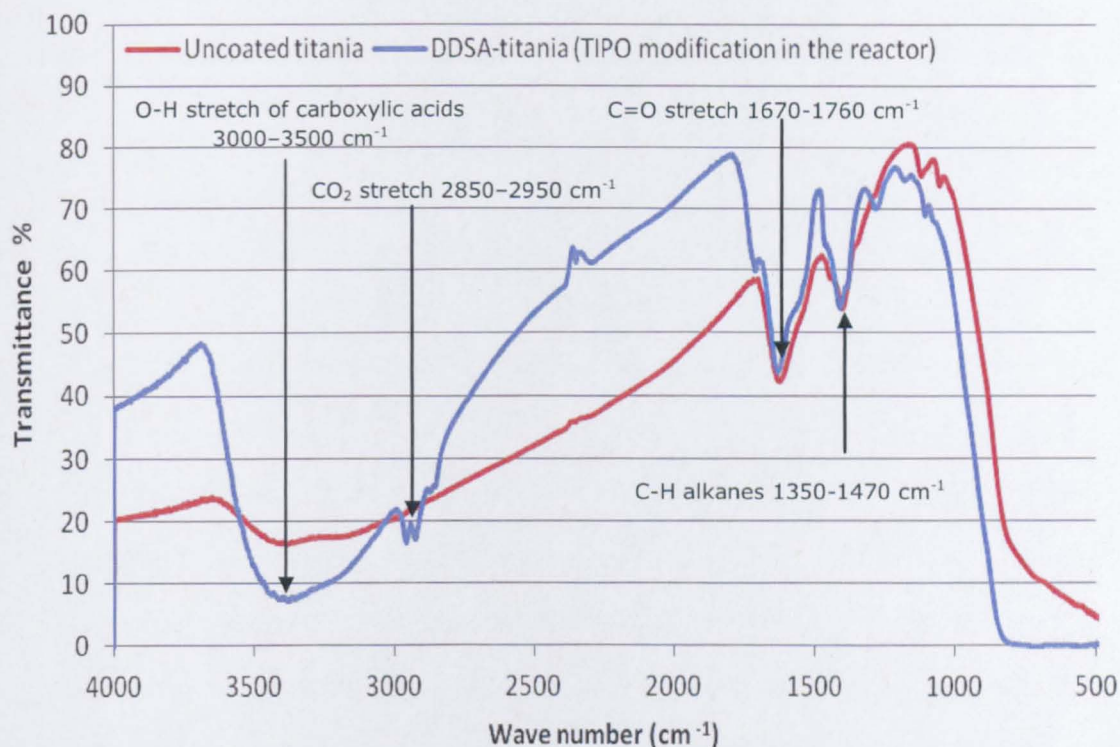


Fig. 5.25: FTIR spectrum of DDSA-titania produced by TIPO modification directly within the reactor

The additional IR absorption peaks in the DDSA-titania compared to the uncoated titania were correlated to the carboxylic group stretch (O-H and C=O stretch) of the attached DDSA, and to the hydrogen bonding to the nanoparticle surface. The DDSA loading level was evaluated and found to be 7.7 wt % from a combination of the TGA profile (Figure 5.26) and Equation 5.1.

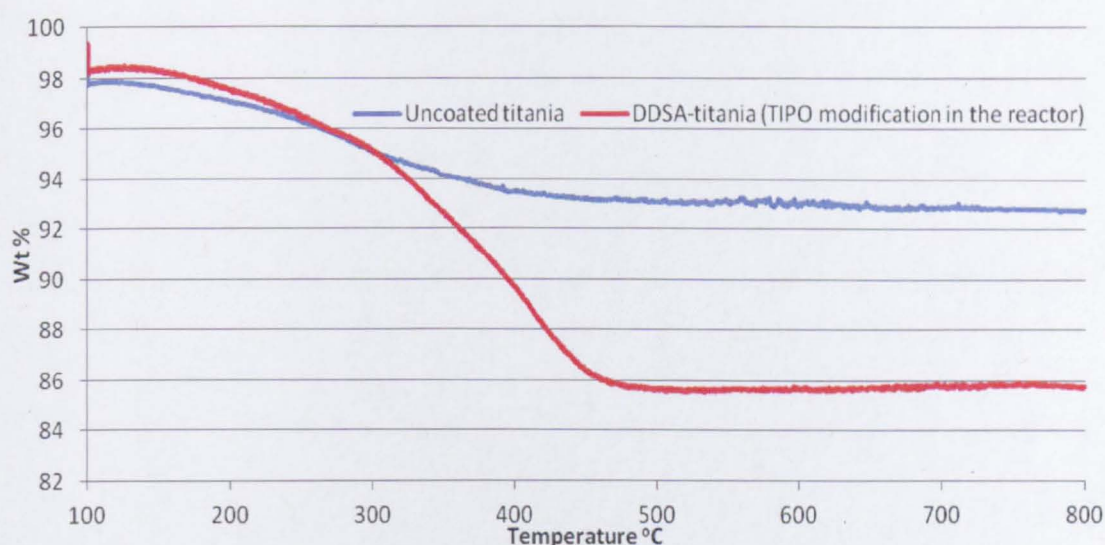


Fig. 5.26: TGA profile of DDSA-titania produced by TIPO modification in the reactor compared to uncoated titania

This DDSA loading level was 2.2 times the loading level that had been achieved via surface modification at the capping point. This higher surfactant loading level was attributed to the fact that an enhanced efficiency of surface modification had been achieved within the reactor compared when surface modification was conducted at the capping point using the same hydrothermal conditions adopted in the reactor. The solvent chosen was IPA, and it was also concluded that this may be a more appropriate solvent for TIPO and DDSA than either ethanol or toluene.

5.4.2 Surface modification in the reactor for aqueous metal salt precursor

The metal salt feed was 0.05 M TIBALD with 0.0025 M DDSA in a solvent mixture (water 80 V % and IPA 20 V %) (10 ml/min). IPA was required to increase the solubility of DDSA which was immiscible with pure water. The adopted ScW conditions were 240 bars and 400 °C (20 ml/min). Again, toluene was pumped at the capping point (5 ml/min) to extract the coated titania. DDSA-titania was extracted to the organic layer. Titania

nanoparticles of 6 nm average particle size were reported from TEM image (Figure 5.27).



Fig. 5.27: TEM image of DDSA-titania produced via TIBALD modification directly within the reactor using water:IPA mixed solvent system

The DDSA loading level of DDSA-titania dry powder was evaluated by TGA and found to be 2.9 wt % by evaluating of the TGA profile and Equation 5.1. The surfactant loading level was lower by 2.7 times compared with surface modification in the reactor of using IPA and TIPO.

Therefore, it was concluded that the solvent mixture (water 80 V % and IPA 20 V %) used was not as efficient at completely dissolving the precursors DDSA and TIBALD as the IPA was at dissolving DDSA and TIPO. Thus it was concluded that the achievement of good surface modification directly in the reactor depends on the following parameters:

- The ability of the surfactant to survive the reactor aggressive conditions i.e. high temperature.
- No side reactions should take place between the metal precursor and the surfactant. This can lead to discolouration of the product.

- The high affinity of the metal salt and the surfactant to be dissolved in the solvent used.
- The molar ratio of the metal salt and the surfactant agent.

5.5 Titania surface modification with tributyl phosphate

Surface modification can potentially be optimised for the purposes of achieving flame retardancy (FR) by including known FR active elements, such as phosphorous (P), into the surfactant molecule (Xie et al., 2002). Phosphorous can be considered as a particularly efficient FR element where the efficiency of phosphorous-based FRs can be directly linked to how much phosphorous they contain (Green, 1996, Pinfa, 2010). Phosphonate ligands can bind strongly to titania nanoparticles creating Ti-O-P bond which is strongly resistant toward hydrolysis (Forget et al., 2003). Figure 5.28 shows the chemical structure of commonly used phosphonate ligands.

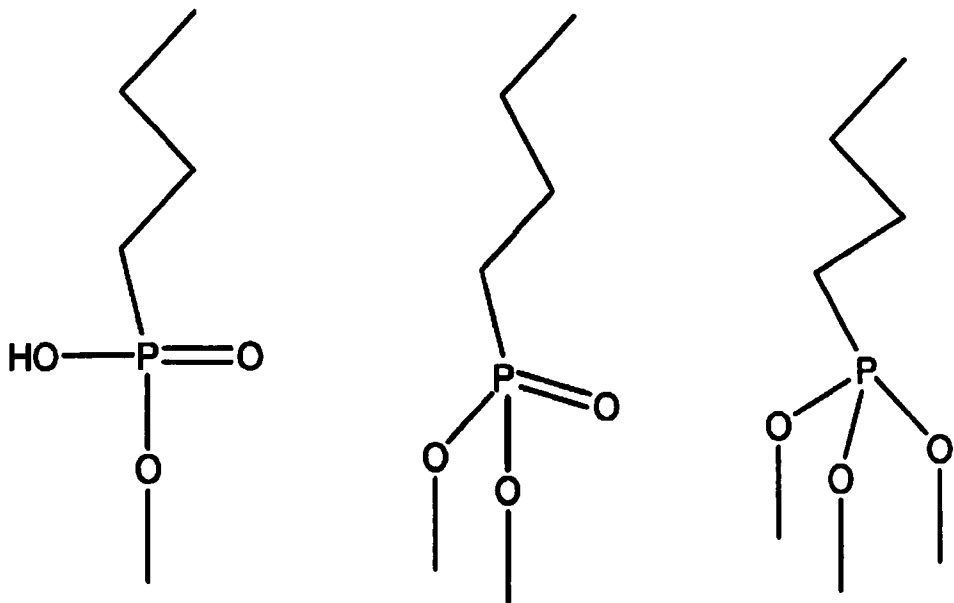


Fig. 5.28: Mono-, bi-, and tridentate anchorage of phosphonate ligands, adapted from (Neouze and Schubert, 2008)

Consequently, the feasibility of optimising the titania nanoparticles for FR applications via achieving surface modification with phosphorous compounds was investigated by using tributyl phosphate (TBP) (Aldrich, 99 %) as a surfactant agent. TBP was chosen because it has been reported to form stable hydrophobic complexes with some metals (Antczak, 2008). Additionally, TBP has a phosphorous content higher than most commonly used phosphorous-based FR additives such as Tri phenyl phosphate (TPP) and Bisphenol A Bis(Diphenyl phosphate) (BDP) (Ebdon et al., 2001, Pinfa, 2010). Figure 5.29 shows the molecular structure of TBP.

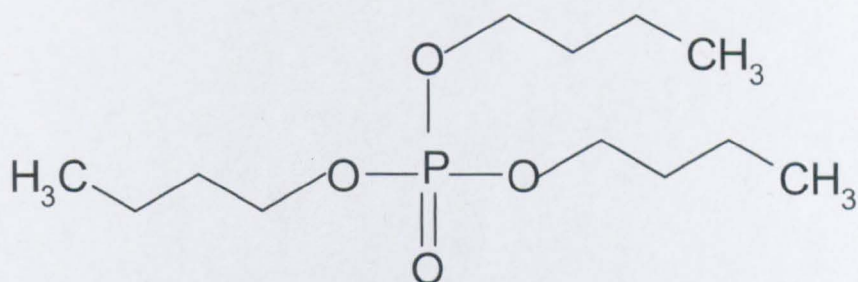


Fig. 5.29: The molecular structure of TBP

Titania surface modification with TBP was performed via post-synthesis surface modification approach. 0.01 M TBP in cyclohexane was employed as a capping agent (5 ml/min) at the same hydrothermal conditions that were used for titania synthesis. Again the TBP-titania nanoparticles were extracted to the top of the aqueous layer (Figure 5.30).



Fig. 5.30: Extraction of TBP-titania using post-modification process

It was proposed that the TBP may bind to the titania surface via the P=O group. However, it was also thought that the aliphatic segments would not be long enough to completely extract TBP-titania to the organic layer. Therefore, the TBP-titania was separated from the aqueous layer and freeze dried. The particle size of the dried powder was analysed by SEM and TBP-titania nanoparticles of 46 nm average particle size were reported (see Figure 5.31).

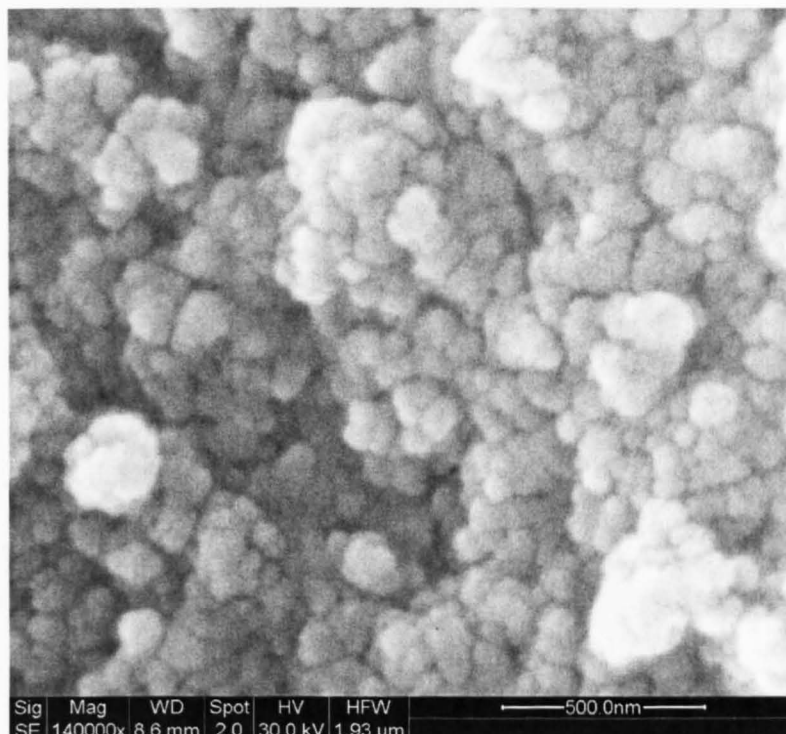


Fig. 5.31: SEM image of TBP-titania

TBP-titania nanoparticles were found to be agglomerated to large features. This agglomeration was attributed to the lyophobic nature of the colloid system which resulted in there being little or no affinity between the colloidal nanoparticles and the dispersing medium (water). (Miller et al., 1983). The chemical structure of the dried powder was investigated with FTIR to verify the attachment of TBP to the titania surface. Figure 5.32 shows the FTIR spectrum of TBP-titania compared to uncoated titania and

ascribes the peaks observed to key functional groups (Skog and Holler, 1999).

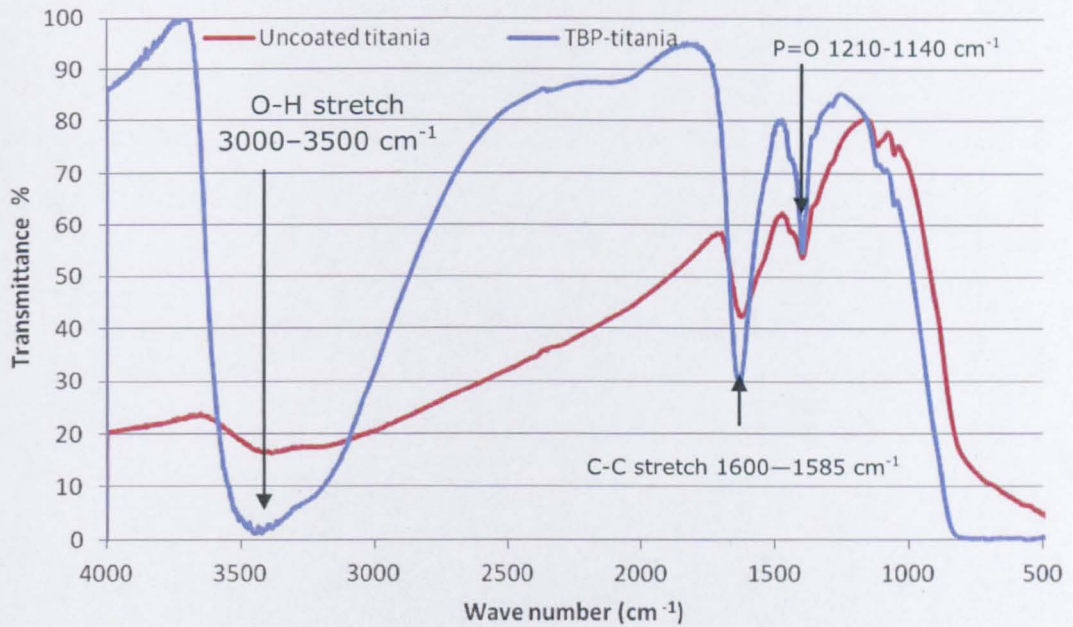


Fig. 5.32: FTIR spectrum of TBP-titania to that of uncoated titania

The enhanced IR absorption of TBP-titania compared to that of uncoated titania was attributed to the surfactant attached to titania surface via hydrogen bonding and to the C-C stretch of the surfactant aliphatic chains. The TBP-titania dry powder chemical structure was investigated using EDX to verify the elemental composition. This was found to be $\text{Ti}_{26.75} \text{P}_{1.15} \text{O}_{62.44} \text{C}_{9.66}$. The summary formula of TBP-titania can be normalized as $\text{Ti} \text{O}_{2.33} \text{P}_{0.04} \text{C}_{0.36}$. The excess oxygen, phosphorous, and carbon can be ascribed to the attached TBP surfactant. Again, the TBP loading level was evaluated by TGA (Figure 5.33). TBP-titania showed 1.2 wt % retained mass compared to uncoated titania at 800 °C; this can be ascribed to a chemical reaction between titania nanoparticles and TBP at high temperature, as detailed below.

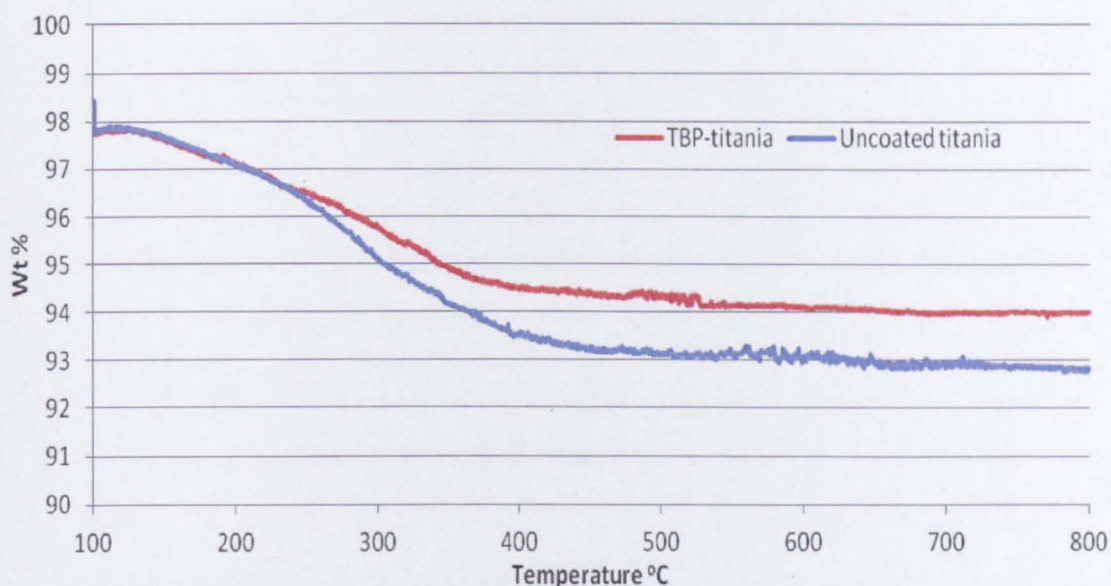
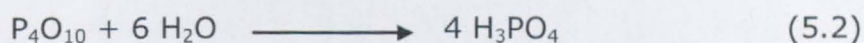


Fig. 5.33: TGA profile of TBP-titania to that of uncoated titania

It was proposed that phosphorus pentoxide P_4O_{10} was formed as a result of heating in the flowing air; P_4O_{10} is a potent dehydrating agent as indicated by equation 5.2 (Corbridge, 1995, Meier, 2004).



The phosphoric acid which results from the reaction with water can be cross linked by titania nanoparticles as described by Scharaf (see Figure 10.3) (Scharf and Nalepa, 1992). Therefore, it can be concluded that TBP can give bulk titania nanoparticles a potential to exhibit improved FR performance by anchoring onto the nanoparticle surface. However, it may not produce good quality nanoparticle dispersion when the particles are introduced into a polymeric matrix due to compatibilising problems.

5.6 Summary of titania surface modification with organic ligands

This Chapter investigated titania surface modification with different organic ligands and the optimization of the CHS parameters in order to achieve a uniform nanoparticle surface modification. Nanoparticles were surface modified via either post-synthesis surface modification at the capping point or exclusive surface modification directly within the reactor. It was not possible to achieve different surfactant loading level via post-synthesis surface modification. Rather an effective surface modification approach was developed. Using this method, the nanoparticles were uniformly surface modified, extracted to the organic layer, and separated from excess (non-reacted) DDSA and toluene.

Nanoparticle surface modification in the reactor (i.e. surfactant agent included with the metal salt prior the reactor) was found to be more efficient than surface modification at the capping point, as higher surfactant loading level was achieved using the same adopted hydrothermal conditions. Surface modification for the purpose of flame retardancy by using phosphorous compound (TBP) was also achieved. However, organic ligands can not secure a durable organic coating due to the hydrolysis reactions at the nanoparticle surface. Polymeric surfactants which have several anchoring groups along the polymer chains can have the potential of forming durable organic coating as will be described in Chapter 6.

CHAPTER 6

6. STERIC AND ELECTROSTATIC STABILIZATION OF COLLOIDAL TITANIA NANOPARTICLES

A stable nano-colloidal suspension is essential to prevent aggregation, and to produce mono-dispersed particles for different applications. This work reported in this Chapter investigated two methods of achieving this: (a) steric stabilization of colloidal titania nanoparticles via surface modification with organic polymeric dispersants of different polarities and (b) electrostatic stabilization of colloidal titania nanoparticles via creating a repulsive electrostatic potential associated with each particle. The tunable hydrothermal conditions (i.e. temperature, pressure, residence time, surfactant addition and flow rate) were also investigated to ascertain whether this processing technique could enable controlled steric and electrostatic stabilization of colloidal nanoparticle in a continuous fashion (i.e. online steric and electrostatic stabilization).

6.1 Steric stabilization via surface modification with polymeric surfactants

Polymeric dispersants differ from low molecular weight species because of their long backbone chains. Additionally, they are able to bind to numerous surface sites at the same time, forming a durable adsorption surfactant layer (Pettersson et al., 2000, Vernardakis et al., 2001, Zhu et al., 2006). Anchoring groups that can be used to anchor polymeric chains to oxide surface are amine (Farrokhpay et al., 2004), ammonium (Morris et al., 1999), carboxylic (Das and Somasundaran, 2001, Liufu et al., 2005),

6. Steric and electrostatic stabilization of colloidal titania nanoparticles

sulphonic and phosphoric acid functional groups (Neouze and Schubert, 2008).

The molecular weight of the polymeric dispersant should be sufficient to provide the optimum chain length to produce a molecular barrier of sufficient thickness that it can overcome van der Waals forces of attraction between particles (Kim and McKean, 1998, Buchholz and Wilks, 2001). The molecular weights that are too high can cause dispersion instability, as there will be an increased tendency for the long chains to fold back onto themselves causing flocculation (Boisvert et al., 2001, Buchholz and Wilks, 2001). Polymers with molecular weight above 10^6 gm mol⁻¹ are generally used as flocculants (Buchholz and Wilks, 2001), whilst the preferred molecular weight for polymeric dispersants was reported to be less than 20,000 g mol⁻¹ (Farrokhpay, 2009).

The conformation of the adsorbed polymer is a major controlling factor in determining the steric barrier stability (Fleer et al., 1993). The adsorbed polymer has three possible segments: (a) segments at the solid-liquid interface, called trains; (b) segments bound at both ends, called loops; (c) segments bound at one end, called tails (Farrokhpay, 2004). Non-interacting groups are responsible for the occurrence of tails and loops (Fleer et al., 1993). Variation in train, loop, and tail length controls the adsorbed layer thickness (Farrokhpay, 2009). Figure 6.1 is a schematic drawing of polymer conformation at the solid-liquid interface.

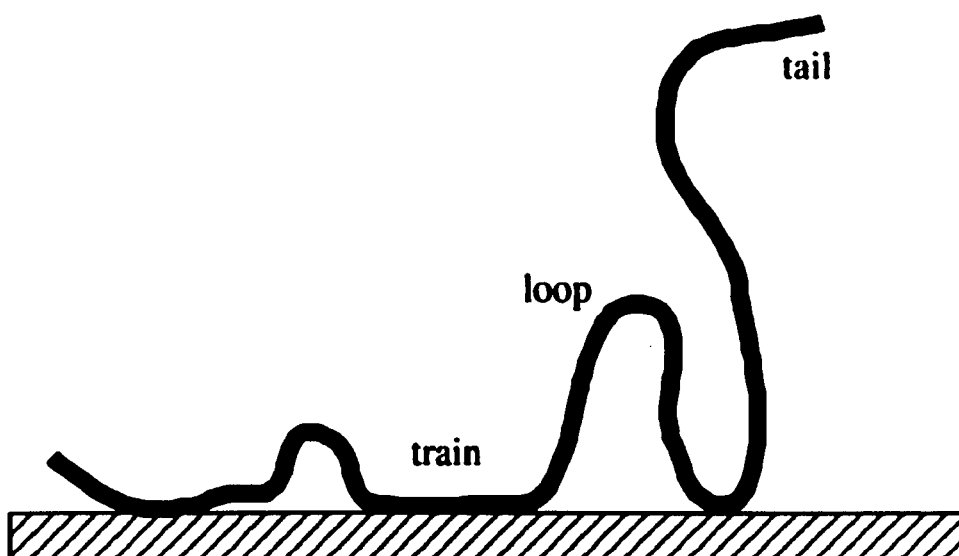


Fig. 6.1: Schematic diagram of adsorbed polymer molecule at the solid-liquid interface, adapted from (Yu and Somasundaran, 1996)

6.1.1 Titania surface modification with poly acrylic acid

Titania nanoparticles are used in a number of different applications ranging from ultraviolet light absorber, photocatalyst, ceramic industries, and painting pigments (Farrokhpay, 2009). In particular, there has been a rapid increase in the use of water-based pigments due to the introduction of more rigorous regulations which restricting the use of organic solvents in paints and coatings (Clerici et al., 2009). The use of poly(acrylic acid) (PAA) to disperse titania in water has been documented which is aimed to improve the discrepancy of titania pigment in water to meet these new regulatory requirements (Strauss et al., 1993, Clerici et al., 2009). Therefore, in this study, titania surface modification with PAA via CHS was investigated using PAA (Aldrich) with an average molecular weight (M_w) of 1800 g mol^{-1} as a dispersant agent. Figure 6.2 shows the chemical structure of PAA.

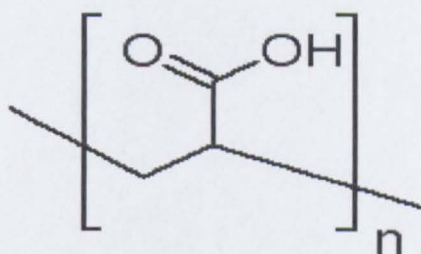


Fig. 6.2: Chemical structure of poly acrylic acid

The metal salt precursor used was 0.05 M TIBALD dissolved in water (10 ml/min). ScW conditions were 240 bars and 400 °C (20 ml/min) and PAA dissolved in water was injected at the capping point (5 ml/min); therefore titania was surface modified via post-synthesis surface modification approach. The minimum PAA feed required to stabilize colloidal titania in water was investigated by injecting different PAA concentrations at the capping point. It was demonstrated that this sample of titania was effectively stabilized in water by using a capping agent of 0.0005 M of this PAA. Figure 6.3 shows the stabilized PAA-titania colloid in water.

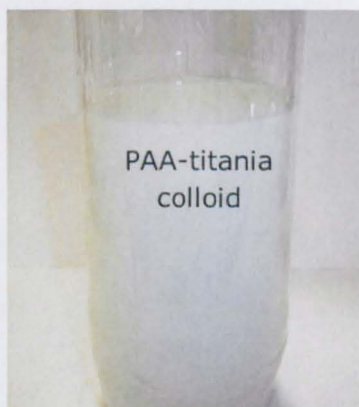


Fig. 6.3: Sterically stabilized PAA-titania colloid in water after one month, (Non stabilised TiO₂ would drop to the bottom within minutes of production)

PAA was able to bind effectively to the titania surface through the COOH groups along the polymer chains and to completely disperse the nanoparticles in water as a result. The adsorbed polymer layer could stabilize the nanoparticles through steric stabilization by volume restriction

6. Steric and electrostatic stabilization of colloidal titania nanoparticles

which prevents nanoparticle approaching one another, and through the created osmotic effect where the solvent molecules surrounding the particles are squeezed out upon close approach. The generated osmotic pressure tends to suck the liquid into the space between the particles, thus increasing the energy required for the particles to coagulate (Gebhardt and Fuerstenau, 1983, Davis et al., 1984) (Figure 6.4).

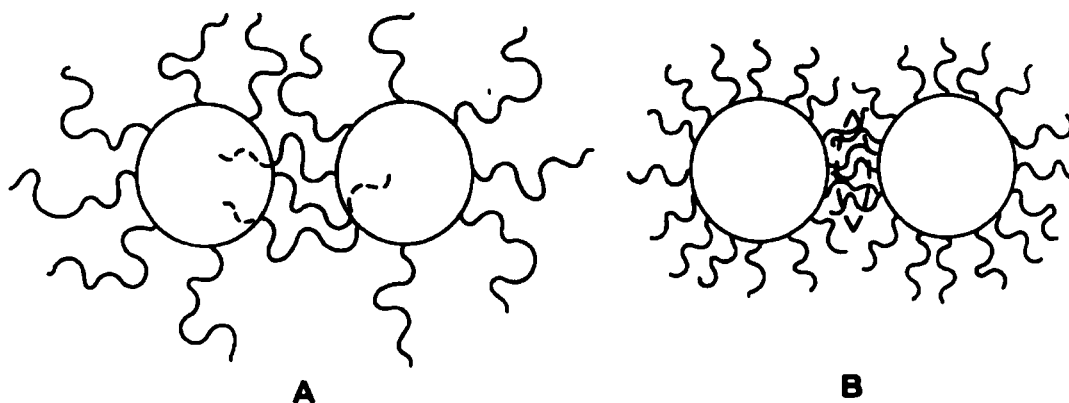


Fig. 6.4: Schematic of steric stabilization through: (A) the volume restriction, and (B) the osmotic effect, adapted from (Scheutjens and Fler, 1982)

Furthermore, the PAA-titania colloid stability was visually inspected over time and no noticeable flocculation was observed over a period of two months. Thus, it was concluded that this PAA steric barrier was sufficiently efficient that it can keep the particles outside the range of van der Waals force of attraction for extended period of time.

6.1.1.1 Characterization of PAA-titania

The size of PAA-titania nanoparticles was visualized by using TEM and PAA-titania nanoparticles of 5.8 nm average particle size were observed (Figure 6.5).

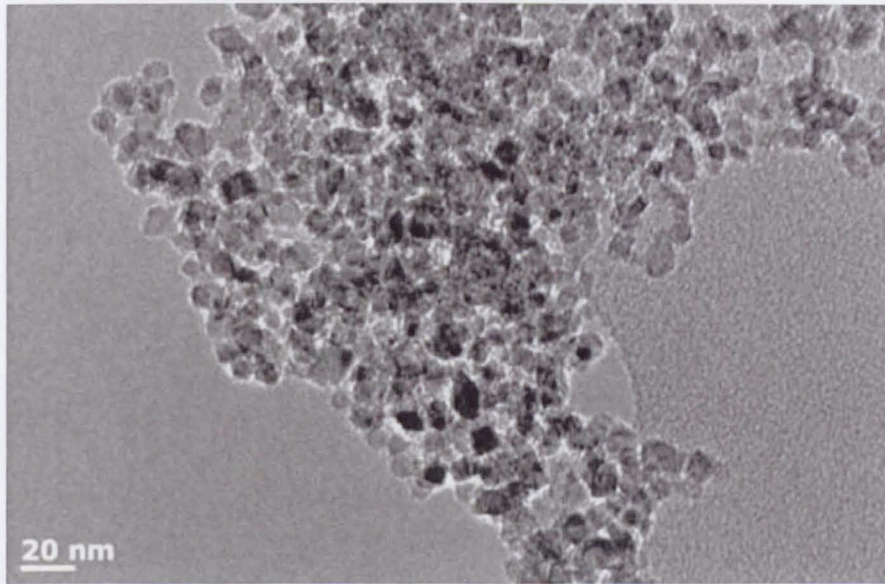


Fig. 6.5: TEM image of PAA-titania

The thickness of the adsorbed PAA layer was investigated through further magnification and it was concluded that a durable amorphous polymeric layer of 2 nm thickness was present around the particles (Figure 6.6).

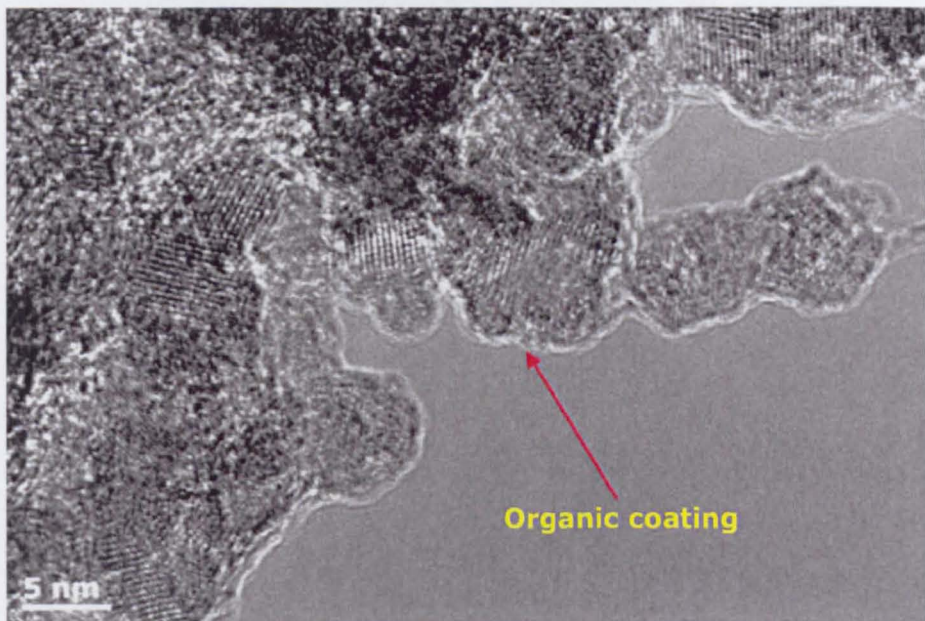


Fig. 6.6: The thickness of the adsorbed PAA layer

6. Steric and electrostatic stabilization of colloidal titania nanoparticles

Therefore, it was also concluded that an overall steric barrier of 4 nm total thickness (i.e. a sum of the coatings on each of two adjacent particles) was sufficient to be able to keep the points of closest approach outside the van der Waals attractive force range. The size of colloidal PAA-titania was also evaluated by dynamic light scattering (DLS). Colloidal nanoparticles of 112 nm particle size were reported from DLS results (Figure 6.7).

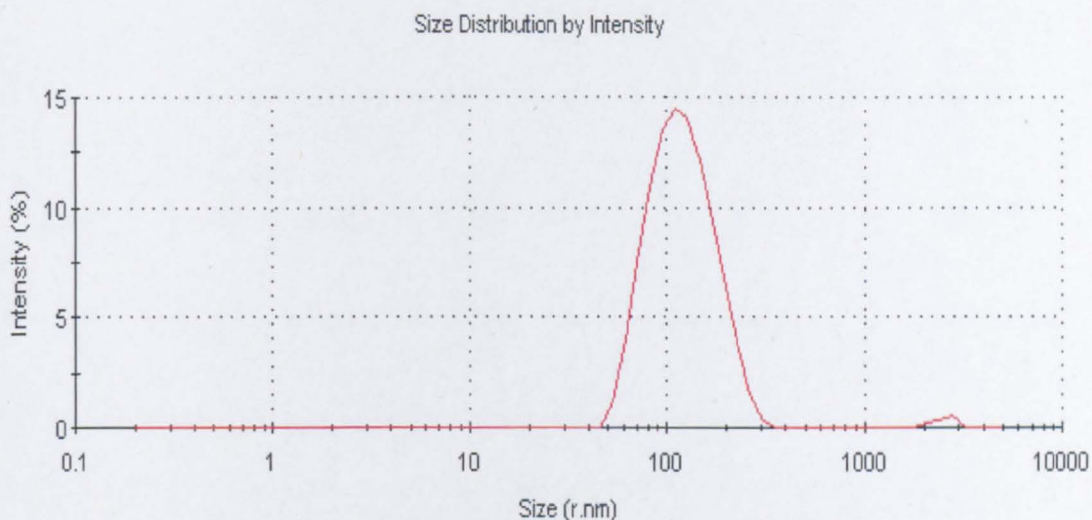


Fig. 6.7: Size of colloidal PAA-titania particles by DLS

Whilst the suspension of TiO_2 particles appeared to be relatively stable, it was clear that the DLS was measuring colloidal aggregates of approximately 100 nm width of titania nanoparticles that become attached to the same polymer chain through the abundant COOH groups along the polymer chain. The chemical structure of PAA-titania produced was investigated with FTIR to verify the attachment of PAA to titania surface. Figure 6.8 shows the FTIR spectrum of PAA-titania compared to uncoated titania and ascribes absorption correlations to certain functional groups present in the spectrum (Skog and Holler, 1999).

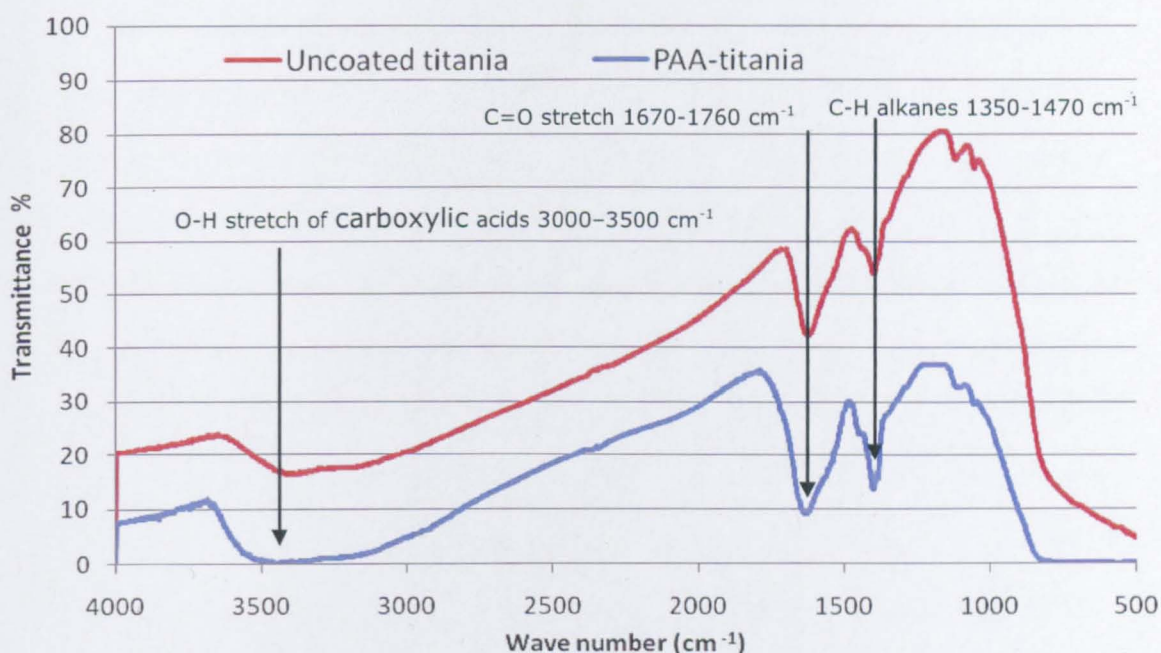


Fig. 6.8: FTIR spectrum of PAA-titania

The enhanced IR absorption of PAA-titania relative to that of uncoated titania was correlated to the carboxylic group stretch (O-H and C=O stretch) of the attached PAA, and to the hydrogen bonding to titania surface. The loading level of PAA was also evaluated by using TGA. PAA loading level of 2.2 wt % was reported from the TGA profile and Equation 5.1.

6.1.1.2 Stability mechanism of PAA-titania colloid

The PAA-titania colloid was found to be a long-term stable colloid; no visible flocculation, resulting in particle settling, took place over two months. As discussed above, the stability mechanism, could be steric, or electrostatic, or combination of both. Consequently the stability mechanism of PAA-titania colloidal system was investigated by measuring its zeta potential. An electrostatically stabilized colloidal system is said to be long term stable if it has a zeta value >30 mV or < -30 mV (Morris et al., 1999).

6. Steric and electrostatic stabilization of colloidal titania nanoparticles

The zeta potential measurement of titania colloid was found to be zero mV. According to zeta value, the colloid should aggregate extensively as there was no enough repulsive force to prevent the particles from coming together to flocculate. Therefore, the PAA-titania colloidal stability of this system was concluded to be mainly due to the steric stabilization and there was no role for electrostatic stabilization. It can be speculated that, due to the large molecular weight of the dispersant used and the the abundance of COOH groups along its polymer chains, in fact this coating could take the form of both/either (a) many titania nanoparticles could be attached to the same polymer chain and/or (b) many chains could be attached to the same nanoparticle. Therefore, in this case the polymer layer conformation at the solid-liquid interface could be mainly in trains with minimum loops; as there were a plenty of COOH anchoring groups along the polymer chains. This type of polymer conformation mechanism could eliminate any possible effects of electrostatic stabilization.

The impact of the colloidal pH on its stability was then investigated. Stabilized PAA-titania colloid (pH 7.4) was found to flocculate extensively at low pH. At low pH, the nanoparticle surface charge could be altered from $M-O^-$ to $M-OH_2^+$ and PAA dissociation constant could be minimized as a result of the increased H^+ ion concentration. Hence, flocculation occurs because adsorption is not favoured when the adsorbate and the substrate have the same charge (Parks, 1965, Gebhardt and Fuerstenau, 1983). The colloidal system also flocculated at high pH as the acidic dispersant might be involved in a neutralization reaction with the basic species ions present in the system.

Titania surface modification with PAA in the reactor was then investigated as this approach might be necessary to produce an effective surface

coating. In this experimental work, an esterification reaction appeared to take place between the metal precursor, specifically hydroxyl groups of TIBALD salt, and the PAA. A white precipitated product appeared in the precursor feed mixture; as PAA was added to TIBALD solution. This is not unexpected because esterification reaction with alcohols is one of the main reactions of PAA (Dippy et al., 1959).

6.1.2 Titania surface modification with poly(ethylene-co-acrylic acid) copolymers

PAA is a polar polymer which is well known to act as an efficient stabilizing agent for materials being dispersed in polar media such as water (Gebhardt and Fuerstenau, 1983). However, it was proposed that the hydrophobic nature of the polar dispersant might be improved if it also contained aliphatic segments in addition to the hydrophilic acidic anchoring groups along the polymer backbone chain. Therefore, the dispersant could still anchor itself to the nanoparticle surface (via the acidic pendant groups) but also undergo phase transfer in order to successfully extract the nanoparticles to the organic phase (due to the aliphatic backbone segments). Therefore, the feasibility for different poly(ethylene-co-acrylic acid) copolymers to act as amphipathic polymeric dispersant to both anchor to the titania surface and effectively extract the nanoparticles to the organic phase was investigated via a post synthesis surface modification approach. Amphipathic materials are species which contain both hydrophilic and hydrophobic segments in the same molecule. Figure 6.9 shows the chemical structure of poly(ethylene-co-acrylic acid) copolymer.

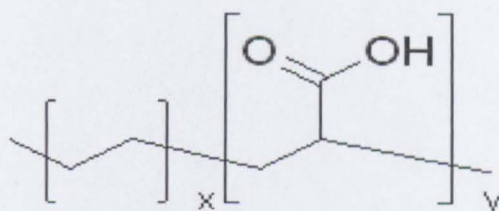


Fig. 6.9: Chemical structure of poly(ethylene-co-acrylic acid) copolymer

6.1.2.1 Titania surface modification with poly(ethylene-co-AA 5 wt %)

Poly(ethylene-co-acrylic acid 5 wt %) (Aldrich) was employed as an amphipathic polymeric dispersant. To do this a solution 0.05 g of poly(ethylene-co-AA 5 wt %) was dissolved in 100 ml toluene; this solution was employed as a capping agent (5 ml/min). The ScW conditions were 240 bar and 400 °C (20 ml/min) and the metal precursor was 0.05 M TIBALD in water (10 ml/min). The adopted poly(ethylene-co-AA 5 wt %) anchored titania nanoparticles and extracted the nanoparticles to the organic phase (Toluene). However, the extracted poly(ethylene-co-AA 5 wt %)-titania nanoparticles did not show uniform extraction to the organic phase as visually recognized from Figure 6.10.

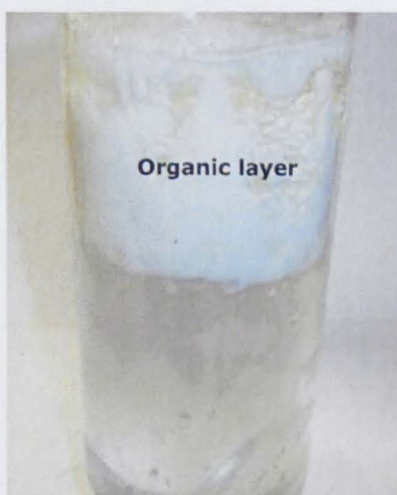


Fig. 6.10: Extraction of poly(ethylene-co-AA 5 wt %)-titania to the organic phase

6. Steric and electrostatic stabilization of colloidal titania nanoparticles

This result was attributed to the low level of acid comonomer present in the dispersant material. Poly(ethylene-co-AA 5 wt %) is a random copolymer with only 5 wt % acrylic acid. Therefore, both/either some copolymer chains might have only aliphatic segments which have no role in surface modification and/or there is not sufficient functional group present to make a strong enough bond to the titania. As a result, the wt % of the polar anchoring groups seems to have an impact on the extraction pattern to the organic layer. The size of the nanoparticles was visualized by TEM and poly(ethylene-co-AA 5 wt%)-titania nanoparticles of 5 nm average particle size were reported (Figure 6.11).

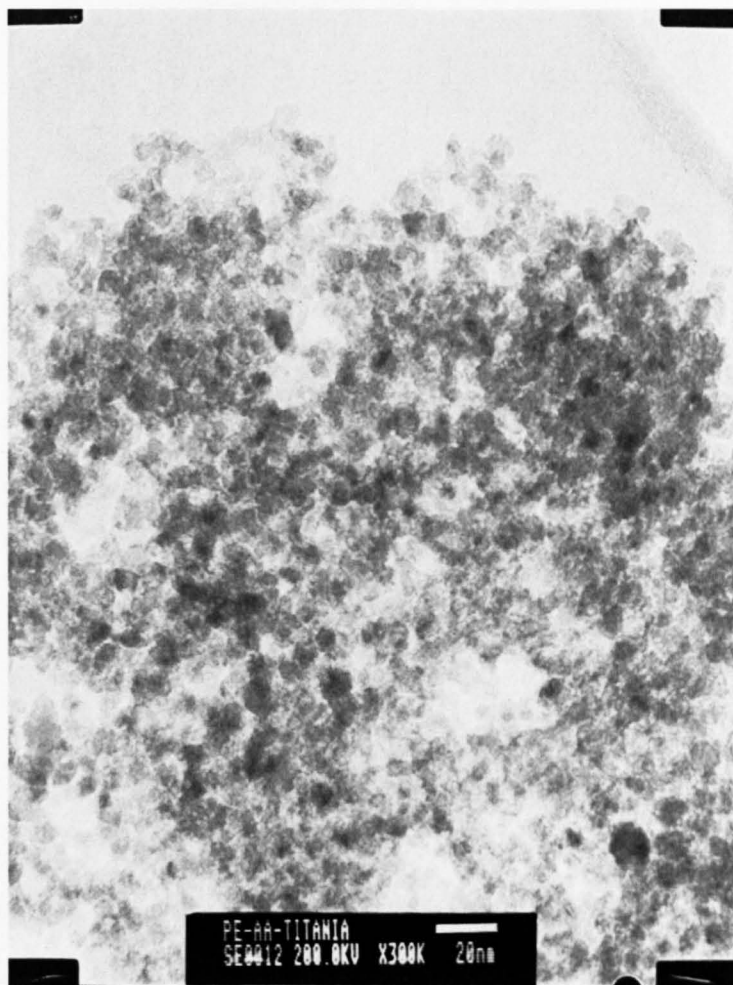


Fig. 6.11: TEM image of poly(ethylene-co-AA 5 wt %)-titania

6. Steric and electrostatic stabilization of colloidal titania nanoparticles

The chemical structure of poly(ethylene-co-AA 5 wt %)-titania dry powder was investigated with FTIR to verify the attachment of poly(ethylene-co-AA 5 wt %) to titania nanoparticles. Figure 6.12 shows the FTIR spectrum of poly(ethylene-co-AA 5 wt %)-titania compared to uncoated titania and allocates absorption correlations to certain functional groups (Skog and Holler, 1999).

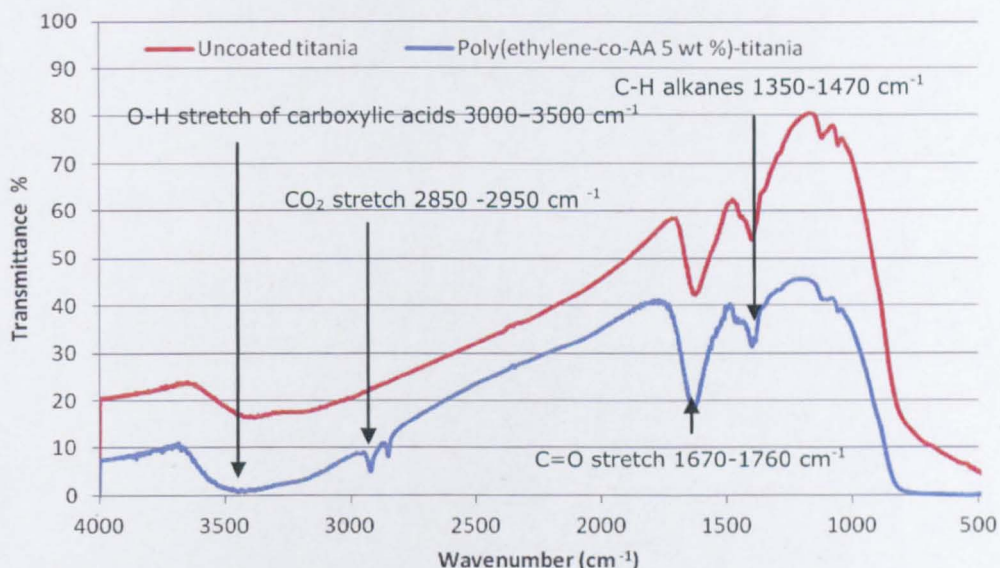


Fig. 6.12: FTIR spectrum of poly(ethylene-co-AA 5 wt %)-titania

The enhanced IR absorption of poly(ethylene-co-AA 5 wt %)-titania relative to uncoated titania was correlated to the carboxylic group stretch (O-H and C=O stretch) of the attached polymer, the hydrogen bonding to the nanoparticle surface, and to the C-H stretch of the attached polymer. The polymeric surfactant loading level was determined by TGA. Poly(ethylene-co-AA 5 wt %) of 5 wt % loading level was reported from the TGA profile and Equation 5.1. This high dispersant agent loading level was ascribed to the extraction of the dispersant aliphatic chains, that could have no role in surface modification, to the organic layer.

6.1.2.2 Titania surface modification with poly(ethylene-co-AA 15 wt %)

Consequently, the prospect of achieving uniform nanoparticle extraction to the organic phase by using a copolymer dispersant with a higher loading level of anchoring groups was investigated. Poly(ethylene-co-AA 15 wt%) (Aldrich) was employed as a dispersant using the same hydrothermal conditions. The poly(ethylene-co-AA 15 wt %) anchored titania was observed to be more uniformly extracted to the organic phase. Figure 6.13 shows the impact of the polar anchoring group wt % on the organic modified titania extraction pattern.

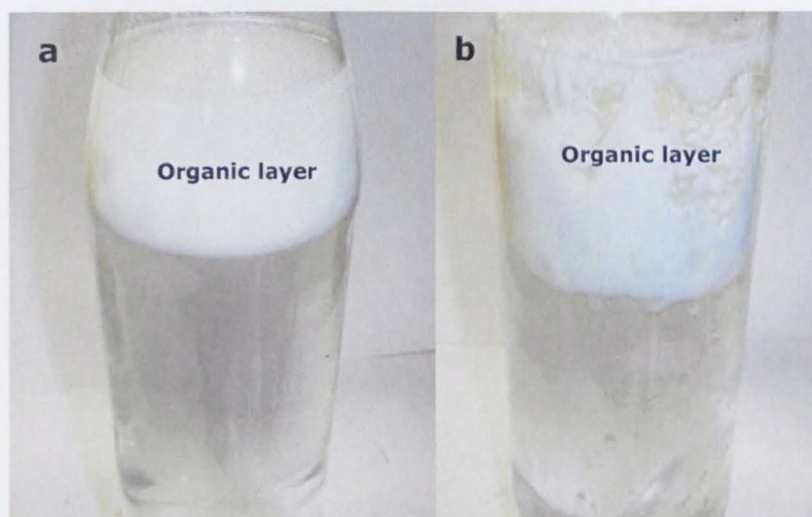


Fig. 6.13: Extraction of: (a) poly(ethylene-co-AA 15 wt %)-titania, (b) poly(ethylene-co-AA 5 wt %)-titania to the organic phase

The uniform nanoparticle extraction into the organic phase was ascribed to the fact that almost all the polymeric chains could be involved into surface modification as the functional group content had been increased. The organic layer was visualized by TEM (Figure 6.14) and poly(ethylene-co-AA 15 wt %)-titania nanoparticles of 4.1 nm average particle size was observed.

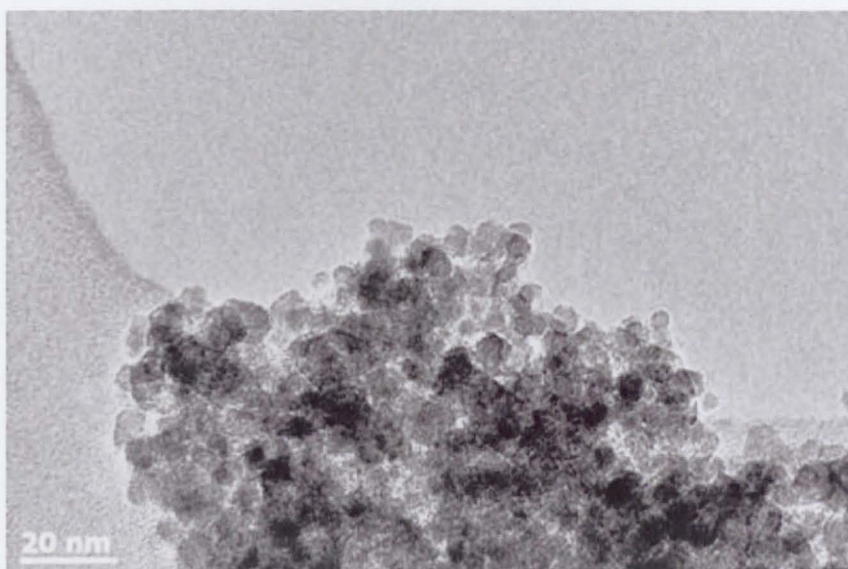


Fig. 6.14: TEM image of poly(ethylene-co-AA 15 wt %)-titania

Subsequently, the organic layer was separated, centrifuged, and freeze dried and the chemical structure of the dried powder investigated using FTIR to verify the attachment of poly(ethylene-co-AA 15 wt %) to the titania nanoparticles (Figure 6.15).

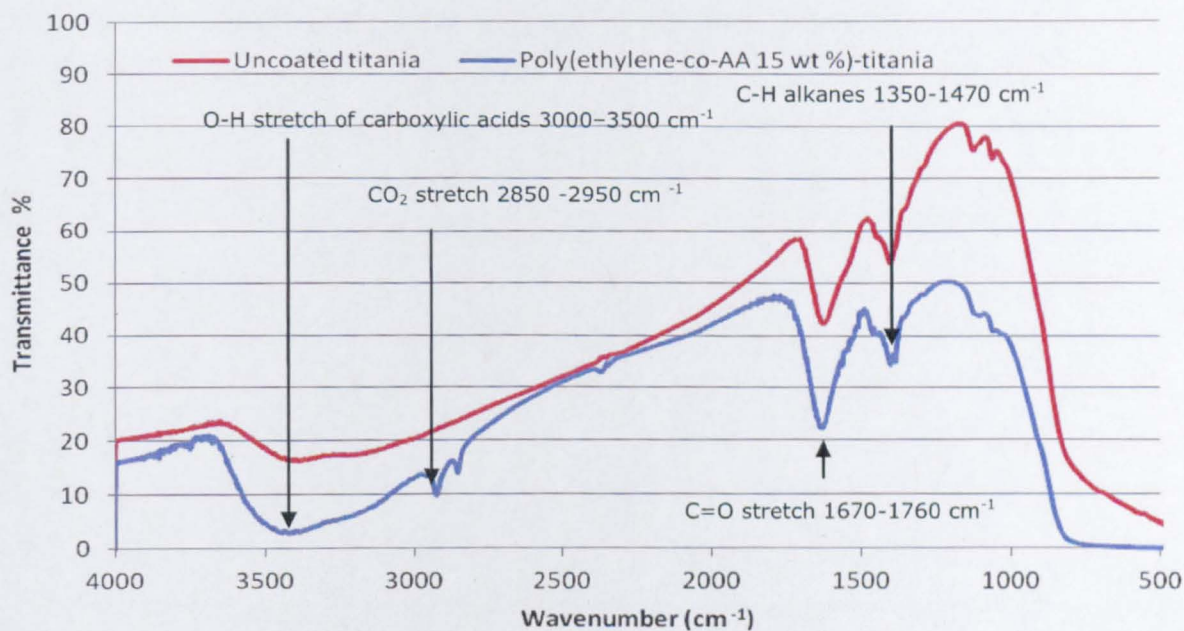


Fig. 6.15: FTIR spectrum of poly(ethylene-co-AA 15 wt %)-titania

The enhanced levels of IR absorption of poly(ethylene-co-AA 15 wt %)-titania compared to uncoated titania was ascribed to the carboxylic group (O-H and C=O) stretch of the attached copolymer, the hydrogen bonding to the nanoparticle surface, and to the C-H stretch of the attached surfactant. A polymeric surfactant loading level of 2 wt % was reported from the TGA profile and Equation 5.1.

6.2 Electrostatic stabilization of titania colloid

Nano-oxides produced by CHS are produced in the form of colloids and so they are likely to aggregate extensively due to Brownian motion (Grate and Abraham, 1991, Khanna, 1997). The continuous Brownian motion of colloidal nanoparticles will result in countless collisions (Ottewill, 1977) which will induce a temporary dipole-dipole interaction (London attractive force) (Figure 6.16) (Napper, 1983).

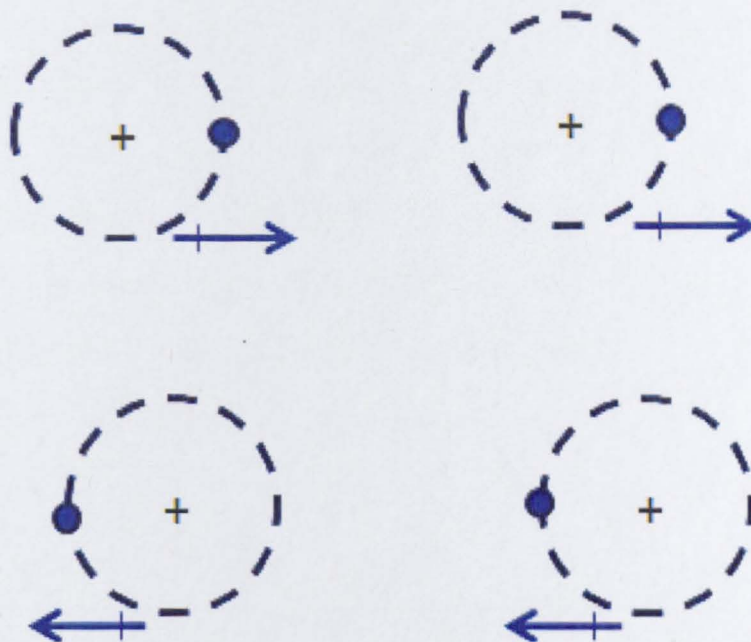


Fig. 6.16: Schematic of London attractive forces, adapted from (Napper, 1983)

6. Steric and electrostatic stabilization of colloidal titania nanoparticles

Einstein showed that, theoretically the average square displacement X^2 of a particle of radius r in a medium of viscosity η could be evaluated using Equation 6.1 (Parfitt, 1981).

$$X^2 = \frac{R T t}{3 \pi N_o \eta r} = 2 D t \quad (6.1)$$

Where: D is the diffusion coefficient, R is the universal gas constant, T is the absolute temperature, t is the time, and N_o is the Avogadro's number.

According to Einstein's equation, a particle of 1 nm radius in water at 20 °C can travel 1 μm in 2.3 ms. Consequently, this random Brownian motion can cause rapid colloidal flocculation (Mysels, 1959).

According to DLVO theory (named after its principle creators, Derjaguin, Landau, Verwey, and Overbeek), nanoparticles can be stabilized in aqueous systems through electrostatic stabilization via ion adsorption (Bouvy and Opstaele, 1995). The adsorbed ions can build up a repulsive electrical double layer associated with each particle (Verwey and Overbeek, 1948, Bouvy and Opstaele, 1995). This double layer is responsible for generating an electrostatic repulsive force between two neighbouring particles (Hunter, 1981). Figure 6.17 shows the electrical double layer of a negatively charged colloidal particle.

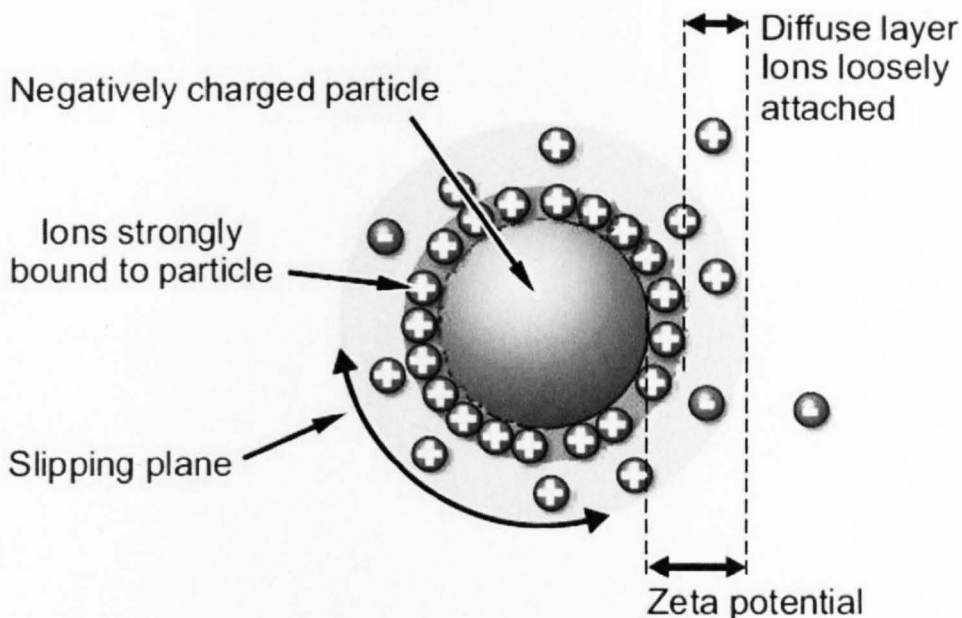


Fig. 6.17: Electrical double layer and corresponding potentials near the surface of negatively charged colloidal particle, adapted from (Brinker and Scherer, 1990).

The electrical double layer includes a boundary called a slipping plane. Ions within this boundary move with the dispersed particles whereas ions outside the slipping plane do not travel with the particles (Voyutsky, 1978, Hunter, 1981). The potential at this boundary (slipping plane) is known as the zeta potential (Verwey and Overbeek, 1948). The magnitude of the zeta potential gives an indication of the colloidal system stability. Particles with a zeta potential more positive than +30 mV or more negative than -30 mV are normally considered stable (Morris et al., 1999); as there will be enough force for the particles to repel each other and there will be no tendency to flocculate (Hunter, 1981). The colloidal system stability can be related to the total interaction energy (V_{tot}) of the system. V_{tot} is the summation of double layer repulsion (V_{R}) and van der Waals attraction (V_{A}) of colloidal charged particles (Parfitt, 1981). Figure 6.18 shows the potential energy curves for the interaction of two charged particles.

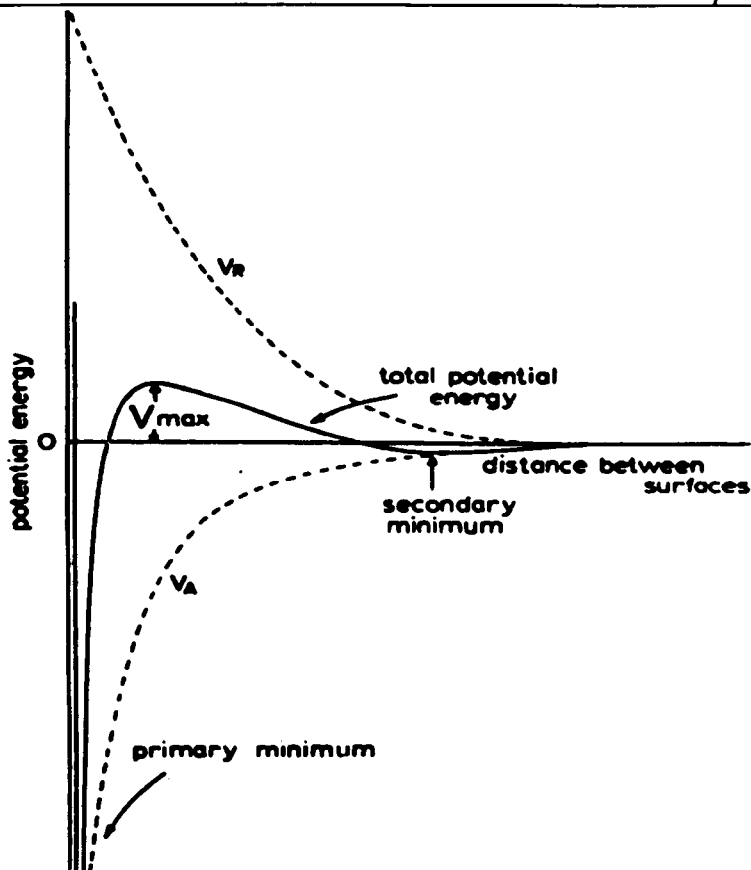


Fig. 6.18: Potential energy curves for the interaction of two charged particles, adapted from (Parfitt, 1981)

Near the particle surface is a deep minimum in the potential energy produced by the van der Waals attraction (primary minimum). Further away is a maximum (repulsive barrier) produced by the electrostatic double layer (V_{\max}) (Brinker and Scherer, 1990). If the repulsive barrier energy is greater than $10 KT$, where K is the Boltzmann constant, the Brownian motion will not overcome the repulsive barrier, and no aggregation could take place over time (Parfitt, 1981).

6.2.1 Post-synthesis electrostatic stabilization of titania colloid

Both ammonium and phosphate ions are known to act as anchoring groups for polymeric dispersants to nano-oxide surfaces (Farrokhpay, 2009).

6. Steric and electrostatic stabilization of colloidal titania nanoparticles

Therefore, the potential for these ions to create an electrical double layer and stabilize titania colloid in water was investigated as a part of this study. Consequently, the colloidal titania nanoparticles were electrostatically stabilized by using ammonium phosphate dibasic (AP) $(\text{NH}_4)_2\text{HPO}_4$ (Aldrich, 98%) via post-synthesis stabilization approach such that the electrostatic stabilization was carried out at the capping point (point D on Figure 2.31). ScW conditions were 240 bars and 400 °C (20 ml/min) and the metal salt feed was 0.05 M TIBALD in water (10 ml/min).

The optimum AP molar feed, required for electrostatic stabilization, was investigated by employing different AP concentrations (0.005-0.05 M) at the capping point (5 ml/min). AP of 0.05 M was found to be capable of stabilizing the nanoparticles and preventing any visual signs of aggregation. The molar feed of these stabilizing ions were 10 times that of the organic dispersants used in the steric stabilization work. This was because it is known that a high concentration of ions is typically required to secure the formation of a sufficient repulsive electric double layer associated with each particle. Figure 6.19 shows electrostatically stabilized titania colloid via post-synthesis electrostatic stabilization.



Fig. 6.19: Titania colloid, stabilized via post-synthesis electrostatic stabilization using ammonim phosphate ions

6. Steric and electrostatic stabilization of colloidal titania nanoparticles

The size of the dispersed particles was visualized by TEM and showed titania nanoparticles of 5 nm particle size with a double layer ions of 2.5 nm thickness around each particle (Figure 6.20).

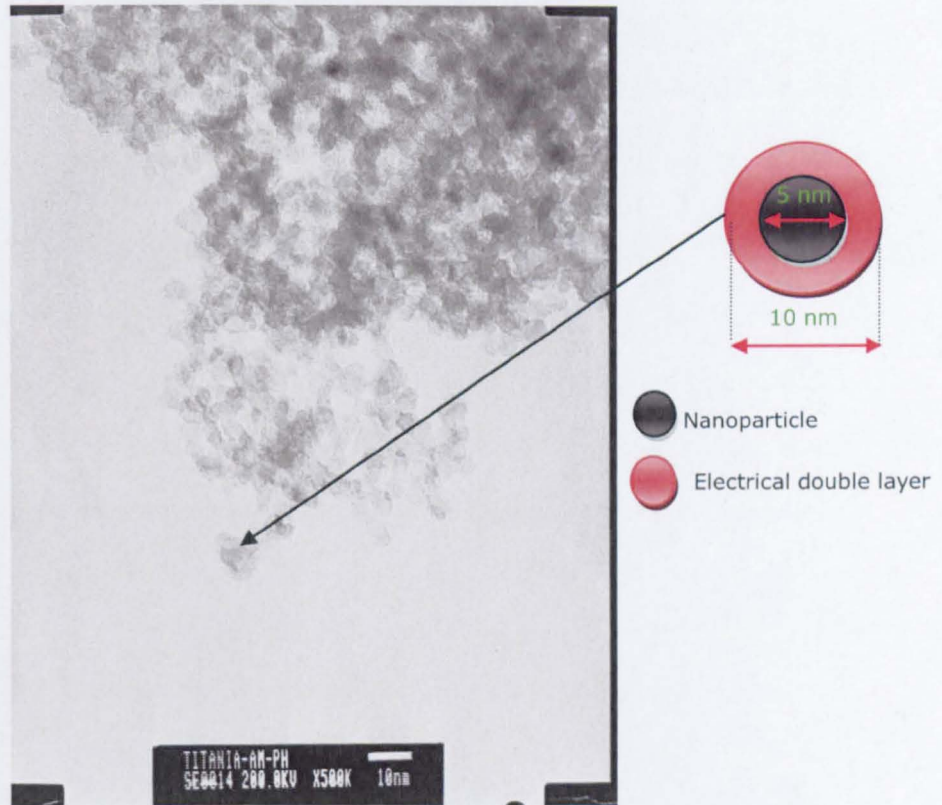


Fig. 6.20: TEM image of electrostatically stabilized titania colloid

The size of titania nanoparticles in their colloidal state was also determined by DLS and colloidal titania nanoparticles of 164 nm average particle size were reported from the DLS result (Figure 6.21).

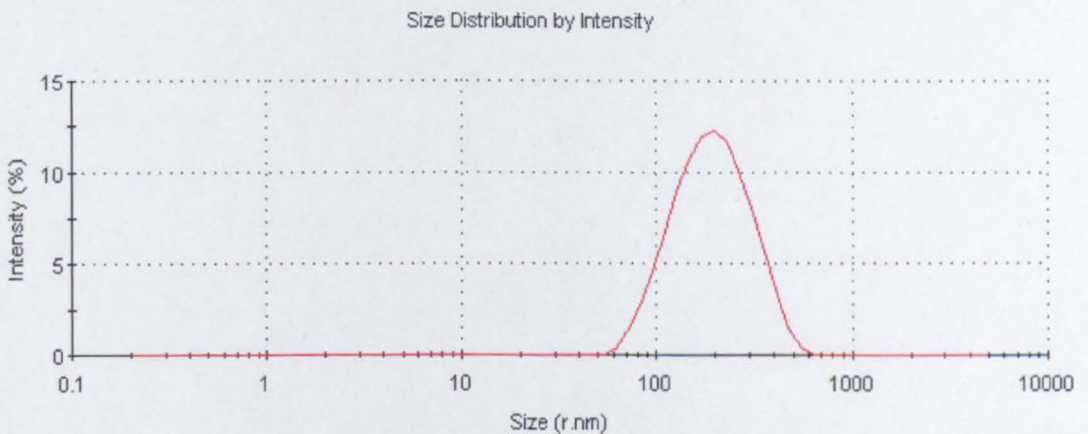


Fig. 6.21: The size of electrostatically stabilized titania colloid by DLS

6. Steric and electrostatic stabilization of colloidal titania nanoparticles

The increased size of colloidal titania nanoparticles from DLS measurement (164 nm) compared with TEM measurement (5 nm), could be ascribed to the great tendency of the colloidal nanoparticles to reduce in number with time due to their collisions. Furthermore, small titania nanoparticles (5 nm diameter) could have the tendency to dissolve and reprecipitate onto larger particles in a phenomenon called Ostwald ripening.

It took over 5 days for electrostatically stabilized titania colloid to flocculate whilst the non-stabilized titania colloids were found to flocculated in 10 minutes. Furthermore, it was concluded that the stabilized titania colloid could not be long-term stable as the repulsive potential V_R was less than 10 KT. Furthermore, the interaction between the approaching particles might cause distortion of the double layer.

6.2.1.1 Stability of electrostatically stabilized titania colloid

The stability of titania colloid was evaluated by measuring the zeta potential. A stable colloid requires a repulsive potential more positive than +30 mV or more negative than -30 mV (Rulon E, 1984, Morris et al., 1999) and the titania colloids manufactured in this study demonstrated a zeta potential value of zero mV (Figure 6.22).

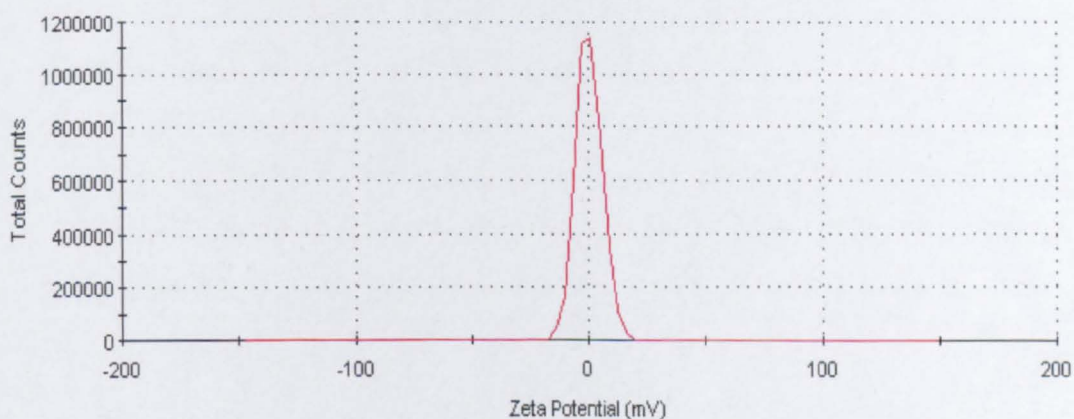


Fig. 6.22: Zeta potential of electrostatically stabilized titania colloid

6. Steric and electrostatic stabilization of colloidal titania nanoparticles

This measurement confirmed that the colloidal system should not be a long-term stable colloid. However, the zero zeta value was correlated to the pH of the colloid (pH was 7.4) which resulted in non-charged titania surface. It has been reported that the zeta potential depends strongly on the colloidal pH see Figure 6.23 (Rulon E, 1984).

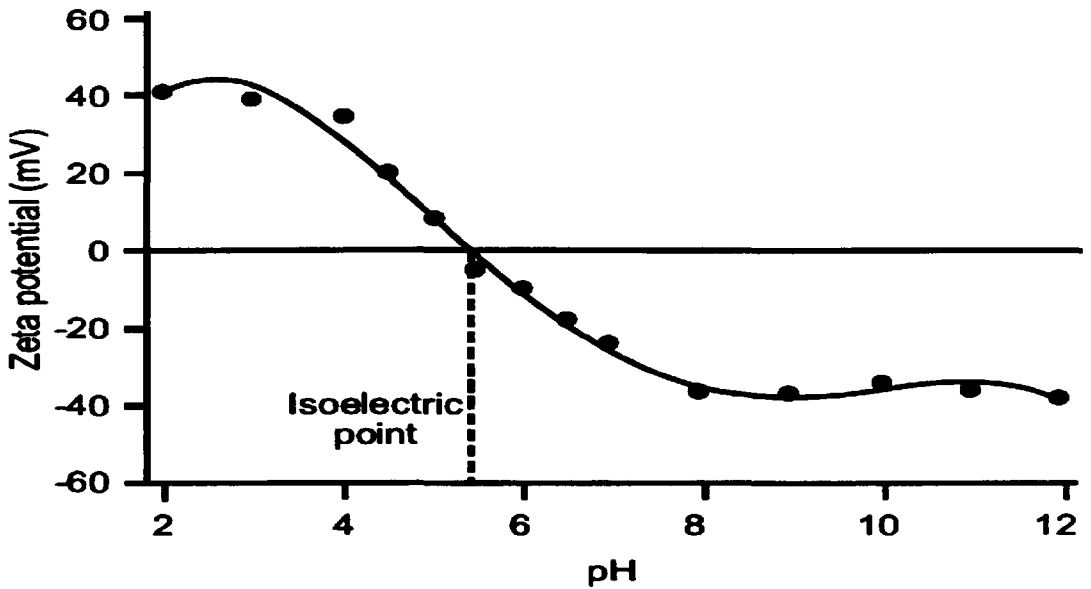


Fig. 6.23: The dependence of zeta potential on colloid pH, adapted from (Malvern-Instruments-Manual, 2004)

This behaviour can be explained by the fact that colloidal nanoparticles can acquire more charge by changing the pH of the suspension. Consequently, the isoelectric point is the point where the system is least stable as the dispersed particles are neutrally charged (Brinker and Scherer, 1990).

The pH of the collids produced in this section of the study was found to be 7.4, which is close to the colloidal titania isoelectric point (i.e. pH 6). Therefore, further assessment of the colloidal titania nanoparticles stability over an extended pH range was conducted via the addition of excess double layer ions. In this case, phosphoric acid (pH = 2) and ammonium

6. Steric and electrostatic stabilization of colloidal titania nanoparticles

hydroxide (pH = 12). In both cases the dispersed colloidal nanoparticles were observed to flocculate extensively (Figure 6.24).

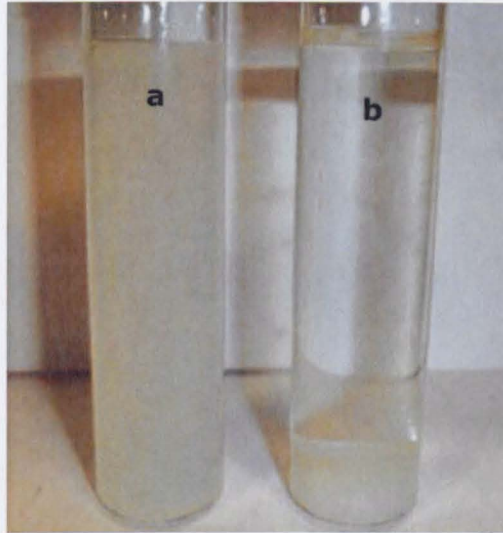


Fig. 6.24: Image of: (a) electrostatically stabilized titania colloid, (b) the flocculated titania colloid

This colloidal flocculation was attributed to a compression of the double layer structure with the increase of the counter ion concentration. In other words, the same number of charges that are required for balancing the particle surface will be available in a smaller volume of layer surrounding the particle (Frens and Overbeek, 1972). Furthermore, it has been reported that the coagulating power of the counter ion increases exponentially with the magnitude of its charge (Spielman, 1970) and this could to be the case in stabilizing colloidal titania with AP double layer ions over extended pH range. Figure 6.25 shows the linear relation between critical coagulation concentrations (CCC) of counter ions as a function of the counter ion charge for different nanocolloidal systems.

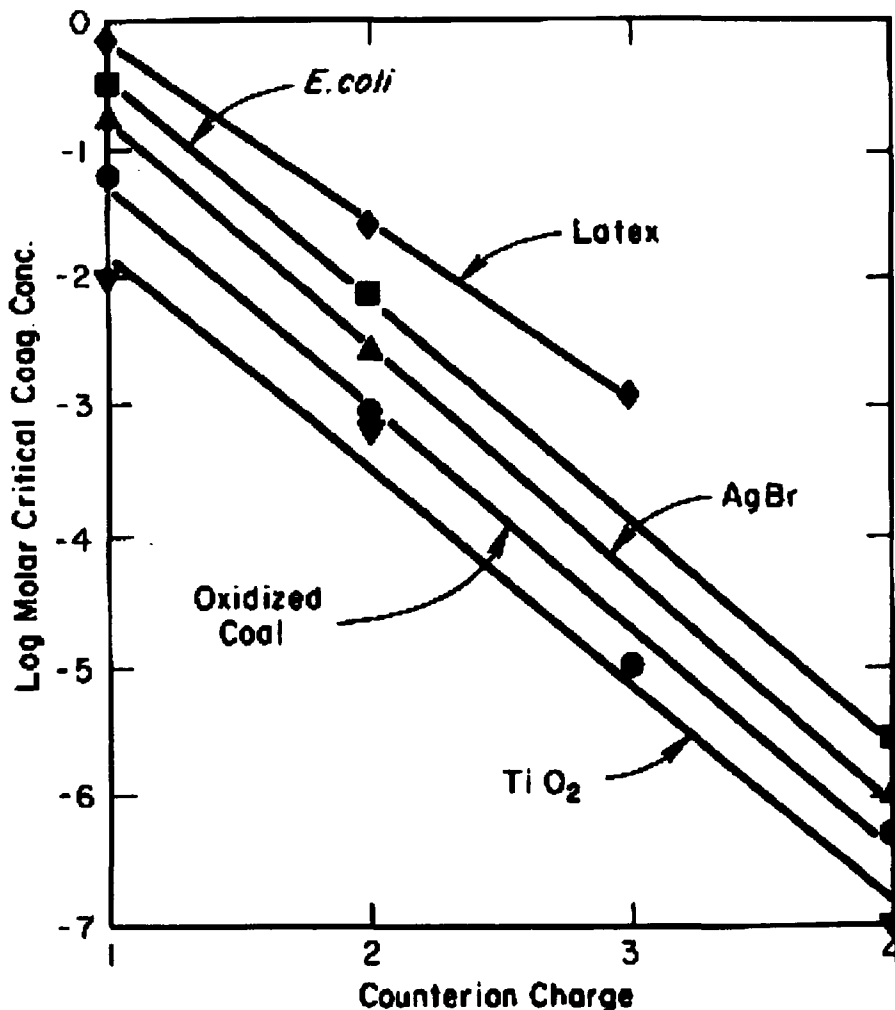


Fig. 6.25: Critical coagulation concentrations against counter ion charge, adapted from (Davis et al., 1984)

The strong dependence of CCC on counter ion charge can be ascribed to the ability of highly charged ions to screen the surface potential (Brinker and Scherer, 1990).

6.2.2 In situ electrostatic stabilization of titania colloid

Most aggregated colloidal nanoparticles (described in Figure 6.18) do not return spontaneously to the dispersed state, even when the coagulating conditions are removed (Parfitt, 1981). Therefore, the potential of minimizing any possible aggregation in the primary minimum region and

6. Steric and electrostatic stabilization of colloidal titania nanoparticles

so achieve an electrostatically stabilized colloidal system with smaller particles via exclusive stabilization in the reactor was investigated. TiO_2 was produced and stabilized using 0.05 M TIBALD (10 ml/min) in the upflow against 20ml/min of supercritical water at 400 °C and 240 bars with the addition of 0.01 M AP in the ScW and a transparent stabilized titania colloid was obtained. The size of the colloidal nanoparticles was determined by DLS which demonstrated that colloidal titania nanoparticles of 56 nm particle size had been synthesised (Fig. 6.26).

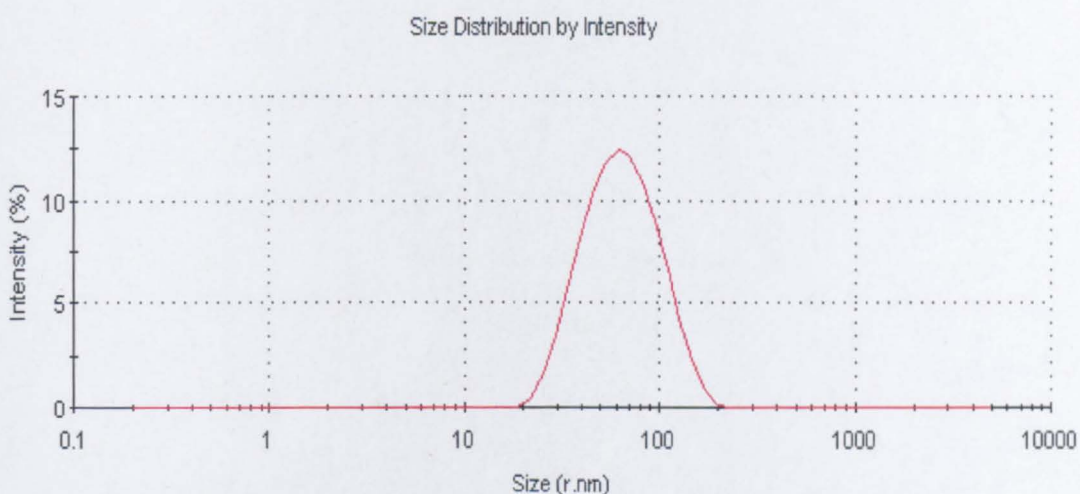


Fig. 6.26: DLS of stabilized titania colloid via electrostatic stabilization in the reactor

The DLS measurements indicated that a more stable colloid had been achieved via electrostatic stabilization in the reactor compared with post-synthesis electrostatic stabilization at the capping point as smaller colloidal particles were achieved. Fuchs (Fuchs, 1934) proposed that the repulsive potential (V_R) could minimize the colloidal coagulation rate by minimizing the attachment of single particles to big clusters. Therefore, V_R can enhance the colloidal system stability by a factor W (called stability ratio) (Fuchs, 1934).

6. Steric and electrostatic stabilization of colloidal titania nanoparticles

The main drawback of electrostatic stabilization in the reactor was the drop in the post mixing temperature by 100 °C. The post mixing temperature is defined as the temperature of the flow after the ScW and the metal precursor become mixed together in the reactor. Experimentally it was found that this drop in post mixing temperature dramatically reduced the reaction conversion. However, it was also found that temperature drop could be avoided by injecting the stabilizing ions into the reactor directly after nanoparticle formulation. By adopting this approach, any possible aggregation in the primary minimum region could be minimized. Figure 6.27 is a schematic drawing of the proposed reactor design for electrostatic stabilization in the reactor.

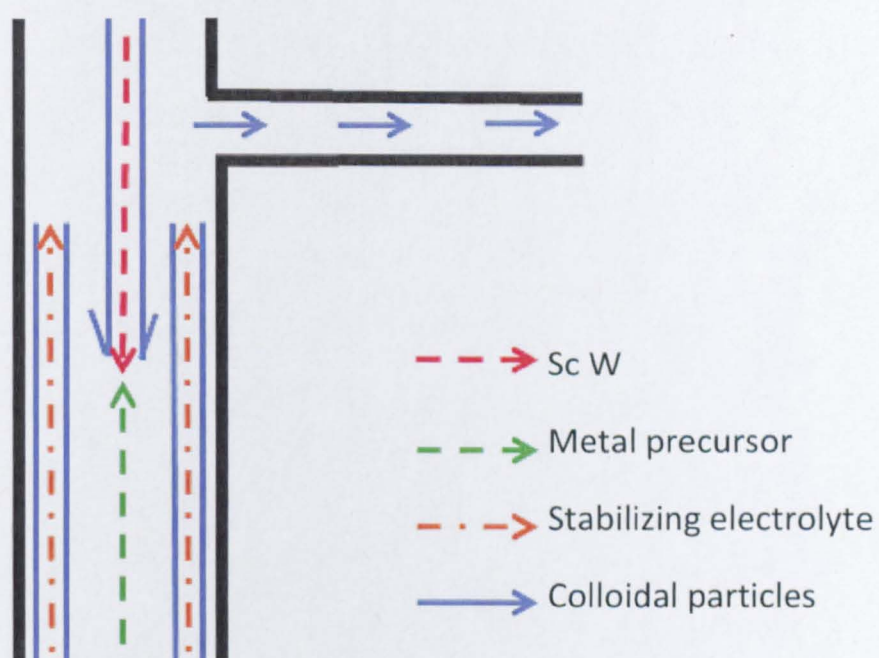


Fig. 6.27: The proposed reactor design for in situ electrostatic stabilization

6.2.3 Post-collection electrostatic stabilization of titania colloid

It was reported that phosphate and phosphonate groups can bind strongly to titania surface and form Ti-O-P bond which is a bond type that is very

6. Steric and electrostatic stabilization of colloidal titania nanoparticles

resistant to hydrolysis (Forget et al., 2003). Furthermore, the phosphoric acid group was reported to be capable of anchoring to the titania nanoparticle surface (Neouze and Schubert, 2008). Consequently, the colloidal titania nanoparticles produced by CHS were stabilized using phosphoric acid.

The colloidal nanoparticles, produced by CHS, were centrifuged to remove water along with any side reaction products. The nanoparticles were redispersed in deionized water and phosphoric acid (Aldrich, 60 wt %) was added to adjust the colloidal pH to 2 and a stable colloidal system was successfully achieved in which the nanoparticles were observed not to flocculate with time. An assessment of the zeta potential of the colloidal system was investigated as described in Section 3.3.6. The obtained data demonstrated that the colloidal system had a zeta value of 37.3 mV as included in Figure 6.28.

Temperature (°C): 25.1	Zeta Runs: 52
Count Rate (kcps): 363.4	Measurement Position (mm): 2.00
Cell Description: Clear disposable zeta cell	Attenuator: 8

	Mean (mV)	Area (%)	Width (mV)
Zeta Potential (mV): 37.3	Peak 1: 0.00	0.0	0.00
Zeta Deviation (mV): 0.00	Peak 2: 0.00	0.0	0.00
Conductivity (mS/cm): 33.8	Peak 3: 0.00	0.0	0.00

Result quality : Good

Fig. 6.28: The Zeta potential of electrostatically stabilized titania colloid by phosphoric acid

Thus, the colloidal system can be classified as long term stable colloid as the electrostatic repulsive force (V_R) between two neighbouring particles could be enough to overcome the van der Waals force of attraction (V_A) and consequently no flocculation took place with time. However, it was not

6. Steric and electrostatic stabilization of colloidal titania nanoparticles

possible to achieve electrostatic stabilization by using other acids such as HCL. Figure 6.29 shows a schematic for titania electrostatic stabilization with phosphoric acid where titania surface could be positively charged with H^+ (charge determining ions). HPO_4^{-2} ions (counter ions) could bind strongly to titania positively surface. The long term stabilization can be correlated to the strong bonding of HPO_4^{-2} to positively charged titania surface.

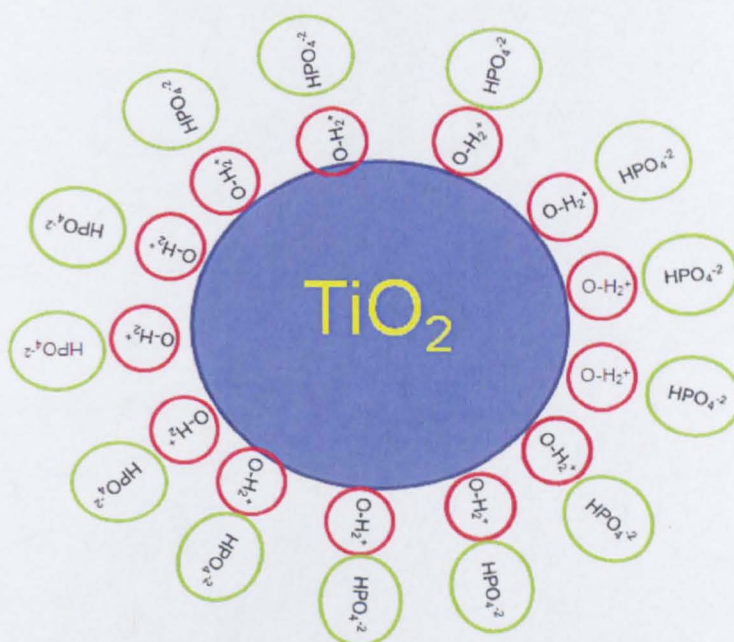


Fig. 6.29: Schematic for titania electrostatic stabilization with phosphoric acid

The adsorbed ions could be able to create a repulsive electrical double layer associated with each particle. The developed repulsive potential could be able to keep the colloidal particles outside the range of van der Waals force of attraction.

6.3 Summary of steric and electrostatic stabilization of colloidal titania nanoparticles

Chapter 6 represented experiments for the steric stabilization of colloidal titania nanoparticles via surface modification with polymeric surfactants and using copolymers as amphiphathic surfactants. Titania nanoparticles were sterically stabilized in water by using poly(acrylic acid). PAA-titania colloid can be classified as a long-term sterically stabilized colloid; as there was no flocculation over time. Titania was organic modified with poly(ethylene-co-AA) as an amphiphathic dispersant. The effectiveness of titania surface modification with poly(ethylene-co-AA) was reported to depend on the ratio of the polar anchoring groups. Poly(ethylene-co-AA 15 wt%) anchored titania more effectively compared with poly(ethylene-co-AA 5 wt %). Furthermore the electrostatic stabilization of titania colloid was investigated and it was not possible to achieve long term electrostatically stabilized titania colloid by using AP due to double layer compression. On the other hand, it was possible to stabilize colloidal titania by using phosphoric acid. The created repulsive potential was sufficient to overcome van der Waals attractive force and to achieve a long-term stable colloid.

CHAPTER 7

7. FORMULATION AND FUNCTIONALIZATION OF NANOPARTICLES WITH FLAME RETARDANT PROPERTIES

Nanoparticles can have a flame retardant (FR) action through the release of effective flame inhibitors such as PO_2^* , PO^* , and HPO^* (Levchik and Weil, 2006), by absorbing heat with the release of H_2O and CO_2 (Rothon, 2003c), or by preventing the access of oxygen to the burning material (Camino and Delobel, 2000). Such nanoparticles can act as nano-fire extinguishers. Polymer Nanocomposites (PNs) based on nano-fire extinguishers might also show improved polymer rheology and flame retardancy at low solid loading level through the nanoscale dispersion of these nanoparticles (Fu and Qu, 2004). This Chapter represented the work conducted for the formulation and the surface modification of bespoke nanoparticles (i.e. hydroxyapatite and aluminum-oxide-hydroxide) that could deliver a FR performance to the polymeric material using CHS technique.

7.1 Formulation and functionalization of hydroxyapatite ($\text{Ca}_5(\text{OH})(\text{PO}_4)_3(\text{HA})$)

Phosphorous can be considered as the key FR element; the efficiency of phosphorous-based FRs can be evaluated by how much phosphorous they have (Pinfa, 2010). Hydroxyapatite (HA), which is the most important bio ceramic material for medical applications (Li, 2008), was found to have a phosphorous content of 18.5 wt %. This phosphorous content is much

higher than most commercially available phosphorous-based FR additives such as triphenyl phosphate (TPP) and resorcinol bis-(diphenyl phosphate) (RDP) (Horrocks and Price, 2008). This high phosphorous content could give HA a FR action. HA might exhibit a dual function as a nano-filler that could improve the polymer rheology under firing conditions, as well as a nano phosphorous-based FR agent. HA could show a gas phase effect due to the release of active flame scavengers species such as PO_2^* , PO^* , and HPO^* . These species are the most effective free radical scavengers. They are 10 times more effective than chlorine, and 5 times more effective than bromine (Babushok and Tsang, 2000, Laoutid et al., 2009). Furthermore, HA could have a condensed phase effect via the formation of a protective char layer. HA morphology, crystallinity, and particle size greatly affect its applications. It was reported that a small change in HA morphology and particle size had a significant effect on the mechanical properties of HA/polyethylene composites (Wang et al., 1998).

Different HA crystalline forms such as nanorods, nanoplates, and nanoparticles were synthesized via CHS (Li, 2008). The HA crystal growth, size, and morphology could be controlled by monitoring the reaction temperature and pH (Li, 2008). HA in the shape of platelets was reported to be the most thermally stable crystalline form. The aim of this work was to synthesize and functionalize a stable crystalline HA form that could be effectively dispersed into polymeric matrix. The developed nanoparticles could have a FR action. To the knowledge of the author, this is the first time HA nanoparticles have been considered as a FR agent.

7.1.1 Synthesis of hydroxyapatite (HA)

0.015 M ammonium phosphate dibasic ($(\text{NH}_4)_2\text{HPO}_4$) (Aldrich, 98%) solution was employed as the superheated downflow at 200 °C and 240 bars (20 ml/min). The precursor feed upflow was 0.05 M calcium nitrate tetrahydrate ($\text{Ca}(\text{NO}_3)_2 \cdot 4\text{H}_2\text{O}$) (Aldrich, 99%) (10 ml/min). A few drops of HA dispersed in water were visualized by TEM to investigate the nanoparticle shape and size, and a typical data obtain from this technique is included as Figure 7.1.

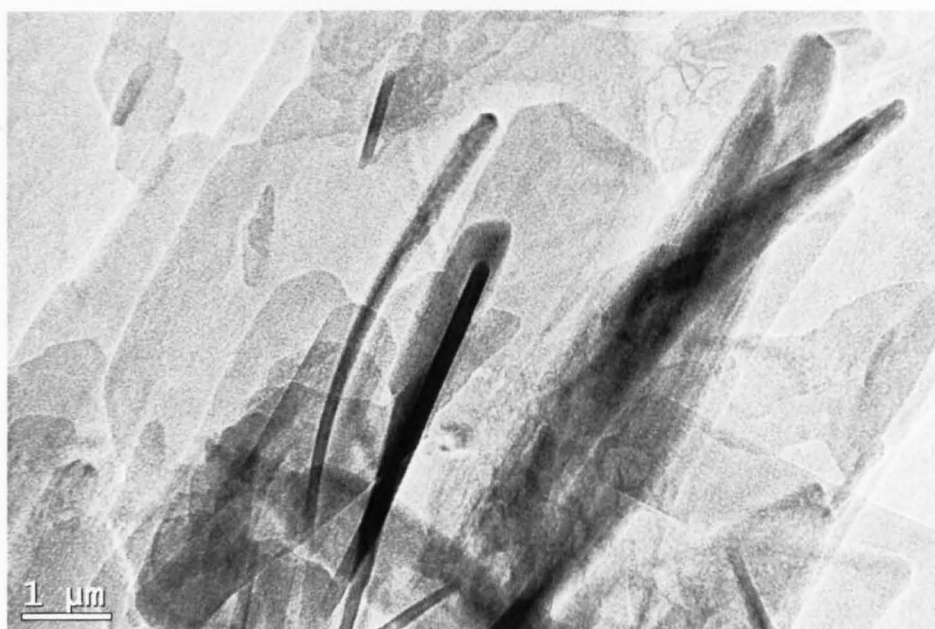


Fig. 7.1: TEM image for HA

HA in the shape of platelet of 2 μm width and 5 μm length was reported from TEM image. HA dried powder was tested with XRD to investigate the crystalline structure. Figure 7.2 shows the obtained XRD diffractogram of HA nanoparticles.

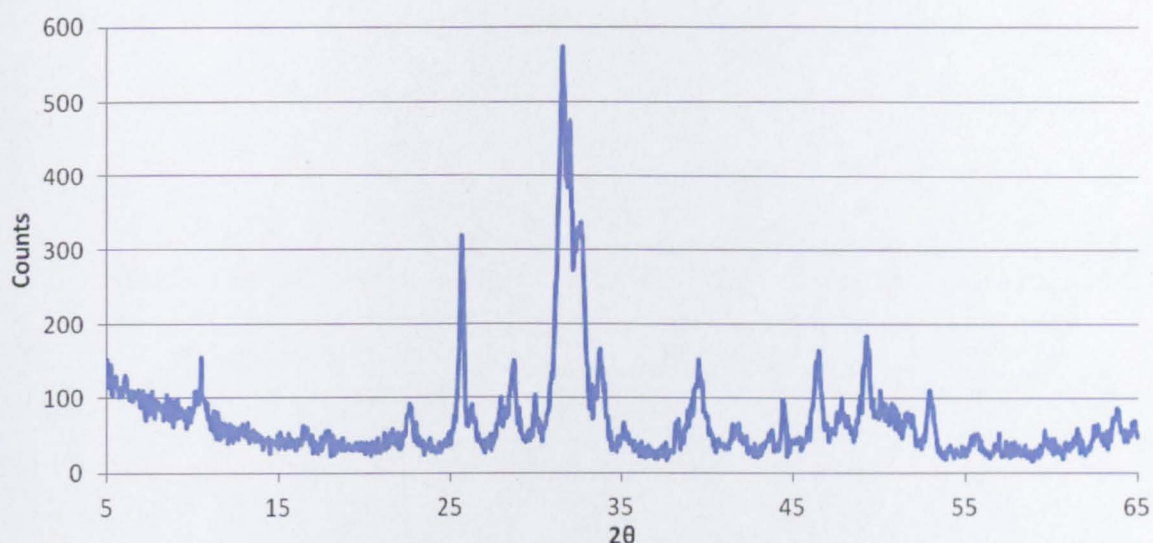


Fig. 7.2: The XRD diffractogram of HA

A crystalline hexagonal HA structure was observed from the XRD result, by comparing the obtained diffractogram to standard data from joint committee on powder diffraction standards (JCPDS).

7.1.2 Hydroxyapatite surface modification with DDSA

The surface properties of nanoparticles can be significantly altered from hydrophilic to hydrophobic via surface modification (Adden et al., 2006, Neouze and Schubert, 2008). HA platelets have plenty of surface hydroxyl groups that could act as sites of attachment for organic surfactants. A chemical reaction rather than hydrogen bonding might take place at the nanoparticle surface allowing a stable and durable surface modification to be achieved. HA surface modification with organic ligands was performed via a post-synthesis surface modification approach. 0.01 M DDSA in toluene (5 ml/min) was employed as the capping agent with the same hydrothermal conditions for HA synthesis. DDSA was attached to the HA surface and extracted HA to the organic phase. DDSA-HA showed uniform extraction to the organic phase with a clear aqueous layer (Figure 7.3).

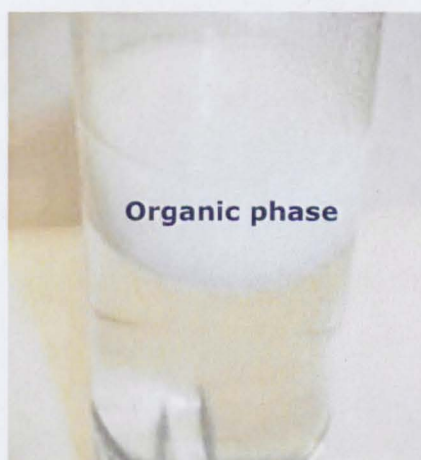


Fig. 7.3: DDSA-HA extraction to the organic layer

The DDSA-HA nanoparticles were visualized by TEM. DDSA-HA in the shape of platelets of 400 nm length and 200 nm width were reported from the TEM image (Figure 7.4).



Fig. 7.4: TEM image for DDSA-HA

7. Formulation and functionalization of nanoparticles with FR properties

The reduced platelet dimensions of DDSA-HA ($0.400\ \mu\text{m} \times 0.200\ \mu\text{m}$) to uncoated HA ($5\ \mu\text{m} \times 2\ \mu\text{m}$) was correlated to the surfactant agent conformation at the solid-liquid interface, whereby further growth of the platelets could be hindered by the attachment of DDSA. Sterically stabilized DDSA-HA in the organic layer might be unable to grow further by approach and attachment.

The impact of the reduced platelet dimensions on HA surface area was evaluated by measuring the surface area of DDSA-HA to uncoated HA. DDSA-HA showed a BET N_2 surface area of $5.95\ \text{m}^2\ \text{g}^{-1}$ whereas uncoated HA showed surface area less than $3\ \text{m}^2\ \text{g}^{-1}$. DDSA-HA dry powder was investigated with FTIR to verify the attachment of DDSA to HA surface. Figure 7.5 shows the FTIR spectrum of DDSA-HA to that of uncoated HA and highlights the key functional groups that give rise to the absorption level in the spectrum which were compared to those that have been reported in the literature (Skog and Holler, 1999).

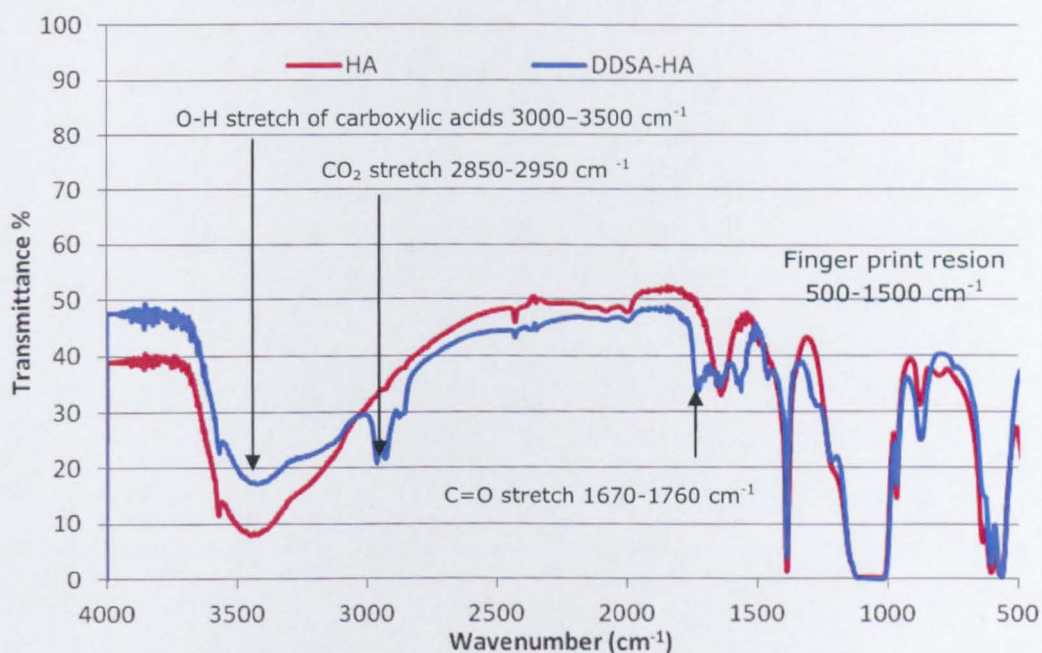


Fig. 7.5: FTIR spectrum of DDSA-HA and uncoated HA

7. Formulation and functionalization of nanoparticles with FR properties

DDSA-HA and HA showed an intense and identical absorption in the region to the right-hand side of the diagram (from about 500 to 1500 cm^{-1}); this region is called finger print region. Finger print region contains a very complicated series of absorptions which are mainly due to all manner of bending vibrations within the molecule; such absorptions act as a finger print of the chemical structure and can not be correlated. Consequently, it was concluded that HA and DDSA-HA have identical crystalline structure.

The differences in the IR spectrum of DDSA-HA compared to uncoated HA was correlated to the carboxylic group stretch (O-H and C=O stretch) of the attached surfactant. DDSA-HA showed a decrease in the O-H group absorption compared with uncoated HA; as the hydroxyl surface groups of HA could be involved into covalent bonding with DDSA dispersant. The decrease in O-H group absorption gives an indication that covalent bonding rather than hydrogen bonding could take place at HA surface. The DDSA loading level was evaluated by using TGA (Figure 7.6).

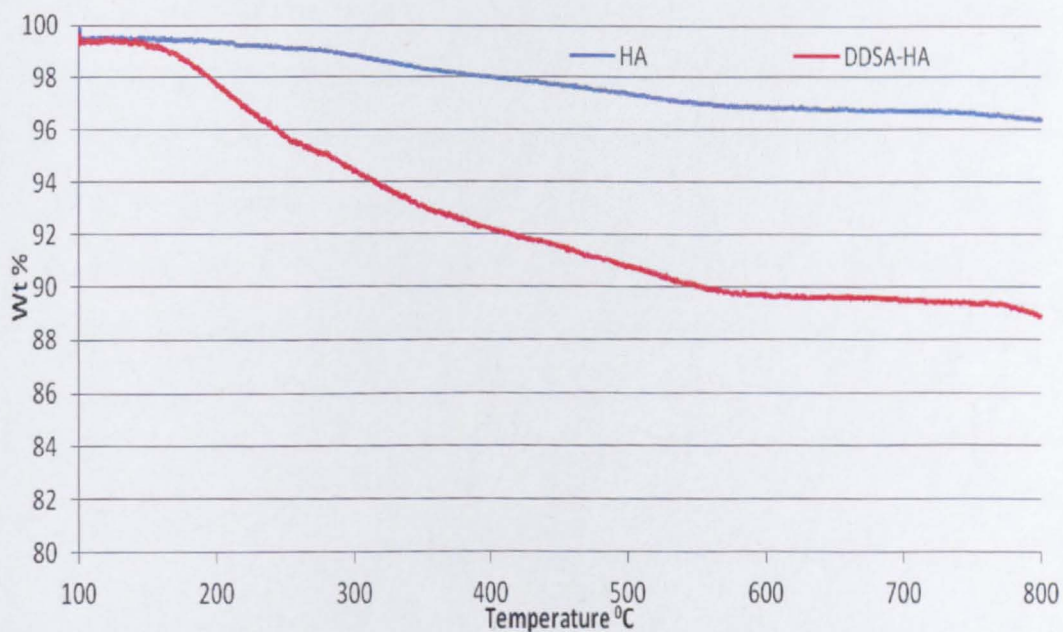


Fig. 7.6: The TGA profile of DDSA-HA

A DDSA loading level of 7.3 wt % was observed from the TGA profile and Equation 5.1. The enhanced surfactant (DDSA) loading level of HA to titania nanoparticles can be ascribed to the covalent bonding at the HA surface rather than the hydrogen bonding to titania surface.

7.1.3 HA surface modification with poly(ethylene-co-acrylic acid 15 wt %)

Polymeric surfactants are able to bind to numerous surface sites at the same time, forming durable surfactant layers (Pettersson et al., 2000, Vernardakis et al., 2001, Zhu et al., 2006). HA surface modification with poly(ethylene-co-AA 15 wt %) was performed via the post-synthesis surface modification approach. 0.06 g of poly(ethylene-co-AA 15 wt %) (Aldrich) in 100 ml toluene was injected at the capping point (5 ml/min), at the same hydrothermal conditions for HA synthesis.

The polymeric surfactant anchored the HA surface and extracted the nanoparticles to the organic phase. Poly(ethylene-co-AA 15 wt %)-HA showed uniform extraction to the organic phase. Poly(ethylene-co-AA 15 wt %) could bind to the HA surface via covalent bonding and extracted HA to the organic phase via the aliphatic backbone. A few drops of the organic layer were visualized with TEM. Poly(ethylene-co-AA 15 wt %)-HA platelets of 300 nm length and 100 nm width were observed from the TEM image (Figure 7.7).



Fig. 7.7: TEM image of poly(ethylene-co-AA 15 wt %)-HA

The platelet dimensions were less than those of DDSA-HA. This can be mainly ascribed to the polymeric surfactant conformation at the solid-liquid interface. The abundant COOH groups along the polymeric chains could secure surfactant conformation in the form of trains (polymeric segments at the solid/liquid interface) as described in Section 6.1 (Figure 6.1). This polymer conformation mechanism at the solid-liquid interface, and extraction of organic modified HA to the organic layer might hinder any further platelet growth. Poly(ethylene-co-AA 15 wt %)-HA dried powder was tested with FTIR to verify the attachment of the polymeric surfactant to HA surface. Figure 7.8 shows the FTIR spectrum of poly(ethylene-co-AA 15 wt %)-HA to uncoated HA and highlights the key functional groups that

give rise to the absorption level in the spectrum which were compared to those that have been reported in the literature (Skog and Holler, 1999).

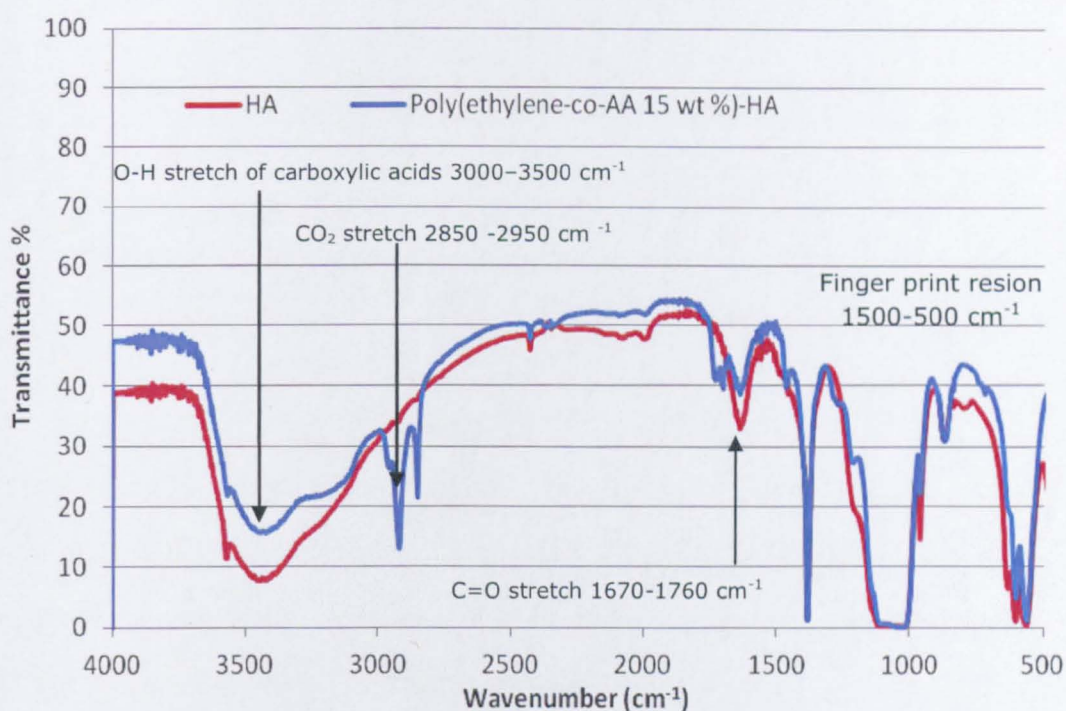


Fig. 7.8: FTIR spectrum of HA and poly(ethylene-co-AA 15 wt %)-HA

Again, poly(ethylene-co-AA 15 wt %)-HA and HA showed intense and identical absorption in the the finger print region which is the region to the right-hand side of the diagram (from about 500 to 1500 cm^{-1}).

The difference in IR absorption of poly(ethylene-co-AA 15 wt %)-HA compared with uncoated HA was correlated the carboxylic group stretch (C=O and O-H stretch) of the attached polymer. Poly(ethylene-co-AA 15 wt%)-HA showed a decrease in the O-H absorption compared with uncoated HA; as the hydroxyl surface groups of HA could be involved into covalent bonding with the polymeric surfactant. The polymeric surfactant loading level of poly(ethylene-co-AA 15 wt %)-HA was evaluated with TGA (Figure 7.9).

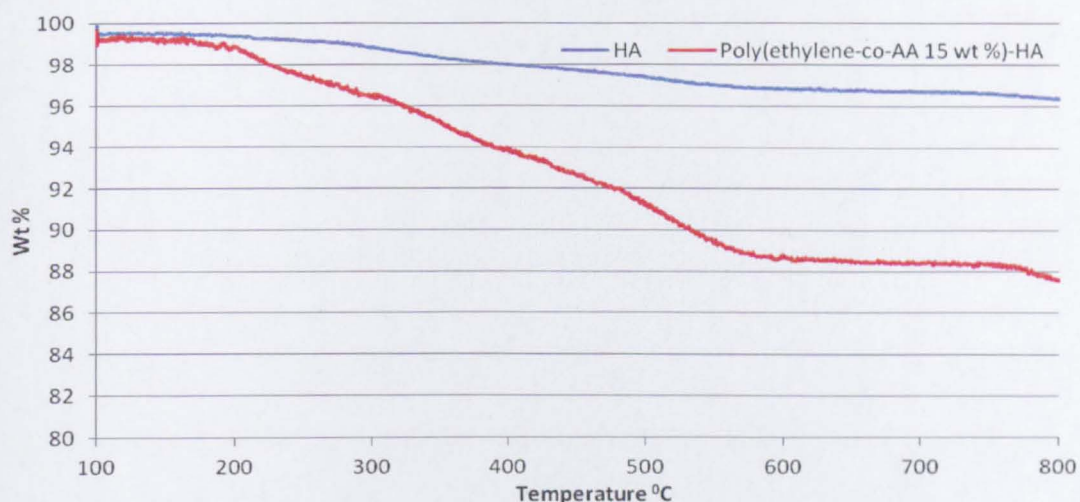


Fig. 7.9: TGA profile of poly(ethylene-co-AA 15 wt %)-HA

A polymeric surfactant loading level of 8.6 wt % was determined from the TGA profile and Equation 5.1. This high surfactant loading level can be ascribed to the high affinity of the polymeric surfactant to anchor HA platelet surface via strong covalent bonding.

7.1.4 HA surface modification with dodecanedioic acid

The integration of HA nanoparticles into a polymeric matrix resulted in a random distribution of HA platelets with increased viscosity and entrapped air bubbles, as will be described in Chapter 8. The synthesis of exfoliated HA platelets (linked together and separated by a constant interspacing distance) was investigated in an attempt to achieve HA nanocomposites with fully separated platelets (individually dispersed or delaminated within the polymeric matrix). A dispersant which has the ability to anchor two platelets at the same time might have the ability to keep them separated at a constant distance. HA surface modification was adjusted for the purpose of achieving exfoliated HA platelet with a constant interspacial distance. Dodecanedioic acid (DDA) (Aldrich, 99%) was employed as a surface modifier. Figure 7.10 shows the chemical structure of DDA.

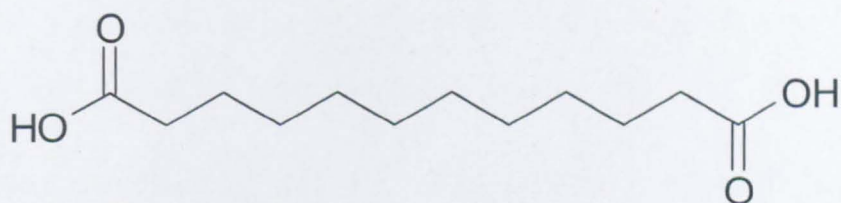


Fig. 7.10: The chemical structure of dodecanedioic acid

HA surface modification was performed via a post-synthesis surface modification approach. 0.01 M DDA in ethanol was employed as a capping agent (5 ml/min), at the same hydrothermal conditions for HA synthesis. Figure 7.11 shows the proposed chemical structure of DDA-HA; where the HA platelets might be linked together.

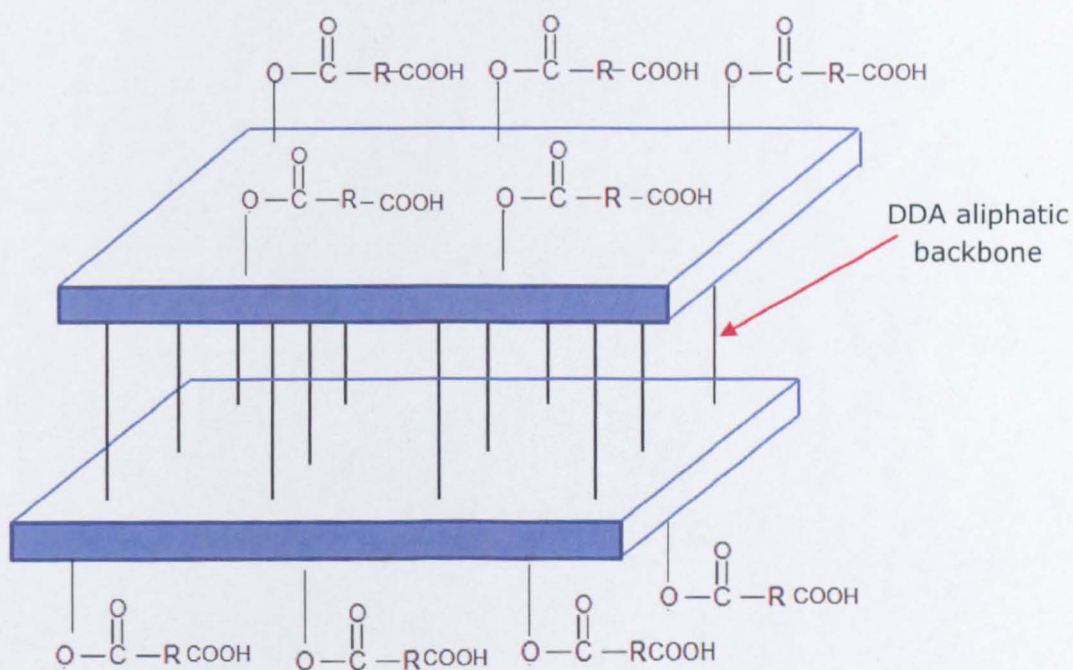


Fig. 7.11: The proposed chemical structure of DDA-HA

This structure could lead to HA nanocomposites with an exfoliated structure similar to that of modified layered silicates. Well-dispersed HA platelets into a polymeric matrix with polymer chains into the galleries

between the parallel plates, might improve the mechanical properties as well as the flammability performance of the developed nanocomposites.

DDA-HA was collected from the water/ethanol layer, centrifuged, and freeze dried. The dried powder was investigated with FTIR to verify the attachment of DDA to HA surface. Figure 7.12 shows the FTIR spectrum of DDA-HA to uncoated HA and ascribes the peaks observed to key functional groups (Skog and Holler, 1999).

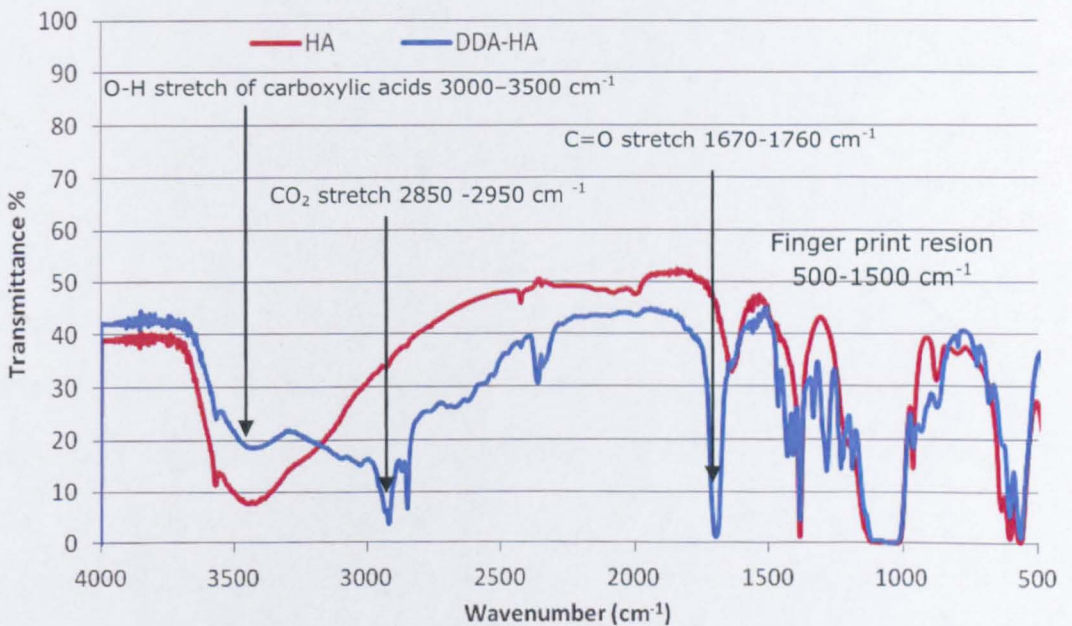


Fig. 7.12: FTIR spectrum of DDA-HA

Again, poly(ethylene-co-AA 15 wt %)-HA and HA showed intense and identical absorption in the the finger print region which is the region to the right-hand side of the diagram (from about 500 to 1500 cm⁻¹).The difference in IR absorption of DDA-HA compared with uncoated HA was correlated the carboxylic group stretch (C=O and O-H stretch) of DDA. DDA-HA showed a decrease in the O-H absorption compared with uncoated HA; as OH groups of HA could be involved into covalent bonding with DDA.

DDA-HA exhibited enhanced levels of IR absorption which can be correlated to C=O stretch. The DDA loading level was determined by TGA. DDA loading level of 27 wt % was reported from TGA profile (Figure 7.13) and Equation 5.1.

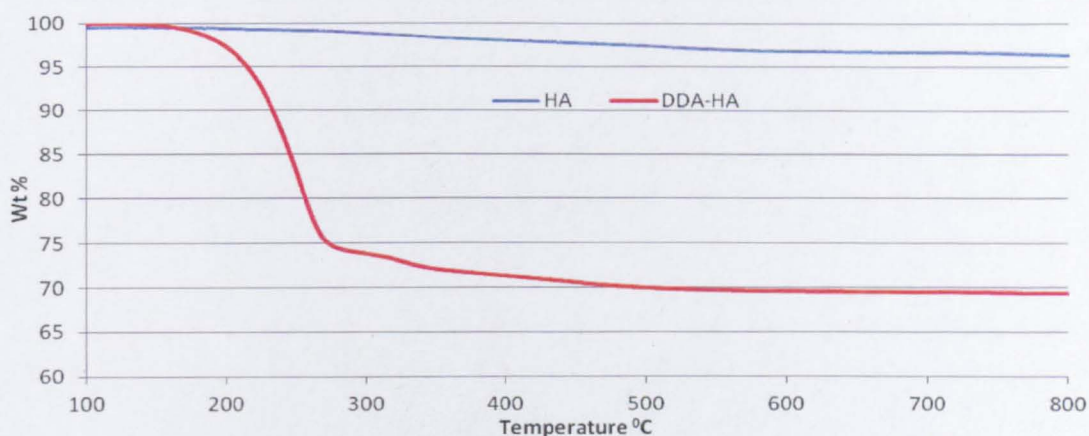


Fig. 7.13: TGA profile of DDA-HA

This high surfactant loading level could be ascribed to the high affinity of DDA to bind to the HA surface. The DDA carboxylic groups could be chemically bonded as they were easily exposed without steric hindrance. This high surfactant loading level might secure HA platelets with uniform interspacing distance; therefore exfoliated HA nanocomposites could be developed.

7.2 Formulation and functionalization of aluminium-oxide-hydroxide ALOOH (AOH)

As mentioned in chapter 2, inorganic hydroxides represent more than 50% of FRs sold globally due to their low cost, low toxicity, and minimum corrosivity (Wilkie and Morgan, 2010). They act as heat sink materials by consuming energy during their thermal decomposition, releasing water, and forming an oxide layer. Therefore they cool down the burning polymer,

dilute the combustion gasses, and shield the polymer under-layers via the formed oxide layers (Pinfa, 2010). The formed oxide layer also absorbs soot leading to low smoke levels. Figure 7.14 shows the endothermic decomposition of the commonly used inorganic hydroxides (i.e. ATH, MDH, and AOH).

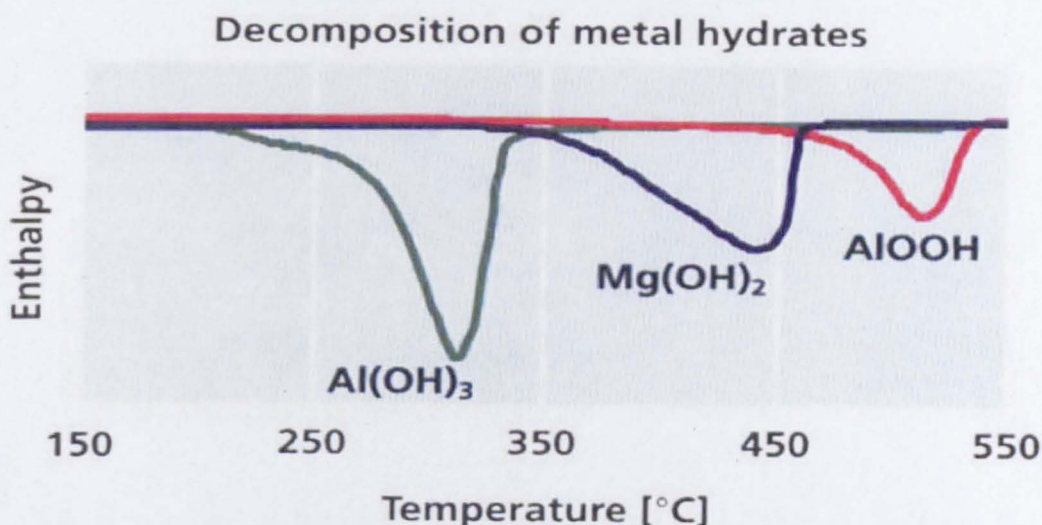


Fig. 7.14 : Endothermic decomposition of metal hydroxides versus temperature, adapted from (Pinfa, 2010)

The relatively low initial decomposition temperature of these compounds restricts their applications e.g. high processing temperatures are certainly a challenge for hydroxides, particularly Aluminium tri-hydroxide (ATH). Whilst Aluminum-oxide-hydroxide (AOH) exhibits the highest thermal stability compared with the other hydroxides (decomposing at 450 °C) isothermal studies showed that ATH starts to decompose at 200 °C. There is also a noted decrease in ATH thermal stability with increasing particle size (Rothon, 2003a). In each case, the decomposition of the hydroxide leads to the formation aluminium oxide. Equation 7.1 shows the endothermic decomposition of AOH.



Eventhough the decomposition of AOH is not as effective as ATH (ΔH of ATH = 1050 kJ Kg⁻¹), it still has potential in mixtures with other FRs due its excellent thermal stability which is why it has become a useful FR material (Katz and Milewski, 1987). The particle size of inorganic hydroxides was reported to have a significant impact on their flammability performance; which can be ascribed to the rate of filler decomposition and/or the formation of more stable ash (Hughes et al., 1993, Fu and Qu, 2004). Improved flammability performance could be achieved at low solid loading level if AOH or modified AOH nanoparticles can be effectively dispersed at the nanoscale level into epoxy resin.

7.2.1 Synthesis of AOH

The main routes for AOH synthesis include reactive precipitation from sodium aluminate solution (Paniias and Krestou, 2007), and batch hydrothermal synthesis from metal alkoxides (Buining et al., 1991). Both approaches are laborious and time consuming; up to 14 processing days are needed to obtain a product. Additionally they show poor control of particle morphology (Buining et al., 1991, Wang et al., 2008). Formulation and functionalization of AOH nanoparticles with controlled morphology via the CHS technique was investigated. Aluminum nitrate nonahydrate ($\text{Al}(\text{NO}_3)_3 \cdot 9\text{H}_2\text{O}$) (Aldrich, 98 %) was employed as the metal precursor, different concentrations of the metal salt feed were investigated (0.05–0.2 M) at a flow rate of 10 ml/min. The hydrothermal conditions were 240 bars and 400 °C (20 ml/min) in the downflow. High concentration of the metal precursor was required to show nanoparticles in the colloidal product.

Figure 7.15 shows the AOH colloid for 0.05 M and 0.2 M metal salt precursor.

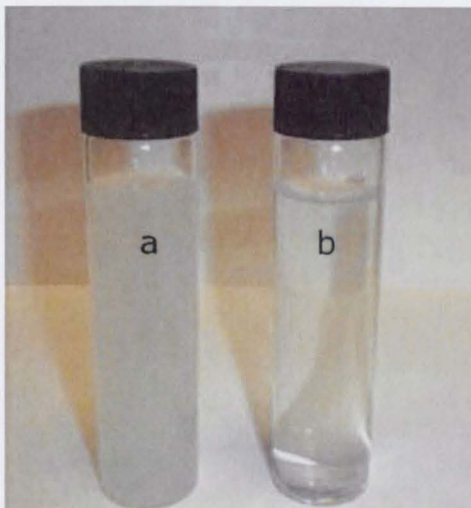


Fig. 7.15: AOH colloid for metal salt precursor (aluminium nitrate nonahydrate) at: (a) 0.2 M, (b) 0.05 M

The formation of AOH follows a very rapid nucleation process, which requires high supersaturation degree. High supersaturation is the key factor for the formation of nano-hydrated mineral gels (Wang et al., 2007a, Panias and Krestou, 2007). This is why a high metal salt concentration (0.2 M) was needed for the formation of nano AOH colloidal gel. The colloidal nanoparticles did not flocculate with time as no visible flocculation was observed over two months time.

The colloidal AOH dispersion was dried in an oven. The crystalline structure of AOH nanoparticles was investigated with XRD. Different crystalline structures were obtained which could be related to the initial precursor (aluminium nitrate). The thermal stability of the dried powder was evaluated by TGA which showed a weight loss of 51.5 wt % after being heated to 100 for 30 minutes. This thermal behaviour could be ascribed to the nitrate counterions (from the initial metal salt precursor). Harvesting (extracting and separating) AOH nanoparticles from the reaction medium is

the next step towards AOH formulation, in order to rise above problems with counterions or residual precursor.

7.2.2 Surface modification of AOH

The extraction of AOH gels from aqueous colloidal dispersions via surface modification was investigated; different surfactant agents were employed for AOH surface modification. The employed surfactants were DDSA, poly(ethylene-co-AA 15 wt %), and amphipathic surfactant commercially known as K500 from Lubrizol. It was not possible to surface modify and extract AOH to the organic phase. AOH did not show a highly crystalline structure, but rather a colloidal gel which was difficult to surface modify and extract to the organic layer.

The use of flocculating agents in hydrated mineral synthesis was reported to act as a filter aid (Gitzen, 1970). Polymeric surfactants with molecular weight higher than 10^6 gm mol⁻¹ are generally used as flocculants (Buchholz and Wilks, 2001). Functional groups that can be used to anchor polymeric surfactants to mineral surfaces include amine, amide, phosphoric, and carboxylic groups (Farrokhpay et al., 2004). Poly(acrylamide-co-acrylic acid) of 5000 000 gm mol⁻¹ was employed as a flocculating agent. Figure 7.16 shows the chemical structure of poly(acrylamide-co-acrylic acid).

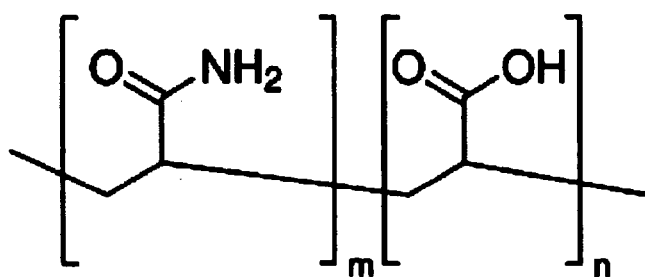


Fig. 7.16: The chemical structure of poly(acrylamide-co-acrylic acid)

7. Formulation and functionalization of nanoparticles with FR properties

0.4 gm of poly(acrylamide-co-AA) was dissolved in 1 litre of water and injected at the capping point (5 ml/min) at the same hydrothermal parameters for AOH synthesis. Poly(acrylamide-co-AA)-AOH nanoparticles flocculated from the water colloid within 30 minutes (Figure 7.17).

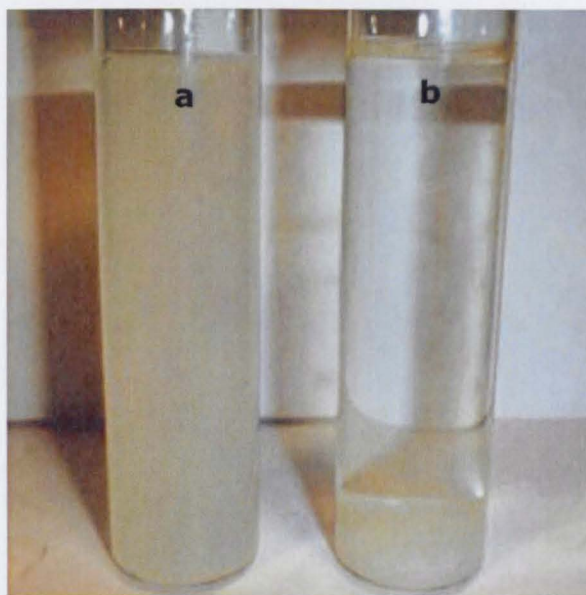


Fig. 7.17: The AOH colloidal gel (a), the flocculated poly(acrylamide-co-AA)-AOH nanoparticles (b)

The attachment of the nanoparticles to the long polymer chains acted to destabilise the colloids and aid precipitation. This offered a potential means to 'harvest' or concentrate the products without having to dry out the product stream completely. The flocculated poly(acrylamide-co-AA)-AOH nanoparticles were separated from the reaction medium and a sample of AOH was re-dispersed in deionized water. The size of poly(acrylamide-co-AA)-AOH was analysed using a TEM. Fibrous poly(acrylamide-co-AA)-AOH nanoparticles of 250 nm length and 8 nm thickness were observed by TEM (Figure 7.18).

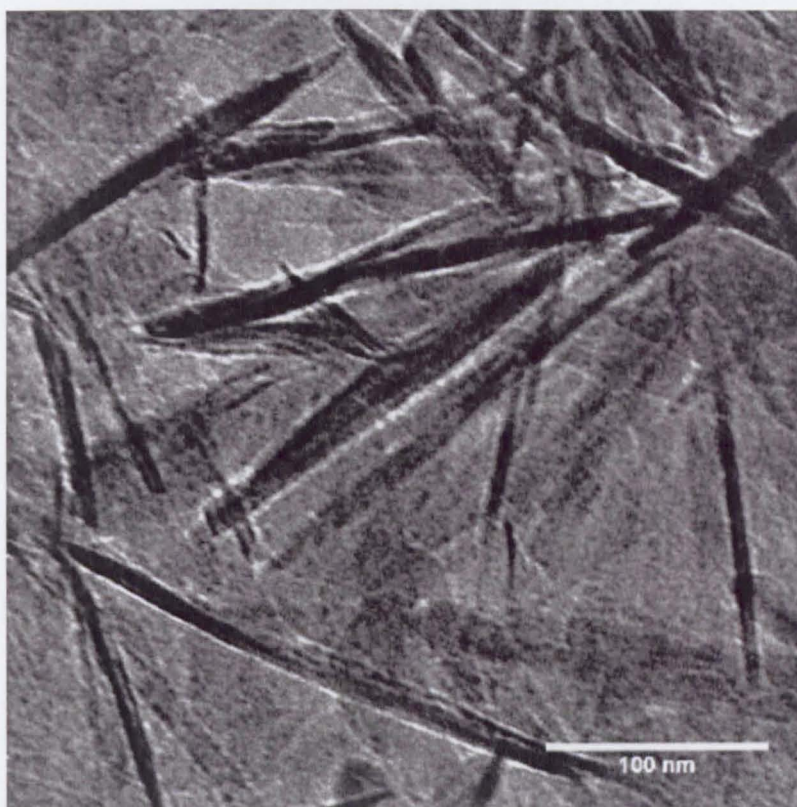


Fig. 7.18: TEM of poly(acrylamide-co-AA)-AOH

The crystalline structure of poly(acrylamide-co-AA)-AOH was investigated with XRD to verify the crystalline phase. A typical XRD diffractogram of poly(acrylamide-co-AA)-AOH is included as Figure 7.19.

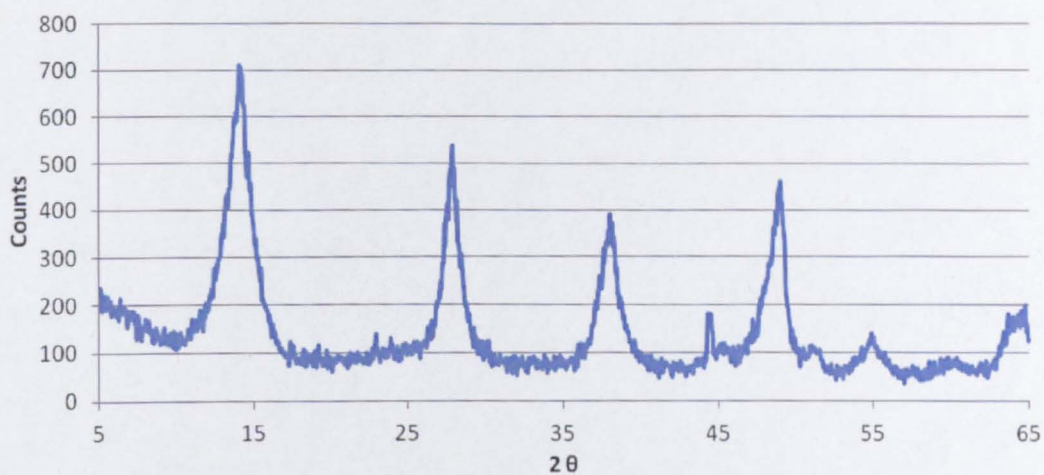


Fig. 7.19: XRD diffractogram for poly(acrylamide-co-AA)-AOH

The sample identification was achieved by comparing the obtained XRD diffractogram with standard data from joint committee on powder

diffraction standards (JCPDS). The XRD pattern corresponded to that of crystalline AlOOH.

7.2.3 The endothermic action of AOH

The thermal stability of AOH nanoparticles and the initiation temperature of its heat sink action were investigated with TGA (Figure 7.20).

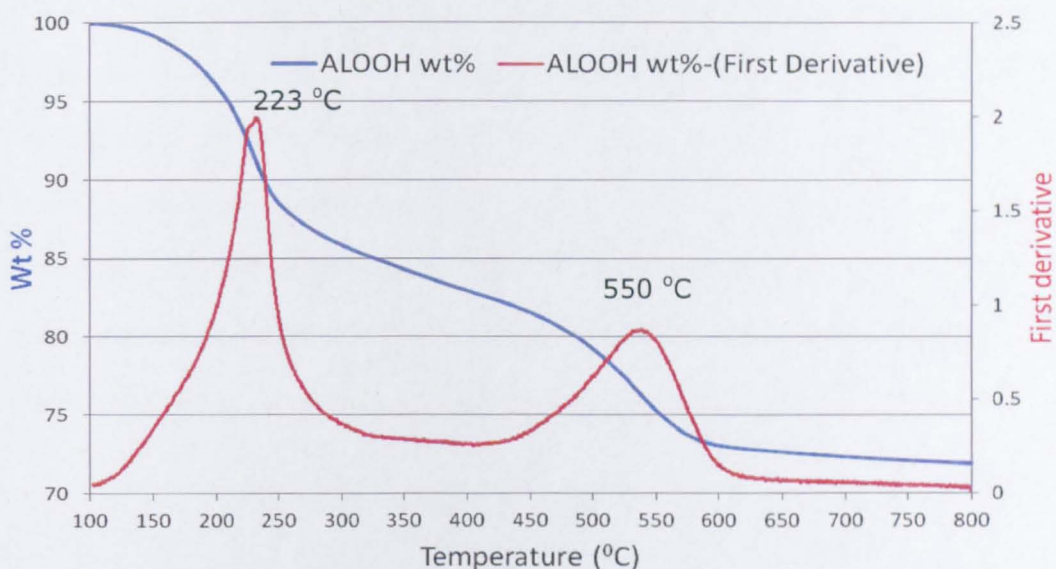


Fig. 7.20: TGA profile of poly(acrylamide-co-AA)-AOH

AOH showed thermal decomposition in two main separated stages at 223 °C and 550 °C. The first decomposition stage at 223 °C was ascribed to the release of water bound to AOH surface and to the release of the flocculating polymer. Buining reported that AOH nanoparticles prepared by hydrothermal treatment contained 0.14 mole of excess H₂O per 1 mole of AOH (Buining et al., 1991). The second decomposition step at 550 °C was ascribed to the endothermic heat sink action of AOH which was described in Figure 7.15 and Equation 7.1.

AOH could effectively produce a dual FR action by releasing the surface water at low decomposition temperature (223 °C) and as a heat sink

material via an endothermic decomposition reaction with the formation of Al_2O_3 at high decomposition temperature (550 °C). In both decomposition stages the released water will cool the burning polymer surface and dilute the surrounding burnable gasses. Additionally the oxide residue (alumina) can act as a barrier protecting the polymeric under-layers from further decomposition.

The endothermic heat action of AOH was evaluated by differential scanning calorimetry (DSC). The sample was heated up from 25 °C to 800 °C; the heating rate was 5 °C/min under a flow of argon at 200 ml/min. The heat flow to or from the sample was recorded as a function of temperature. The DSC profile of AOH is included as Figure 7.21. DSC outcome confirmed that endothermic nature of AOH decomposition, and the ability of the developed material to have a FR action as a heat sink material.

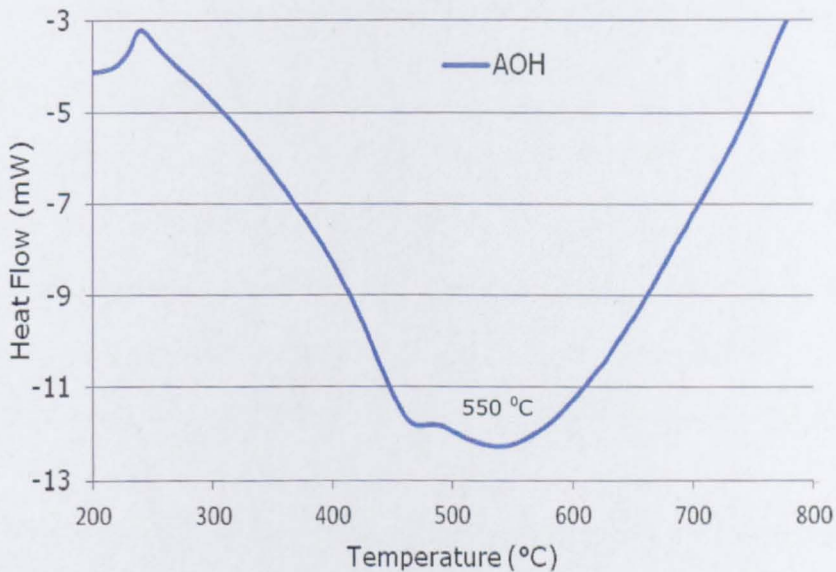


Fig. 7.21: DSC thermogram of AOH

DSC result showed that the two AOH decomposition actions: (a) surface release water at (223 °C) and (b) endothermic decomposition at (550 °C)

7. Formulation and functionalization of nanoparticles with FR properties

were merged together to an intense endothermic heat sink action. The phase transition action of AOH to Al_2O_3 with temperature was investigated with XRD. The tested sample was heated from 200 °C to 700 °C and an XRD scan was performed with each 100 °C increase.

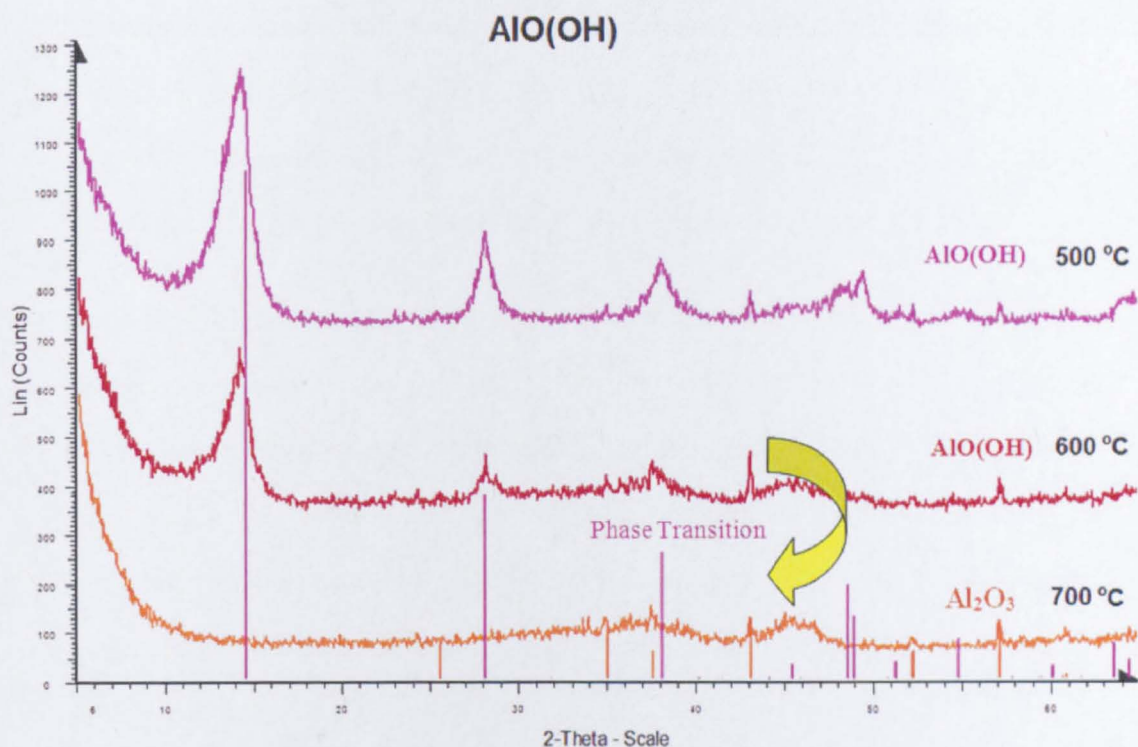


Fig. 7.22: Phase transition of AOH with XRD

XRD results confirmed that AOH began to decompose to Al_2O_3 over the temperature range 500-600 °C; as the characteristic AOH peaks started to decrease. Full crystalline transformation to Al_2O_3 was completed by 700 °C. This finding confirmed the obtained results from TGA and DSC.

7.3 Summary for formulation and functionalization of nanoparticles with flame retardant properties

This Chapter presented a route to formulation and the functionalization of nanoparticles that can deliver a FR action to the polymeric material (i.e. HA and AOH). HA has a phosphorous content of 18.5 % which can provide HA

7. Formulation and functionalization of nanoparticles with FR properties

a phosphorous-based FR action. HA is neither hygroscopic nor soluble in water, and shows high thermal stability. Furthermore, HA was surface modified with different surfactants via covalent bonding. Organic modified HA showed smaller platelet size, and higher surface area than uncoated counterparts. These advantages can enhance HA dispersion into polymeric matrices of different polarities, and diversify HA applications as a nano phosphorous-based FR agent. To the knowledge of the author, this is the first time that HA has been studied as a phosphorous-based FR agent.

AOH was formulated and surface modified by using the CHS technique. AOH exhibited a FR action by consuming energy during thermal decomposition, releasing water, and forming an oxide layer. Thereby it can cool down the burning polymer surface, dilute combustion gasses, and shield the under-layers by the formed oxide. These nano-fire extinguishers were developed in a form that can be easily integrated into the polymeric matrix either as dry powders or as colloidal particles. Chapter 8 investigates the integration and the dispersion of such nanoparticles into epoxy resin.

CHAPTER 8

8. INTEGRATION AND DISPERSION OF

NANOPARTICLES INTO POLYMERIC MATRIX

Dispersing nanomaterials into polymers is not straightforward, not least because polymers tend to be hydrophobic and im-miscible with inorganic nanoadditives (Wilkie and Morgan, 2010); but also the nanoparticle intrinsic high surface energy causes extensive aggregation into the dispersing medium (Zhu et al., 2006, Grate and Abraham, 1991). The successful achievement of polymer nanocomposites (PNs) requires the dispersion of the nanoadditives at the molecular level with minimum aggregation (LeBaron et al., 1999). Most polymers are hydrophobic and as a result they are neither compatible nor miscible with inorganic nanoadditives, because the nanoparticle surface is typically more hydrophilic in nature. These properties may in turn lead to the inability to achieve PNs which possess a high quality nanoscale dispersion of the nanoadditives.

In this Chapter, the dispersion of different nanoparticles of different morphologies ranging from nanospheres (TiO_2), nanoplates ($\text{Ca}_5(\text{OH})(\text{PO}_4)_3$), to nanorods (AlOOH) into epoxy resin was investigated. Nanoparticle surface modification with organic dispersants has been reported to be one way to achieve an increase in the compatibility of the nanoadditive with the polymeric matrix (Moon et al., 2005). In this study, the impact of surface modification on dry nanoparticle dispersion was evaluated by quantifying the dispersion of organic modified nanoparticles to uncoated counterparts at the same solid loadings.

A solvent blending approach to integrate colloidal organic modified nanoparticles into epoxy resin was developed. This approach showed enhanced nanoparticle dispersion compared with the dispersion of dry nanoparticles, as the nanoparticles were kept in dispersion during all processing stages. Furthermore, this approach allowed for the elimination of nanoparticle freeze drying stage that had been required to obtain dry nanopowder. Nanoparticles were found to aggregate while being freeze dried as described in Section 5.3.3.

8.1 The impact of nano-oxide size and shape on dry nanoparticle dispersion

The impact of nano-oxide morphology, size and shape, upon the ability to achieve good quality dispersion was investigated. The dispersion of dry titania nanoparticles, produced by CHS as described in Section 5.1, with particle size of 5.7 nm was compared to the dispersion of commercially purchased titania P25 with a particle size of 25 nm which had been produced by aerosol flame synthesis.

In this study, two different titania loading levels of 5 and 10 wt % were investigated. The nanocomposite formulations were prepared by mechanical mixing for 1 hour followed by vacuum cast as described in Section 4.1. The quality of the nanoparticle dispersion was investigated with SEM and quantified by image analysis using Labview National instruments as described in Section 4.2. Figure 8.1 shows the dispersion of different titania nanoparticles at 5 wt % solid loading level in epoxy resin.

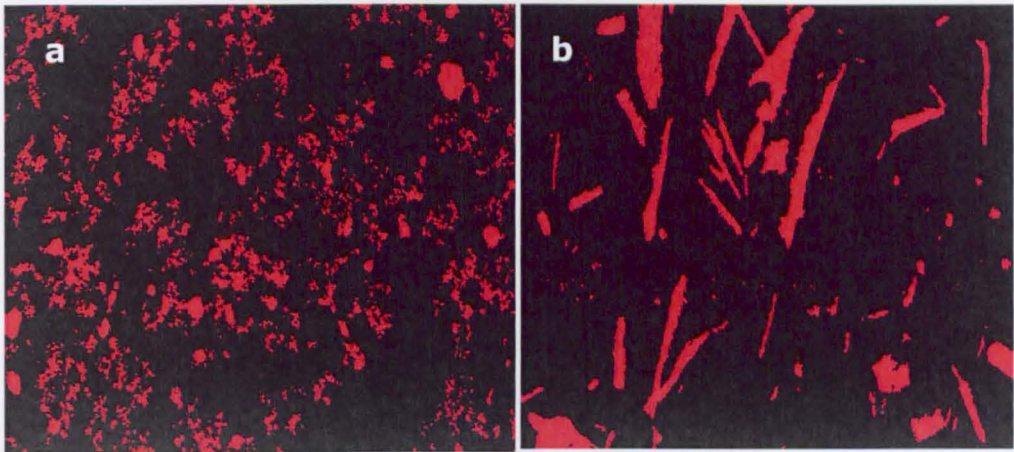


Fig. 8.1: The dispersion of 5 wt %: (a) titania P25, and (b) titania produced by CHS, in epoxy resin

Both types of titania nanoparticles showed an aggregation, the polymer area % of the investigated formulations was calculated by using image analysis (as described in Section 4.2) and equation 4.1. The polymer area was almost the same for both types of titania, within ± 3 % difference. However, titania nanoparticles produced by CHS exhibited bigger aggregate features in the shape of sheets compared with titania P25. This aggregation pattern of titania produced by CHS was ascribed to the freeze drying process and the tendency of the nanoparticles to aggregate to big features while being freeze dried (see Figure 8.2).

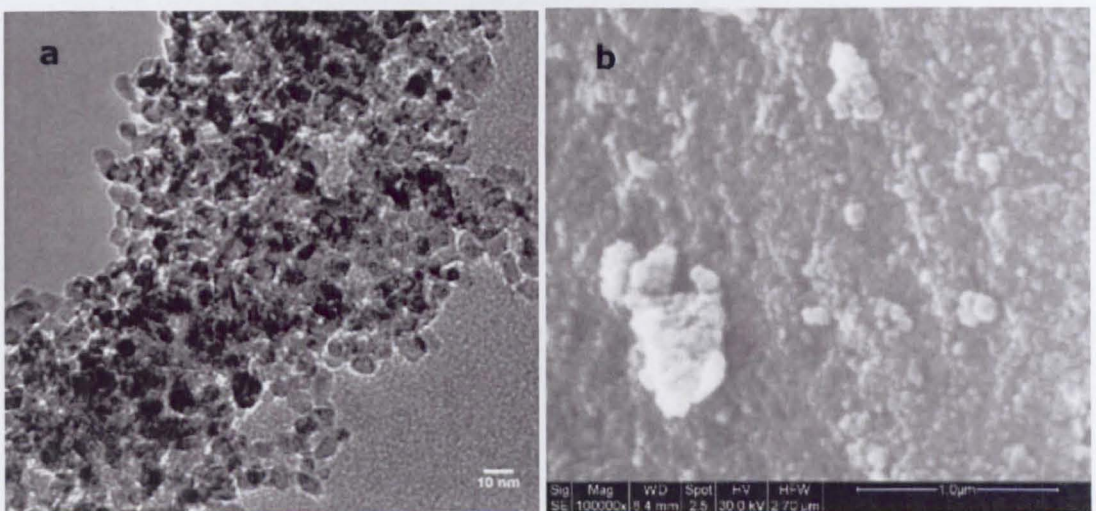


Fig 8.2: The size of titania produce by CHS: (a) in its colloidal state by TEM, (b) dry powder by SEM

8. Integration and dispersion of nanoparticles into polymeric matrix

The conclusion from this experiment is that dried nanoparticles do not readily redisperse into polymers regardless of the nature of their manufacture i.e. dry or wet manufacture. Once dried out, the aggregated nanomaterials will not redisperse effectively.

The Labview (National Instruments) software enabled the quantification of different characteristic dimensions of the thresholded aggregates as described in Section 4.4. The average aggregate perimeter, size, and maximum feret diameter of titania P25 and titania produced by CHS were quantified as included in Table 8.1.

Table 8.1: The quantified aggregate size, perimeter, and maximum feret diameter of titania P25 and titania produced by CHS in epoxy resin

	Titania produced by CHS		Titania P25	
	5 wt %	10 wt %	5 wt %	10 wt %
Average aggregate size (μm)	8	11	2	0.3
Average aggregate perimeter (pixel)	57	46	25	7
Average aggregate maximum feret diameter (pixel)	24	18	9	3

The quantified aggregate morphology confirmed the finding that titania nanoparticles produced by CHS tended to aggregate to bigger clumps with higher aggregate size, perimeter, and maximum feret diameter compared

with P25 when dispersed into epoxy resin; this aggregation pattern was ascribed to the freeze drying process to obtain dry titania nanoparticles.

However aggregated dry nanoparticles inevitably require redispersion using high energy intensive techniques regardless the manufacture method. There are major advantages to any technique that is able to produce and stabilize nanoparticles via surface modification such technique is CHS. Consequently nanoparticle surface modification by CHS might minimize the aggregation and increase the compatibility between the nanoparticles and the dispersing medium.

8.2 The impact of surface modification on dry nano-oxide dispersion

The nanoparticle surface properties can be altered from hydrophilic to hydrophobic via surface modification with an appropriate interfacially active agent. Therefore, in principle by overcoming the hydrophilic/phobic compatibilisation issue, improved compatibility with the polymeric matrix can be achieved. The impact of surface modification on the rate of dispersion of surface modified dry titania nanoparticles was evaluated, by quantifying the dispersion of DDSA-titania developed by using CHS as described in Section 5.2 to commercially obtained titania P25 at 5 and 10 wt % solid loading levels. The nanocomposite formulations were prepared by mechanical mixing and vacuum casting as described in Section 4.1. The nanoparticle dispersion was investigated with SEM and quantified by image analysis as described in Section 4.2. Figure 8.3 shows the dispersion of dry DDSA-titania to titania P25 at 10 wt % solid loading level.

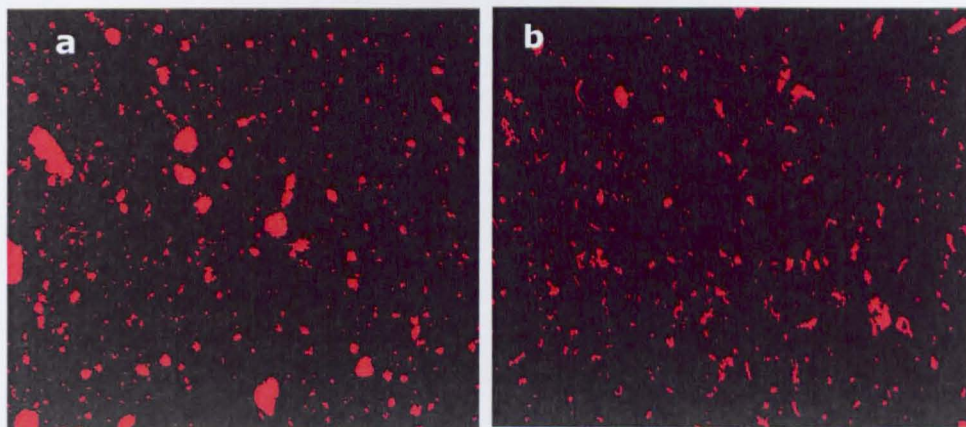


Fig. 8.3: The dispersion of 10 wt %: (a) titania P25, (b) DDSA-titania in epoxy resin

The dry DDSA-titania showed enhanced nanoparticle dispersion in which the formation of aggregated structures was minimized when compared with titania P25. Thus it was concluded that the chosen dispersant (DDSA) had indeed increased the nanoparticle affinity to the organic medium. The polymer area of the investigated formulations was quantified by using image analysis (as described in Section 4.2) and Equation 4.1. Figure 8.4 shows the quantified dispersion (polymer area) of DDSA-titania compared to uncoated titania P25 at different solid loading levels.

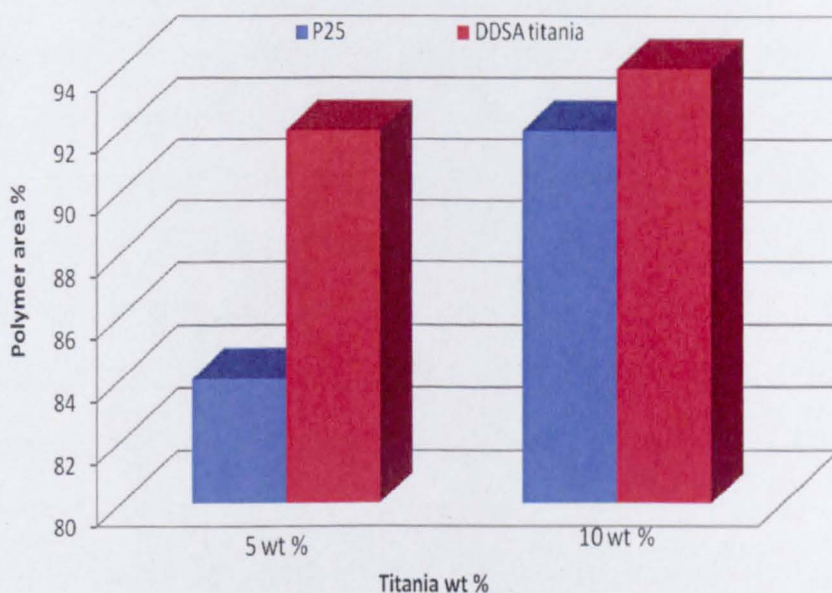


Fig. 8.4: The quantified dispersion of dry DDSA-titania to titania P25

The impact of introducing the DDSA coating on titania dispersion was found to be more effective at a low solid loading levels. This is because, at low nanoparticle loading (i.e. 5 wt %), the induced attrition effect between the nanoparticles could be minimized as a result of the reduced polymer viscosity (as described in Section 4.3); this could minimize the nano-oxide dispersion.

It was concluded that the presence of the organic dispersant on the titania increased the compatibilisation between the nanoadditive and the polymeric matrix and was able to compensate for the reduced attrition effect at low solid loadings and so enhanced the nanoparticle dispersion.

8.3 The impact of the capping solvent on dry DDSA-titania dispersion

The impact of the capping solvent on the dry DDSA-titania dispersion was investigated. DDSA-titania was produced by using ethanol as a capping solvent as described in Section 5.3.3. The dispersion of dry DDSA-titania produced by using ethanol as a capping solvent was quantified to the dispersion of commercially obtained uncoated titania P25 in epoxy resin. The nanocomposite formulations were prepared by mechanical mixing and vacuum cast as described in Section 4.1. The nanoparticle dispersion was investigated with SEM and quantified by using image analysis Labview (National instruments) as described in Section 4.2. Figure 8.5 shows the dispersion of 10 wt % DDSA-titania compared to titania P25 at 10 wt % solid loading level.

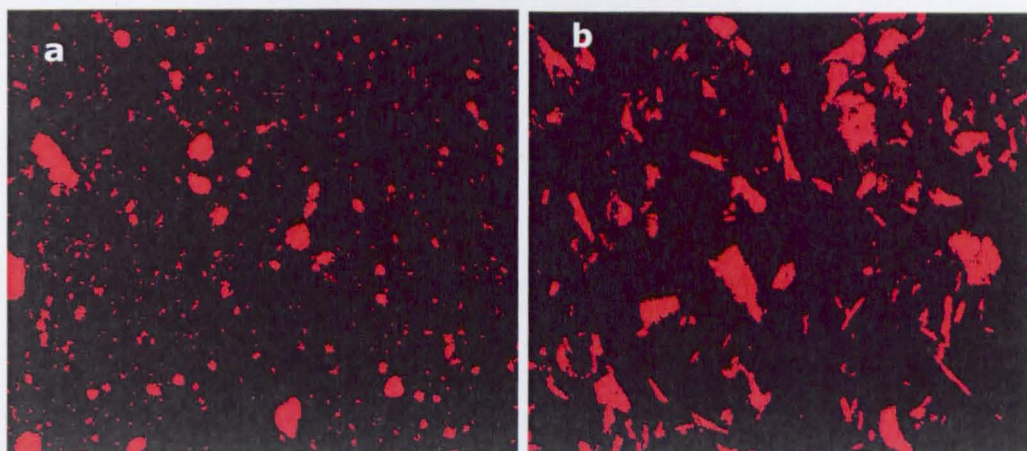


Fig. 8.5: Dispersion of 10 wt %: (a) uncoated titania P25, (b) DDSA-titania (produced by using ethanol as a capping solvent) in epoxy resin

The DDSA-titania synthesized using ethanol capping solvent exhibited a poorer quality dispersion compared to that of titania P25. This was attributed to the fact that the DDSA-titania was collected from the water layer and there was no affinity between the hydrophobic dispersant (DDSA) and the dispersing medium (water). DDSA-titania water system could be classified as a lyophobic colloid. The DDSA (dispersant) hydrocarbon backbone would be repelled by water. This effect could increase the tendency of DDSA aliphatic chains to fold back onto themselves from water and inducing nanoparticle agglomeration, as described in Section 5.3.3 (Figure 5.19). The high affinity between the dispersing agent and the dispersing medium seems to be vital to minimize nanoparticle aggregation; this is why enhanced dispersion was achieved when DDSA-titania was extracted to toluene as described in Section 8.2.

8.4 Direct integration and dispersion of colloidal DDSA-titania into epoxy resin

As the nanoparticles produced by CHS are in the colloidal state; freeze drying process is a route to produce dry nanoparticles. However, freeze

drying is a time consuming process and so might limit the viability of using CHS as a commercial manufacturing route. Additionally, the fact that an organic solvent is involved might also affect the vacuum pumping unit of the freeze drying apparatus on a commercial scale, thus rendering such a process technically impossible. Furthermore, the nanoparticles were found to aggregate and agglomerate while being freeze dried as described in Section 5.2 (Figure 5.20). This was attributed to the fact that nanoparticle might come into direct contact during solvent sublimation.

Therefore, nanocomposite formulation via a solvent blending approach directly utilising the colloidal organic modified nanoparticles (dispersed in organic solvent) was investigated. Adopting this approach would enable the elimination of freeze drying stage and the resulting need to redisperse the aggregated dry nanoparticles into polymeric matrix. There are major advantages of CHS technique as it is able to produce and maintain the nanoparticle in dispersion via surface modification.

To investigate this, DDSA-titania synthesized by CHS (as described in Section 5.2) was extracted to an organic layer of toluene (see Figure 5.9). The organic layer with the colloidal nanoparticles was then separated and centrifuged. As a result of this processing method, toluene with any excess DDSA was separated at the top, DDSA-titania in the middle layer, and water at the bottom. Consequently, the excess liquid layers were removed and the DDSA-titania viscous colloid was collected (see Figure 8.6).

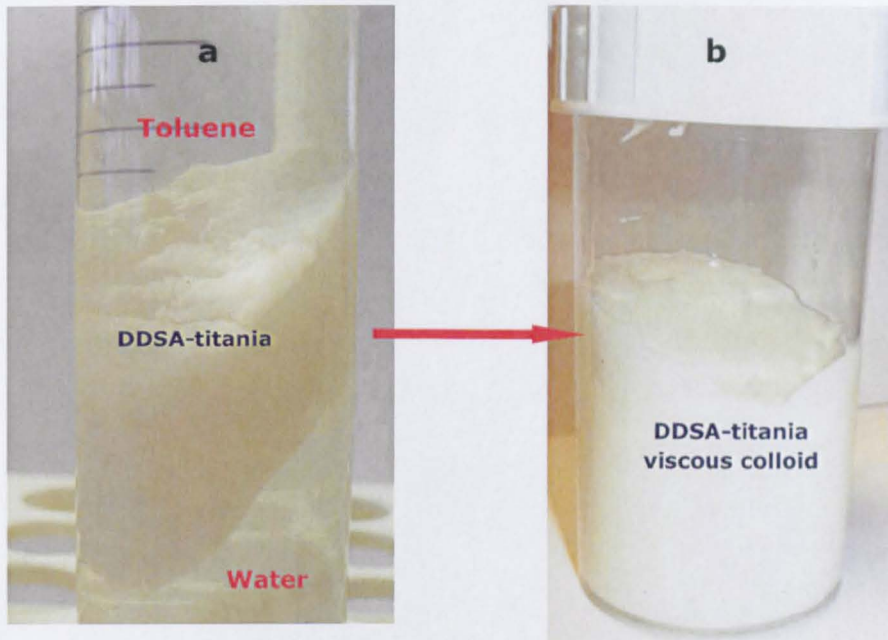


Fig. 8.6: The centrifuged colloidal DDSA-titania (a), the collected DDSA-titania viscous colloid material (b)

The solid loading level of the viscous colloidal DDSA-titania (wt % of DDSA-titania) was evaluated by drying a certain weight of the colloidal sample in the oven to remove excess toluene. The DDSA-titania loading level was found to be 2.5 wt %.

This colloidal material was then used to directly manufacture a composite material. To do this, the appropriate sample weight to provide the required solid loading level of the colloidal DDSA-titania dispersed in toluene (the concentration of which has been defined by the dry weight method discussed above) was weighed into a flask to which epoxy resin was directly introduced and the mixture was mixed using magnetic stirring for 30 minutes to ensure nanoparticle dispersion into epoxy resin. Following this, the sample was left in vacuum oven at 50 °C overnight to remove the excess toluene. Afterwards, the sample was mixed by mechanical mixing for 30 minutes; this mixing regime was required to ensure nanoparticle

8. Integration and dispersion of nanoparticles into polymeric matrix

dispersion and sample homogeneity. The necessary cross linking agent was added at the end of the mixing time. The sample was then cast under vacuum and cured at 60 °C for 48 hours.

The nanoparticle dispersion was investigated with SEM and quantified by image analysis using Labview (national instruments). The dispersion of 10 wt % colloidal DDSA-titania into epoxy resin was quantified and compared with the commercial titania P25 (see Figure 8.7).

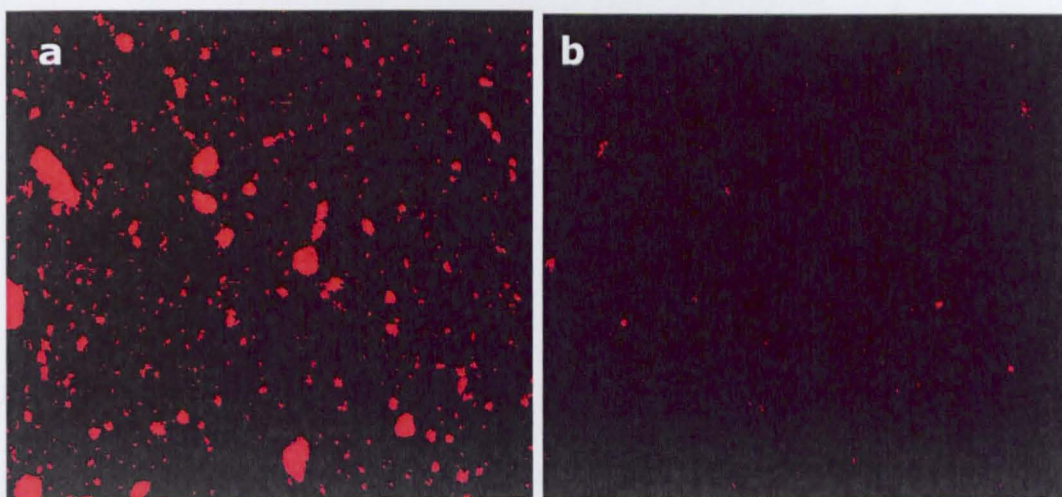


Fig. 8.7: Dispersion of 10 wt %: (a) titania P25, (b) colloidal DDSA-titania, in epoxy resin

It was observed that enhanced nanoparticle dispersions was achieved using this direct mixing approach, as the nanoparticles were maintained as dispersed species in all the processing stages. Colloidal DDSA-titania showed enhanced dispersion with negligible levels of aggregation compared with commercial titania P25 and dry DDSA-titania. Figure 8.8 shows the quantified dispersion (polymer area) for colloidal DDSA-titania to dry DDSA-titania and commercial titania P25 at different solid loading levels.

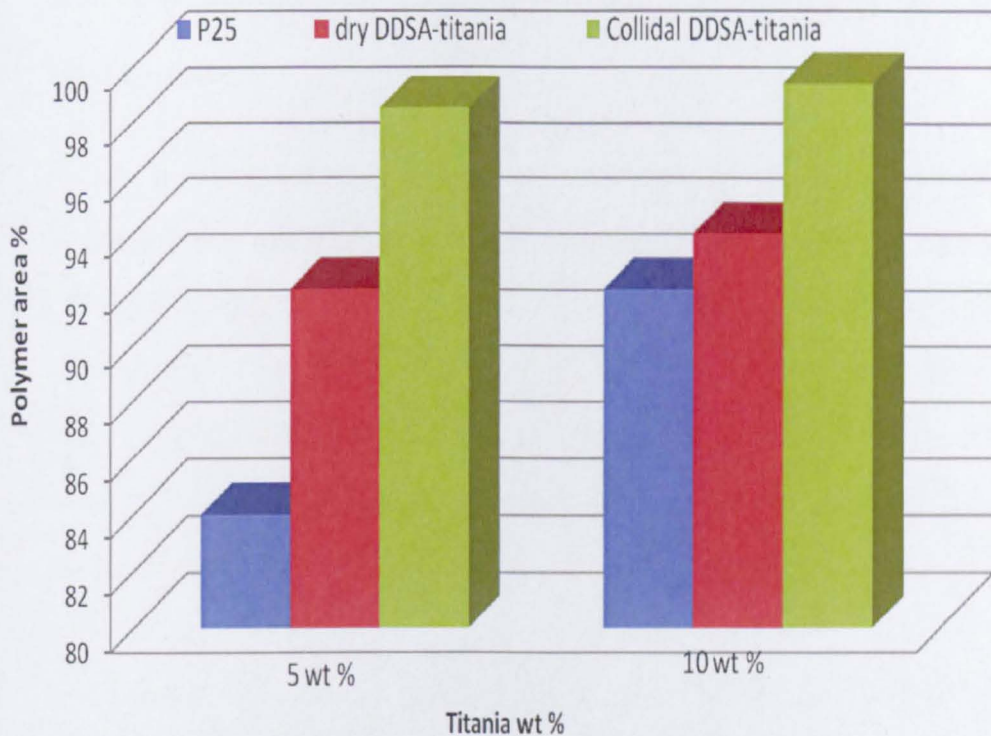


Fig. 8.8: The quantified dispersion of colloidal DDSA-titania to dry DDSA-titania and titania P25

It was concluded that, toluene was a good dispersing medium for DDSA-titania and was also a good solvent for epoxy resin. DDSA-titania had remained well dispersed into epoxy resin while toluene was evaporated slowly. This meant that, throughout the whole solvent blending approach, the nanoparticles were maintained in dispersion until the cross-linking process. Furthermore, this approach eliminated the need for freeze drying process and the problems that are related in achieving a good redispersion of aggregated dry nanoparticles which resulted from the freeze drying process.

8.5 Integration and dispersion of hydroxyapatite into epoxy resin

As has been discussed at length in this thesis, the nanoparticles tend to aggregate and agglomerate in polymeric matrices and act like micron-sized particles rather than nanoparticles (Zheng et al., 2005). In the case of additives which are designed to deliver a FR performance to the overall material, the nanocomposite fire performance is expected to rely on how effective the dispersion of the nanoparticles within the material has been achieved. HA was developed as a nano phosphorous-based FR agent and was surface modified with DDSA using CHS technique as described in Section 7.1. The aim of the current research work is to investigate the dispersion characteristics of dry HA and DDSA-HA into epoxy resin as well as the integration and dispersion of colloidal DDSA-HA in toluene into epoxy resin via solvent blending approach.

8.5.1 Dispersion of dry HA and DDSA-HA nanoparticles in epoxy resin

The dispersion of dry HA nanoparticles in epoxy resin, was investigated with SEM and quantified by image analysis. HA-epoxy nanocomposites, of different HA loading levels of 5 and 10 wt %, were prepared by mechanical mixing and vacuum casting. The impact of DDSA on dry HA dispersion was evaluated; the dispersion of DDSA-HA into epoxy resin was quantified and compared with the dispersion of uncoated HA at the same solid loading levels of 5 and 10 wt % (Figure 8.9).

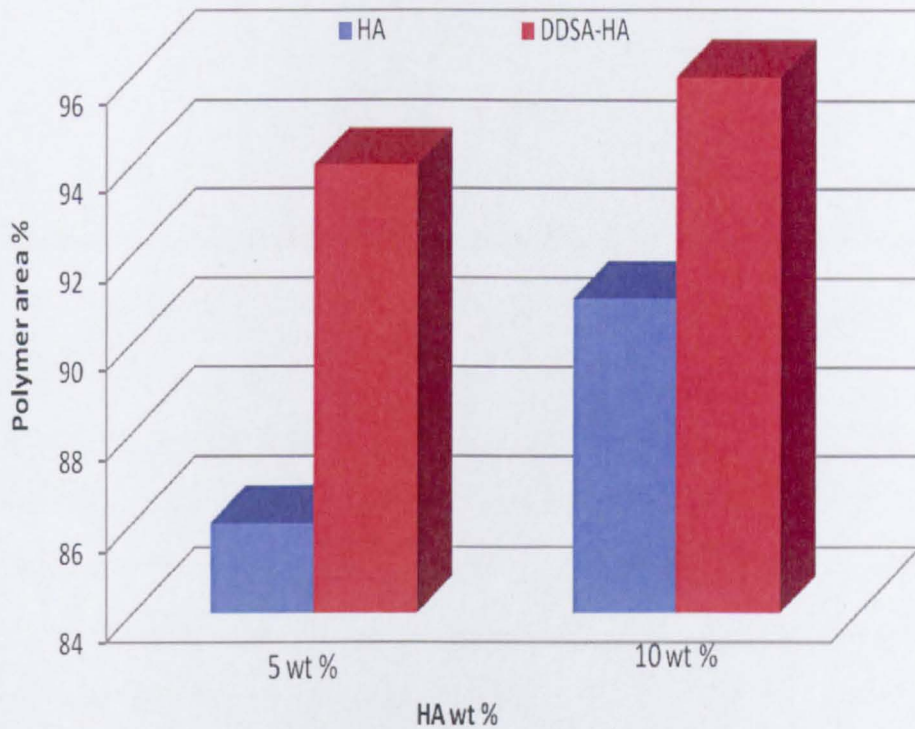


Fig. 8.9: The quantified dispersion of dry HA to DDSA-HA in epoxy resin
 As previously, there was an improvement observed in both the HA and DDSA-HA dispersion with the increase in solid loading level. This improved dispersion was attributed to the induced attrition action between the nanoparticles under the effect of mechanical mixing. Figure 8.10 shows the dispersion of dry DDSA-HA to HA at 5 wt % solid loading level.

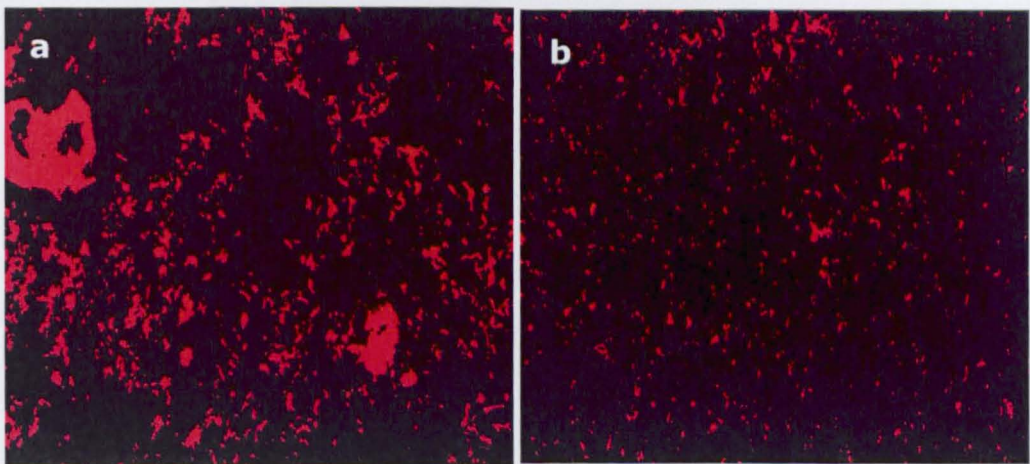


Fig. 8.10: Dispersion of 5 wt %: (a) uncoated HA, (b) DDSA-HA, in epoxy resin

DDSA-HA showed data demonstrated that the dispersant effect was higher at low solid loading level (5 wt %). As before, the presence of the dispersant could compensate for the reduced attrition action between the nanoparticles at this low solid loading level. This enhanced dispersion of DDSA-HA was ascribed to the increased level of surface area retained with the DDSA-HA to that of the uncoated HA. This increase in the surface area was ascribed to the fact that the nanoparticles were surface modified effectively and so they did not agglomerate. As a result, this surface area increase could increase the attrition action between the nanoparticles under mechanical mixing. Furthermore, the high dispersant loading level 7.3 wt % (see Figure 7.6) could improve the compatibility between the HA nanoparticles and the polymeric matrix.

8.5.2 The direct integration and dispersion of colloidal DDSA-HA into epoxy resin

Colloidal DDSA-HA dispersed in toluene was integrated into epoxy resin via solvent blending approach in a similar manner to colloidal DDSA-titania decscribed in Section 8.4. The dispersion of colloidal DDSA-HA in epoxy resin was investigated using SEM and quantified by image analysis compared with the dispersion of dry uncoated HA nanoparticles at 5 and 10 wt % solid loading level. The colloidal DDSA-HA showed enhanced dispersion compared with that of the uncoated HA. Figure 8.11 shows the dispersion of colloidal DDSA-HA to uncoated HA at 10 wt % solid loading level.

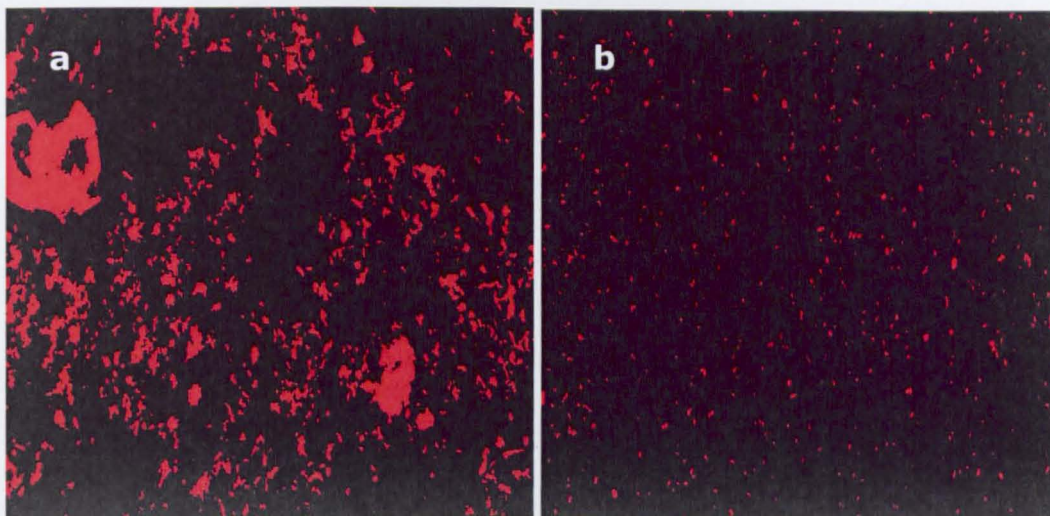


Fig. 8.11: The dispersion of 10 wt %: (a) HA, (b) colloidal DDSA-HA, in epoxy resin

Colloidal DDSA-HA integrated directly into the epoxy resin via solvent blending approach showed enhanced dispersion to uncoated HA; as the nanoparticles were maintained in a good dispersed state over the all processing stages till cross linking.

8.6 Integration and dispersion of poly(acrylamide-co-AA)-AOH into epoxy resin

Colloidal AOH gel was surface modified with poly(acrylamide-co-AA) to flocculate the nanoparticles from their dispersing medium (water) and the flocculated nanoparticles were separated, centrifuged, and freeze dried as described in Section 7.2. The dispersion of the dried AOH nanoparticles into epoxy resin was investigated and AOH/epoxy nanocomposites with solid loading levels 5 and 10 wt % were prepared by mechanical mixing and vacuum cast. Again the nanoparticle dispersion into epoxy resin was investigated with SEM and quantified by image analysis. Figure 8.12 shows

the dispersion of 5 and 10 wt % poly(acrylamide-co-AA)-AOH into epoxy resin.

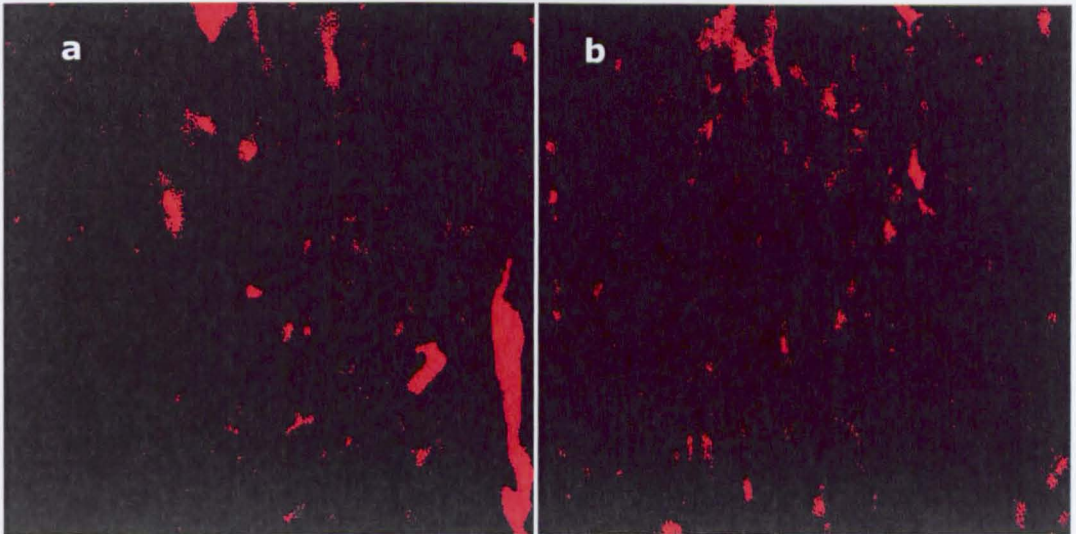


Fig. 8.12: The dispersion of poly(acrylamide-co-AA)-AOH in epoxy resin at:
(a) 5 wt %, (b) 10 wt %

In this case, there was no significant impact of the AOH loading level applied upon the level of dispersion achieved. The polymer areas in both samples were essentially identical ($95\pm 2\%$) for both 5 and 10 wt % AOH. Even though AOH was flocculated from water, it showed enhanced dispersion compared with the dispersion of titania produced CHS and titania P25 as described in Section 8.1. This enhanced dispersion was ascribed to the fact that poly(acrylamide-co-AA) (flocculating agent) has NH_2 groups which are also the key functional groups within the cross linking agent (tri-ethylene tetramine). Therefore, it is believed that the flocculating polymer might be able to integrate the nanoparticles into the polymeric chain via chemical bonding thus appear to increase the compatibility between the nanoparticles and the polymeric matrix.

8.7 Summary of integration and dispersion of nanoparticles into polymeric matrix

Chapter 8 represented the work done to integrate different nanoparticles of different morphological forms ranging from nanospheres (TiO_2), nanoplates ($\text{Ca}_5(\text{OH})(\text{PO}_4)_3$), to nanorods ($\text{AlO}(\text{OH})$) into epoxy resin. Nano-oxide morphology (size and shape) did not show a significant impact on their dispersion. However, enhanced nanoparticle dispersion was achieved via surface modification. It was also shown that some surfactants might be able to integrate the nanoparticles into polymeric matrix via covalent bonding to the polymeric matrix.

A solvent blending approach to integrate colloidal organic modified nanoparticles directly into the polymeric matrix was developed. This approach was shown to enhance the nanoparticle dispersion compared with the dispersion by using dry nanoparticles. Furthermore, this approach enabled the freeze drying and the associated redispersion of aggregated dry nanoparticles into polymeric matrix to be eliminated. Effective nanoparticle dispersions should in principle enhance the mechanical, thermal, and flame resistance of the polymeric matrix via the strong interaction between the nanoparticles and the polymeric chains; as will be discussed in Chapter 9.

CHAPTER 9

9. IMPACT OF NANOPARTICLES ON POLYMERIC

MATRIX

It has been suggested that the incorporation of nanoparticles into polymeric matrices could result in improved mechanical, thermal, and flammability properties when compared with conventional filled polymers (Vaia et al., 1999, Wilkie and Morgan, 2010). Through nanoscale dispersion, nanocomposites could have improved mechanical barrier and rheological properties under firing conditions with minimized flammable dripping and reduced heat release rate (Mailhot et al., 2003). This can be accredited to the strong interaction between the polymeric chains and the nanoparticles (Laoutid et al., 2009).

Chapter 9 investigated the impact of nanoparticle morphology on mechanical, thermal, and flame resistance properties of epoxy resin. Epoxy nanocomposites based on nanomaterials in the form of nanospheres, nanoplates, and nanorods were tested and compared to virgin epoxy. The mechanical properties of epoxy nanocomposites were evaluated by a mechanical compressive test, as described in Section 3.4.1. Thermal stability was evaluated by TGA as described in Section 3.4.2. Nanocomposite stability during heating was quantified using video footage. The tested samples initial decomposition and dimensional stability was assessed while being heated in an oven at a controlled rate.

The direct flame resistance of several nanocomposites was evaluated using a Bunsen test with video footage and image analysis. Through image

analysis of the video footage, it was possible to quantify direct flame resistance from initial ignition, flame shape and size, flammable dripping, and time until self-extinguish. To the knowledge of the author, this is the first time image analysis has been used to quantify direct flame resistance in a repeatable fashion.

9.1 Mechanical properties of epoxy nanocomposites

9.1.1 Mechanical properties of titania-epoxy nanocomposites

The impact of titania P25 nanoparticles on epoxy mechanical properties was evaluated by a mechanical compressive test. Titania-epoxy nanocomposites of different titania loading levels of 5, 10, and 15 wt % were prepared by mechanical mixing with heating at 80 °C for 1 hour followed by vacuum casting. The compressive stress-strain response of titania-epoxy nanocomposites was evaluated and compared with virgin epoxy using universal mechanical testing machine as described in Section 3.4.1. Figure 9.1 shows the compressive stress-strain response of titania-epoxy nanocomposites to virgin epoxy. The nanocomposite formulations showed enhanced compressive stress-strain response after the maximum compressive stress (enhanced mechanical failure resistance) compared with virgin epoxy.

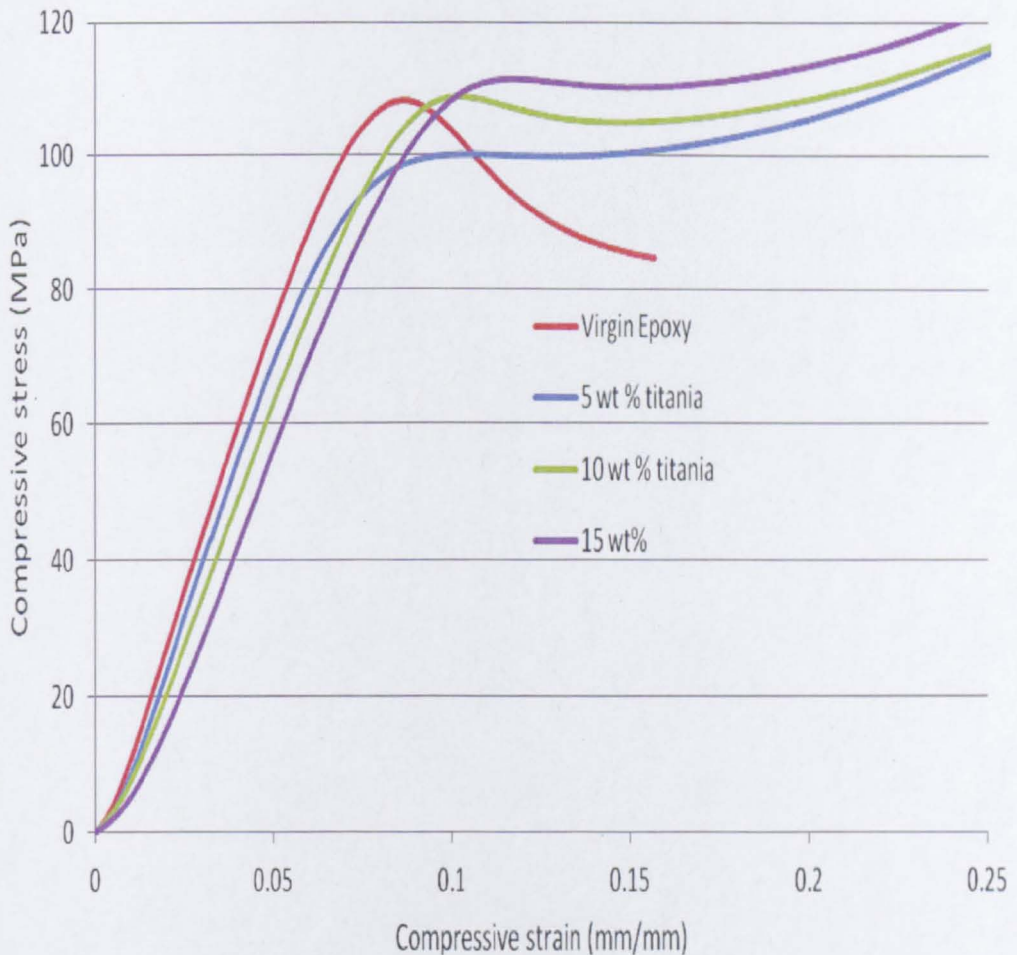


Fig. 9.1: Compressive stress-strain response of titania-epoxy nanocomposites (P25 TiO_2)

This enhanced mechanical performance of titania/epoxy nanocomposites was attributed to the restriction of the polymeric chain mobility under compressive stress by the nanoparticles. Two samples of each formulation were prepared and tested. Table 9.1 shows the mean values of the compressive mechanical parameters of all investigated formulations.

Table 9.1: Compressive mechanical properties of titania-epoxy nanocomposites

Sample	Compressive stress at yield (offset 0.2%) (MPa)	Compressive strain at yield (offset 0.2%) (%)	Compressive stress at max. comp. load (MPa)	Compressive strain at max. comp. load (%)
Normal Epoxy	88.1±0.5	5.8±0.1	107.9±0.5	8.8±0.2
5 wt % titania	85.1±6.5	6.8±1.0	109.1±8.6	11.0±1.0
10 wt % titania	84.3±6.9	6.4±1.2	105.1±3.9	9.0±1.0
15 wt % titania	85.9±2.5	6.4±1.1	106.0±5.7	9.9±2.2

It was found that titania nanoparticles did not badly impact the compressive stress and the compressive strain values of the virgin polymer; this was ascribed to the achievement of a compact nanocomposite structure with minimum entrapped air bubbles, as described in Section 4.1. However, titania nanoparticles enhanced the mechanical resistance of virgin epoxy at failure; as higher stress-strain response was achieved after maximum compressive stress. This enhanced mechanical failure resistance was ascribed to the strong interaction between TiO₂ nanoparticles and the polymeric chains.

9.1.2 Mechanical properties of HA-epoxy nanocomposites

The impact of HA nanoparticles (produced by CHS as described in Section 7.1) in the shape of platelets (5 µm length and 2 µm width) on epoxy

mechanical properties was evaluated by mechanical compressive test. HA-epoxy nanocomposites of different HA loading levels 5 and 10 wt %, were prepared by mechanical mixing for 1 hour followed by vacuum casting. The compressive stress-strain response of HA-epoxy nanocomposites was evaluated and compared with those of virgin epoxy (Figure 9.2).

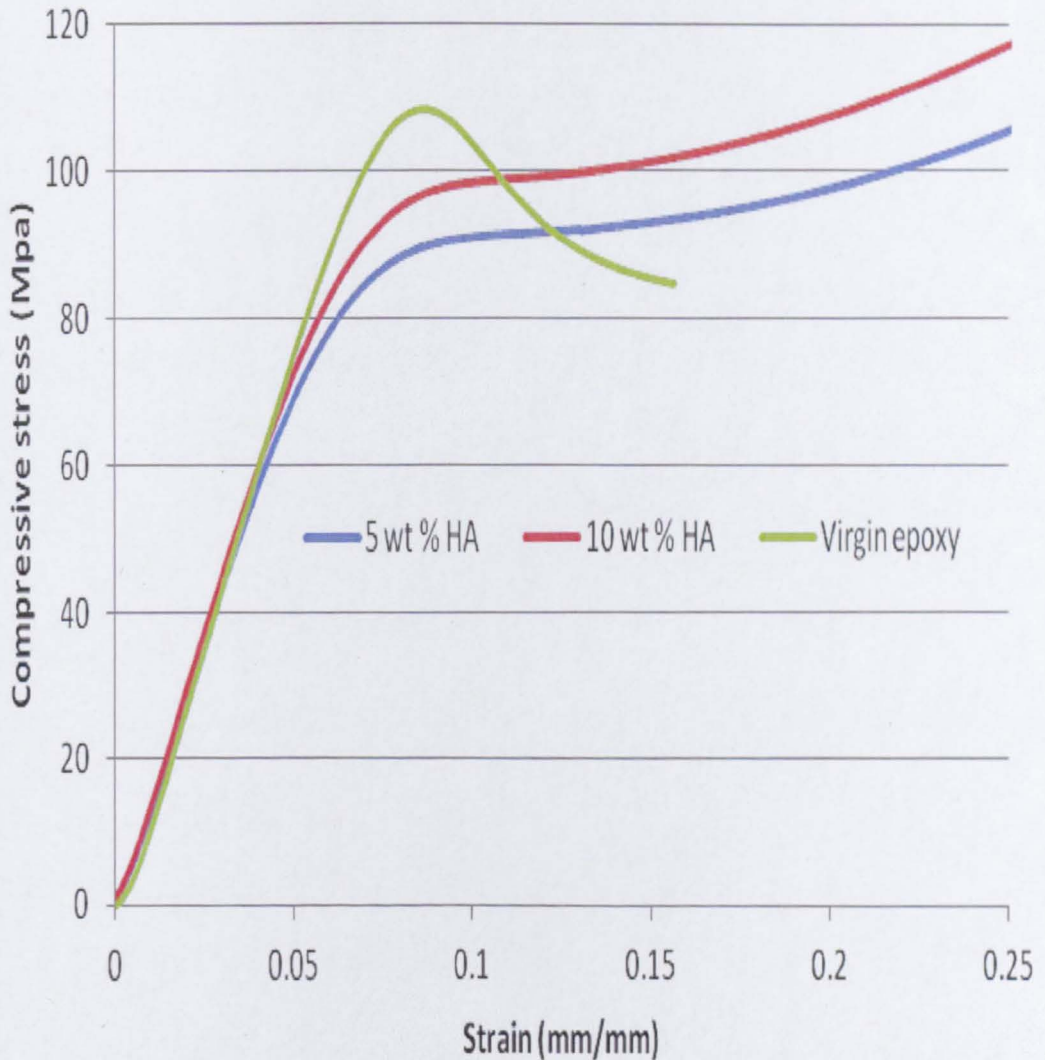


Fig. 9.2: The compressive stress-strain response of HA-epoxy nanocomposites

HA-epoxy nanocomposites showed enhanced compressive stress-strain response after maximum compressive stress (enhanced mechanical failure resistance) compared with virgin epoxy. This improved mechanical

behaviour was correlated to the strong interaction between the HA platelets and the polymeric chains; as HA nanoparticles have hydroxyl surface functional group which could integrate the nanoparticle into the polymeric chains by either or both hydrogen bonding to the polymer chains or chemical bonding by inducing ring opening of epoxy resin as described in Section 4.1 (Figure 4.1) (Ravve, 1995). However, HA-epoxy nanocomposites showed lower yield stress and yield strain compared with virgin epoxy; this could be a result of entrapped air bubbles that were introduced during the mixing process. HA-epoxy nanocomposites showed an increased viscosity during processing, hence increasing the amount of entrapped air bubbles (also seen by SEM). Furthermore, HA prevented the heat generated during cross linking from being dissipated; the accumulated heat rapidly increased the cross linking rate. One solution to this problem would be to use HA at low solid loading levels, say 2.5 wt %, to minimize the entrapped air bubbles, the increased viscosity, and reduce the accumulated heat during cross linking.

9.1.3 Mechanical properties of AOH-epoxy nanocomposites

The impact of AOH nanoparticles in the shape of nanorods of 250 nm length and 8 nm thicknesses on epoxy mechanical properties was evaluated by a mechanical compressive test. AOH-epoxy nanocomposites of different AOH loading levels 2.5, 5 and 10 wt % were prepared by mechanical mixing and vacuum casting. The mechanical properties of the prepared formulations were evaluated by mechanical compressive testing. Figure 9.3 shows the compressive stress-strain response of AOH-epoxy nanocomposites compared with virgin epoxy.

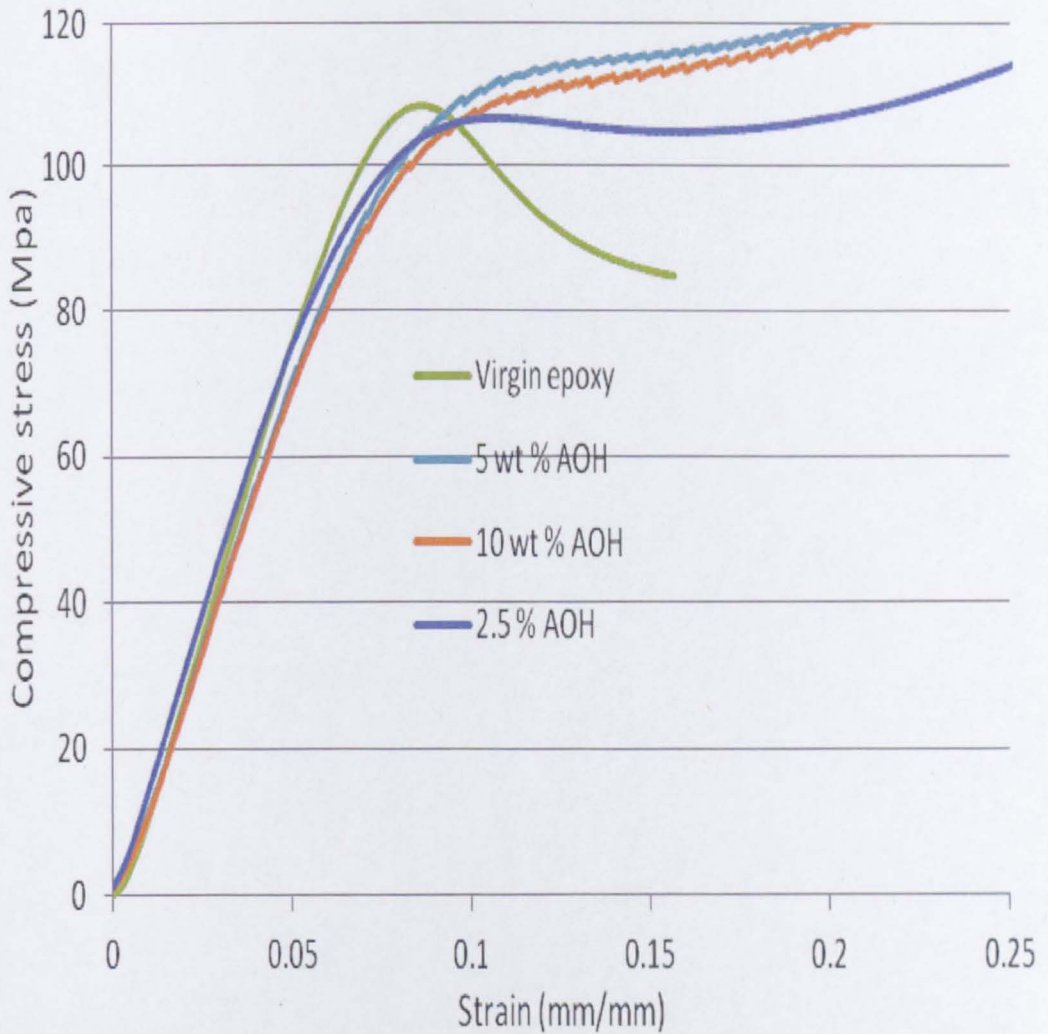


Fig. 9.3: The mechanical properties of AOH-epoxy nanocomposites

AOH-epoxy nanocomposites showed enhanced compressive stress-strain response after maximum compressive stress (enhanced mechanical failure resistance) compared with virgin epoxy. This enhanced mechanical behaviour was correlated to the strong interaction between AOH nanorods and epoxy resin. The AOH colloidal gel was flocculated with poly(acrylamide-co-AA) which has NH_2 groups which are also the key functional groups within the cross linking agent (tri-ethylene tetramine). This reactive surface coating could have a role to increase the interaction and the compatibility between AOH nanoparticles and the polymeric matrix.

9.2 Thermal stability of titania-epoxy nanocomposite

It was reported that nanoparticles can improve the hosting polymer rheology under heating and can improve the polymer viscosity in the molten state (Fu and Qu, 2004). The synergism between nanoparticles and polymeric matrix can result in improved flammability performance with minimal heat released as a result of the induced insulating barrier and the enhanced viscosity (Horrocks and Price, 2008).

In this research work, the impact of titania P25 nanoparticles on epoxy thermal stability was evaluated with TGA, as described in Section 3.4.2. Titania-epoxy nanocomposites of different titania loading levels 1-30 wt % were prepared by mechanical mixing with heating at 80 °C and vacuum casting. Figure 9.4 shows the TGA profile of titania-epoxy nanocomposites compared with virgin epoxy.

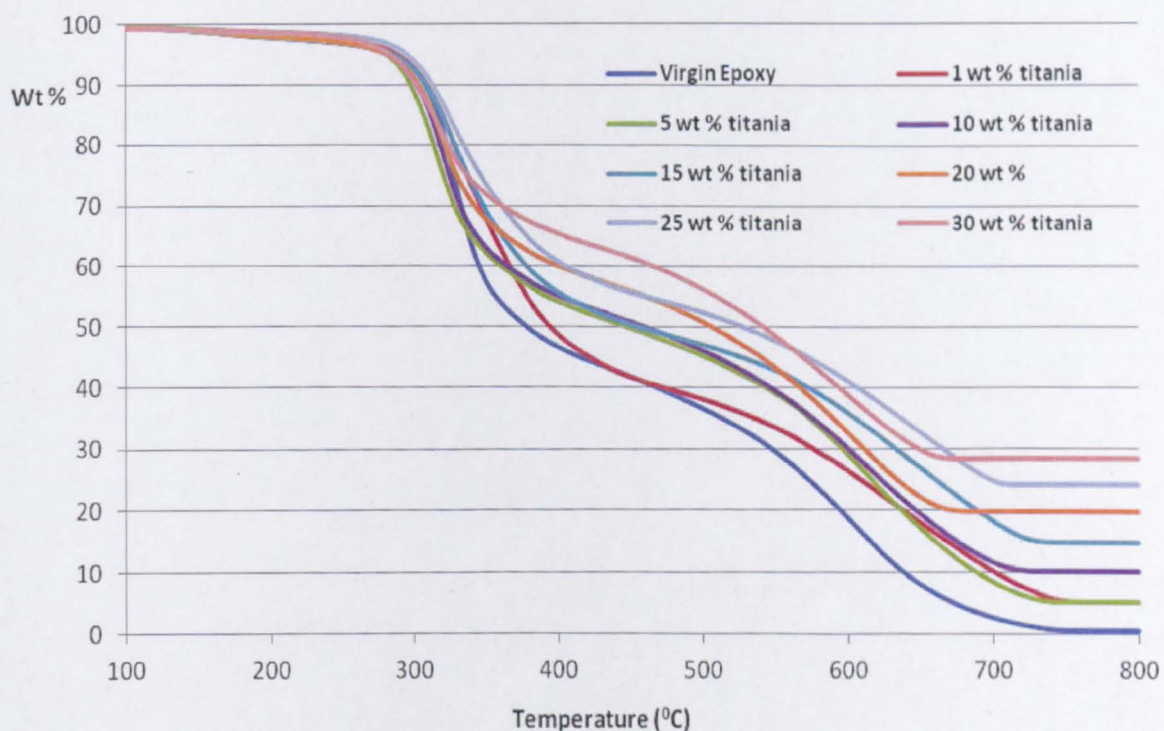


Fig. 9.4: TGA profile for titania-epoxy nanocomposites

9. Impact of nanoparticles onto polymeric matrix

Titania/epoxy thermal decomposition took place in three separate steps (Figure 9.5a). This is clearer from a dW/dt plot rather than a simple weight loss profile. An initial small weight loss around 140 °C, is consistent with all samples. The main peak (referring to onset pyrolysis due to dehydration and dehydrogenation reactions) is at 320 °C, which is consistent with all samples although the width of this peak appears to be dependant on the weight loading of the TiO_2 . Figure 9.5b shows that the introduction of 1 wt% TiO_2 increases the width of this peak i.e. widening the temperature range required for the pyrolysis of the more volatile organics to occur. The final, broader, combustion peak (refereeing to combustion and chain scission reactions) occurs at 580 °C.

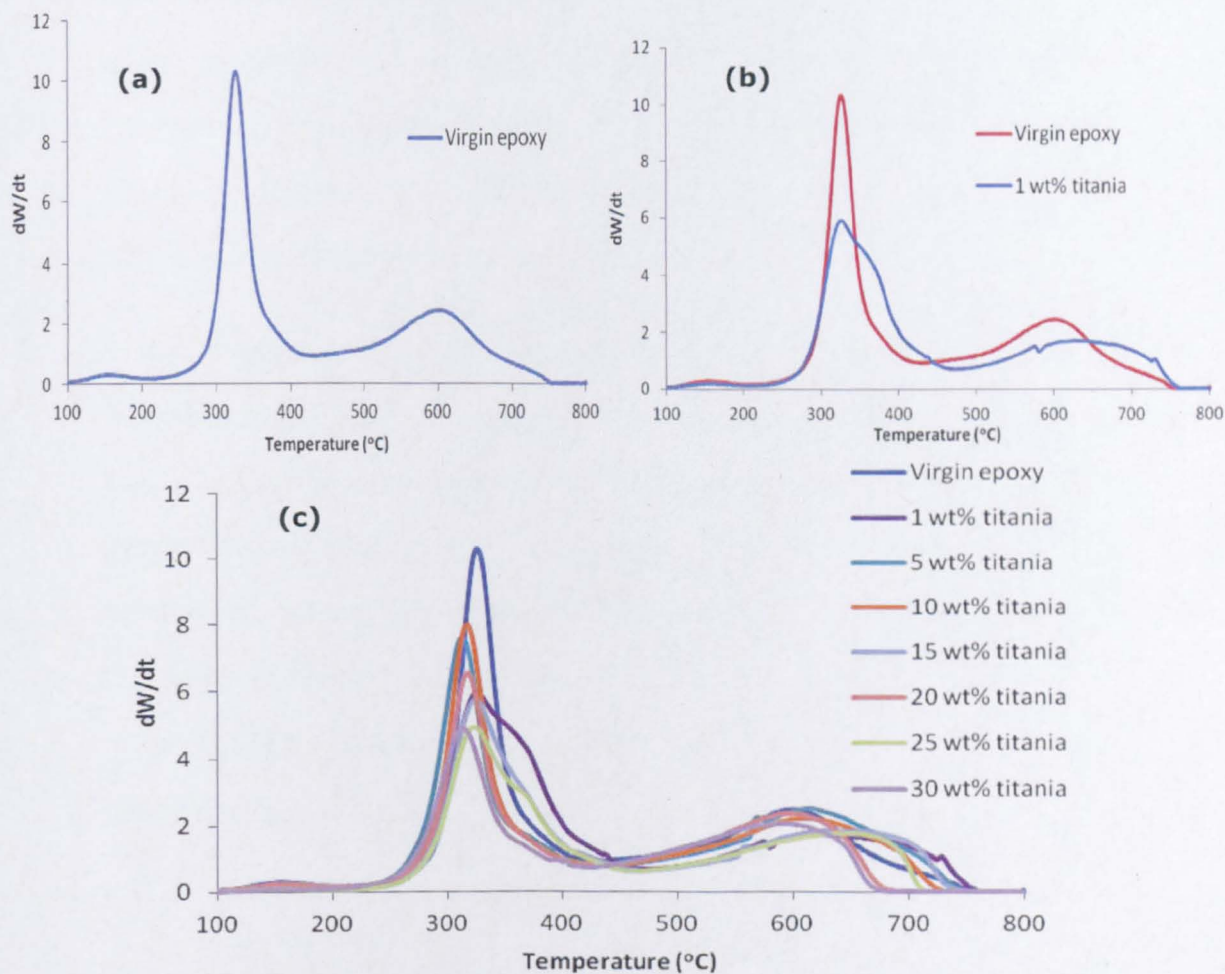


Fig. 9.5: The dW/dt profiles for: (a) virgin epoxy, (b) virgin epoxy and the 1% TiO_2 , (c) all the composite samples

In order to really see a positive affect from the addition of nanoparticles, one would expect to a shift in the peak positions rather than just a peak broadening (Figure 9.5c) i.e. if the onset of pyrolysis and then combustion is to be delayed through the addition of a nanomaterial, then peak positions should move to higher temperatures from the virgin epoxy values of 320°C and 580°C. Whilst there is some deformation of the peaks, there is clearly no 'enhanced' flame retardant effect.

9.2.1 The impact of DDSA surfactant on epoxy nanocomposite thermal stability

Surface modified nanoparticles showed enhanced dispersion into epoxy resin compared with uncoated counterparts. However, it would be counterproductive to use surfactants if it is less thermally stable, not least because it may induce degradation during processing or at early fire stages (Gilman et al., 2002, Lewin et al., 2006).

Titania nanoparticles were surface modified with DDSA using CHS as described in Section 5.2. Consequently, the impact of DDSA dispersant on epoxy nanocomposite thermal stability was investigated; (DDSA-titania)-epoxy nanocomposite of 10 wt % solid loading level was prepared by mechanical mixing and vacuum casting. The thermal stability of the prepared formulation was investigated with TGA. Figure 9.6 shows the TGA profile of (DDSA-titania)-epoxy to virgin epoxy and uncoated titania/epoxy nanocomposite.

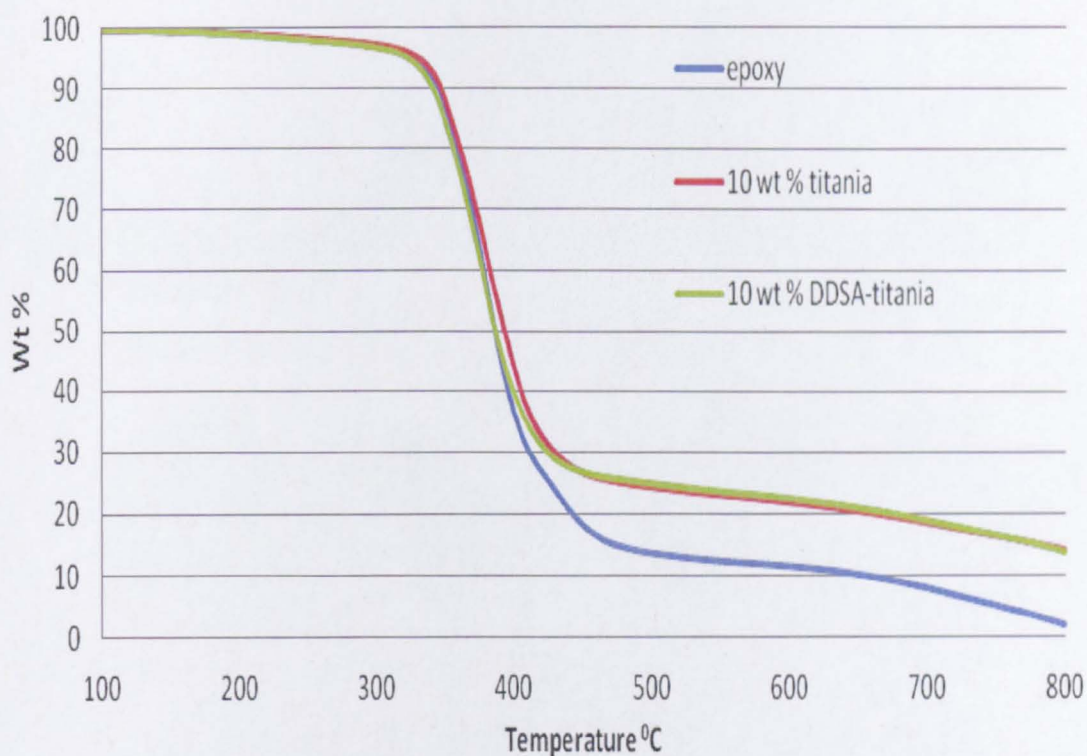


Fig. 9.6: The impact of DDSA on epoxy nanocomposite thermal stability

DDSA did not minimize the initial decomposition temperature of epoxy nanocomposite to virgin epoxy. It can be concluded that the introduction of DDSA doesn't affect the thermal stability of the composite.

9.3 Changes in titania-epoxy nanocomposite structure as a result of heating

The impact of titania nanoparticles on epoxy structural integrity under heating was investigated. Titania-epoxy nanocomposites of different titania P25 loading levels 5, 10, and 15 wt % were prepared in the shape of cylinders of 30 mm diameter and 12 mm height. The samples were heated in a muffle furnace at 500 °C for 5 minutes. The morphological change of titania-epoxy nanocomposites was evaluated by visual inspection of the tested sample compared with virgin epoxy (Figure 9.7).



Fig. 9.7: The morphological evolution of virgin epoxy and epoxy nanocomposite with 10 wt % titania

The virgin epoxy sample structure was severely damaged and showed burning with flame. The epoxy nanocomposite with 10 wt % titania showed enhanced structural integrity compared with virgin epoxy. It retained some of its original shape after thermo-oxidative degradation for 5 minutes. The tested sample weight loss percentage was investigated as an evaluating parameter but it did not give representative results; as the tested sample might show severe structural damage with minimum weight loss percentage.

9.3.1 Quantifying titania-epoxy nanocomposite structural integrity under heating

An approach to visualize and to quantify the nanocomposite thermal stability and structural integrity under heating was developed. In this approach, a cylindrical sample of 10 mm diameter and 10 mm length was

heated at controlled rate (10 °C/min) in an oven where a video camera captured a set of frames. A frame was captured with each °C increase. The captured frames were processed to investigate the tested sample's decomposition, dimensionality, and structural integrity with temperature.

The structural integrity of titania-epoxy nanocomposites, of different titania loading levels 5, 10, and 15 wt %, was investigated by recording the tested sample dimensions with oven temperature. Figure 9.8 shows the structural integrity under heating effect of titania-epoxy nanocomposites compared with virgin epoxy. Virgin epoxy showed initial decomposition at 250 °C; titania-epoxy nanocomposites of titania loading level 10-15 wt % showed initial decomposition at 275 °C with more stable dimensionality and structural integrity compared with virgin epoxy.

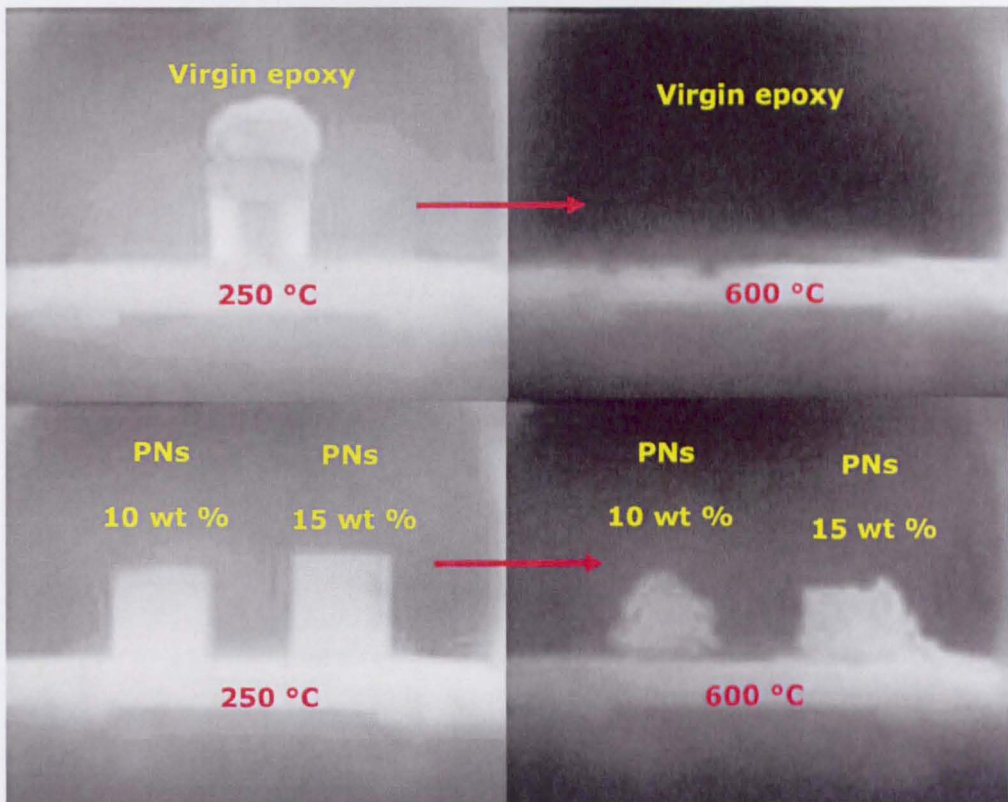


Fig. 9.8: Structural integrity of titania-epoxy nanocomposites to virgin epoxy under heating

This enhanced thermal stability and structural integrity of titania-epoxy nanocomposite was correlated to the strong interaction between the nano-oxides and the polymer chains. The tested sample height was measured with temperature. The relative height which is the ratio of the sample height L to its initial height L_0 (L/L_0), was employed as an evaluating parameter of the dimensional stability with temperature (Cheng Heng Pang, 2013). Figure 9.9 shows the dimensional stability under heating of titania-epoxy nanocomposites to virgin epoxy.

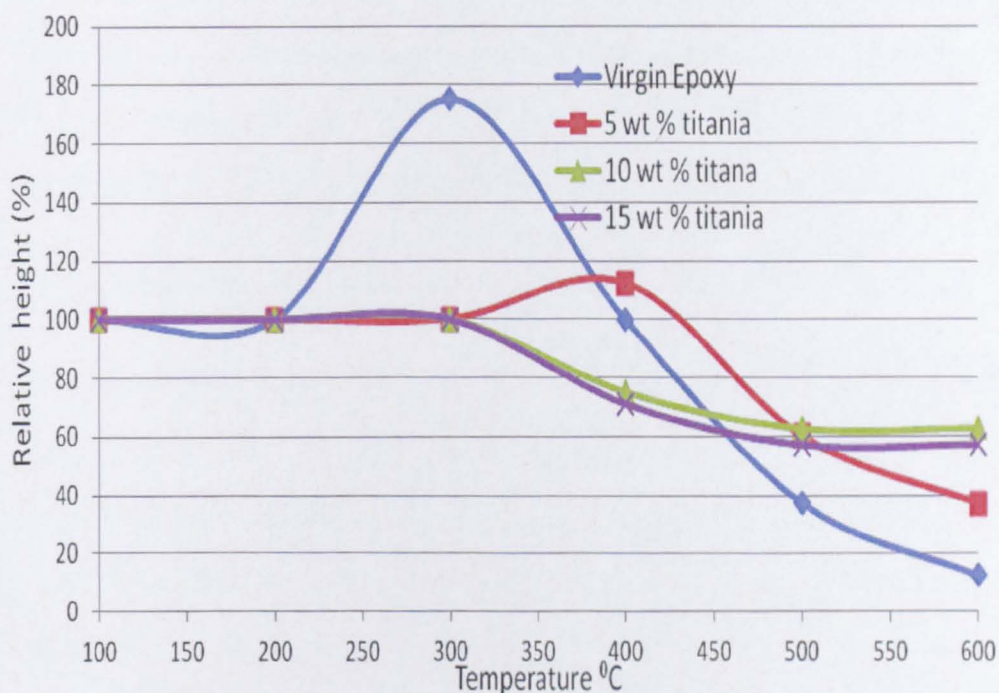


Fig. 9.9: The dimensional stability of titania-epoxy nanocomposites to virgin epoxy

Titania-epoxy nanocomposites with titania loading levels 5-15 wt% retained its initial height at 300 °C (100 % dimensional stability); whilst virgin epoxy height increased by 75 % as a result of the evolved decomposition gasses and the molten surface. The improved thermal and dimensional stability of titania-epoxy nanocomposites compared with virgin epoxy was ascribed to the induced barrier effect against heat and mass loss.

These results were found to be in good accordance with the research done by Laachachi in 2005 on titania-PMMA nanocomposites (Laachachi et al., 2005a, Laoutid et al., 2009), where titania nanoparticles improved PMMA flammability performance by decreasing the released heat in cone calorimeter testing as described in Section 2.3.8.3 (see Figure 2.22).

9.4 The direct flame resistance of epoxy resin

Standard flammability tests are relatively expensive and limited to certain fire research centres. A simple laboratory Bunsen testing technique was developed in order to quantify epoxy direct flame resistance and to retrieve some flammability parameters in a repeatable fashion.

9.4.1 The Bunsen flame test

The Bunsen flame test that simulated the standard limiting oxygen index (LOI) test and UL 94V test (Laoutid et al., 2009) was developed to assess flammability parameters repeatably. In this test, a sample of 1 cm diameter and 3 cm length was exposed vertically in a Bunsen flame for 20 seconds. The flame temperature was 1700 °C (Williams, 1985). The flame was extinguished and the sample behaviour was reported for the following 3 minutes. According to standard LOI testing, the sample could be classified as a flammable material if it maintained the flame for three minutes; as the oxygen in the air was sufficient to support the flame for this time period (Laoutid et al., 2009). If the sample did not maintain a flame for three minutes it could be classified as a self extinguishing material; as the oxygen in the air was not sufficient to support the flame for this time period (Laoutid et al., 2009). According to UL 94V, the time

required for the tested sample to self-extinguish (Afterflame time t_1) could be considered as an evaluating parameter.

9.4.2 The direct flame resistance of virgin epoxy

The resistance of virgin epoxy to direct flame exposure was evaluated by Bunsen test. Virgin epoxy sample was subjected to the direct flame for 20 seconds. After the flame was removed, the tested sample showed progressive burning (extensive increase in the flame size) with complete consumption of the tested sample mass and length. Figure 9.10 shows the flammability behaviour of virgin epoxy in direct flame.

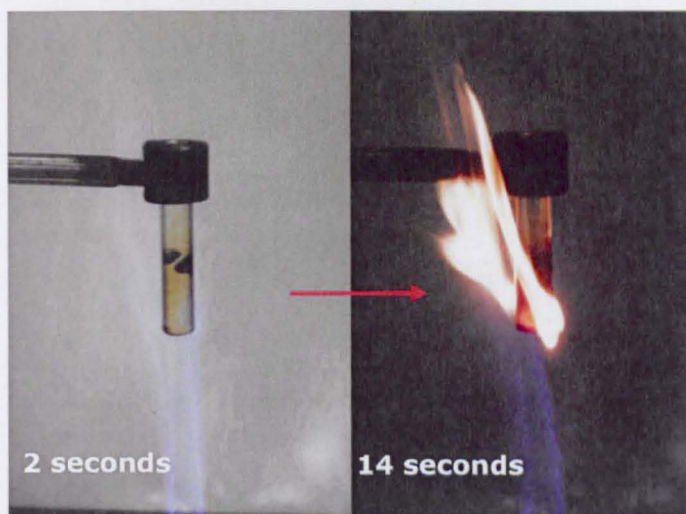


Fig. 9.10: The flammability behaviour of virgin epoxy in direct flame

According to the LOI test, the oxygen in the air was sufficient to support the flame for 3 minutes. Thus, epoxy resin can be classified as a flammable material. Flammable dripping took place within 30 seconds after the flame source was removed. This flammable dripping could be correlated to chain scission reactions and the peak profiles shown in Figure 9.5a. In the early degradation stages, epoxy thermal degradation is a competitive dehydration and dehydrogenation reactions with the formation of double bonds (peak at 320 °C in Figure 9.5a). At high degradation temperatures,

chain scission reactions take place as the aliphatic segments break down mainly into methane and ethylene, whereas the aromatic segments break down mainly into phenol (Bishop and Smith, 1970). The peak around 580 °C in Figure 9.5a corresponds to this more aggressive oxidation stage.

9.4.3 Quantifying virgin epoxy direct flame resistance using image analysis

There is a potential for using video footage to quantify the direct flame resistance, from initial ignition, flame shape and size, flammable dripping, until self-extinguish. The Bunsen flame test events were video recorded using a video recorder fixed at 115 cm distance from the tested sample. Figure 9.11 shows the flammability behaviour of virgin epoxy.

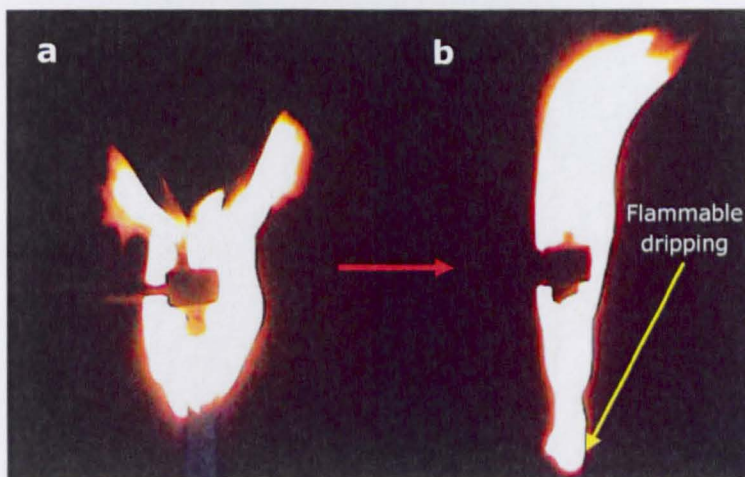


Fig. 9.11: (a) Virgin epoxy resistance to direct flame, (b) flame removed

The recorded video was processed to develop comprehensive data set that characterise and quantify the flammability behaviour. For each tested sample, the recorded video was processed to capture a set of frames (25 frames/second). The captured set of frames was processed by using image analysis labview (National Instruments) to threshold out the flame and to transform the video footage to a binary image (Figure 9.12).

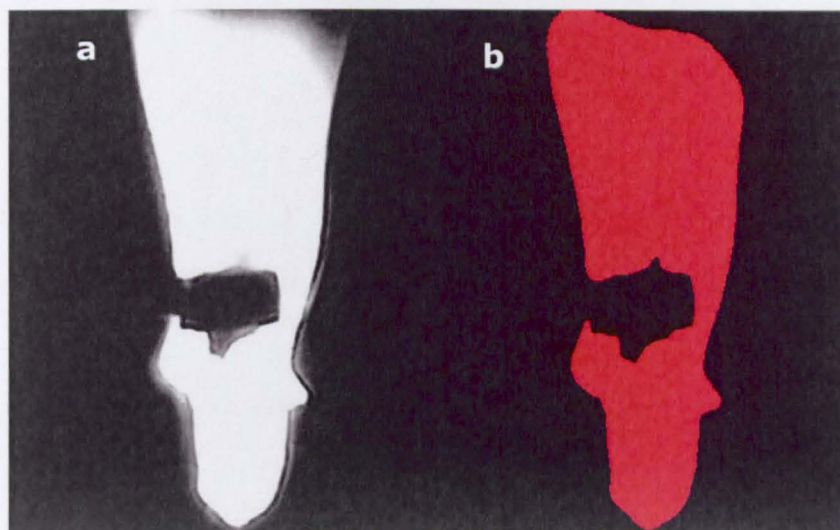


Fig. 9.12: Image processing of virgin epoxy, (a) footage frame, (b) binary image

The flame size of virgin epoxy was quantified over 120 seconds after the flame source was removed (Figure 9.13).

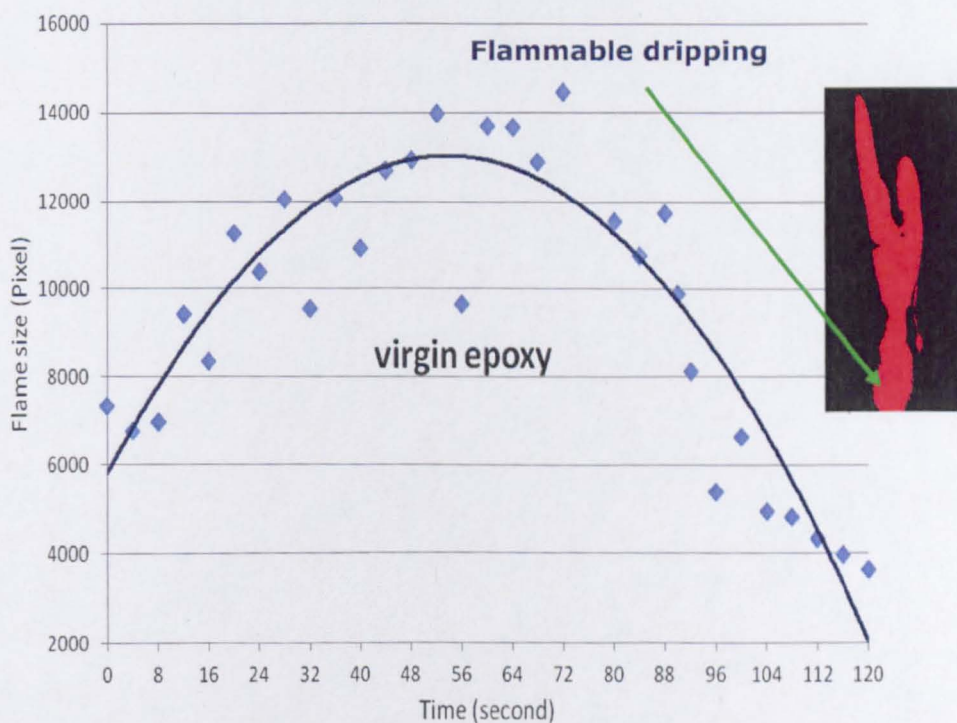


Fig. 9.13: The quantified flame size with time of virgin epoxy

Again, image analysis verified that virgin epoxy burned with an increase in the flame size with flammable dripping at high degradation temperature.

9.5 The direct flame resistance of titania-epoxy nanocomposites

Nano-oxides have been reported to improve the hosting polymer rheology and viscosity in the molten state under firing conditions (Fu and Qu, 2004). Titania P25-epoxy nanocomposites of different titania loading levels 5, and 10 wt % were prepared by mechanical mixing and vacuum casting. The resistance of titania-epoxy nanocomposites to direct flame was evaluated by Bunsen test and image analysis. The main target was to determine the minimum titania loading level at which epoxy nanocomposite might be able to self extinguish after being subjected to a direct flame source at 1700 °C for 20 seconds. Figure 9.14 shows the quantified flame size of titania/epoxy nanocomposites to virgin epoxy.

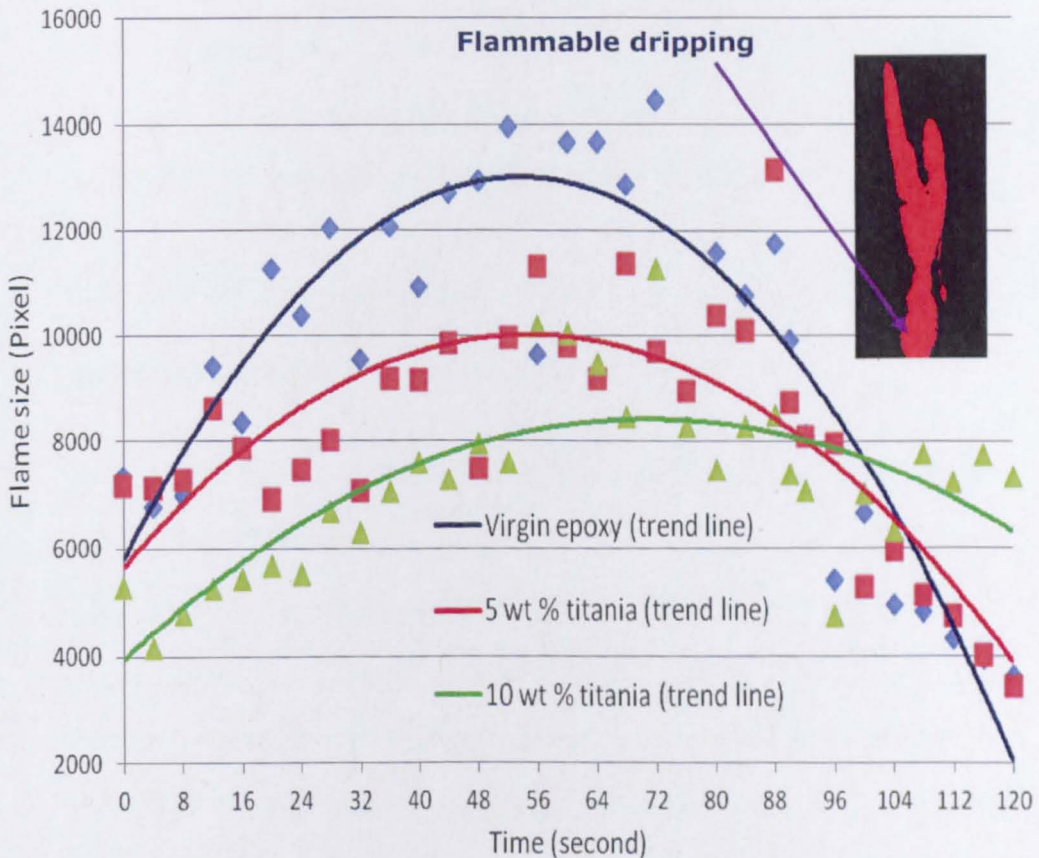


Fig. 9.14: The quantified flame size of titania-epoxy nanocomposite

Titania-epoxy nanocomposites showed enhanced resistance to direct flame compared with virgin epoxy. While virgin epoxy showed a progressive burning with flammable dripping, titania-epoxy nanocomposites burned with smaller flame size over a longer period of time with flammable dripping.

The apparent direct flame resistance of titania-epoxy nanocomposites could be ascribed to the induced barrier against mass and heat loss and to the improved polymer viscosity in the molten state. The burning behaviour of titania-epoxy nanocomposite corresponded well with the work done by Lachachi in 2005 on TiO_2 -PMMA nanocomposites; as the PHRR was reduced by 45% in cone calorimeter testing when 15 wt % nano TiO_2 was mixed with PMMA as described in Section 2.4 (Figure 2.23). Even though the titania nanoparticles did not directly change the thermal resistance of the epoxy directly it did act as a partial barrier against heat and mass loss. Over time this barrier was not sufficient to provide a FR action (self extinguish) or elimination of the flammable dripping.

9.6 The direct flame resistance of epoxy nanocomposite based on nano-fire extinguishers

Clearly TiO_2 has no intrinsic flame retardant properties, other than to act as an inert high temperature ceramic 'filler' material. Further experiments were carried out with HA and AOH to evaluate composite resistance to direct flame. This should be through reduction of surface oxygen, or by absorbing heat with the release of water. Epoxy nanocomposites of 10 wt % HA and 10 wt % AOH were prepared by mechanical mixing and vacuum casting. The nanocomposite resistance to direct flame was evaluated by Bunsen test and image analysis (Figure 9.15).

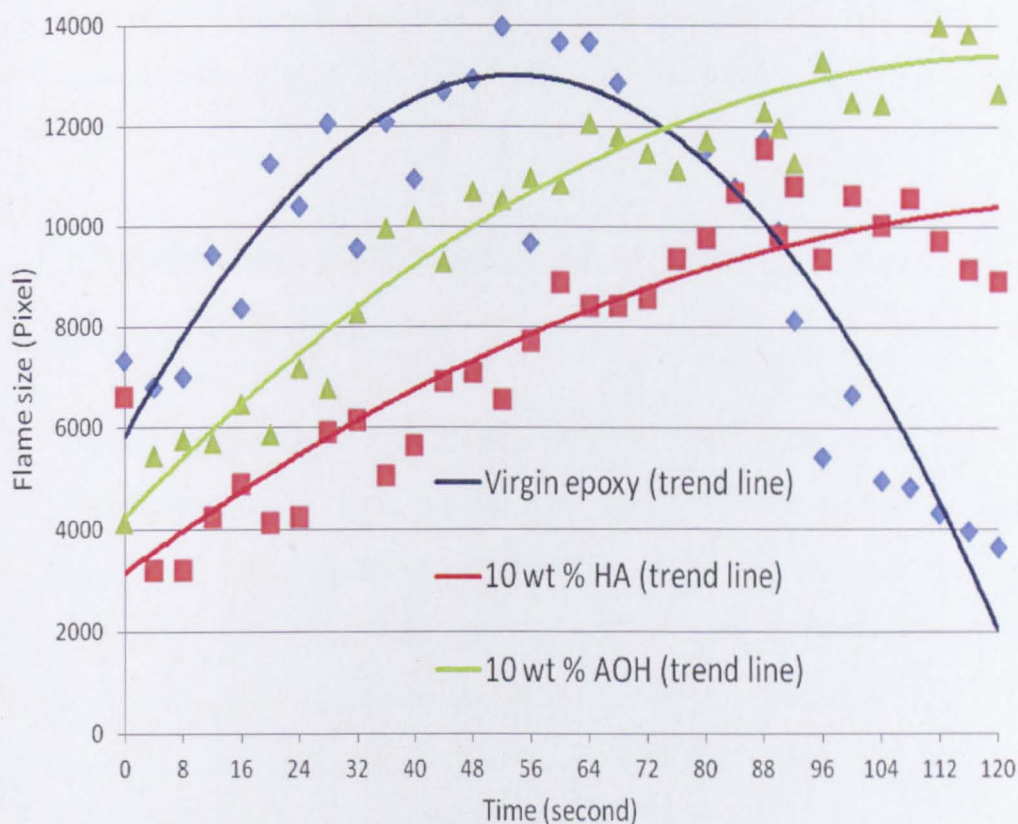


Fig. 9.15: The quantified flame size of epoxy nanocomposites based on nano-fire extinguishers

From Figure 9.15 HA and AOH both appeared to provide epoxy resin a FR action; as the nanocomposites did not show a flammable dripping. Epoxy nanocomposites based on HA and AOH burned at a lower rate over an extended period of time compared with virgin epoxy. However, epoxy nanocomposites based on HA and AOH were not able to resist the direct flame and self-extinguish after the flame source was removed. These nanocomposites can be classified as flammable materials. Higher solid loading could be required to secure self-extinguishing behaviour. The commonly used loading level of phosphorus-based FRs is 30 wt % and 60 wt % for hydrated minerals (Grand and Wilkie, 2000).

Nanoparticles alone could be a part of the flame retardancy solution but not the whole solution. The combination between selected nanoparticles

and conventional FR systems seems to be vital to fulfil the flammability standards at low solid loading level (Zammarano et al., 2005, Laoutid et al., 2009).

9.7 Summary of the impact of nanoparticles on polymeric matrix

Chapter 9 investigated the impact of different nanoparticle of different morphologies on epoxy mechanical, thermal, and flame resistance properties. These particles ranged from nanospheres (TiO_2), nanoplates (HA), to nanorods (AOH). The enhanced performance of epoxy nanocomposites can be ascribed to the strong interaction between the well dispersed nanoparticles and the polymer chains and the improved viscosity in the molten state under firing conditions.

Image analysis was found to be a useful method to quantify direct flame resistance and to investigate the nanocomposite thermal stability and structural integrity under heating in a repeatable fashion. To the knowledge of the author, this is the first time image analysis has been used to quantify direct flame resistance.

Nanoparticles alone, however, were not able to induce a self extinguishing effect at 10 wt % solid loading. The particles were able to slow down the onset of combustion in the composite but not enough to extinguish the flame. It might be possible to combine these nanoparticles with convenient FR material to achieve self extinguishing behaviour. The nanomaterials would act as a thermal barrier, but the conventional FR material would extinguish the flame. This would be particularly advantageous if it could be achieved at low solid loading levels. This will be discussed in Chapter 10.

CHAPTER 10

10. MULTI-COMPONENT FLAME RETARDANT SYSTEMS

The incorporation of nanoparticles such as nano-oxides, oMMT, CNTs, and POSS can improve the polymer rheology, mechanical, thermal, and flame resistance properties under fire conditions (Nachtigall et al., 2006). Even though these nanoparticles can improve the host polymer's fire performance by lowering the burning rate and extending the burning time; PNs still burn eventually with almost the same total heat released as the virgin polymer (Marosi et al., 2003). In order to achieve a high flammability performance at low solids loading, these nano-fillers need to be used in combination with conventional FR systems (Almeras et al., 2003, Morgan, 2006, Si et al., 2007).

The purpose of the FR system is to reduce the heat supplied to the polymer surface below the critical level for flame stability (Roma et al., 1997). The intumescent FR system is a condensed phase mechanism which interrupts the self sustained combustion of the polymer at its earliest stages (Bourbigot et al., 2004). The intumescence process is a combination of charring and foaming at the burning polymer surface. The resulting foamed cellular char layer can protect the underlying material from the effect of heat flux or from flame (Camino et al., 1985a). The common components of intumescent system are ammonium polyphosphate (APP) as an acid source, melamine (ME) as a blowing agent, and penta erithritol (PE) as a carbonific agent (Bourbigot and Duquesne, 2007).

APP with an aromatic ester of tris(2-hydroxy methyl)-isocyanurate, commercially known as Exolit AP750 (AP750) developed by Clariant, showed better performance than normal intumescent additives APP/PE 3:1 (Morice et al., 1997, Kandola et al., 2002, Morgan and Wilkie, 2007). AP750 is not hygroscopic and has a high processing thermal stability. Materials containing AP750 can foam upon exposure to flame (Pinfa, 2010), however, high loading levels of this intumescent material up to 30 wt % are required to achieve LOI values higher than 30 and Vo rating (Morice et al., 1997, Morgan and Wilkie, 2007).

Owing to the strong increase in polymer viscosity, impaired processability, and also due to the breakdown of ultimate mechanical properties; the acceptable limit of solids loading to improve flame retardancy is restricted to 10 wt % or less (Wilkie and Morgan, 2010). The synergism between AP750 and selected nanoparticles, mainly nano-oxides (TiO_2 , SiO_2 , Al_2O_3) and nanoparticles with flame retardant properties ($\text{Ca}_5(\text{OH})(\text{PO}_4)_3$, AlOOH), was investigated in an attempt to achieve a self extinguishing epoxy nanocomposite at 10 wt % total solid loading level.

10.1 Development of multi-component epoxy nanocomposite

Nano-oxides, such as ceramics like titania, could be an essential constituent in multi-component FR systems (Wang et al., 2005, Laachachi et al., 2006). They are able to improve the polymer viscosity in the molten state and have the potential to react with different FR agents (Fu and Qu, 2004). The impact of the partial substitution of AP750 with titania nanoparticles on epoxy structural integrity under heating was investigated. Multi-component epoxy nanocomposites of different ratios of titania to

10. Multi-component flame retardant systems

AP750 at total solid loading level of 10 wt % were prepared by mechanical mixing and vacuum casting. Table 10.1 shows the multi-component epoxy nanocomposite formulations.

Table 10.1: The investigated combination ratios of titania to AP750 in epoxy resin

Formulation No.	AP750 wt %	Titania wt %
Formulation 1	10	---
Formulation 2	7.5	2.5
Formulation 3	5	5
Formulation 4	2.5	7.5
Formulation 5	-----	10

The formulations in Table 10.1 were prepared in the shape of cylindrical blocks (30 mm diameter, 12 mm height) and were heated in a muffle furnace at 500 °C for 5 minutes. The structural integrity of the tested formulations was visually inspected after this thermo-oxidative degradation. The aim of this work was to determine the necessary ratio of titania to AP750 in epoxy resin in order to achieve a thermally stable epoxy nanocomposite that could retain its shape and dimensions under extreme heating conditions.

The virgin epoxy sample did not retain its shape or dimensions. Formulation 1 (AP750/epoxy) showed an intumescent action; a delicate char layer, with no noticeable mechanical properties, was developed. The sample height was increased 5 fold. Formulation 2 (titania/AP750/epoxy)

showed a cohesive and less expanded char layer (compact/dense char layer) with more dimensional stability compared with formulations 3-5. Figure 10.1 shows the structural integrity of titania/AP750/epoxy to AP750/epoxy and virgin epoxy after thermo-oxidative degradation for five minutes at 500 °C.

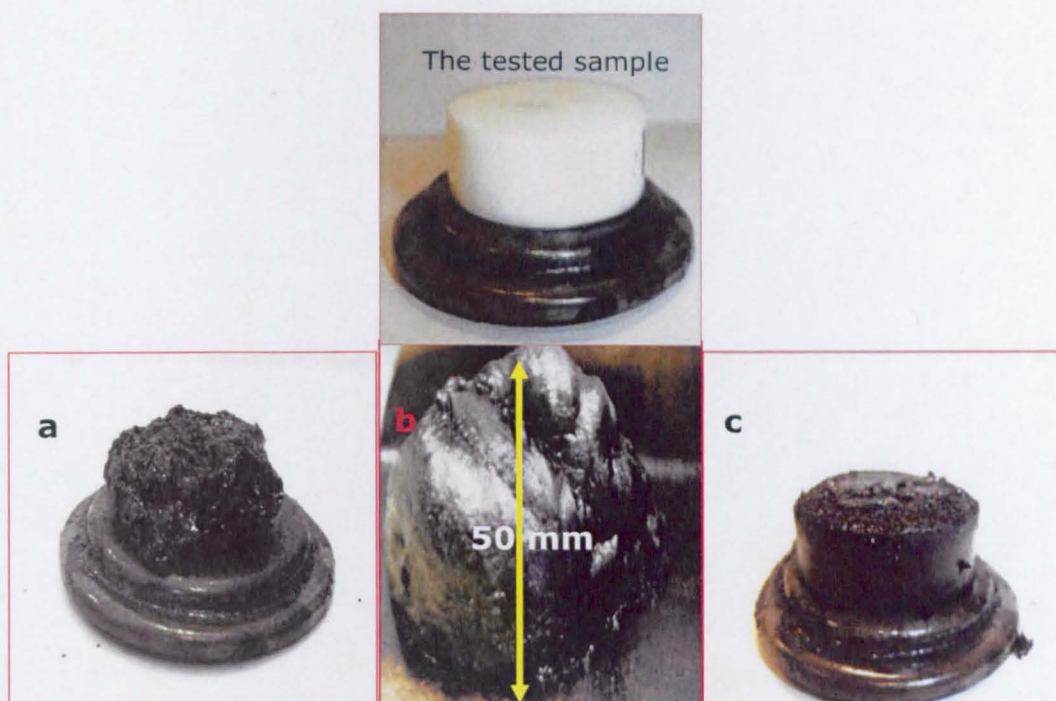


Fig. 10.1: The structural integrity of: (a) virgin epoxy, (b) AP750/epoxy, (c) and titania/AP750/ epoxy

The enhanced structural integrity of the multi-component FR system was ascribed to the synergism between titania nanoparticles and AP750; as titania nanoparticles improved the formed char layer strength where a more compact and cohesive char layer was developed. It has been reported that the improvement in fire protection can be correlated to the char layer strength and its specific heat rather than the height of the expanded char (Wilkie and Morgan, 2010).

10.1.1 Synergism between titania nanoparticles and AP750

Formulation 2 [(2.5 wt% titania-7.5 wt% AP750)/epoxy] showed the most cohesive and compact char layer after being subjected to aggressive oxidative degradation conditions at 500 °C for five minutes. The char layer formed was investigated by XRD to assess the possibility of any developed crystalline structures due to the synergism between titania and AP750. Figure 10.2 shows the XRD diffractogram of the formed char layer, to the PNs ingredients (i.e. titania P25, and AP750).

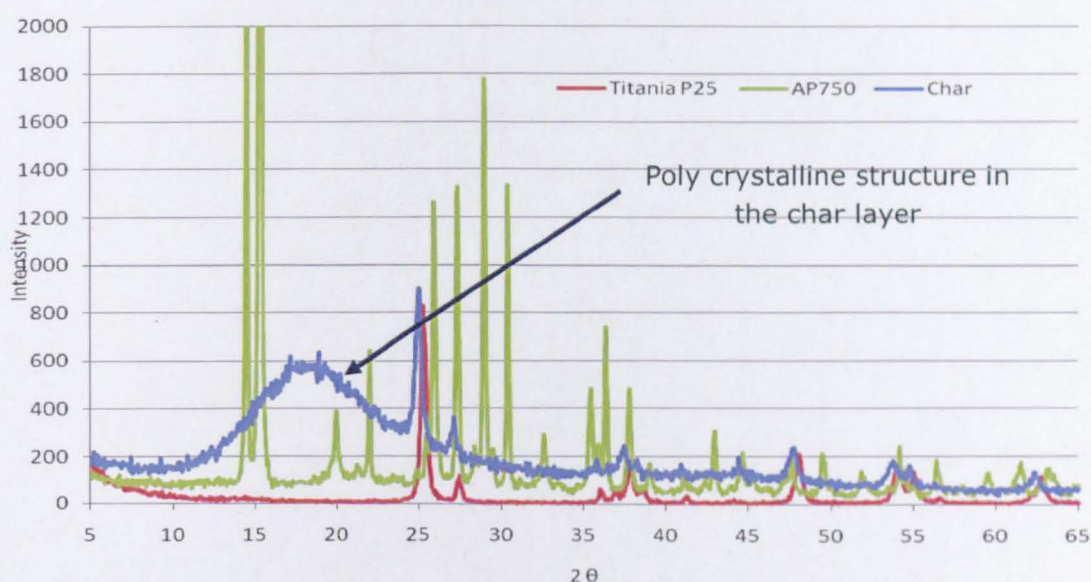


Fig. 10.2: The X-ray diffractogram of the formed char layer

XRD results showed the formation of different crystalline structures in the condensed phase (char layer) mainly titanium phosphate and pyrophosphate; these polycrystalline forms were identified by comparing the XRD diffractogram to standard data from the joint committee on powder diffraction standards (JCPDS).

Upon decomposition, AP750 produced polyphosphoric acid which was able to provoke dehydration process of the polymer surface (Laoutid et al., 2009). Titania nanoparticles could show a catalytic reaction with

polyphosphoric acid via the formation of stable crystalline forms such as titanium phosphate, and pyrophosphate. These stable crystalline forms could increase the formed char strength and density. The synergism between titania and AP750 was found to be in accordance with the research work done by Scharf on APP-titania synergism (Scharf and Nalepa, 1992); as he proposed that titania would have the potential to cross link polyphosphoric acid chains produced by APP decomposition (Figure 10.3).

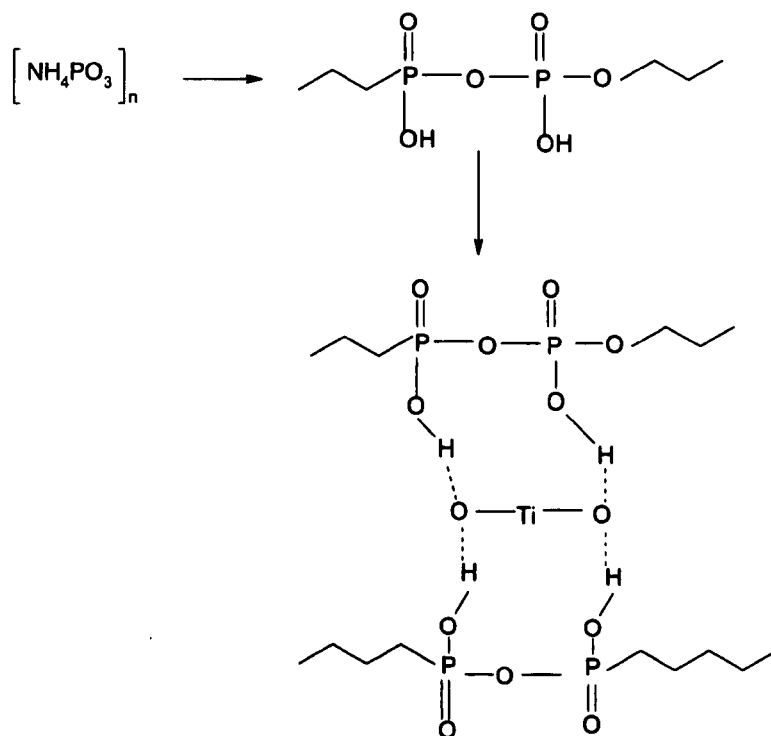


Fig. 10.3: Effect of TiO₂ on the degradation of APP, adapted from (Scharf and Nalepa, 1992).

This synergistic effect between titania and AP750 was found to improve char strength; therefore a more compact insulating barrier was developed, protecting the polymer under-layers from further mass and heat losses. From these results the optimal ratio of titania to AP750 appeared to be 1:3.

10.1.2 Synergism between bespoke nanoparticles and AP750

The partial substitution of 10 wt % AP750 with 2.5 wt % titania nanoparticles into epoxy resin reported enhanced structural integrity under heating. The effect of partial substitution of AP750 with selected nano-oxides mainly titania P25, silica (10 nm from Aldrich), alumina nanoparticles (50 nm from Degussa) and HA and AOH (from CHS) on epoxy thermal stability was investigated. Table 10.2 shows the investigated multi-component epoxy nanocomposite formulations.

Table 10.2: The investigated multi-component epoxy nanocomposites

	AP750 wt %	Silica wt %	Titania wt %	Alumina wt %	HA wt %	AOH wt %
Virgin epoxy	----	----	----	----	----	----
Formulation 1	10	----	----	----	----	----
Formulation 2	7.5	2.5	----	----	----	----
Formulation 3	7.5	----	2.5	----	----	----
Formulation 4	7.5	----	----	2.5	----	----
Formulation 5	7.5	----	----	----	2.5	----
Formulation 6	7.5	----	----	----	----	2.5

The investigated formulations, in the shape of cylindrical blocks (30 mm diameter, 12 mm height) were heated in a muffle furnace at 500 °C for 5 minutes. The structural integrity of the investigated formulations was evaluated after this aggressive thermal degradation condition.

Formulation 2 (silica/AP750/epoxy) resisted charring as the tested sample structure was severely damaged, and it did not show an intumescent action. This can be ascribed to an antagonistic effect between silica nanoparticles and polyphosphoric acid produced by AP750 decomposition; as silica could breakdown the polyphosphoric chain. Formulations 3-6 developed an intumescent char which protected the under-layers from further degradation. These formulations retained their original shape after these thermo-oxidative degradation conditions (Figure 10.4).

(a) The protective char layer



(b) The structural integrity



Fig. 10.4: The structural integrity under heating effect of multi-component epoxy nanocomposites based on nanofire extinguishers and nano-oxides

The structural integrity of formulations 3 and 4 could be ascribed to the synergism between titania and alumina nanoparticles with AP750; a catalytic reaction in the condensed phase between these nano-oxides and AP750 could result in the formation of cross linked and thermally stable forms that might increase char strength and insulating properties. This synergistic effect was found to agree with the work done by Laachachi who reported a synergism between alumina and phosphinate FR in PMMA (Figure 2.23) (Laachachi et al., 2005b); and the work done by Scharf who

reported a synergism between titania and APP (Figure 10.3) (Scharf and Nalepa, 1992).

The synergistic effect of HA and AOH with AP750 (Formulations 5 and 6) could be ascribed to their FR action with the formation of oxides in the burning surface; the developed oxides such as alumina could have a synergism with AP750.

HA could have a phosphorous-based FR action via the release active flame scavengers such as PO_2^* , PO^* , and HPO^* (Laoutid et al., 2009). These species are the most effective free radical scavengers. They are ten times more effective than chlorine, and five times more effective than bromine (Wilkie and Morgan, 2010). The released flame scavengers might decrease the reaction exothermicity. Furthermore, HA could have a condensed phase effect by promoting the burning surface dehydration.

AOH nanoparticles can act as a heat sink material during thermal decomposition, releasing water, and forming an oxide layer. Therefore, they cool down the polymer burning surface, dilute the combustion gasses, and shield the polymer under-layers via the formed alumina layers. Furthermore, the formed oxide layer (alumina) might have a synergistic effect with AP750.

10.2 Synchronization between AP750 FR action and epoxy initial degradation

The relationship between the FR action and the onset of polymer initial degradation is of utmost importance; otherwise the polymer could continue burning and the FR ingredient would not work (Levchik et al., 1995, Laoutid et al., 2009). The synchronization between AP750 intumescent

action and epoxy initial degradation was investigated by video recording the thermal behaviour of titania/AP750/epoxy nanocomposite (Formulation 3 in Table 10.2) compared with virgin epoxy. The investigated formulations were heated in an oven (10 °C/min), in front of a digital camera. A frame was captured with each 1 °C increase. These frames were employed to determine the initiation temperature of the intumescent action and virgin polymer initial degradation. Figure 10.5 shows the synchronization between AP750 FR action and virgin epoxy initial degradation.

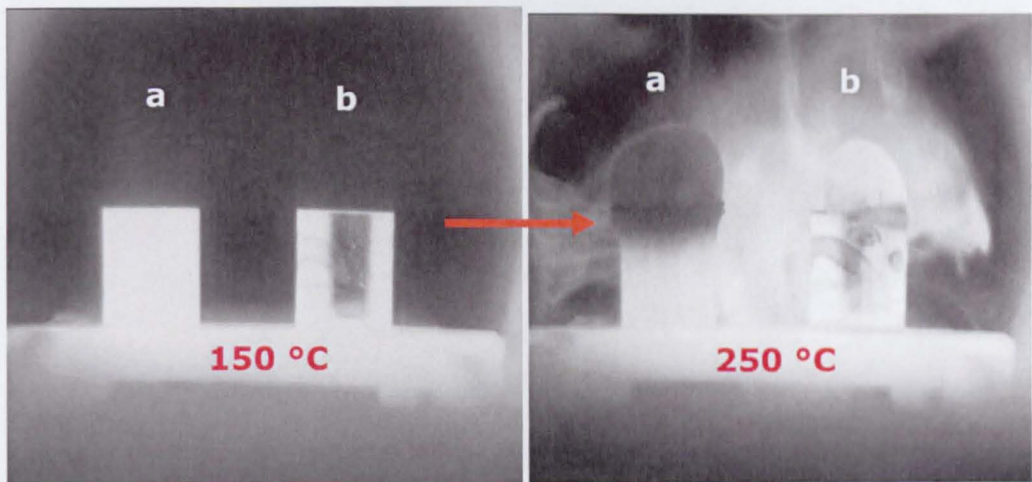


Fig. 10.5: The harmonization between, AP750 FR action (a), and virgin epoxy initiation (b)

Whereas virgin epoxy started degradation at 250 °C with the evolution of heat and combustion gases; titania/AP750/epoxy nanocomposite decomposed with the formation of a protective insulating char layer, which prevented the layers below from further degradation. This test confirmed the synchronization between AP750 intumescent FR action and epoxy initial degradation. At 600 °C the virgin epoxy sample was completely burned, while the multi-component epoxy nanocomposite (Formulation 3) showed enhanced structural integrity compared to virgin epoxy (Figure 10.6).

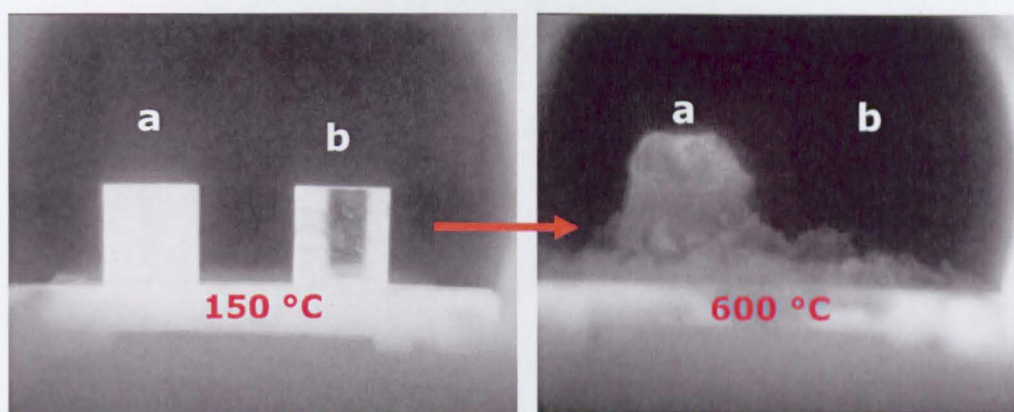


Fig. 10.6: The structural integrity under heating effect of, multi-component epoxy nanocomposite (a), and virgin epoxy (b)

This improved thermal stability and structural integrity of the multi-component epoxy nanocomposite (titania/AP750/epoxy) compared with virgin epoxy was ascribed to the enhanced mechanical, barrier, and rheological properties under heating conditions.

10.3 Direct flame resistance of multi-component epoxy nanocomposite

The ability of the developed multi-component epoxy nanocomposite formulations (Table 10.2) to resist direct flame and to self-extinguish was investigated via the developed Bunsen testing with video footage and image analysis.

10.3.1 The direct flame resistance of multi-component epoxy nanocomposite based on nano-oxides

Nano-oxides are able to improve the polymer viscosity in the molten state under firing conditions, and have the potential to react with different FR agents (Fu and Qu, 2004). The impact of bespoke oxide nanoparticles (titania, silica, and alumina) on AP750-epoxy direct flame resistance was

investigated via partial substitution of AP750 with nano-oxides (formulations 1-4 in Table 10.2).

Formulation 1 (10 wt % AP750) did not self extinguish; the tested specimen burned with a smaller flame size over extended period of time with no flammable dripping compared with virgin epoxy. The partial substitution of AP750 with silica nanoparticles (Formulation 2) did not improve the performance; formulation 2 burned with an increased flame size compared with formulation 1 (Figure 10.7) which is probably as a result of the inactive SiO_2 phase and the reduced quantity of AP750 in the composite.

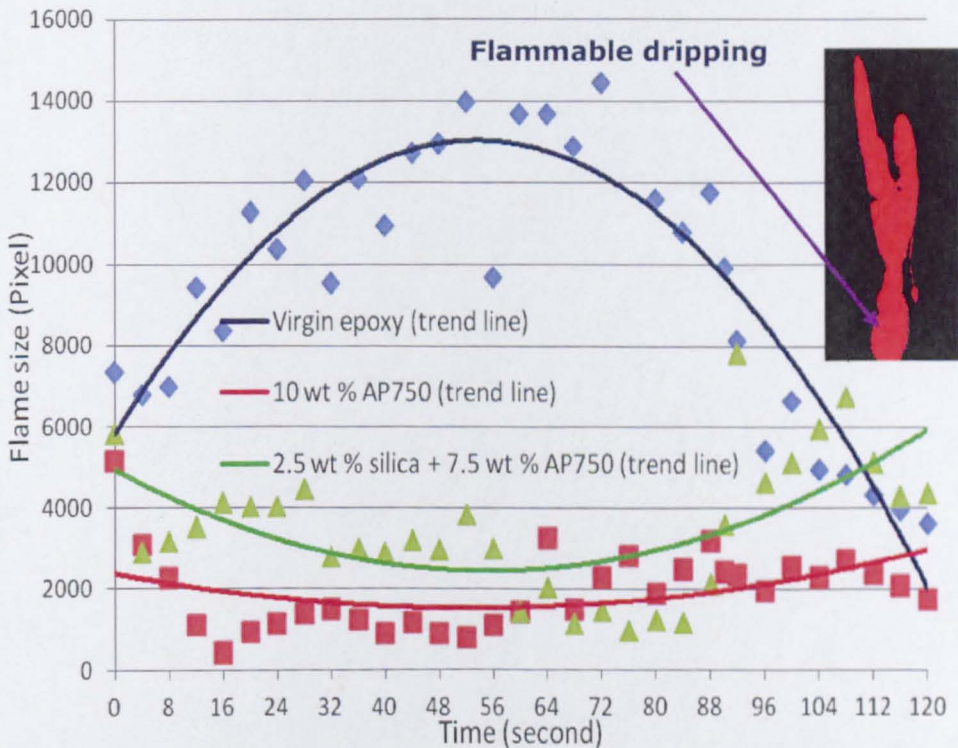


Fig. 10.7: The impact of silica on AP750/epoxy direct flame resistance

Titania and alumina nanoparticles showed a synergistic effect with AP750; formulation 3 and 4 (Table 10.2) were able to self extinguish directly after the flame source was removed (Figure 10.8).

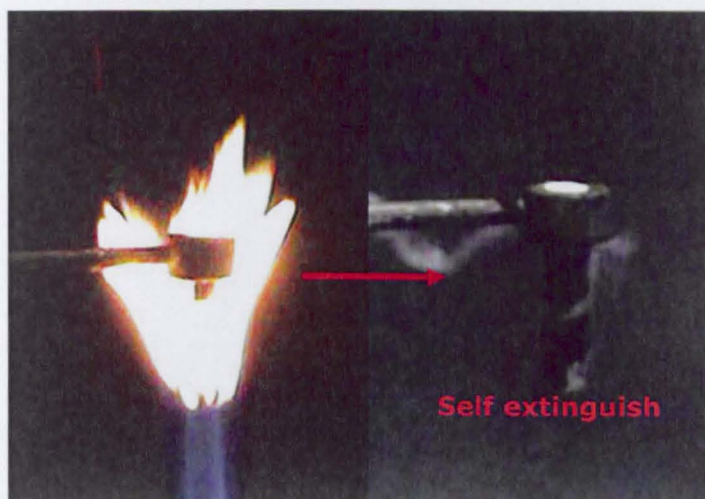


Fig. 10.8: Direct flame resistance of self-extinguishing multi-component epoxy nanocomposite based on nano-oxides

The flame size of formulations 3 and 4 was quantified and compared with virgin epoxy (Figure 10.9).

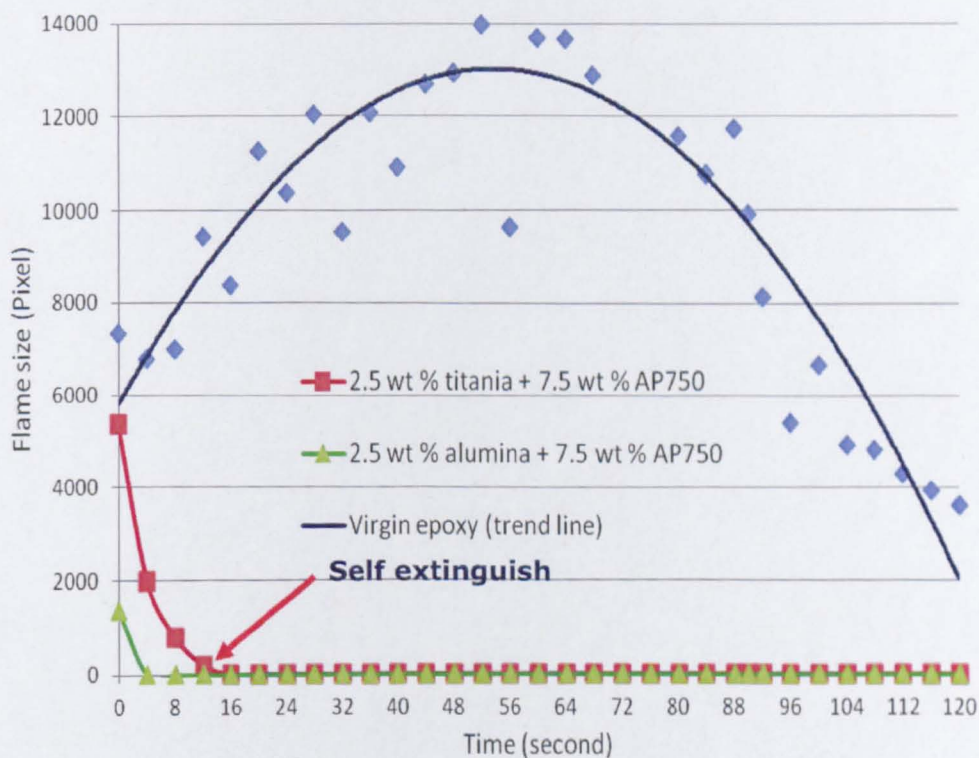


Fig. 10.9: The quantified flame size of titania/AP750/epoxy and alumina/AP750/epoxy compared with virgin epoxy

Titania and alumina might be able to cross link the polyphosphoric acid produced by AP750 FR action; this catalytic effect could enhance char

strength. The developed multi-component epoxy nanocomposites based on titania and alumina can be classified as self extinguishing materials.

10.3.2 The direct flame resistance of multi-component epoxy nanocomposite based on nano-fire extinguishers

The partial substitution of AP750 with nano-fire extinguisher nanoparticles mainly HA and AOH showed a synergistic effect; nanocomposite formulations based on HA and AOH (formulations 5, 6 in Table 10.2) were able to resist direct flame and to self-extinguish after the flame source was removed. Figure 10.10 shows the quantified flame size of multi-component epoxy formulations based on HA and AOH to virgin epoxy.

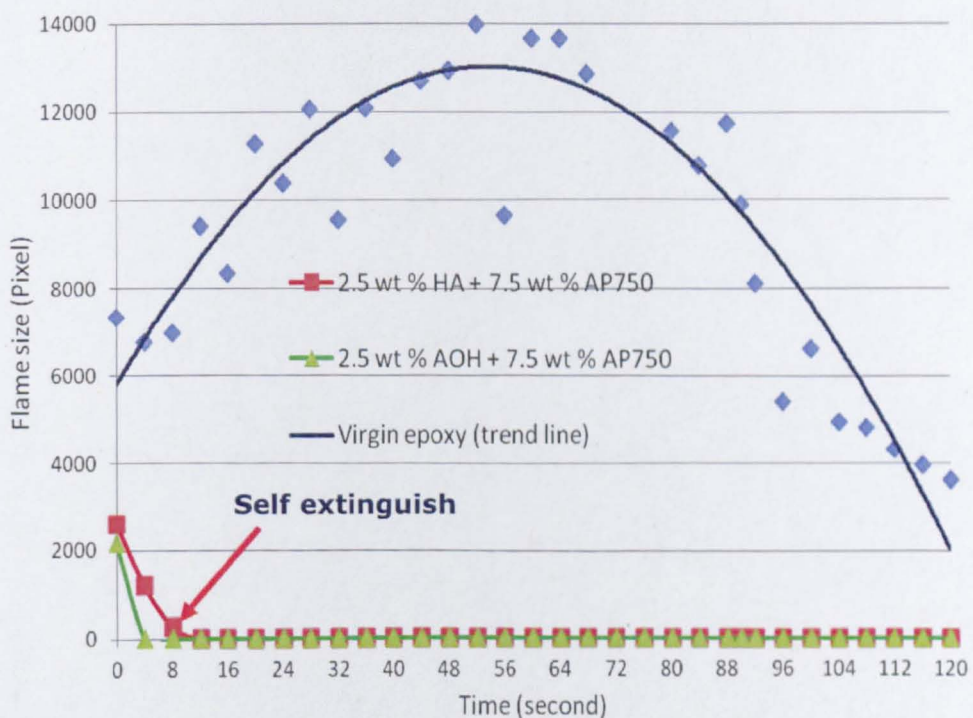


Fig. 10.10: The quantified flame size of multi-component epoxy nanocomposite based on nano-fire extinguishers

In contrast to virgin epoxy, formulations 5 and 6 self extinguished directly after the flame source was removed. The enhanced direct flame resistance could be ascribed to the synergism between the nanoparticle FR action (HA

phosphorous-based FR action and AOH heat sink FR action) and AP750 intumescent action. In both cases, the formed oxides in the condensed phase could act as an insulating barrier. Furthermore, the synchronized FR actions of HA and AOH with AP750 could greatly enhance the direct flame resistance of multi-component epoxy nanocomposites to AP750/epoxy.

10.3.3 Summary of multi-component epoxy nanocomposite direct flame resistance

Virgin epoxy was burned completely; formulation 1 (AP750/epoxy) showed an intumescent action (fragile expanded char layer). Silica nanoparticles did not appear to improve the performance of AP750; formulation 2 (silica/AP750/epoxy) burned with an increased flame size compared with AP750/epoxy. Multi-component epoxy nanocomposites (formulations 3-6) showed enhanced direct flame resistance compared with virgin epoxy and AP750/epoxy. These nanocomposite formulations were able to self extinguish and to retain their dimensionality after being subjected to direct flame at 1700 °C for 20 seconds (Figure 10.11).

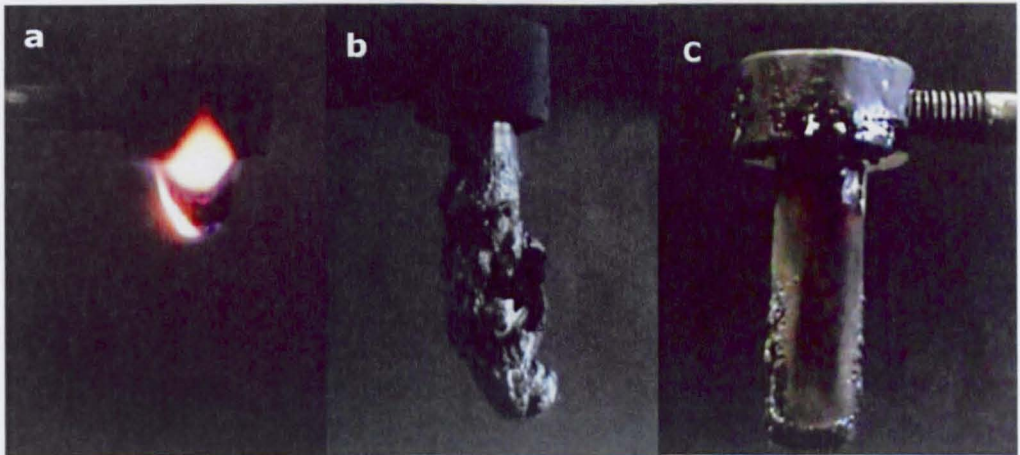


Fig. 10.11: The dimensional stability of: (a) virgin epoxy, (b) AP750-epoxy, and (c) multi-component epoxy nanocomposite, after Bunsen flame test

10. Multi-component flame retardant systems

The Bunsen test with video recording and image analysis enabled the quantification of the flame size with time. Furthermore, some flammability parameters, mainly: flammable dripping, time to flammable dripping, self extinguish, and time to self extinguish were observed. A refinement of the image analysis program would allow dripping and dripping rates to be quantified as well. Table 10.3 gives a summary of the quantified data for all investigated epoxy nanocomposite formulations.

Table 10.3: The quantified direct flame resistance parameters

	self extinguish	time to self extinguish (seconds)	flammable dripping	time to flammable dripping (seconds)
Virgin epoxy	×	-----	√	30
Formulation 1 (AP750/epoxy)	×	----	×	----
Formulation 2 (silica/AP750/epoxy)	×	----	×	----
Formulation 3 (titania/AP750/epoxy)	√	12	×	----
Formulation 4 (alumina/AP750/epoxy)	√	4	×	----
Formulation 5 (HA/AP750/epoxy)	√	8	×	----
Formulation 6 (AOH/AP750/epoxy)	√	4	×	----

The enhanced direct flame resistance of multi-component epoxy nanocomposites to AP750-epoxy can be ascribed to:

- An alignment of the FR action to fit the polymer burning behaviour; as epoxy is a charring polymer and intumescent FR action is based on char formation.
- The synchronization between the intumescent FR action and the polymer initial degradation.
- The synergistic effect between the bespoke nanoparticles and the intumescent FR agent.

10.4 Flammability properties of multi-component epoxy nanocomposites

The flammability performance of multi-component epoxy nanocomposites (Table 10.2) was evaluated by standard cone calorimeter testing. Cone calorimetry is one of the most efficient polymer fire behaviour tests. In this test, a sample of dimensions 100×100×4 mm was placed on a load cell and subjected to a constant heat flux of 35 Kw/m². The sample was uniformly irradiated from above. The measurement of oxygen concentration in the combustion gases was employed to quantify the heat released per unit time and surface area. Figure 10.12 shows the cone calorimeter test set up.

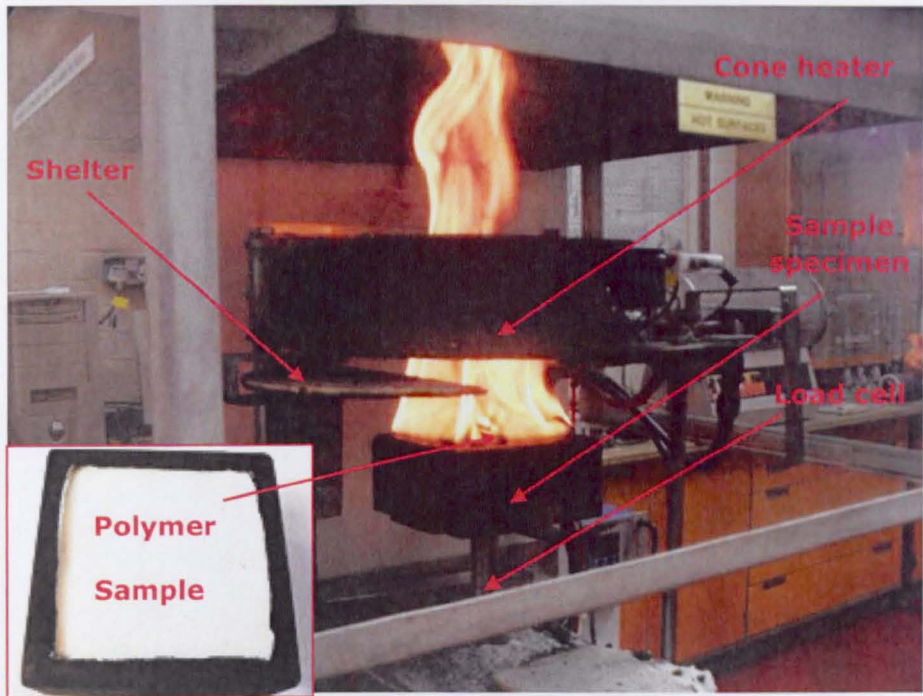


Fig. 10.12: The cone calorimeter test set up

The measurement of heat released rate (HRR), specifically the peak heat released rate (PHRR), is the main valuable flammability parameter from cone calorimeter testing. PHRR is considered the key point in polymer flame retardancy; as it can be employed to predict whether the material will easily develop a dramatic combustion after ignition or not (Lie et al., 2009).

10.4.1 The impact of AP750 on epoxy flammability performance

The impact of AP750 on epoxy flammability performance was evaluated by cone calorimeter testing; the flammability performance of formulation 1 (AP750/epoxy) was evaluated and compared to virgin epoxy. Virgin epoxy showed a dramatic increase in HRR. AP750 showed an intumescent action; a fragile expanded char layer was developed; the tested specimen height increased 25 fold (Figure 10.13).

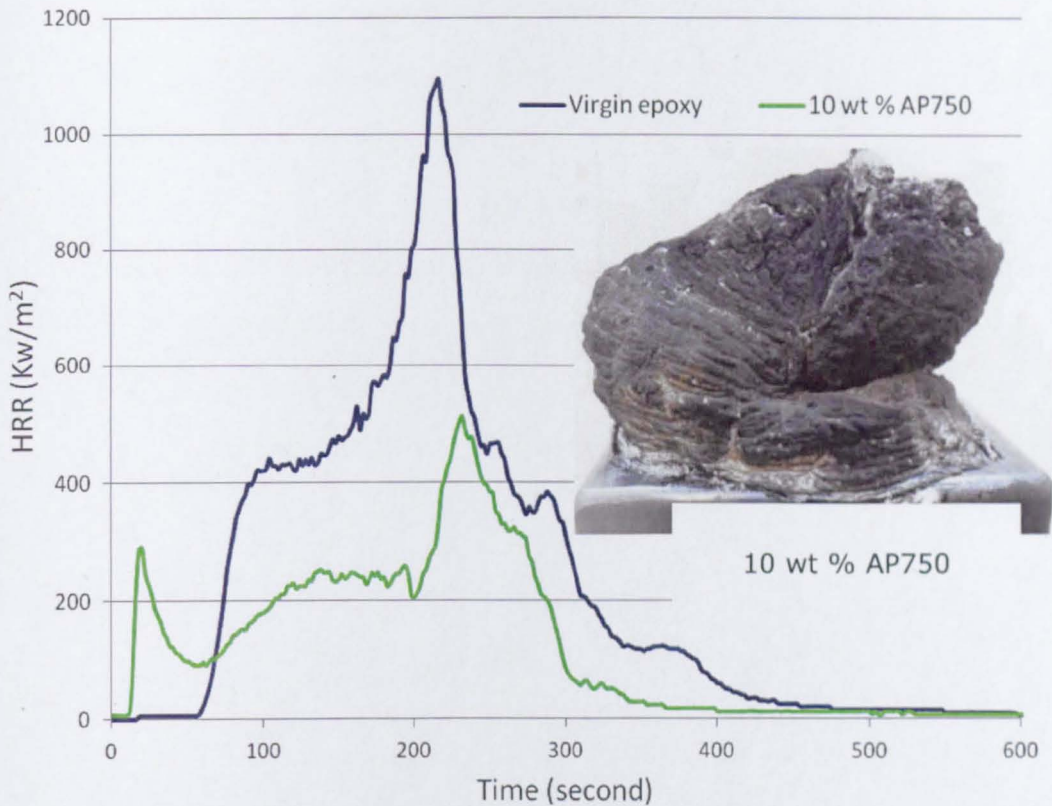


Fig. 10.13: Evolution of HRR for AP750/epoxy to virgin epoxy

The intumescent FR action countered the released heat; this is why AP750/epoxy showed less HRR compared with virgin epoxy. AP750 reduced the PHRR by 53 %. On the other hand, AP750 reduced the time to ignition (TTI) of virgin epoxy by 50 seconds; as solid particles might increase the nanocomposite thermal conductivity causing the surface temperature to rise up more rapidly when subjected to constant heat flux compared with virgin epoxy.

10.4.2 The flammability performance of multi-component epoxy nanocomposites based on nano-oxides

The impact of the partial substitution of AP750 with different nano-oxides on AP750/epoxy flammability performance was evaluated. The

flammability performance of multi-component epoxy nanocomposites based on nano-oxides (formulation 2-4 in Table 10.2) was evaluated by cone calorimeter testing relative to AP750/epoxy and virgin epoxy. Silica nanoparticles showed an antagonistic effect with AP750. Formulation 2 based on silica/AP750/epoxy resisted charring; the HRR was increased compared with AP750/epoxy (Figure 10.14).

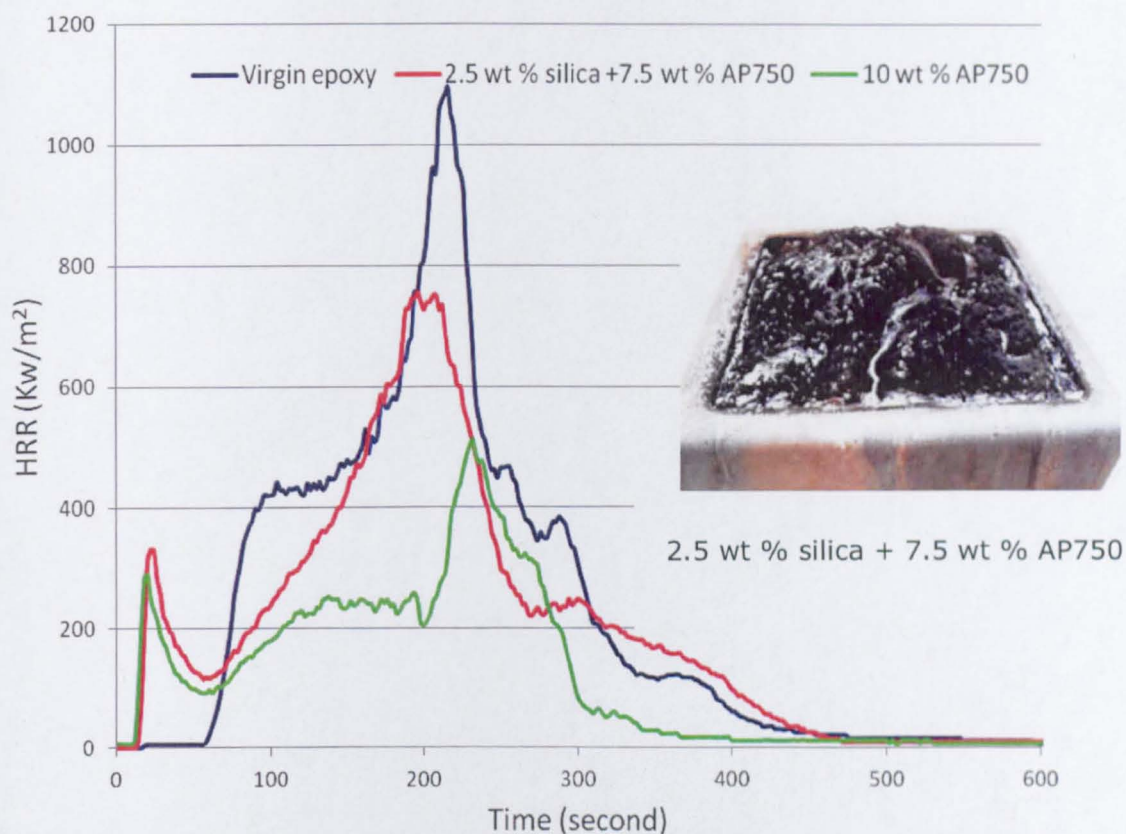


Fig. 10.14: Evolution of HRR for silica/AP750/epoxy, AP750/epoxy, and virgin epoxy

AP750 decomposed with the formation of polyphosphoric acid as a dehydrating agent in the condensed phase. The antagonistic effect between silica nanoparticles and AP750 might be caused by the breakdown of the polyphosphoric acid chains by silica nanoparticles. Formulations 3 (titania/AP750/epoxy) and 4 (alumina/AP750/epoxy) did not show a great impact on the PHRR of AP750/epoxy; but rather titania and alumina

extended the TTI and the time to peak heat released (TTPHR) (Figure 10.15).

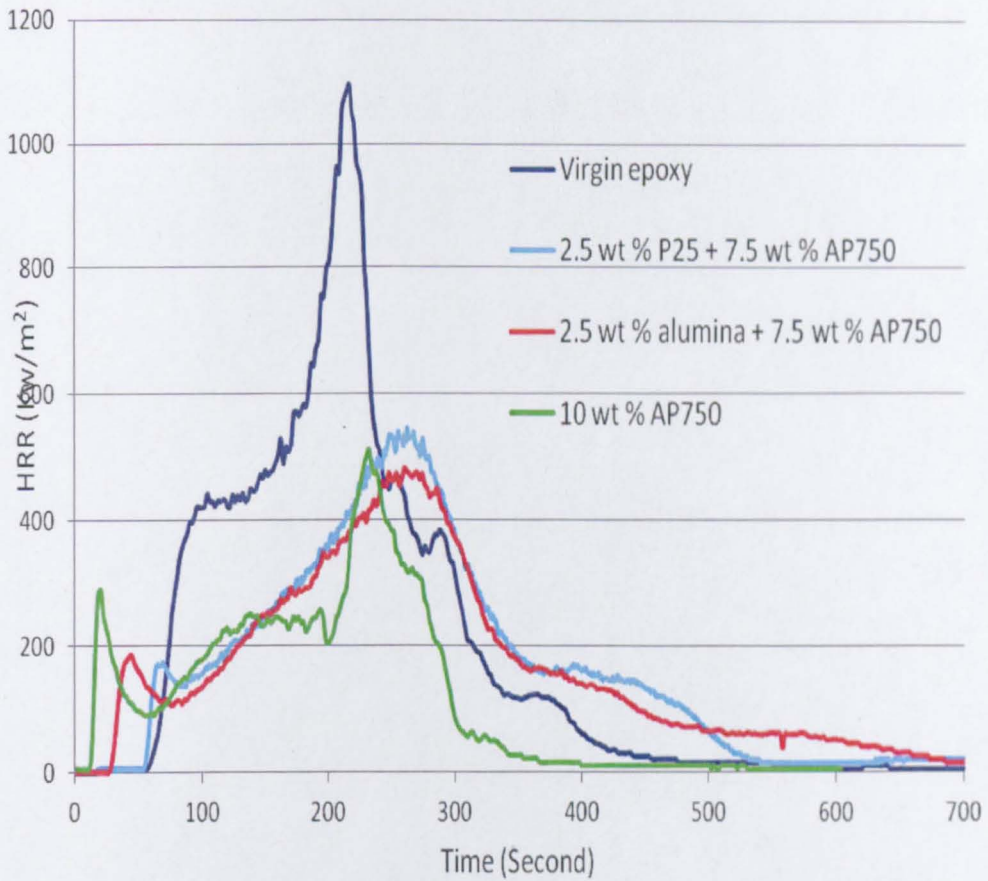


Fig. 10.15: Evolution of HRR for multi-component epoxy nanocomposites based on titania and alumina nanoparticles

The enhanced flammability performance of multi-component epoxy nanocomposites based on titania and alumina can be ascribed to the continuous, cohesive, and compact char layer that was developed as a result of the interaction between these nano-oxides and AP750 (see Figure 10.16).

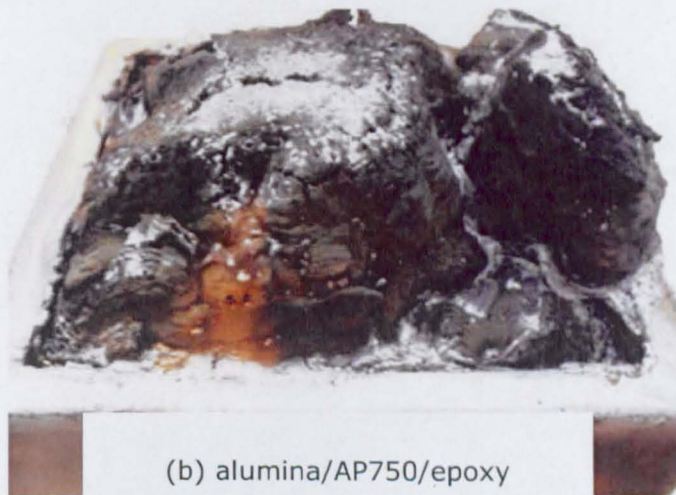


Fig. 10.16: The intumescent action of multi-component epoxy nanocomposite based on: (a) titania, (b) alumina, nanoparticles

A flammability performance index (FPI) was developed by dividing TTPHR over PHRR. FPI was employed as an evaluating parameter, the higher the FPI the better the flammability performance. The FPI of virgin epoxy was employed as a reference value. The relative fire performance index (RFPI) was developed, to quantify the developed nanocomposite flammability performance relative to virgin polymer. Table 10.4 shows the main/developed flammability parameters of multi-component epoxy nanocomposites based on nano-oxides compared with virgin epoxy.

Table 10.4: The main/developed flammability parameters of multi-component epoxy nanocomposites based on nano-oxides

Formulation	TTI (secs)	PHR (kW/m ²)	Reduction in PHR	TTPHR (secs)	FPI (sm ² /kW)	RFPI
Virgin epoxy	68	1094	0%	216	0.20	1
Formulation 1 (AP750/epoxy)	14	512.3	53%	232	0.45	2.25
Formulation 2 (silica/AP750/epoxy)	16	755.9	31%	196	0.26	1.3
formulation 3 (titania/AP750/epoxy)	58	530	52%	274	0.52	2.6
formulation 4 (alumina/AP750/epoxy)	34	475.7	56%	270	0.57	2.8

From RFPI values, it was possible to enhance virgin epoxy flammability performance 2.8 fold at 10 wt % solid loading via the synergism between alumina nanoparticles and AP750. Furthermore, there was a marked increase in TTI and TTPHR compared with AP750/epoxy this enhanced flammability performance can be ascribed to the developed cohesive char layer which acted as an insulating barrier.

The obtained results were found to be in good agreement with the findings of Laachachi in 2005 (Laachachi, 2005); where the partial substitution of phosphinate FR at 15 wt % solid loading by nano-alumina showed a synergistic effect with a marked decrease in peak/maximum heat released rate (PHRR) in cone calorimeter test. On the other hand, no significant improvement was achieved through the partial substitution of phosphinate FR by nano-TiO₂ (Figure 2.23).

In the current research, enhanced flammability performance was achieved compared with the work done by Laachachi in 2005, as the PHR of virgin epoxy was decreased by 56 % and the TTPHR was extended by 54 seconds via the synergism between alumina and AP750 at total solid loading level of 10 wt % (Formulation 4).

10.4.3 Flammability performance of multi-component epoxy nanocomposite based on nano-fire extinguishers

The impact of the partial substitution of AP750 with nano-fire extinguisher nanoparticles on epoxy flammability performance was evaluated. The flammability performance of multi-component epoxy nanocomposites based on HA and AOH (formulations 5 and 6 in Table 10.2) was evaluated by cone calorimeter testing and compared with virgin epoxy and AP750/epoxy (Figure 10.17).

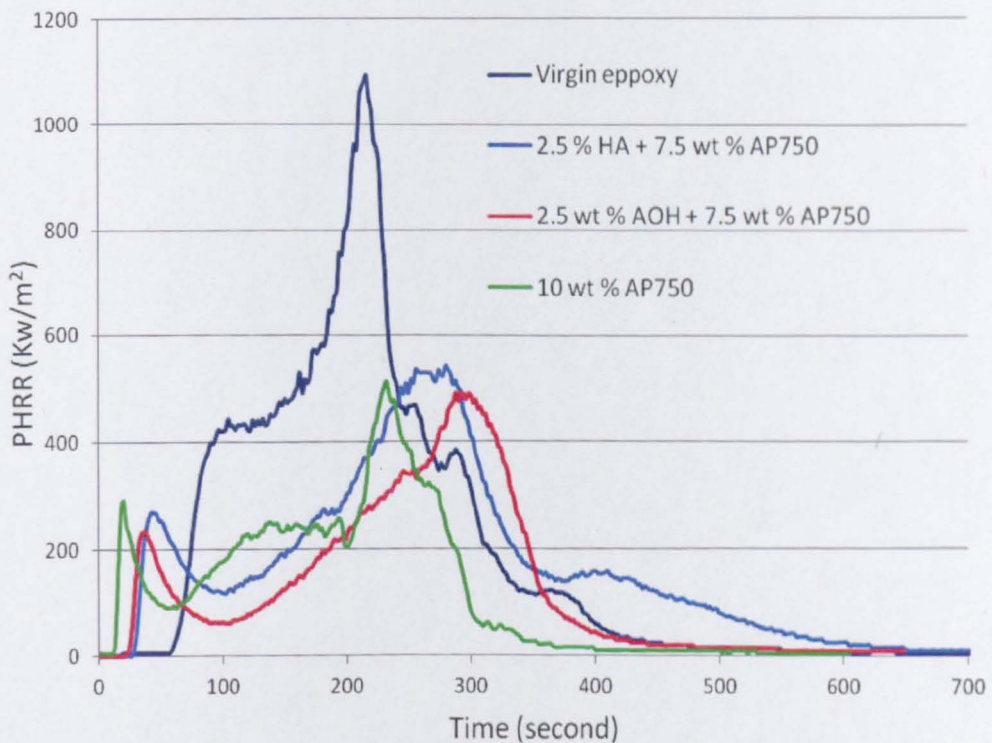


Fig. 10.17: Evolution of HRR for multi-component epoxy nanocomposites: HA/AP750/epoxy and AOH/AP750/epoxy

HA and AOH again showed a synergistic effect with AP750; as they reduced the HRR and extended the TTI and TTPHR of AP750/epoxy. Formulation 5, based on HA nanoparticles, showed an intumescent action with the formation of a compact cohesive char layer. The sample height increased 9 fold. Formulation 6, based on AOH nanoparticles, promoted char expansion as the tested specimen height increased 25 fold (Figure 10.18).



Fig. 10.18: The intumescent action of multi-component epoxy based on:
(a) HA, and (b) AOH nanoparticles

HA nanoparticles could promote charring in the condensed phase, as a result of the high phosphorous content (18.5 wt %). HA could have a gas

10. Multi-component flame retardant systems

phase action due to the released active flame scavenger species such as PO_2^* , PO^* , and HPO^* . This gas phase effect could dilute the reactive species and reduce the reaction exothermicity.

AOH can release surface water at low decomposition temperature (223 °C). At high decomposition temperature (550 °C), AOH can absorb a great amount of heat (700 kJ/Kg) with the release of water and with the formation of alumina in the burning surface. The released water could support intumescent action of AP750, dilute the burning gases, and cool down the burning surface. The produced alumina in the burning surface could have a synergistic effect with AP750 via the formation of stable crystalline forms which could improve the formed char mechanical strength and insulating properties. Table 10.5 shows the main/developed flammability parameters of multi-component epoxy nanocomposite based on these nano-fire extinguishers compared with virgin epoxy.

Table 10.5: The main/developed flammability parameters of multi-component epoxy nanocomposites based on nano-fire extinguishers

Formulation	TTI (second)	PHR (Kw/m ²)	Reduction in PHR	TTPHR (second)	FPI (S. Kw/m ²)	RFPI
Virgin epoxy	68	1094	0%	216	0.20	1
Formulation 1 (AP750/epoxy)	14	512.3	53%	232	0.45	2.25
Formulation 5 (HA/AP750/epoxy)	32	535.7	51%	282	0.53	2.7
Formulation 6 (AOH/AP750/epoxy)	28	489.8	55%	288	0.56	2.8

Formulations 5 and 6 showed RFPI of 2.7 and 2.8 respectively compared with virgin epoxy; this enhanced flammability performance can be ascribed to the synergism between nano-fire extinguisher FR action and AP750 intumescent FR action. To the knowledge of the author, this is the first time HA has been used as a FR agent, and the first time the combination between HA or AOH nanoparticles with an intumescent FR agent (AP750) has been investigated.

10.5 Intumescent coating

Intumescent coatings have seen a large increase in popularity as a method of passive fire protection over the past few years (Xiao, 2010). Under the effect of heat, the coating swells forming a protective barrier against heat transfer from the heat source to the substrate (Wladyka-Przybylak and Kozlowski, 1999). Thermoset nanocomposites (TSNCs) are capable of substantially improving the coating performance, in terms of the coating's mechanical, barrier, and flame resistance properties (Xiao et al., 2010).

Protection of metallic structures against fire has become an important issue in construction, petrochemical industries, as well as in the marine and military fields (Jimenez et al., 2006b). Steel structures lose a significant part of their load-carrying ability when their temperature exceeds 500 °C (Kruppa et al., 1998).

The epoxy nanocomposite based on HA and AP750 showed the most cohesive and integrated char layer in cone calorimeter testing; therefore it was employed as an intumescent coating. A multi-component epoxy nanocomposite based on HA and AP750 at 12 wt % total solid loading (3 wt% HA + 9 wt% AP750) was prepared by mechanical mixing for one hour

and vacuum casting. A coating layer of 3 mm thickness was applied on a steel plate. The steel plate dimensions were 13.5 cm width \times 22 cm length \times 1.2 mm thickness. The intumescent coating was cured at 70 °C for 48 hours.

In this test, a muffle furnace was heated up to 900 °C. The furnace inlet of 9.5 cm \times 18 cm was opened; the coated steel plate was fixed at the muffle furnace inlet with the coating facing the furnace. A thermocouple was fixed at the backside of the steel plate. The temperature of the steel plate was recorded as a function of time by using picolog software. The fireproofing parameter (the time required for steel substrate to reach 500 °C) was evaluated. Figure 10.19 shows the temperature/time curve for intumescent coated steel to uncoated steel plate.

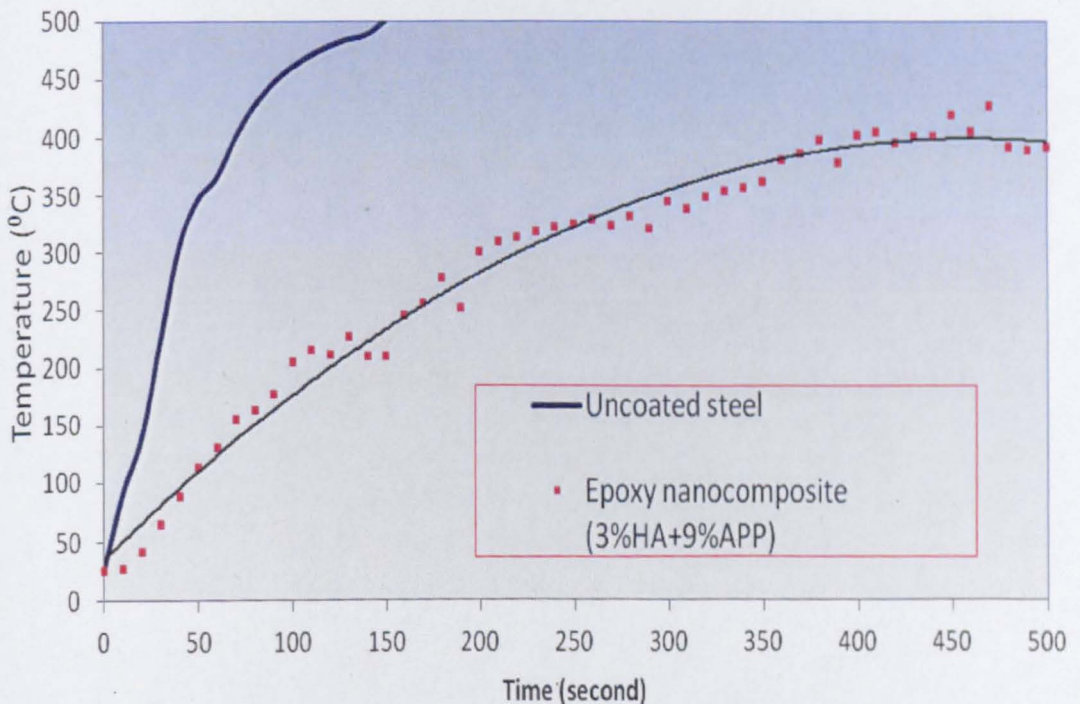


Fig. 10.19: The temperature/time curve for steel and coated steel

The uncoated steel plate was heated up rapidly; its temperature reached 500 °C within 150 seconds. The coated steel plate appeared to heat at a lower rate, and seemed to plateau at 400 °C after 500 seconds. A

protective insulating char layer was developed; this char layer insulated the steel substrate from the heat source.

Enhanced fireproofing performance was achieved at 12 wt % solid loading compared with the work done by Li in 2007 (Li et al., 2007) as He used 60 wt % solids. Guoxin used thermally unstable binder (acrylic resin) which started to decompose at low temperatures (125 °C); in this work, the more thermally stable binder (epoxy resin) was employed.

10.6 Conclusion of multi-component flame retardant systems

In this chapter, the impact of selected nanoparticles (nano-oxides: titania, silica, alumina and nano-fire extinguishers: HA , AOH) on AP750/epoxy direct flame resistance was investigated in an attempt to achieve a self extinguishing epoxy nanocomposite at 10 wt % total solid loading level. Nano-oxides, mainly titania and alumina, as well as nano-fire extinguishers, mainly HA and AOH, showed a synergistic effect with AP750. The self extinguishing epoxy nanocomposite with balanced mechanical, thermal, and flammable properties was developed at 10 wt % solid loading. The optimal combination of these nanoparticles to AP750 appeared to be 1:3. The self extinguishing multi-component epoxy naocomposites showed enhanced flammability performance in cone calorimeter testing compared with AP750/epoxy and virgin epoxy; this enhanced flammability performance could be ascribed to the catalytic action between nanoparticles and AP750 intumescent agent.

A multi-component epoxy nanocomposite based on HA and AP750 at 12 wt % total solid loading was developed as an intumescent coating. The

10. Multi-component flame retardant systems

intumescent coating was able to prevent the heat transfer from the heat source to the substrate and an equilibrium was achieved at 400 °C. This fireproofing performance, was ascribed to the developed cohesive char layer.

CHAPTER 11

11. Conclusions and future work

11.1 Conclusions

The key challenge when attempting to produce a nanocomposite, is avoiding aggregation of nanomaterials that need to be evenly dispersed throughout the polymer matrix.

Commercial P25 titania nanoparticles were used as a base case to investigate how dry nanoparticles could be effectively dispersed into polymeric matrix. The processing factors that could affect dry nano-oxide dispersion into epoxy resin were investigated. The investigated parameters included solids loading level, mechanical mixing, and heating. There was an improvement in the dispersion of dry nanoparticles with increasing solids loading level, and with mechanical mixing as a result of the induced attrition effect between the nanoparticles under mechanical mixing. Heating was required to improve polymer processing at high solids loading level. However, heating also dramatically increased aggregation levels in the final composite as a result reduced shear which is responsible for the separation of the aggregates during mixing.

Two main types of nanoparticles were formulated and surface modified using CHS devised by the University of Nottingham tested in this thesis; those that could have a synergistic effect with traditional FR systems (mainly titania nanoparticles); and those that might also have a flame retardant action (mainly HA and AOH). Regardless of the nature of the manufacturing process nanoparticles, once dry, form aggregates that

are difficult to redisperse. Keeping the nanomaterials in a slurry therefore was found to be an important way of avoiding poor dispersion characteristics. However, if unformulated there was still a tendency for the colloidal nanoparticles (from CHS) to flocculate over time due to steric instability in suspension. It was possible to sterically stabilize colloidal nanoparticles via surface modification with different organic ligands and with different polymeric surfactants. Some of the chosen surfactants had amphipathic character (containing hydrocarbon backbone and ionic groups) therefore they were able to anchor the nanoparticle surface and to extract the nanoparticles to the organic layer. Steric stabilization was performed either at the capping point, post reaction but prior to collection, or exclusively in the reactor during nanoparticle formation.

CHS parameters were synchronized together in an attempt to achieve an effective surface modification of titania nanoparticles with DDSA via a post synthesis surface modification approach. An effective post-synthesis surface modification approach was developed through which titania was uniformly surface modified with DDSA and extracted to the organic layer. Titania surface modification with DDSA in the reactor was investigated. Surface modification in the reactor (i.e. during nanoparticle production) was reported to be more efficient than modification at the capping point; which resulted in a higher surfactant loading level and uniform coating layer was achieved at the same hydrothermal conditions. Titania surface modification could also be targeted towards flame retardancy by employing a phosphorous based compound as the surfactant.

Polymeric surfactants are able to bind to numerous surface sites at the same time, forming durable adsorption surfactant layers. Titania was effectively stabilized in water colloid with a polar polymeric surfactant

(PAA). Furthermore, titania was surface modified with different amphipathic polymeric surfactants mainly poly(ethylene-co-AA) of different polarities; this kind of surface modification can improve and diversify the nanoparticle dispersion into polymeric matrices with different polarities.

Nanoparticles which can have a flame retardant action mainly HA and AOH, were formulated and surface modified using CHS. HA has a phosphorous content of 18.5 wt %. This high phosphorous content might produce flame retardant action. To the knowledge of the author, this is the first time to use HA as a phosphorous-based flame retardant agent. HA was formulated and functionalized with different amphipathic surfactants mainly DDSA and poly(ethylene-co-AA 15 wt %). Organic modified HA showed smaller platelet dimensions and higher surface area to the unmodified counterparts. HA surface modification was adjusted for the purpose of achieving exfoliated HA nanocomposites (HA platelet at constant interspacing distance) by using DDA surfactant. Organically modified HA showed enhanced surfactant loading levels compared with titania nanoparticles, as HA surfaces undergo covalent bonding rather than hydrogen bonding.

AOH nanoparticles can act as heat sink material by consuming energy during thermal decomposition, releasing water, and forming an oxide layer. AOH was formulated during CHS; furthermore AOH was flocculated from its colloidal gel by using poly(acrylamide-co-AA) as a flocculating agent. Separating AOH nanoparticles from their synthesis medium was vital to have a clean product, free from counter ions. AOH showed a FR action by releasing the surface water at low decomposition temperature (223 °C), and a heat sink action via an endothermic decomposition reaction with the formation of Al₂O₃ at high decomposition temperature (550 °C). In both decomposition stages the released water would cool the burning polymer

surface and dilute the surrounding burnable gasses. Additionally the oxide residue (alumina) could act as a barrier protecting the polymeric underlayers from further decomposition.

Surface modified nanoparticles (titania, HA, and AOH) showed an enhanced compatibility with the polymeric matrix than unmodified counterparts. A solvent blending approach to integrate colloidal organic modified nanoparticles, dispersed in organic solvent, into epoxy resin was developed. Through this approach enhanced nanoparticle dispersion was achieved compared with the dispersion of dry nanoparticles; as the nanoparticles were maintained dispersed in all processing stages. Furthermore, this solvent blending approach enabled the elimination of freeze drying and the redispersion of aggregated dry nanoparticles into polymeric matrix.

The impact of different nanoparticles of different morphologies ranging from nanospheres (titania), nanoplates (HA), to nanorods (AOH) onto epoxy mechanical properties was evaluated by mechanical compressive strength test. Nanoparticles were able to improve the compressive stress-strain response of epoxy resin after maximum compressive stress (enhanced resistance to mechanical failure). The enhanced compressive stress-strain response of epoxy nanocomposites to virgin epoxy can be explained by the strong interaction between the nanoparticles and the polymer chains. Titania/epoxy nanocomposites showed enhanced thermal stability, and structural integrity under heating effect compared with virgin polymer.

A laboratory testing technique including Bunsen testing, video recording, and image analysis was developed to quantify the nanocomposite direct

flame resistance. It was possible to quantify the flammability behaviour starting from initial ignition, flame shape and size, flammable dripping, until self-extinguishing. To the knowledge of the author this is the first time image analysis has been used to quantify direct flame resistance.

It was not possible to achieve self extinguishing epoxy nanocomposite by using inert nano-oxides like titania or even nanoparticles with a flame retardant action, like HA and AOH, at 10 wt % solid loading. These nanocomposites did burn more slowly over an extended period of time compared to virgin epoxy.

It could be concluded that nanoparticles are a part of the flame retardancy solution, although not the whole solution. The synergism between bespoke nanoparticles, nano-oxides (titania, silica, and alumina) and flame retardant materials (HA and AOH) with AP750 intumescent FR agent was investigated in order to achieve self extinguishing epoxy nanocomposite at 10 wt % solid loading.

Silica nanoparticles showed little (or a slight antagonistic) effect with AP750; the epoxy nanocomposite based on silica/AP750 was not able to resist a direct flame and self extinguish. Nano-oxides, mainly titania and alumina, as well as nano-fire extinguishers mainly HA and AOH showed a synergistic effect with AP750; epoxy nanocomposites based on any of these nanoparticles with AP750 at 10 wt % total solid loading were able to resist direct flame source and self extinguish.

The developed self extinguishing multi-component epoxy nanocomposites showed enhanced flammability performance during cone calorimetry testing compared with AP750/epoxy and virgin polymer. This enhanced

flammability performance is due to the synergism between these nanoparticles and the intumescent FR system.

Multi-component epoxy nanocomposite based on HA and AP750 and a total solid loading level of 12 wt% was tested as an intumescent coating of 3 mm thickness for steel substrate protection. The temperature of steel substrate was recorded with time while the coated steel side was subjected to 900 °C. The intumescent coating successfully insulated the substrate from heat source maintaining a surface temperature of only 400 °C after 500 seconds. The effectiveness of the developed intumescent coating is through the development of a cohesive insulating char barrier.

11.2 Future work

The formulation of TiO₂ 1 D nano-structural based materials via alkaline hydrothermal treatment was discovered by Kasuga and colleagues in 1998 (Fujishima et al., 1999, Bavykin et al., 2006). TiO₂ 1D nano-structural based materials might offer a real answer to the need for strength in composites and be a plausible substitute for CNTs. CNT's provide excellent strengthening properties as a result of their high aspect ratio, but (in the end) they are still an expensive carbon based material in a flammable polymer. In contrast to CNTs, titanate and titanium oxide nanotubes are high temperature ceramics and can be readily synthesized by employing simple chemical methods and using low cost materials (Prescott and Schwartz, 2008b, Bavykin and Walsh, 2010). Figure 11.1 shows the different titanate 1 D nano-structured morphologies that can be produced by alkaline hydrothermal synthesis.

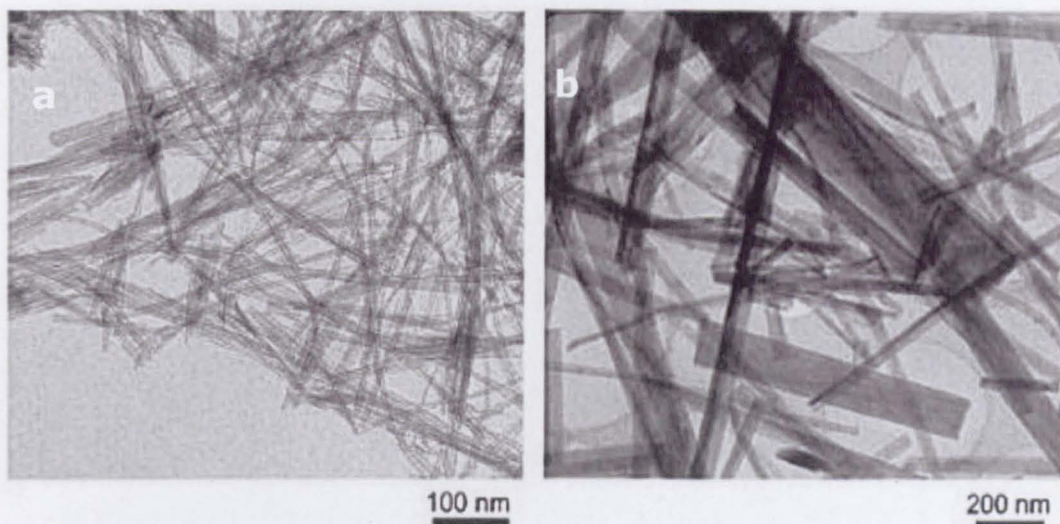


Fig. 11.1: TEM Images of: titanate nanotubes (a), titanate nanofibers (b), adapted from (Bavykin et al., 2004).

The surface chemistry of CNTs requires special treatment under aggressive conditions. By contrast, the abundance of $-OH$ groups on the surface of titanate nanotubes can readily allow functionalization (Figure 11.2) (Bavykin and Walsh, 2010).

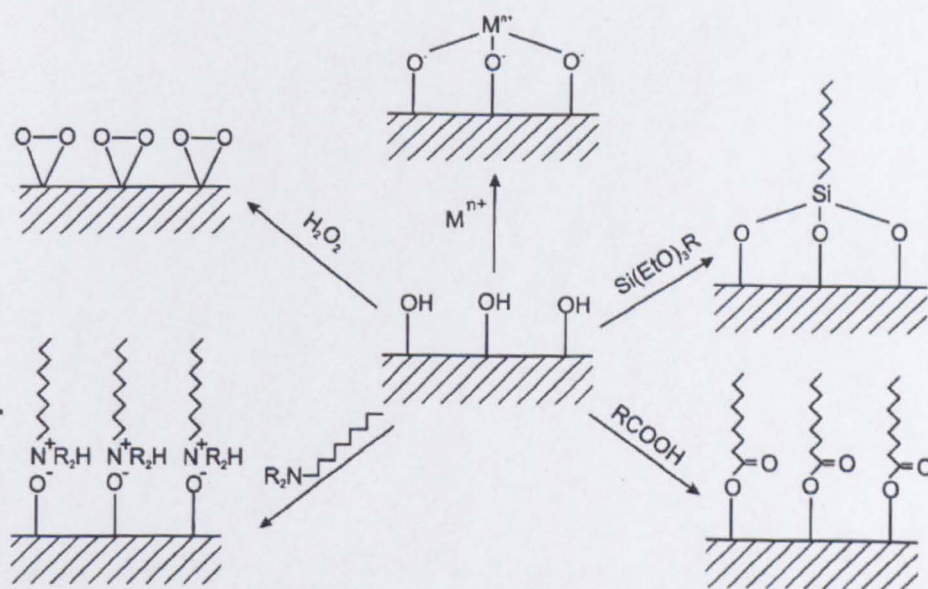


Fig. 11.2: Surface functionalization of titanate nanotubes using chemical reactions, adapted from (Bavykin and Walsh, 2010).

Titania nanoparticles produced by CHS are in their colloidal state; these colloidal nanoparticles could be employed for the synthesis of titanate nanorods and nanotubes via alkaline hydrothermal treatment. It could be possible to use the CHS technique to perform online alkaline hydrothermal treatment, downstream of the reactor but prior to collection point. Therefore TiO_2 1D nano-structural based materials might be formulated continuously. TiO_2 1D nano-structural based materials could be used for the purpose of improving the heat resistance of composites at solid loading levels of 0.5 wt % as described for CNTs in Figure 2.19. Therefore, nanocomposites with optimised mechanical and flame retardancy could be achieved at low solid loadings (<5%).

The production of hybrid nanomaterials could also be a way forward for flame retardant composites. CNT surface modification with carboxylic groups is documented (Yang et al., 2010). In 2010, Shin Yang investigated the effect of functionalized carbon nanotubes onto epoxy thermal stability. MWCNTs were grafted with benzene tricarboxylic acids (BTC) (Figure 11.3). However, the functionalized MWCNTs reported less thermal stability than the pristine ones.

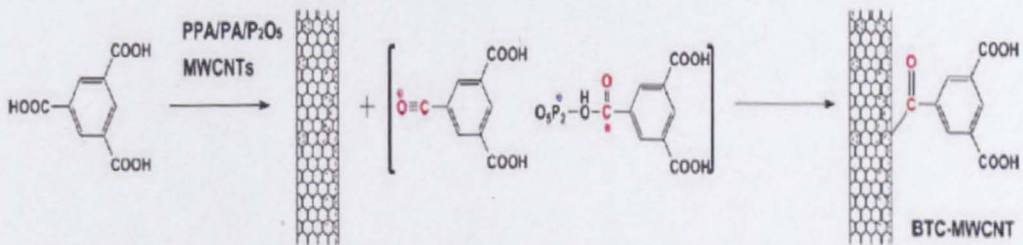


Fig. 11.3: Preparation of BTC-MWCNTs/epoxy composites, adapted from (Yang et al., 2010).

In this Thesis, thermally stable carboxylic polymeric surfactants were employed for nano-fire extinguishers (HA and AOH) surface modification; and these surfactants could be anchored to the surface of a CNT. A CNT coated with 'fire extinguisher nanoparticles' might grant CNT a FR action as well as its enhanced strength and condensed phase effects. Enhanced flammability and mechanical performance could be achieved at extremely low solid loading.

Inorganic hydroxides represent more than 50% of FRs sold globally yet high loading levels are needed to fulfil the flammability standards (Wilkie and Morgan, 2010). These levels could be decreased to sensible levels if controlled high quality particles are used and dispersed efficiently throughout the matrix of the polymer with minimum agglomeration. The CHS technique, devised by the University of Nottingham, has been shown to be a benign route for the formulation and functionalization of such clean and non-toxic flame retardant materials.

References

- ADDEN, N., GAMBLE, L. J., CASTNER, D. G., HOFFMANN, A., GROSS, G. & MENZEL, H. 2006. Phosphonic acid monolayers for binding of bioactive molecules to titanium surfaces. *Langmuir*, 22, 8197-8204.
- ADDINK, R. & OLIE, K. 1995. MECHANISMS OF FORMATION AND DESTRUCTION OF POLYCHLORINATED DIBENZO-P-DIOXINS AND DIBENZOFURANS IN HETEROGENEOUS SYSTEMS. *Environmental Science & Technology*, 29, 1425-1435.
- ADSCHIRI, T., HAKUTA, Y. & ARAI, K. 2000. Hydrothermal synthesis of metal oxide fine particles at supercritical conditions. *Industrial & Engineering Chemistry Research*, 39, 4901-4907.
- ADSCHIRI, T., KANAZAWA, K. & ARAI, K. 1992. Rapid and continuous hydrothermal synthesis of boehmite particles in subcritical and supercritical water. *the American Ceramic Society*, 75, 2615-2618.
- ALEXANDRE, M. & DUBOIS, P. 2000. Polymer-layered silicate nanocomposites: preparation, properties and uses of a new class of materials. *Materials Science & Engineering R-Reports*, 28, 1-63.
- ALEXENDER, M. & DUBBIES, P. 2000. Polymer Layered Silicate Nanocomposites: Preparation, Properties, and uses of a new class of materials. *Materials Science & Engineering R-Reports*, 28, 1-63.
- ALMERAS, X., LE BRAS, M., HORNSBY, P., BOURBIGOT, S., MAROSI, G., KESZEI, S. & POUTCH, F. 2003. Effect of fillers on the fire retardancy of intumescent polypropylene compounds. *Polymer Degradation and Stability*, 82, 325-331.
- ANTCZAK, M. 2008. *New methodologies for the synthesis of organophosphorous compounds*. Ph.D., Texas Cristian University.
- BABRAUSKAS, V. 1984. DEVELOPMENT OF THE CONE CALORIMETER - A BENCH-SCALE HEAT RELEASE RATE APPARATUS BASED ON OXYGEN-CONSUMPTION. *Fire and Materials*, 8, 81-95.
- BABUSHOK, V. & TSANG, W. 2000. Inhibitor rankings for alkane combustion. *Combustion and Flame*, 123, 488-506.
- BALLICE, L. & REIMERT, R. 2002. Classification of volatile products from the temperature-programmed pyrolysis of polypropylene (PP), atactic-polypropylene (APP) and thermogravimetrically derived kinetics of pyrolysis. *Chemical Engineering and Processing: Process Intensification*, 41, 289-296.
- BARATON, M. 2003. *Synthesis, Functionalization and Surface Treatment of Nano Particles*, ASP.
- BARR, T. (ed.) 1994. *The Principles and Practice of X-ray Photoelectron Spectroscopy* Boca Raton: CRC Press.

- BAVKIN, D. V., FRIEDRICH, J. M. & WALSH, F. C. 2006. Protonated titanates and TiO₂ nanostructured materials: Synthesis, properties, and applications. *Advanced Materials*, 18, 2807-2824.
- BAVKIN, D. V., PARMON, V. N., LAPKIN, A. A. & WALSH, F. C. 2004. The effect of hydrothermal conditions on the mesoporous structure of TiO₂ nanotubes. *Journal of Materials Chemistry*, 14, 3370-3377.
- BAVKIN, D. V. & WALSH, F. C. (eds.) 2010. *Titanate and Titania Nanotube*, London: RSC.
- BECKER, O. & SIMON, G. P. 2005. Epoxy Layered Silicate Nanocomposites. *Adv. Polym. Sci.*, 179, 29-82.
- BELLUCCI, F., CAMINO, G., FRACHE, A. & SARRA, A. 2007. Catalytic charring-volatilization competition in organoclay nanocomposites. *Polymer Degradation and Stability*, 92, 425-436.
- BENT 2010. Business Publications. http://findarticles.com/p/articles/mi_m0EIN/is_2007_Oct_22/ai_n2_1055514/.
- BISHOP, D. P. & SMITH, D. A. 1970. COMBINED PYROLYSIS AND RADIOCHEMICAL GAS CHROMATOGRAPHY FOR STUDYING THERMAL DEGRADATION OF EPOXY RESINS AND POLYIMIDES .1. DEGRADATION OF EPOXY RESINS IN NITROGEN BETWEEN 400 DEGREES C AND 700 DEGREES C. *Journal of Applied Polymer Science*, 14, 205-&.
- BOISVERT, J. P., PERSELLO, J., CASTAING, J. C. & CABANE, B. 2001. Dispersion of alumina-coated TiO₂ particles by adsorption of sodium polyacrylate. *Colloids and Surfaces a-Physicochemical and Engineering Aspects*, 178, 187-198.
- BOURBIGOT, S. & DUQUESNE, S. 2007. Fire retardant polymers: recent developments and opportunities. *Journal of Materials Chemistry*, 17, 2283-2300.
- BOURBIGOT, S., LE BRAS, M., DUQUESNE, S. & ROCHERY, M. 2004. Recent advances for intumescent polymers. *Macromolecular Materials and Engineering*, 289, 499-511.
- BOUVY, A. & OPSTAELE, A. (eds.) 1995. *Waterborne Coating and Additives*, London: Royal Chemical Society.
- BRAS, M. L. & GAMINGO, G. 1998. *Fire Retardancy of polymers the use of Intumescence*, Royal Society
- BRASS, M., WILKIE, A. & BOURBIGOT, S. (eds.) 2005. *New Applications of Mineral Fillers*, Cambridge: Royal Society of Chemistry.
- BRINKER, J. & SCHERER, G. W. (eds.) 1990. *Sol-Gel Science: The Physics and Chemistry of Sol-Gel Processing* San Diego: Academic Press.

- BRITISH-STANDARD-INSTITUTE 1972. Test methods and criteria for the fire resistance of elements of building construction. *BS 476, Part 8*. London: British Standard Institute.
- BUCHHOLZ, F. & WILKS, E. (eds.) 2001. *Industrial Polymer Handbook*: Wiley.
- BUINING, P. A., PATHMAMANOхарAN, C., JANSEN, J. B. H. & LEKKERKERKER, H. N. W. 1991. PREPARATION OF COLLOIDAL BOEHMITE NEEDLES BY HYDROTHERMAL TREATMENT OF ALUMINUM ALKOXIDE PRECURSORS. *Journal of the American Ceramic Society*, 74, 1303-1307.
- BUSER, H.-R. 1987. Brominated and brominated/chlorinated dibenzodioxins and dibenzofurans: potential environmental contaminants. *Chemosphere*, 16, 1873-1876.
- BYRAPPA, K. & YOSHIMURA, M. (eds.) 2001. *Handbook of hydrothermal technology*, Norwich, US: William Andrew.
- CABAÑAS, A., DARR, J. A., LESTER, E. & POLIAKOFF, M. 2000. A continuous and clean one-step synthesis of nano-particulate Ce1. *Chemical Communications*, 11, 901-902.
- CAMINO, G., COSTA, L. & TROSSARELLI, L. 1984. Study of the mechanism of intumescence in fire retardant polymers: Part II—Mechanism of action in polypropylene-ammonium polyphosphate-pentaerythritol mixtures. *Polymer Degradation and Stability*, 7, 25-31.
- CAMINO, G., COSTA, L. & TROSSARELLI, L. 1985a. Study of the mechanism of intumescence in fire retardant polymers: Part V--Mechanism of formation of gaseous products in the thermal degradation of ammonium polyphosphate. *Polymer Degradation and Stability*, 12, 203-211.
- CAMINO, G., COSTA, L. & TROSSARELLI, L. 1985b. Study of the mechanism of intumescence in fire retardant polymers: Part V—Mechanism of formation of gaseous products in the thermal degradation of ammonium polyphosphate. *Polymer Degradation and Stability*, 12, 203-211.
- CAMINO, G. & DELOBEL, R. (eds.) 2000. *Fire Retardancy of Polymeric Materials*, New York: Marcel Dekker.
- CAMINO, G., MAFFEZZOLI, A., BRAGLIA, M., DE LAZZARO, M. & ZAMMARANO, M. 2001. Effect of hydroxides and hydroxycarbonate structure on fire retardant effectiveness and mechanical properties in ethylene-vinyl acetate copolymer. *Polymer Degradation and Stability*, 74, 457-464.
- CHANG, S. J. & CHANG, F. C. 1999. Synthesis and characterization of copolyesters containing the phosphorus linking pendent groups. *Journal of Applied Polymer Science*, 72, 109-122.

- CHENG HENG PANG, B. H., TAO WU, EDWARD LESTER 2013. An automated ash fusion test for characterisation of the behaviour of ashes from biomass and coal at elevated temperatures. *Fuel*, 103, 454-466.
- CHINESE-STANDARD 1995. Classification and test methods for fire retardancy of finishing fire retardant paints GB 15442.2 China.
- CIPIRIANO, B. H., KASHIWAGI, T., RAGHAVAN, S. R., YANG, Y., GRULKE, E. A., YAMAMOTO, K., SHIELDS, J. R. & DOUGLAS, J. F. 2007. Effects of aspect ratio of MWNT on the flammability properties of polymer nanocomposites. *Polymer*, 48, 6086-6096.
- CLERICI, C., GU, X. & FORSTER, M. (eds.) 2009. *Service Life Prediction of Polymeric Material*, New York: Springer.
- COLEMAN, B. (ed.) 1993. *Practical Sampling Techniques for Infrared Analysis*, Boca Raton: CRC Press.
- CONNOLLY, J. R. 2007. Introduction to x-ray powder diffraction. Accessed <http://epswww.unm.edu/xrd/xrdclass/01-XRD-Intro.pdf> [Apr. 2007].
- CORBRIDGE, D. E. C. (ed.) 1995. *Phosphorus: An Outline of its Chemistry, Biochemistry, and Technology*, Amsterdam: Elsevier.
- COSTACHE, M. C., HEIDECKER, M. J., MANIAS, E., CAMINO, G., FRACHE, A., BEYER, G., GUPTA, R. K. & WILKIE, C. A. 2007a. The influence of carbon nanotubes, organically modified montmorillonites and layered double hydroxides on the thermal degradation and fire retardancy of polyethylene, ethylene-vinyl acetate copolymer and polystyrene. *Polymer*, 48, 6532-6545.
- COSTACHE, M. C., HEIDECKER, M. J., MANIAS, E., CAMINO, G., FRACHE, A., BEYER, G., GUPTA, R. K. & WILKIE, C. A. 2007b. The influence of carbon nanotubes, organically modified montmorillonites and layered double hydroxides on the thermal degradation and fire retardancy of polyethylene, ethylene-vinyl acetate copolymer and polystyrene. *Polymer*, 48, 6532-6545.
- CULLIS, F. & HIRSCHLER, M. (eds.) 1981. *The combustion of organic polymers*, Oxford: Oxford University Press.
- CUNLIFFE, L. 2005. *Decomposition studies of fire retardant action of phosphorous compounds in poly(methyl methacrylate), polystyrene and their copolymer* Ph.D., University of Salford.
- DALMAS, F., CHAZEAU, L., GAUTHIER, C., CAVAILLÉ, J.-Y. & DENDIEVEL, R. 2006. Large deformation mechanical behavior of flexible nanofiber filled polymer nanocomposites. *Polymer*, 47, 2802-2812.
- DARR, J. A. & POLIAKOFF, M. 1999. New directions in inorganic and metal-organic

- coordination chemistry in supercritical fluids. *Chemical Reviews*, 99, 495-541.
- DAS, K. K. & SOMASUNDARAN, P. 2001. Ultra-low dosage flocculation of alumina using polyacrylic acid. *Colloids and Surfaces A: Physicochemical and Engineering Aspects*, 182, 25-33.
- DAVIDE, R. (ed.) 1994. *CRC hand book of Chemistry and Physics*, Boca Raton: CRC Press.
- DAVIS, R., PALMOUR, H. & PORTER, R. (eds.) 1984. *Emergent Process Methods for High-Technology Ceramics*, New York: Plenum Press.
- DHARAIYA, D. & JANA, S. C. 2005. Thermal decomposition of alkyl ammonium ions and its effects on surface polarity of organically treated nanoclay. *Polymer*, 46, 10139-10147.
- DIGGES, K. H., GANN, R. G., GRAYSON, S. J., HIRSCHLER, M. M., LYON, R. E., PURSER, D. A., QUINTIERE, J. G., STEPHENSON, R. R. & TEWARSON, A. 2008. Human survivability in motor vehicle fires. *Fire and Materials*, 32, 249-258.
- DIPPY, J. F. J., HUGHES, S. R. C. & ROZANSKI, A. 1959. THE DISSOCIATION CONSTANTS OF SOME SYMMETRICALLY DISUBSTITUTED SUCCINIC ACIDS. *Journal of the Chemical Society*, 2492-2498.
- DRINKER 1937. The problem of possible systemic effects from certain chlorinated hydrocarbons. *Industrial Hygiene and Toxicology*, 7, 283-311.
- DYKSTRA, M. J. & REUSS, L. E. (eds.) 2003. *Biological electron microscopy: Theory, Techniques and troubleshooting*, New York: Springer.
- EBDON, R., HUNT, J., JOSEPH, P. & KONKEL, S. (eds.) 2001. *Flame-retarding thermoplastics: Additive versus reactive approach* London: Blackwell Science.
- EGERTON, F. (ed.) 1996. *Electron Energy-loss Spectroscopy in Electron Microscope*, New York: Springer.
- ELBHIRI, Z., CHEVALIER, Y., CHOVELON, J.-M. & JAFFREZIC-RENAULT, N. 2000. Grafting of phosphonate groups on the silica surface for the elaboration of ion-sensitive field-effect transistors. *Talanta*, 52, 495-507.
- EWALD, P. P. 1962. *Fifty years of X ray Diffraction*, Netherlands, Utrecht.
- FARROKHPAY, S. 2004. *Interaction of Polymeric Dispersants with Titania Pigment Particles* South Australia.
- FARROKHPAY, S. 2009. A review of polymeric dispersant stabilisation of titania pigment. *Advances in Colloid and Interface Science*, 151, 24-32.

- FARROKHPAY, S., MORRIS, G. E., FORNASIERO, D. & SELF, P. 2004. Effects of chemical functional groups on the polymer adsorption behavior onto titania pigment particles. *Journal of Colloid and Interface Science*, 274, 33-40.
- FINA, A., TABUANI, D., FRACHE, A. & CAMINO, G. 2005. Polypropylene-polyhedral oligomeric silsesquioxanes (POSS) nanocomposites. *Polymer*, 46, 7855-7866.
- FLEER, J., COHEN, A. & SCHEUTJENS, M. (eds.) 1993. *Polymers at Interfaces*, London: Chapman & Hall.
- FONTAINE, G., BOURBIGOT, S. & DUQUESNE, S. 2008. Neutralized flame retardant phosphorus agent: Facile synthesis, reaction to fire in PP and synergy with zinc borate. *Polymer Degradation and Stability*, 93, 68-76.
- FORGET, L., WILWERS, F., DELHALLE, J. & MEKHALIF, Z. 2003. Surface modification of aluminum by n-pentanephosphonic acid: XPS and electrochemical evaluation. *Applied Surface Science*, 205, 44-55.
- FRENS, G. & OVERBEEK, J. T. G. 1972. Repeptization and the theory of electrostatic colloids. *Journal of Colloid and Interface Science*, 38, 376-387.
- FU, M. & QU, B. 2004. Synergistic flame retardant mechanism of fumed silica in ethylene-vinyl acetate/magnesium hydroxide blends. *Polymer Degradation and Stability*, 85, 633-639.
- FUCHS, N. 1934. Theory of coagulation. *Zeitschrift Fur Physikalische Chemie-Abteilung a-Chemische Thermodynamik Kinetik Elektrochemie Eigenschaftslehre*, 171, 199-208.
- FUJISHIMA, A., HASHIMOTO, K. & WATANABE, T. (eds.) 1999. *TiO₂ Photocatalysis Fundamentals and Applications*, USA: BKC.
- GALLO, E., SCHARTEL, B. & RUSSO, P. 2010. Synergistic Flame retardant Halogen-Free Combination of Aluminium Phosphinate and Metal Oxides in PBT. *Fire Science and Engineering*, 12, 629.
- GEBHARDT, J. E. & FUERSTENAU, D. W. 1983. Adsorption of polyacrylic acid at oxide/water interfaces. *Colloids and Surfaces*, 7, 221-231.
- GIANNELIS, E. P. 1996. Polymer Layered Silicates Nanocomposites. *Adv. Mater.*, 8, 29-35.
- GIANNELIS, E. P., KRISHNAMOORTI, R. & MANIAS, E. 1999. Polymer-silicate nanocomposites: Model systems for confined polymers and polymer brushes. *Polymers in Confined Environments*, 138, 107-147.
- GILMAN, W., AWAS, W. & DAVIS, D. 2002. Polymer/layered silicate nanocomposites from thermally stable trialkylimidazolium-treated montmorillonite. *Chemistry of Materials*, 14, 10.

- GITIZEN, W. (ed.) 1970. *ALUMINAL AS A CERAMIC MATERIAL*, Ohio: The American ceramic society.
- GODDARD, G. 1995. Summary of statistics United Kingdom.
- GRAND, A. F. & WILKIE, C. A. 2000. *Fire Retardancy of polymeric Materials*, Dekker.
- GRATE, J. W. & ABRAHAM, M. H. 1991. Solubility interactions and the design of chemically selective sorbent coatings for chemical sensors and arrays. *Sensors and Actuators B: Chemical*, 3, 85-111.
- GREEN, J. 1996. A review of phosphorous containing flame retardants. *Fire Science and Engineering*, 13, 14.
- GRIFFITH, E. M. & DANILATOS, G. D. 1993. *Environmental scanning electron microscopy*, Wiley-Liss.
- HALPERN, Y., MOTT, D. M. & NISWANDER, R. H. 1984. FIRE RETARDANCY OF THERMOPLASTIC MATERIALS BY INTUMESCENCE. *Industrial & Engineering Chemistry Product Research and Development*, 23, 233-238.
- HASTIE, J. W. 1973. Mass spectrometric studies of flame inhibition: Analysis of antimony trihalides in flames. *Combustion and Flame*, 21, 49-54.
- HOBBS, H. 2006. *Biocatalysis in 'green solvents'*. Ph.D., University of Nottingham.
- HORROCKS, A. & PRICE, A. (eds.) 2000. *Mechanisms and modes of action in flame retardancy in polymers*, London: Woodhead Publishing Limited.
- HORROCKS, A. R. & PRICE, D. 2008. *Advances in fire retardant materials*, CRC.
- HORROCKS, R. 1986. Flame retarding finishing for textile. *Revis. Prog. Colouration*, 16, 62-101.
- HSE-OFFSHORE-TECHNOLOGY 1996. Jet fire resistance test of passive fire protection materials. OTI 95634. London.
- HUGHES, P., JACKSON, V. & ROTHON, N. 1993. Particle morphology effects in the performance of PMMA filled with aluminum hydroxide in a variety of fire tests. *Makromol. Chem. Makromol. Symp.*, 74, 179.
- HUNTER, R. J. (ed.) 1981. *Zeta Potential in Colloid Science*, New York: Academic Press.
- JEOL. 2006. *JEOL Transmission Electron Microscopes* [Online]. JEOL Ltd. [Accessed 2012].

- JIMENEZ, M., DUQUESNE, S. & BOURBIGOT, S. 2006a. High-throughput fire testing for intumescent coatings. *Industrial & Engineering Chemistry Research*, 45, 7475-7481.
- JIMENEZ, M., DUQUESNE, S. & BOURBIGOT, S. 2006b. Multiscale experimental approach for developing high-performance intumescent coatings. *Industrial & Engineering Chemistry Research*, 45, 4500-4508.
- JIMENEZ, M., DUQUESNE, S. & BOURBIGOT, S. 2006c. Multiscale Experimental Approach for Developing High Performance Intumescent Coatings. *Ind. Eng. Chem.*, 4500-4508.
- JOEL. 2006. *JEOL Scanning Electron Microscopes* [Online]. JEOL Ltd. . [Accessed 2012].
- KANDOLA, B. K., HORROCKS, A. R., MYLER, P. & BLAIR, D. 2002. The effect of intumescent on the burning behaviour of polyester-resin-containing composites. *Composites Part A: Applied Science and Manufacturing*, 33, 805-817.
- KASHIWAGI, T., DU, F. M., WINEY, K. I., GROTH, K. A., SHIELDS, J. R., BELLAYER, S. P., KIM, H. & DOUGLAS, J. F. 2005. Flammability properties of polymer nanocomposites with single-walled carbon nanotubes: effects of nanotube dispersion and concentration. *Polymer*, 46, 471-481.
- KASHIWAGI, T., GRULKE, E., HILDING, J., GROTH, K., HARRIS, R., BUTLER, K., SHIELDS, J., KHARCHENKO, S. & DOUGLAS, J. 2004. Thermal and flammability properties of polypropylene/carbon nanotube nanocomposites. *Polymer*, 45, 4227-4239.
- KATZ, S. & MILEWSKI, V. (eds.) 1987. *Handbook of Fillers for Plastics*, New York: Van Nostrand Reinhold.
- KHANNA, S. K. (ed.) 1997. *Handbook of nanophase materials*, New York: Dekker.
- KIM, S. J. & MCKEAN, D. E. 1998. Aqueous TiO₂ suspension preparation and novel application of ink-jet printing technique for ceramics patterning. *Journal of Materials Science Letters*, 17, 141-144.
- KIRKLAND, E. (ed.) 1998. *Advanced Computing in Electron Microscopy*, New York: Springer.
- KOTA, A. K., CIPRIANO, B. H., POWELL, D., RAGHAVAN, S. R. & BRUCK, H. A. 2007. Quantitative characterization of the formation of an interpenetrating phase composite in polystyrene from the percolation of multiwalled carbon nanotubes. *Nanotechnology*, 18.
- KREVELEN, W. (ed.) 1997. *Properties of Polymers: Their Correlation with Chemical Structure; Their Estimation and Prediction from Additive Group Contribution*, New York: Elsevier.

- KRITZER, P., BOUKIS, N. & DINJUS, E. 1999. Factors controlling corrosion in high-temperature aqueous solutions: a contribution to the dissociation and solubility data influencing corrosion processes. *The Journal of Supercritical Fluids*, 15, 205-227.
- KRUPPA, J., TWILET, L. & WESCHE, J. 1998. Fire Protection of Structural Steel Work. In: COMMUNITIES, C. O. T. E. (ed.). Communication of the European Communities.
- LAACHACHI, A. 2005. *Polymethacrylate de methyl (PMMA) : Developement de nouveaux systems retardateurs de flamme a base de nanocharges minerals. Research de synergies avec des montmorillonite et des composes phosphourous*. Metz.
- LAACHACHI, A., COCHEZ, M., FERRIOL, M., LOPEZ-CUESTA, J. M. & LEROY, E. 2005a. Influence of TiO₂ and Fe₂O₃ fillers on the thermal properties of poly(methyl methacrylate) (PMMA). *Materials Letters*, 59, 36-39.
- LAACHACHI, A., COCHEZ, M., LEROY, E., FERRIOL, M. & LOPEZ-CUESTA, J. M. 2007. Fire retardant systems in poly(methyl methacrylate): Interactions between metal oxide nanoparticles and phosphinates. *Polymer Degradation and Stability*, 92, 61-69.
- LAACHACHI, A., COCHEZ, M., LEROY, E., GAUDON, P., FERRIOL, M. & CUESTA, J. M. L. 2006. Effect of Al₂O₃ and TiO₂ nanoparticles and APP on thermal stability and flame retardance of PMMA. *Polymers for Advanced Technologies*, 17, 327-334.
- LAACHACHI, A., LEROY, E., COCHEZ, M., FERRIOL, M. & LOPEZ CUESTA, J. M. 2005b. Use of oxide nanoparticles and organoclays to improve thermal stability and fire retardancy of poly(methyl methacrylate). *Polymer Degradation and Stability*, 89, 344-352.
- LACHANCE, R. & CLAISSE, F. (eds.) 1995. *Quantitative X-ray Fluorescence Analysis: Theory and Applications* Chichester: John Wiley & Sons.
- LAMBERT, B., SHURVELL, F. & LIGHTNER, A. (eds.) 1998. *Organic Structural Spectroscopy*, Upper Saddle River: Prentice Hall.
- LAOUTID, F., BONNAUD, L., ALEXANDRE, M., LOPEZ-CUESTA, J. M. & DUBOIS, P. 2009. New prospects in flame retardant polymer materials: From fundamentals to nanocomposites. *Materials Science & Engineering R-Reports*, 63, 100-125.
- LAWSON, F., KAY, L. & ROBERTS, T. 1975. Mechanism of smoke inhibition by hydrated fillers. *Rubber Chem. Technol.*, 48, 124.
- LEBARON, P. C., WANG, Z. & PINNAVAIA, T. J. 1999. Polymer-layered silicate nanocomposites: an overview. *Applied Clay Science*, 15, 11-29.
- LEPOITTEVIN, B., DEVALCKENAERE, M., PANTOUSTIER, N., ALEXANDRE, M., KUBIES, D., CALBERG, C., JEROME, R. & DUBOIS, P. 2002a. Poly(epsilon-caprolactone)/clay nanocomposites prepared by melt

intercalation: mechanical, thermal and rheological properties. *Polymer*, 43, 4017-4023.

- LEPOITTEVIN, B., PANTOUSTIER, N., ALEXANDRE, M., CALBERG, C., JEROME, R. & DUBOIS, P. 2002b. Layered silicate/polyester nanohybrids by controlled ring-opening polymerization. *Macromolecular Symposia*, 183, 95-102.
- LESTER, E., BLOOD, P., DENYER, J., GIDDINGS, D., AZZOPARDI, B. & POLIAKOFF, M. 2006. Reaction engineering: The supercritical water hydrothermal synthesis of nano-particles. *Journal of Supercritical Fluids*, 37, 209-214.
- LEVCHIK, S. V. & WEIL, E. D. 2006. A review of recent progress in phosphorus-based flame retardants. *Journal of Fire Sciences*, 24, 345-364.
- LEVCHIK, V., CAMINO, G. & COATA, L. 1995. Mechanism of action of phosphorous-based flame retardants in nylon 6.1 Ammonium polyphosphate. *Fire and Materials*, 19, 10.
- LEWIN, M., PEARCE, E. & LEVON, E. 2006. Nanocomposites at elevated temperatures: Migration and structural changes. *Polymers for Advanced Technologies*, 17, 9.
- LI, G., LIANG, G., HE, T., YANG, Q. & SONG, X. 2007. Effects of EG and MoSi₂ on thermal degradation of intumescent coating. *Polymer Degradation and Stability*, 92, 569-579.
- LI, J. 2008. *Engineering Nanoparticles in Near-critical and Supercritical Water*. Ph.D., University of Nottingham.
- LIE, Y., QIANGHUA, W. & BAOJUN, Q. 2009. Synergistic effects and mechanism of multiwalled carbon nano tubes with magnesium hydroxide in halogen-free flame retardant EVA/MH/MWNT *Polymer Degradation and Stability*, 94, 751-756.
- LIN, C. H. 2004. Synthesis of novel phosphorus-containing cyanate esters and their curing reaction with epoxy resin. *Polymer*, 45, 7911-7926.
- LIUFU, S., XIAO, H. & LI, Y. 2005. Adsorption of poly(acrylic acid) onto the surface of titanium dioxide and the colloidal stability of aqueous suspension. *Journal of Colloid and Interface Science*, 281, 155-163.
- MADORSKY, L. (ed.) 1964. *Thermal degradation of polymers*, New York: Wiley.
- MAHANTY, J. & NINHAM, B. W. (eds.) 1976. *Dispersion Forces*, New York: Academic Press.
- MAILHOT, B., MORLAT, S., GARDETTE, J.-L., BOUCARD, S., DUCHET, J. & GERARD, J.-F. 2003. Photodegradation of polypropylene nanocomposites. *Polymer Degradation and Stability*, 82, 163-167.

- MALVERN-INSTRUMENTS-MANUAL 2004. zetasizer Nano series User Manual. *In: LTD., M. I. (ed.). London.*
- MALVERN-INSTRUMENTS. 2004. zetasizer Nano series User Manual. *In: LTD., M. I. (ed.). London.*
- MAROSI, G., MÁRTON, A., SZÉP, A., CSONTOS, I., KESZEI, S., ZIMONYI, E., TOTH, A., ALMERAS, X. & LE BRAS, M. 2003. Fire retardancy effect of migration in polypropylene nanocomposites induced by modified interlayer. *Polymer Degradation and Stability*, 82, 379-385.
- MARTIN, F. J. & PRICE, K. R. 1968. FLAMMABILITY OF EPOXY RESINS. *Journal of Applied Polymer Science*, 12, 143-&.
- MATHUR, S. & MOUDGIL, B. M. 1997. Adsorption Mechanism(s) of Poly(Ethylene Oxide) on Oxide Surfaces. *Journal of Colloid and Interface Science*, 196, 92-98.
- MATSON, D. W., LINEHAN, J. C., DARAB, J. G. & BUEHLER, M. F. 1994. Nanophase iron-based liquefaction catalysts: synthesis, characterization, and model compound reactivity. *Energy & Fuels*, 8, 10-18.
- MEIER, S. M. 2004. "Phosphorus(V) Oxide" *In: PAQUETTE, L. (ed.) Encyclopedia of Reagents for Organic Synthesis.* J. Wiley & Sons, New York: J. Wiley & Sons.
- MILLER, J. D., LASKOWSKI, J. S. & CHANG, S. S. 1983. Dextrin adsorption by oxidized coal. *Colloids and Surfaces*, 8, 137-151.
- MOON, J. H., SHUL, Y. G., HONG, S. Y., CHOI, Y. S. & KIM, H. T. 2005. A study on UV-curable adhesives for optical pick-up: II. Silane coupling agent effect. *International Journal of Adhesion and Adhesives*, 25, 534-542.
- MORGAN, A. B. & BUNDY, M. 2007. Cone calorimeter analysis of UL-94 V-rated plastics. *Fire and Materials*, 31, 257-283.
- MORGAN, A. B. & WILKIE, C. A. (eds.) 2007. *Flame Retardant Polymer Nanocomposites: Wiley.*
- MORGAN, B. 2006. Flame retardant polymer layered silicate nanocomposites: a review of commercial and open literature system. 17, 17.
- MORICE, L., BOURBIGOT, S. & LEROY, M. 1997. Heat transfer study of polypropylene-based intumescent systems during combustion. *Fire Science and Engineering*, 15.
- MORLAT-THERIAS, S., FANTON, E., GARDETTE, J. L., PEETERBROECK, S., ALEXANDRE, M. & DUBOIS, P. 2007. Polymer/carbon nanotube nanocomposites: Influence of carbon nanotubes on EVA photodegradation. *Polymer Degradation and Stability*, 92, 1873-1882.

- MORLEY, K. S., MARR, P. C., WEBB, P. B., BERRY, A. R., ALLISON, F. J., BROWN, P. D. & HOWDLE, S. M. 2002. Clean preparation on nanoparticulate metals in porous supports: a supercritical route. *Journal of Chemistry of Materials*, 12, 1898-1905.
- MORRIS, G. E., SKINNER, W. A., SELF, P. G. & SMART, R. S. C. 1999. Surface chemistry and rheological behaviour of titania pigment suspensions. *Colloids and Surfaces A: Physicochemical and Engineering Aspects*, 155, 27-41.
- MOSEMAN, M. & INGHAM, J. D. 1978. SMOKE PROPERTIES OF HIGHLY FILLED ETHYLENE PROPYLENE DIENE RUBBERS. *Elastomerics*, 110, 31-31.
- MYSELS, K. J. (ed.) 1959. *Introduction to Colloidal Chemistry*, New York: Interscience.
- NACHTIGALL, S. M. B., MIOTTO, M., SCHNEIDER, E. E., MAULER, R. S. & CAMARGO FORTE, M. M. 2006. Macromolecular coupling agents for flame retardant materials. *European Polymer Journal*, 42, 990-999.
- NAPPER, D. H. 1977. Steric stabilization. *Journal of Colloid and Interface Science*, 58, 390-407.
- NAPPER, D. H. (ed.) 1983. *Polymeric Stabilization of Colloidal Dispersions*, New York: Academic Press.
- NELSON, G. L. & WILKIE, C. A. 2001. Materials and Solutions for Hazards and Prevention. *Fire and polymers*, 797, 293-306.
- NEOUZE, M. A. & SCHUBERT, U. 2008. Surface modification and functionalization of metal and metal oxide nanoparticles by organic ligands. *Monatshefte Fur Chemie*, 139, 183-195.
- NEWBURY, D., JOY, D., ECHLIN, P. & FIORI, C. (eds.) 1986. *Advanced Scanning electron Microscopy and X-ray Microanalysis*, New York: Plenum Press.
- NOTO, T., BABUSHOK, V., BURGESS JR, D. R., HAMINS, A., TSANG, W. & MIIOLEK, A. 1996. Effect of halogenated flame inhibitors on C1-C2 organic flames. *Symposium (International) on Combustion*, 26, 1377-1383.
- OTTEWILL, R. H. 1977. Stability and instability in disperse systems. *Journal of Colloid and Interface Science*, 58, 357-373.
- PANIAS, D. & KRESTOU, A. 2007. Effect of synthesis parameters on precipitation of nanocrystalline boehmite from aluminate solutions. *Powder Technology*, 175, 163-173.
- PARFITT, G. D. (ed.) 1981. *Dispersion of Powders in Liquids*, London: Applied science Publishers Ltd.

- PARKS, G. A. 1965. ISOELECTRIC POINTS OF SOLID OXIDES SOLID HYDROXIDES AND AQUEOUS HYDROXO COMPLEX SYSTEMS. *Chemical Reviews*, 65, 177-8.
- PERRY, R. & GREEN, D. 1984. *Perry's Chemical Engineer's Handbook*, Singapore, Graw-Hill Inc.
- PETTERSSON, A., MARINO, G., PURSIHEIMO, A. & ROSENHOLM, J. B. 2000. Electrosteric Stabilization of Al₂O₃, ZrO₂, and 3Y-ZrO₂ Suspensions: Effect of Dissociation and Type of Polyelectrolyte. *Journal of Colloid and Interface Science*, 228, 73-81.
- PINFA 2010. Innovative Flame Retardants in E & E Applications. In: INCORPORATION, P. (ed.) Second Edition ed.: Pinfa- Phosphorous, Inorganic and Nitrogen Flame Retardant Association.
- PINNAVIA, T. & BEAL, W. (eds.) 2000. *Polymer-clay nanocomposites*, New York: Wiley
- PRESCOTT, W. & SCHWARTZ, A. (eds.) 2008a. *Nanorods, nanotubes and Nanomaterials Research Progress*, New York: Nova Science
- PRESCOTT, W. V. & SCHWARTZ, A. I. (eds.) 2008b. *Nano rods, Nanotubes and Nanomaterials Research Progress*, New York: Nova Science.
- PULOKAS, J., GREEN, C., KISSEBERTH, N., POTTER, C. S. & CARRAGHER, B. 1999. Improving the Positional Accuracy of the Goniometer on the Philips CM Series TEM. *Journal of Structural Biology*, 128, 250-256.
- QIANG, W., CHUCK, Z. & RICHARD, L. 2009. Combustion and thermal properties of epoxy /phenyltrisilanol polyhedral oligomeric silsesquioxane nanocomposites. *Therm. Anal. Calorim.*
- QUIANG, W., CHUCK, Z., LIANG, R. & WANG, B. 2009. Combustion and thermal properties of epoxy/phenyltrisilanol polyhedral oligomeric silsesquioxane nanocomposites. *Therm. Anal. Calorim.*
- RAHATEKAR, S. S., ZAMMARANO, M., MATKO, S., KOZIOL, K. K., WINDLE, A. H., NYDEN, M., KASHIWAGI, T. & GILMAN, J. W. 2010. Effect of carbon nanotubes and montmorillonite on the flammability of epoxy nanocomposites. *Polymer Degradation and Stability*, 95, 870-879.
- RAVVE, A. 1995. *Principles of Polymer Chemistry*, New York, Plenum Press.
- REIMER, L. (ed.) 1998. *Scanning Electron Microscopy, Physics of Image Formation and Microanalysis*, New York: Springer.
- REIMER, L. & KHOL, H. (eds.) 2008. *Transmission Electron Microscopy: Physics of Image Formation*, New York: Springer.
- ROMA, P., CAMINO, G. & LUDA, P. 1997. Mechanistic studies on fire retardant action of flourenated additives in ABS. *Fire and Materials*, 21, 6.

- ROSSER, W. A., WISE, H. & MILLER, J. 1958. Mechanism of combustion inhibition by compounds containing halogen. *Symposium (International) on Combustion*, 7, 175-182.
- ROTHON, N. (ed.) 2003a. *Particulate Filled Polymer Composites*, Shawbury-UK: Rapra Technology.
- ROTHON, N. (ed.) 2003b. *Particulate Filled Polymer Composites*, Shawbury: Rapra Technology Ltd.
- ROTHON, N. (ed.) 2003c. *Particulate Filled Polymer Composites*, Shawbury: Rapra Technology Ltd.
- ROUESSAC, F. & ROUSSAC, A. (eds.) 2000. *Chemical Analysis Modern Instrumentation Methods and Techniques*, New York: John Willey.
- RUBINSON, K. A. & RUBINSON, J. F. (eds.) 2000. *Contemporary Instrumental Analysis*: Printce Hall.
- RULON E, J., JR. 1984. A thermodynamic description of the double layer surrounding hydrous oxides. *Journal of Colloid and Interface Science*, 100, 540-554.
- SALLET, D., MAILHOS, V. & MARTEL, B. 1989. Flame Retardancy of Polyamide 11 with Decabromodiphenyl Antimony Trioxide Mixture. *Fire Retardant Polymer*, Proceeding of the third meeting.
- SAMYN, F., BOURBIGOT, S., DUQUESNE, S. & DELOBEL, R. 2007. Effect of zinc borate on the thermal degradation of ammonium polyphosphate. *Thermochimica Acta*, 456, 134-144.
- SARTOR, M. 2003. DYNAMIC LIGHT SCATTERING: to determine the radius of
of
small beads in brownian motion in a solution. San Diego: Technical report,
University of
California.
- SATO, T. & RUCH, R. (eds.) 1980. *Stabilization of Colloidal Dispersions by Polymer Adsorption*, New York: Marcel Dekker.
- SAVAGE, P., GOPALAN, S., MIZAN, T. & MARTINO, C. 1995. Reactions at supercritical conditions: Applications and fundamentals. *American Institute of
of
Chemical Engineeers (AIChE) Journal*, 41, 1723-1778.
- SAVAGE, P. E. 1999. Organic chemical reactions in supercritical water. *Chemical Reviews*, 99, 603-621.
- SCHARF, D. & NALEPA, R. 1992. Studies on flame retardant intumescent char. *Fire Safety*, 19, 103-117.

- SCHARTEL, B. & BATHOLMAI, M. 2006. Some comments on the main fire retardancy mechanisms in polymer nanocomposites. *Polym. Adv. Technol.*, 17, 772-777.
- SCHÄRTL, W. (ed.) 2007. *Light Scattering from Polymer Solutions and Nanoparticle Dispersions*, New York: Springer-Verlag Berlin Heidelberg.
- SCHEUTJENS, J. M. H. M. & FLEER, G. J. 1982. Effect of polymer adsorption and depletion on the interaction between two parallel surfaces. *Advances in Colloid and Interface Science*, 16, 361-380.
- SCHRADER, B. (ed.) 1995. *Infra Red and Raman Spectroscopy: Methods and Applications*, Weinheim: VCH.
- SHAPMAN, S. K. (ed.) 1986. *Maintaining and Monitoring the Transmission Electron Microscope*, London: Oxford University Press.
- SI, M., ZAITSEV, V., GOLDMAN, M., FRENKEL, A., PEIFFER, D. G., WEIL, E., SOKOLOV, J. C. & RAFAILOVICH, M. H. 2007. Self-extinguishing polymer/organoclay nanocomposites. *Polymer Degradation and Stability*, 92, 86-93.
- SILVERSTEIN, M., BASSLER, C. & MORRILL, C. (eds.) 1991. *Spectrometric Identification of Organic Compounds*, New York: John Wiley & Sons.
- SKOG, D. & HOLLER, F. 1999. *Principles of Instrumental Analysis*, Philadelphia, Sanders Golden.
- SOMMER, L. (ed.) 1989. *Analytical Absorption Spectrophotometry in the Visible and Ultraviolet: The principles*, Amsterdam: Elsevier.
- SPIELMAN, L. A. 1970. Viscous interactions in Brownian coagulation. *Journal of Colloid and Interface Science*, 33, 562-571.
- STRAUSS, H., HEEGN, H. & STRIENITZ, I. 1993. Effect of PAA adsorption on stability and rheology of TiO₂ dispersions. *Chemical Engineering Science*, 48, 323-332.
- TADORS, F. (ed.) 1982. *The Effect of Polymers on Dispersion Properties*, New York: Academic Press.
- TCHATCHOUA, C., SRINIVASAN, S. A. & GHASSEMI, H. 1997. Flame resistant epoxy networks based on aryl phosphine oxide containing diamine. *Polym. Prepr.*, 38(1), 113-14.
- THOMAS, J. & ANDO, J. (eds.) 1996. *Ultraviolet and Visible Spectroscopy*, Chichester: John Wiley & Sons.
- UNDERWRITER-LABORATORIES 1994. UL rapid rise fire tests of protection materials for structural steel. *UL 1709*. Unites States.
- UTAMAPANYA, S., KLABUNDE, K. J. & SCHLUP, J. R. 1991. NANOSCALE METAL-OXIDE PARTICLES CLUSTERS AS CHEMICAL REAGENTS - SYNTHESIS AND PROPERTIES OF ULTRAHIGH SURFACE-AREA

MAGNESIUM-HYDROXIDE AND MAGNESIUM-OXIDE. *Chemistry of Materials*, 3, 175-181.

- VAIA, R. A., LIU, W. D. & KOERNER, H. 2003. Analysis of small-angle scattering of suspensions of organically modified montmorillonite: Implications to phase behavior of polymer nanocomposites. *Journal of Polymer Science Part B-Polymer Physics*, 41, 3214-3236.
- VAIA, R. A., PRICE, G., RUTH, P. N., NGUYEN, H. T. & LICHTENHAN, J. 1999. Polymer/layered silicate nanocomposites as high performance ablative materials. *Applied Clay Science*, 15, 67-92.
- VAIDYANATHAN, G., SENDHILNATHAN, S. & ARULMURUGAN, R. 2007. Structural and magnetic properties of $\text{Co}_{1-x}\text{Zn}_x\text{Fe}_2\text{O}_4$ nanoparticles by co-precipitation method. *Journal of Magnetism and Magnetic Materials*, 313, 293-299.
- VERNARDAKIS, T., STATES, D. & TRACTON, A. (eds.) 2001. *Coating Technology Handbook*, New York: Marcel Dekker.
- VERWERY, E. W. & OVERBEEK, J. G. (eds.) 1948. *Theory of the stability of Lyophobic Colloids*, Amsterdam: Elsevier.
- VOORN, D. J., MING, W. & VAN HERK, A. M. 2006. Polymer-clay nanocomposite latex particles by inverse pickering emulsion polymerization stabilized with hydrophobic montmorillonite platelets. *Macromolecules*, 39, 2137-2143.
- VOYUTSKY, S. (ed.) 1978. *Colloid Chemistry*, Moscow: Mir Publisher.
- WANG, C. S. & LEE, M. C. 2000. Synthesis and properties of epoxy resins containing 2-(6-oxid-6H-dibenz(c,e)(1,2) oxaphosphorin-6-yl) 1,4-benzenediol (II). *Polymer*, 41, 3631-3638.
- WANG, C. S. & LIN, C. H. 1999. Synthesis and properties of phosphorus-containing PEN and PBN copolyesters. *Polymer*, 40, 747-757.
- WANG, D.-G., GUO, F., CHEN, J.-F., SHAO, L., LIU, H. & ZHANG, Z.-T. 2007a. A two-step way to synthesize nano inner-modified aluminum trihydroxide. *Colloids and Surfaces A: Physicochemical and Engineering Aspects*, 293, 201-209.
- WANG, D.-G., GUO, F., CHEN, J.-F., ZHAO, R.-H. & ZHANG, Z.-T. 2008. Synthesis of nano-platelets of modified aluminium hydroxide by high-gravity reactive precipitation and hydrothermal method. *Materials Chemistry and Physics*, 107, 426-430.
- WANG, M., JOSEPH, R. & BONFIELD, W. 1998. Hydroxyapatite-polyethylene composites for bone substitution: effects of ceramic particle size and morphology. *Biomaterials*, 19, 2357-2366.
- WANG, Z., HAN, E. & KE, W. 2005. Influence of nano-LDHs on char formation and fire-resistant properties of flame-retardant coating. *Progress in Organic Coatings*, 53, 29-37.

- WANG, Z., HAN, E. & KE, W. 2007b. Fire-resistant effect of nanoclay on intumescent nanocomposite coatings. *Applied polymer science*, 103, 1681-1689.
- WEIL, E. 1986. *Encyclopedia of Polymer Science and Technology*, 11 New York: Wiley Interscience.
- WILKIE, C. A. & MORGAN, A. B. 2010. *Fire Retardancy of Polymeric Materials*, CRC Press.
- WILLIAMS, A. (ed.) 1985. *Combustion Theory*, San Francisco: The Benjamin/Cummings Publishing Company.
- WLADYKA-PRZYBYLAK, M. & KOZLOWSKI, R. 1999. The thermal characteristics of different intumescent coatings. *Fire and Materials*, 23, 33-43.
- WYATT 2005. DAWN EOS Dynamic Light Scattering Manual. California: Wyatt Corporation.
- WYATT 2010. DAWN EOS Dynamic Light Scattering Manual. California: Wyatt Corporation.
- XIAO, J., HUANG, Y. & MANKE, C. 2010. Computational design of thermoset nanocomposite coatings: Methodological study on coating development and testing. *Chemical Engineering Science*, 65, 753-771.
- XIE, W., XIE, R. C., PAN, W. P., HUNTER, D., KOENE, B., TAN, L. S. & VAIA, R. 2002. Thermal stability of quaternary phosphonium modified montmorillonites. *Chemistry of Materials*, 14, 4837-4845.
- XU, M., CHOI, Y. S., KIM, Y. K., WANG, K. H. & CHUNG, I. J. 2003. Synthesis and characterization of exfoliated poly(styrene-co-methyl methacrylate)/clay nanocomposites via emulsion polymerization with AMPS. *Polymer*, 44, 6387-6395.
- YANG, S. Y., MA, C. C. M., TENG, C. C., HUANG, Y. W., LIAO, S. H., HUANG, Y. L., TIEN, H. W., LEE, T. M. & CHIOU, K. C. 2010. Effect of functionalized carbon nanotubes on the thermal conductivity of epoxy composites. *Carbon*, 48, 592-603.
- YOSHIMURA, M. & BYRAPPA, K. 2007. Hydrothermal processing of materials: past, present and future. *Journal of Materials Science*, 43, 2085-2103.
- YOSHIMURA, M. & BYRAPPA, K. 2008. Hydrothermal processing of materials: past, present and future. *Journal of Materials Science*, 43, 2085-2103.
- YU, X. & SOMASUNDARAN, P. 1996. Role of Polymer Conformation in Interparticle-Bridging Dominated Flocculation. *Journal of Colloid and Interface Science*, 177, 283-287.

- ZAMMARANO, M., FRANCESCHI, M., BELLAYER, S., GILMAN, J. W. & MERIANI, S. 2005. Preparation and flame resistance properties of revolutionary self-extinguishing epoxy nanocomposites based on layered double hydroxides. *Polymer*, 46, 9314-9328.
- ZHANG, S., HORROCKS, A. R., HULL, R. & KANDOLA, B. K. 2006. Flammability, degradation and structural characterization of fibre-forming polypropylene containing nanoclay-flame retardant combinations. *Polymer Degradation and Stability*, 91, 719-725.
- ZHENG, X., JIANG, D. D. & WILKIE, C. A. 2005. Methyl methacrylate oligomerically-modified clay and its poly(methyl methacrylate) nanocomposites. *Thermochimica Acta*, 435, 202-208.
- ZHU, F., KONG, E. S.-W., ZHANG, J. & ZHANG, Y. 2006. Surface modification of TiO₂ nanoparticles through plasma polymerization of acrylic acid. *Chemical Physics Letters*, 423, 270-275.
- ZYKA, J. (ed.) 1993. *Instrumentation in Analytical Chemistry*, New York: Ellis Horwood.